

**Bauhaus-Universität Weimar**

**Research Training Group 1462**

Experimental and semi-analytical multiscale approaches for the  
characterization of the elastic and viscoelastic behavior of  
polymer-modified cement-based materials

## **Dissertation**

zur Erlangung des akademischen Grades  
Doktor-Ingenieur (Dr.-Ing.)

an der Fakultät Bauingenieurwesen  
der Bauhaus-Universität Weimar

vorgelegt von

**Luise Göbel**

geboren am 29.09.1990

in Weimar

Gutachter: Prof. Dr.-Ing. Andrea Osburg  
Prof. Dr. techn. Bernhard Pichler  
Prof. Dr.-Ing. habil. Carsten Könke

Tag der Disputation: 16.11.2018



“Die Fragen sind es, aus denen das, was bleibt, entsteht.”

Erich Kästner (1899-1974), dt. Schriftsteller, Georg-Büchner-Preis 1957



# Preface and Acknowledgments

Die vorliegende Arbeit entstand in den Jahren 2014 bis 2018 während meiner Tätigkeit als wissenschaftliche Mitarbeiterin am Graduiertenkolleg 1462 „Bewertung gekoppelter numerischer und experimenteller Partialmodelle im Konstruktiven Ingenieurbau“ und an der Professur Bauchemie und Polymere Werkstoffe an der Bauhaus-Universität Weimar. Der Deutschen Forschungsgemeinschaft (DFG) danke ich ausdrücklich für die finanzielle Unterstützung.

Weiterhin danke ich der COST Action TU1404 „Towards the next generation of standards for service life of cement-based materials and structures“ für die finanzielle Unterstützung während meines Forschungsaufenthaltes in Wien. Vor allem aber möchte ich mich für die Bereitstellung wertvoller internationaler Kontakte, die wegweisend für meine wissenschaftliche Arbeit waren, bedanken.

Besonderer Dank gilt meiner Mentorin Prof. Dr.-Ing. Andrea Osburg, die mich bereits seit Studienbeginn stets bestmöglich unterstützt und gefördert hat und mir die Chance zur Anfertigung dieser Arbeit gab. Die gute wissenschaftliche Betreuung mit anregenden sowie kritischen Diskussionen war hilfreich für die Bearbeitung der Themenstellung, die zugleich viel Freiraum für eine selbstständige Ausgestaltung bot.

Ich möchte mich herzlich bei Prof. Dr. techn. Bernhard Pichler bedanken, der mit großer Begeisterung meine Idee aufnahm, die bestehenden Multiskalenmodelle für neue Materialien zu erweitern. Er ermöglichte mir die Durchführung eines erfolgreichen und bereichernden Forschungsaufenthaltes am Institut für Mechanik der Werkstoffe und Strukturen an der TU Wien. Auch danach unterstützte er mich durch zahlreiche wissenschaftliche Diskussionen und Denkanregungen bei der Fortführung der Modellierungsaufgaben sowie der Erstellung vielfältiger Publikationen.

Mein Dank gilt abermals Prof. Dr. techn. Bernhard Pichler und Prof. Dr.-Ing. habil. Carsten Könke für die Bereitschaft der Übernahme des Koreferats.

Ich möchte weiterhin Prof. Dr. rer. nat. Tom Lahmer danken, der Initiator dafür war, mich der Modellierung von Baustoffen zuzuwenden und die Brücke zwischen der experimentellen und der computergestützten Beschreibung von Beton zu schlagen.

Die Versuche mit dem Nanoindenter wurden am Karlsruher Institut für Technologie (Institut für Angewandte Materialien) durchgeführt. Hier möchte ich Clémence Bos danken für ihre Bereitschaft, sich auf ein neues Material einzulassen. Ich bedanke mich insbesondere für die Durchführung der Experimente und die Auswertung der Indentationsmoduln. Dr. Ruth Schwaiger danke ich dafür, dass sie die fruchtbare Zusammenarbeit ermöglicht und die Kooperation beratend begleitet hat. Außerdem danke ich ihr für die Unterstützung bei unseren gemeinsamen Veröffentlichungen.

Ich bedanke mich herzlich bei den Mitarbeitern der TU Wien, darunter Wolfgang Dörner, Roland Reihnsner, Olaf Lahayne, Dominic Hassan und Michael Schweigler, die mich tatkräftig bei den Kriechversuchen in der Rella-Halle unterstützt haben. Markus Königsberger danke ich für Diskussionen, Hinweise und Vorschläge auf dem Gebiet der Mikromechanik, insbesondere bei der Implementierung des GWR-Algorithmus.

Meinen Kollegen am Graduiertenkolleg, Tajammal Abbas und Igor Kavrakov, möchte ich für das positive und konstruktive Arbeitsklima danken. Dr.-Ing. Lars Abrahamczyk danke ich für die Möglichkeit der Teilnahme an zahlreichen Workshops und Konferenzen im In- und Ausland, die sehr hilfreich für meine wissenschaftliche Entwicklung waren.

Mein Dank gilt weiterhin den Mitarbeiterinnen und Mitarbeitern des F.A. Finger-Institutes für Baustoffkunde, die mir bei der experimentellen und organisatorischen Durchführung der Arbeit geholfen haben. Meinen Hiwis Felicitas Heumüller und Amir Azimian danke ich ebenfalls recht herzlich für die Unterstützung bei den experimentellen Arbeiten.

Mein größter Dank gebührt meiner Familie sowie meinem Partner Knut. Dank ihrer stetigen Unterstützung und des Rückhaltes verlor ich auch in Zeiten mit Rückschlägen nie die Motivation. Ich danke ihnen für ihr großes Verständnis, ihre Zuversicht und die Stärke, die sie mir gegeben haben.

# Abstract

Polymer-modified cement concrete (PCC) is a heterogeneous building material whose macroscopic material behavior is determined by its specific microstructure. The binder phase consists of both cementitious and polymer components. The microstructural characteristics hamper the applicability of computational models that are originally developed for conventional concretes to PCC. Such models are often empirical and consider only material phenomena that can be observed macroscopically. Multiscale models based on the methods of continuum micromechanics represent a promising complement. By means of a bottom-up approach, homogenized properties at the macroscopic scale are derived considering microstructural characteristics. In the literature, the models have already been successfully used to quantify the elastic stiffness, the compressive strength, and the creep behavior of conventional cement-based materials as functions of the hydration process.

The extension of an existing semi-analytical multiscale model for the application to polymer-modified cement-based materials is the main objective of this work. In this context, two aspects are investigated in more detail. (i) The hierarchical arrangement and the morphology of the material phases are discussed and partly measured. The polymer phase as well as the additional entrapped air porosity introduced as a result of polymer-cement interactions are taken into account. (ii) In addition, the changing microstructure of cementitious materials due to the progressive hydration process must be modeled appropriately. The presence of the polymer phase and the entrapped air requires the adaption of existing hydration models for the representation of the hydration-induced evolutions of the phase volume fractions.

The analytical approaches are complemented and enriched by cross-scale experimental studies. Macroscopic mechanical tests are performed to characterize the elastic and viscoelastic properties of polymer-modified cement pastes, mortars, and concretes. Of particular interest is the evolution of the mechanical behavior during the first week after production. The additional experimental determination of the micromechanical properties of the materials does not only provide model input parameters, but it also allows to establish relations between the material behavior at the macroscale and the microstructure.

The comparison between experiment and model prediction illustrates that the estimation of the elastic and viscoelastic behavior of polymer-modified cement-based materials is feasible by means of the extended multiscale model. The predictive capability is comparable, and in some cases even better, than of selected empirical models taken from standards and guidelines, which are applied to polymer-modified concretes.



# Kurzfassung

Polymermodifizierter Beton ist ein heterogener Baustoff, dessen makroskopisches Materialverhalten durch die spezifische Mikrostruktur bestimmt wird. Die Bindemittelphase besteht aus zementären und polymeren Bestandteilen. Die mikrostrukturellen Besonderheiten polymermodifizierter zementgebundener Materialien beeinträchtigen die Anwendbarkeit von Berechnungsmodellen, die ursprünglich für konventionelle Betone entwickelt wurden. Diese Modelle sind oftmals empirisch und berücksichtigen nur Materialphänomene, die makroskopisch erfasst werden können. Multiskalenmodelle, die auf Methoden der Kontinuumsmikromechanik basieren, stellen eine vielversprechende Ergänzung dar. Durch einen Bottom-up Ansatz werden hierbei homogenisierte Eigenschaften auf der makroskopischen Ebene ausgehend von mikrostrukturellen Charakteristika bestimmt. Die Modelle wurden in der Literatur bereits erfolgreich für die Abschätzung der elastischen Steifigkeit, der Druckfestigkeit und des Kriechverhaltens von konventionellen zementgebundenen Materialien in Abhängigkeit vom Hydratationsfortschritt angewendet.

Die Erweiterung eines bestehenden semi-analytischen Multiskalenmodells für die Anwendung auf polymermodifizierte Betone stellt das Hauptziel dieser Arbeit dar. In diesem Zusammenhang werden zwei Aspekte genauer untersucht. (i) Die hierarchische Anordnung und die Morphologie der Materialbestandteile werden diskutiert und zum Teil messtechnisch erfasst. Dies erfolgt unter Berücksichtigung der Polymerzugabe sowie der infolge von Polymer-Zement-Interaktionen zusätzlich eingebrachten Porosität. (ii) Darüber hinaus muss die sich verändernde Mikrostruktur von Beton aufgrund von fortschreitenden Hydratationsprozessen adäquat abgebildet werden. Das Vorhandensein der Polymerphase und der Lufteinschlüsse erfordert die Adaptierung von bestehenden Hydratationsmodellen zur Beschreibung der zeitabhängigen Volumenanteile der Materialphasen.

Die analytischen Ansätze werden durch skalenübergreifende experimentelle Untersuchungen ergänzt. Die experimentelle Erfassung von mikromechanischen Eigenschaften dient nicht nur der Generierung von Modelleingangsparametern, sondern erlaubt es auch, Korrelationen zwischen dem Materialverhalten auf der Makroskala und der Mikrostruktur herzustellen. Makroskopische mechanische Tests dienen der Charakterisierung der elastis-

chen und viskoelastischen Eigenschaften polymermodifizierter Zementsteine, Mörtel und Betone. Von besonderem Interesse ist dabei das Verhalten während der ersten Woche nach der Herstellung.

Der abschließende Vergleich zwischen Experiment und Modellvorhersage zeigt, dass die Abschätzung des elastischen und viskoelastischen Verhaltens von polymermodifizierten zementgebundenen Materialien mit Hilfe des weiterentwickelten Multiskalenmodells möglich ist. Die Prognosefähigkeit ist vergleichbar und in einigen Fällen sogar besser als die Vorhersagequalität ausgewählter empirischer Modelle, die Normen und Richtlinien entnommen und auf polymermodifizierten Betone angewendet werden.

# Contents

<b>List of figures</b>	<b>viii</b>
<b>List of tables</b>	<b>x</b>
<b>Symbols and abbreviations</b>	<b>xiv</b>
<b>1 Introduction</b>	<b>1</b>
1.1 Motivation . . . . .	1
1.2 Objective and approach . . . . .	2
1.3 Outline of the thesis . . . . .	4
<b>2 State of the art</b>	<b>5</b>
2.1 Polymer-modified cement-based materials . . . . .	5
2.1.1 Polymers in cement-based systems . . . . .	5
2.1.2 Microstructure of PCC . . . . .	7
2.1.3 Fresh concrete properties . . . . .	15
2.1.4 Hardened concrete properties . . . . .	16
2.1.5 Deformation behavior . . . . .	18
2.1.6 Modeling the mechanical behavior of PCC . . . . .	20
2.2 Multiscale modeling of cement-based materials . . . . .	22
2.2.1 Fundamentals of multiscale modeling . . . . .	22
2.2.2 Multiscale modeling approaches . . . . .	23
2.2.3 Multiscale modeling based on continuum micromechanics . . . . .	25
2.2.4 Experimental calibration and validation . . . . .	35
2.3 Creep behavior of cement-based materials . . . . .	38
2.3.1 Long-term deformations in cement-based materials . . . . .	38
2.3.2 Definition and origin of creep in cement-based materials . . . . .	39
2.3.3 Short-term creep testing . . . . .	40
2.3.4 Fundamental formulations of creep . . . . .	41

2.3.5	Multiscale prediction models for creep . . . . .	44
2.4	Summary and scientific questions . . . . .	47
<b>3</b>	<b>Evaluation of semi-analytical multiscale models</b>	<b>49</b>
3.1	Fundamentals of probabilistic evaluation analyses . . . . .	49
3.1.1	Introduction . . . . .	49
3.1.2	Sampling techniques . . . . .	51
3.1.3	Sensitivity analysis . . . . .	52
3.1.4	Uncertainty analysis . . . . .	54
3.2	Uncertainty and sensitivity analysis in material models . . . . .	57
3.2.1	Uncertainty and sensitivity analysis in concrete creep models . . . . .	57
3.2.2	Uncertainty and sensitivity analysis in multiscale models . . . . .	58
3.3	Evaluation of a semi-analytical multiscale model for cement-based materials	59
3.3.1	Hydration models . . . . .	60
3.3.2	Probabilistic input parameters . . . . .	65
3.3.3	Probabilistic model predictions . . . . .	66
3.3.4	Results of the sensitivity analysis . . . . .	69
3.3.5	Results of the uncertainty analysis . . . . .	75
<b>4</b>	<b>Experimental multiscale study of PCC</b>	<b>79</b>
4.1	Materials . . . . .	81
4.1.1	Cement . . . . .	81
4.1.2	Polymers . . . . .	81
4.1.3	Sand and aggregates . . . . .	83
4.1.4	Mixture design . . . . .	83
4.2	Experimental investigations with polymers . . . . .	84
4.2.1	Sample preparation . . . . .	84
4.2.2	Nanoindentation testing . . . . .	85
4.3	Experimental investigations with cement pastes . . . . .	86
4.3.1	Hydration kinetics . . . . .	86
4.3.2	Microstructure . . . . .	87
4.3.3	Fresh cement paste properties . . . . .	88
4.3.4	Hardened cement paste properties . . . . .	88
4.4	Experimental investigations with mortars . . . . .	95
4.4.1	Fresh mortar properties . . . . .	95
4.4.2	Hardened mortar properties . . . . .	95
4.5	Experimental investigations with concretes . . . . .	95
4.5.1	Fresh concrete properties . . . . .	95

4.5.2	Hardened concrete properties . . . . .	96
4.6	Results . . . . .	96
4.6.1	Polymers . . . . .	96
4.6.2	Cement pastes . . . . .	97
4.6.3	Mortars . . . . .	114
4.6.4	Concretes . . . . .	117
4.7	Summary . . . . .	119
<b>5</b>	<b>Early-age characterization of polymer-modified cement-based materials</b>	<b>121</b>
5.1	Experimental campaign . . . . .	121
5.1.1	Mixture design . . . . .	122
5.1.2	Quasi-isothermal differential calorimetry . . . . .	122
5.1.3	Experimental setup of the short-term creep tests . . . . .	124
5.1.4	Test regime . . . . .	125
5.1.5	Test evaluation . . . . .	126
5.2	Experimental results . . . . .	129
5.2.1	Evolution of the elastic properties . . . . .	129
5.2.2	Evolution of the creep properties . . . . .	131
5.2.3	Evolution of the creep strains . . . . .	134
5.2.4	Assumption of a constant power-law exponent . . . . .	136
5.3	Semi-analytical multiscale modeling of polymer-modified cement-based materials . . . . .	138
5.3.1	Micromechanical representation of polymer-modified cement-based materials . . . . .	138
5.3.2	Model input parameters . . . . .	139
5.3.3	Homogenization of isotropic elastic stiffness properties of polymer-modified cement pastes . . . . .	142
5.3.4	Homogenization of creep properties of polymer-modified cement pastes	151
5.3.5	Creep homogenization of polymer-modified concretes . . . . .	161
5.4	Summary . . . . .	164
<b>6</b>	<b>Comparison of empirical and multiscale modeling approaches</b>	<b>167</b>
6.1	Prediction of elasticity . . . . .	167
6.1.1	Empirical models for the prediction of the elastic modulus . . . . .	167
6.1.2	Predictive capabilities of the empirical models applied to PCC . . . . .	169
6.2	Prediction of creep . . . . .	172
6.2.1	Empirical creep compliance functions . . . . .	172
6.2.2	Application of the empirical creep models to PCC . . . . .	176

<b>7 Summary and conclusions</b>	<b>181</b>
<b>8 Outlook</b>	<b>187</b>
<b>References</b>	<b>221</b>
<b>A Appendix</b>	<b>A-1</b>
A.1 Computation of Hill tensors . . . . .	A-1
A.2 Hydration kinetic laws of the Bernard model . . . . .	A-3
A.3 Model input parameters and their stochastic properties . . . . .	A-4
A.3.1 Input parameters for the Powers model . . . . .	A-4
A.3.2 Input parameters for the Bernard model . . . . .	A-5
A.4 The Gaver-Wynn-Rho Algorithm . . . . .	A-8
A.5 List of input parameters for the empirical creep models . . . . .	A-9
<b>Publications of the author</b>	<b>A-11</b>

# List of Figures

2.1	Polymer powder particles after spray drying and after redispersion . . . . .	6
2.2	SEM images of the ITZ in unmodified and polymer-modified mortar . . . . .	14
2.3	Crack between matrix and aggregate, bridged by stretched polymers . . . . .	17
2.4	Rheological model of Heidolf . . . . .	20
2.5	Hierarchical multiscale nature of concrete . . . . .	22
2.6	Approaches for the multiscale modeling of structures . . . . .	24
2.7	Scale of separation principle . . . . .	26
2.8	Micromechanical representation of cement-based materials . . . . .	27
2.9	Approximation of realistic particle shapes in cement pastes by spheroids . .	28
2.10	Stiffness evolution of cement pastes as a function of the degree of hydration	29
2.11	Ellipsoidal inclusion embedded in an infinite matrix . . . . .	33
2.12	Microstructural types of RVE . . . . .	33
2.13	Experiments required in the context of multiscale modeling . . . . .	35
2.14	Principle of nanoindentation testing . . . . .	36
2.15	Statistical nanoindentation and data evaluation . . . . .	37
2.16	Time-dependent deformations in concrete . . . . .	39
2.17	Discretization of the stress history into stress increments and into stress impulses . . . . .	43
2.18	Morphological representation of concrete including sliding planes . . . . .	45
3.1	Workflow of the probabilistic model evaluation. . . . .	50
3.2	Parameter set sampled by means of MCS and LHS . . . . .	51
3.3	Relation between model complexity and uncertainty . . . . .	55
3.4	Evolution of the cement paste-related phase volume fractions using the Powers model . . . . .	61
3.5	Evolution of the cement paste-related phase volume fractions using the Bernard model . . . . .	64
3.6	Adapted morphological model of concrete . . . . .	65

3.7	Stochastic Young's moduli of a multiscale model using the Powers model and the Bernard model . . . . .	68
3.8	Evolution of total order sensitivity indices for the Powers model . . . . .	70
3.9	Evolution of total order sensitivity indices for the Bernard model . . . . .	71
3.10	Total order sensitivity indices at the concrete scale resulting from varying uncertainties exhibited by the aggregates . . . . .	74
3.11	Total order sensitivity indices at the concrete scale resulting from varying uncertainties exhibited by the elastic properties of the aggregates . . . . .	75
3.12	Evolution of the parameter uncertainty for the Powers model and the Bernard model . . . . .	76
3.13	Total uncertainties for the Powers model and the Bernard model . . . . .	77
4.1	Surface images of cement pastes, observed using SEM . . . . .	92
4.2	Storage, loss, and Young's moduli of solid polymer specimens . . . . .	97
4.3	Heat rate and cumulative heat quantity of the cement pastes . . . . .	98
4.4	Temporal evolution of the degree of hydration of the cement pastes . . . . .	98
4.5	Microstructure of the plain cement paste . . . . .	99
4.6	Microstructure of the polymer-modified cement paste P1 . . . . .	100
4.7	Microstructure of the polymer-modified cement paste P2 . . . . .	101
4.8	Microstructure of the polymer-modified cement paste P3 . . . . .	101
4.9	Consistencies of unmodified and polymer-modified cement pastes . . . . .	102
4.10	Compressive strengths of unmodified and polymer-modified cement pastes . . . . .	105
4.11	Dynamic moduli of unmodified and polymer-modified cement pastes . . . . .	106
4.12	Length changes of plain and polymer-modified cement pastes . . . . .	107
4.13	Indentation moduli derived from nanoindentation tests using the Express Test option . . . . .	108
4.14	Indents in the reference cement paste . . . . .	109
4.15	Phase volume fractions derived from nanoindentation tests using the Express Test option . . . . .	110
4.16	Indentation moduli derived from nanoindentation tests using the CSM option . . . . .	110
4.17	Mean indentation moduli of the cement pastes . . . . .	111
4.18	Displacements of the cement pastes during the nanoindentation creep tests . . . . .	112
4.19	Contact creep function of cement pastes obtained by nanoindentation creep tests . . . . .	113
5.1	Time-dependent evolution of the heat rate and the degree of hydration . . . . .	123
5.2	The experimental setup of the short-term creep tests . . . . .	124
5.3	Loading regimes defined for the creep tests . . . . .	126



5.4	Creep strain evolution . . . . .	127
5.5	Evolutions of the Young’s moduli of cement pastes . . . . .	129
5.6	Evolutions of the Young’s moduli of concretes . . . . .	131
5.7	Evolutions of the creep compliances of cement pastes . . . . .	132
5.8	Evolutions of the creep compliances of concretes . . . . .	133
5.9	Evolutions of the power-law exponents of cement pastes . . . . .	133
5.10	Evolutions of the power-law exponents of concretes . . . . .	134
5.11	Experimentally determined creep strain evolutions and corresponding power-law for cement pastes at given time instants . . . . .	135
5.12	Experimentally determined creep strain evolutions and corresponding power-law for cement pastes at given hydration degrees . . . . .	135
5.13	Experimentally determined creep strain evolutions and corresponding power-law for concretes at given time instants . . . . .	136
5.14	Experimentally determined creep strain evolutions and corresponding power-law for concretes at given hydration degrees . . . . .	136
5.15	Creep compliances of the polymer-modified cement pastes P2 and P3 . . .	137
5.16	Micromechanical representation of polymer-modified cement-based materials	139
5.17	Evolution of volume fractions in unmodified and polymer-modified cement pastes . . . . .	141
5.18	Comparison of the model-predicted Young’s modulus and the experimental results for the unmodified mixtures . . . . .	144
5.19	Comparison of the model-predicted and the experimentally determined Young’s moduli for the polymer-modified cement pastes . . . . .	145
5.20	Comparison of the model-predicted and the experimentally determined Young’s moduli for the polymer-modified concretes . . . . .	146
5.21	Experimentally determined versus model-predicted Young’s moduli of polymer-modified cement pastes . . . . .	146
5.22	Experimentally determined versus model-predicted Young’s moduli of polymer-modified mortars . . . . .	147
5.23	Comparison of model-predicted Young’s moduli with experimental data of Flohr . . . . .	148
5.24	Evolution of total order sensitivity indices of the multiscale model for polymer-modified cement-based materials . . . . .	150
5.25	Comparison of experimentally determined and model-predicted viscous strains of the polymer-modified cement pastes, considering constant polymer creep properties . . . . .	156

5.26	Mean errors for age-independent power-law creep exponents and for age-dependent shear creep moduli . . . . .	157
5.27	Comparison of experimental and computed creep strains of the polymer-modified cement pastes, considering age-dependent shear creep moduli and constant power-law creep exponents. . . . .	158
5.28	Evolutions of the shear creep modulus as functions of the material age, considering time-independent power-law creep exponents . . . . .	159
5.29	Evolutions of the shear creep modulus and the power-law creep exponent as functions of the material age . . . . .	160
5.30	Comparison of experimental and computed creep strains of the polymer-modified cement, considering both age-dependent shear creep moduli and age-dependent power-law creep exponents. . . . .	161
5.31	Comparison of experimental and computed creep strains of polymer-modified concretes P2 and P3. . . . .	162
6.1	Estimations of the Young's modulus of concrete . . . . .	168
6.2	Comparison between experimentally determined and model-predicted elastic moduli of polymer-modified concretes . . . . .	170
6.3	Experimentally determined creep strains by Flohr (Test 1) compared with predictions of empirical models and of a multiscale approach . . . . .	179
6.4	Experimentally determined creep strains by Flohr (Test 2) compared with predictions of empirical models and of a multiscale approach . . . . .	179

# List of Tables

3.1	Input parameters required for multiscale modeling . . . . .	66
3.2	Variations of the stochastic parameters assigned to the volume fraction and the elastic parameters of the aggregates . . . . .	73
4.1	Overview of the experimental multiscale study . . . . .	80
4.2	Mass percentage of the chemical components of the Portland cements . . .	81
4.3	Mineralogical compositions of the used Portland cements . . . . .	81
4.4	Characteristics of the polymers . . . . .	82
4.5	Mix design of polymer-modified mortars . . . . .	83
4.6	Mix design of polymer-modified concretes . . . . .	84
4.7	Nanoindentation parameters for the viscoelastic analysis of polymer specimens	86
4.8	Density and porosity of the cement pastes . . . . .	104
4.9	Contact creep modulus and characteristic time obtained from nanoindentation tests . . . . .	114
4.10	Properties of fresh plain and polymer-modified mortars . . . . .	115
4.11	Properties of hardened plain and polymer-modified mortars . . . . .	116
4.12	Properties of fresh unmodified and polymer-modified concretes . . . . .	117
4.13	Properties of hardened plain and polymer-modified concretes . . . . .	118
5.1	Bulk and particle density and porosity of the cement pastes . . . . .	130
5.2	Bulk density, particle density, and porosity of the concretes . . . . .	131
5.3	Elastic properties of the material phases in polymer-modified cement-based materials . . . . .	142
5.4	Validation experiments and corresponding mixture characteristics . . . . .	144
5.5	Mean errors for universal and age-dependent polymer creep properties . . .	157
5.6	Mean errors for universal and age-dependent polymer creep properties for the creep homogenization of polymer-modified concretes . . . . .	163
6.1	Empirical models for the determination of the elastic modulus . . . . .	169

6.2	Goodness-of-fit . . . . .	171
6.3	Experimental parameters and boundary conditions of the long-term creep tests with PCC by Flohr . . . . .	177
A.1	Input parameters and their stochastic properties for the Powers model . . .	A-4
A.2	Input parameters and their stochastic properties for the Bernard model . .	A-5
A.3	Input parameters and their stochastic properties for the Bernard model . .	A-6
A.4	Input parameters and their stochastic properties for the Bernard model . .	A-7
A.5	List of input parameters for the creep models . . . . .	A-9

# Symbols and Abbreviations

Symbols and abbreviations that are not listed in the following tables will be explained in the text.

## Abbreviations of the cement chemistry

A	$\text{Al}_2\text{O}_3$	H	$\text{H}_2\text{O}$
C	CaO	S	$\text{SiO}_2$
F	$\text{Fe}_2\text{O}_3$	$\bar{S}$	$\text{SO}_3$

## Abbreviations of the polymer chemistry

EVA	ethylene-co-vinyl acetate	SA	polystyrene acrylic ester
PVA	polyvinyl alcohol	SBR	polystyrene butadiene rubber
PVAc	polyvinyl acetate		

## Abbreviations of measurement methods

CSM	continuous stiffness measurement	NMR	nuclear magnetic resonance
ESEM	environmental scanning electron microscope	SEM	scanning electron microscope
		XRD	X-ray powder diffraction
ET	Express Test		

## Frequently used abbreviations

AASHTO	American Association of Highway and Transportation Officials	EC	Eurocode
		Eq.	Equation
ACI	American Concrete Institute	EHE	Spanish Code on Structural Concrete
CC	conventional concrete		
CDF	cumulative density function	FIB	Federation Internationale du Beton
CEB	Comite Euro-International du Beton	GWR	Gaver-Wynn-Rho algorithm
C-S-H	calcium silicate hydrate phases	ITZ	interfacial transition zone

DoH	degree of hydration	P3	polymer 3
LC	Laplace Carson	PCC	polymer-modified (cement) concrete
LHS	Latin Hypercube Sampling	PDF	probability density function
LOI	loss on ignition	Ref.	Reference (sample)
LVDT	linear variable differential transducer	RH	relative humidity
MAPE	mean absolute percentage error	RMS	root-mean-squared
MC	Model Code	RVE	representative volume element
MCS	Monte Carlo Simulation	SD	standard deviation
MFT	minimum film formation temperature	$a/c$	aggregate-to-cement mass ratio
NBR	Brazilian Association of technical standards	$p/c$	polymer-to-cement mass ratio
P1	polymer 1	$s/c$	sand-to-cement mass ratio
P2	polymer 2	$w/c$	water-to-cement mass ratio
		unif(..)	uniform distribution

## Frequently used indices

$(..)_{agg}$	aggregates	$(..)_{model}$	model-predicted
$(..)_{c}$	concrete	$(..)_{pol}$	polymer
$(..)_{clin}$	clinker	$(..)_{pore}$	pore phase (water and air)
$(..)_{cp}$	cement paste	$(..)_{ref}$	reference
$(..)_{cyl}$	cylindrical	$(..)_{rel}$	relative
$(..)_{dyn}$	dynamic	$(..)_{san}$	sand
$(..)_{exp}$	experimentally determined	$(..)_{sh}$	shrinkage
$(..)_{hf}$	hydrate foam	$(..)_{sph}$	spherical
$(..)_{hom}$	homogenized	$(..)_{v}$	viscous
$(..)_{hyd}$	hydrates	$(..)_{w}$	water
$(..)_{j}$	refers to phase $j$		

## Latin letters

$\tilde{A}$	affinity		phase $j$
$A_c$	contact area	$E(..)$	expected value
$A$	fourth-order strain concentration tensor	$E$	elastic (Young's) modulus
$A_j$	fourth-order strain concentration tensor of phase $j$	$E_c$	creep modulus
$C$	creep compliance	$E_u$	unloading modulus
$C_0$	basic creep compliance	$E^*$	complex modulus
$C_d$	drying creep compliance	$E'$	storage modulus
$C_i$	contact creep modulus	$E''$	loss modulus
$\mathbb{C}$	fourth-order stiffness tensor	$E_a^*$	adjustment factor
$\mathbb{C}_j$	fourth-order stiffness tensor of	$E_{a,x}$	activation energy
		$\mathbf{E}$	macroscopic strain
		$\mathcal{E}$	error

$F$	force	$V(E(Y X))$	variance of conditional expectation
$\mathbb{I}$	fourth-order identity tensor	$V/S$	volume-surface ratio
$\mathbb{I}^{\text{dev}}$	deviatoric part of fourth-order identity tensor	$X$	parameter
$\mathbb{I}^{\text{vol}}$	volumetric part of fourth-order identity tensor	$Y$	model response
$J$	creep compliance function	$\hat{Y}$	experimental value
$J_v$	viscous part of $J$	$Y_p$	response of adjusted model
$\mathbb{J}_j$	fourth-order creep function of phase $j$	$Y^*$	response of best model
$L$	contact creep compliance	$Y^{\mathcal{M}_i}$	response of model $\mathcal{M}_i$
$L_g$	initial measurement length	$a_u$	contact radius
$M$	indentation modulus	$d$	diameter
$\mathcal{M}$	model	$f_c$	compressive strength of concrete
$N$	number	$f_d$	resonance frequency of the expansion wave
$P$	total porosity	$f_j$	volume fraction of phase $j$
$P(\cdot)$	probability	$f_j^{\text{hf}}$	hydrate foam-related volume fraction of phase $j$
$P_{\text{max}}$	applied maximum load	$f_j^{\text{cp}}$	cement paste-related volume fraction of phase $j$
$\mathbb{P}_r$	fourth-order Hill tensor of inclusion with shape $r$ , $r \in \{\text{sph, cyl}\}$	$h$	indentation depth
$Q$	heat release	$k_j$	bulk modulus of phase $j$
$\mathcal{R}$	universal gas constant	$l$	length
$\mathbb{R}_j$	fourth-order relaxation function of phase $j$	$m_i$	initial weight
$S$	contact stiffness	$m_o$	output weight
$S_i$	first order sensitivity index	$p$	complex variable in LC domain
$S_{T_i}$	total order sensitivity index	$s$	slump
$T$	temperature	$t$	chronological time
$V$	volume	$t_d$	time when drying starts
$V(\cdot)$	variance	$t_{\text{ref}}$	reference time
$V(Y)$	unconditional variance	$v_l$	sound velocity of longitudinal waves
$V(Y X)$	conditional variance	$v_t$	sound velocity of transversal waves
		$x$	position vector

## Greek letters

$\Gamma(\cdot)$	gamma function of quantity $(\cdot)$	$\gamma_c$	unit weight of concrete
$\Sigma$	macroscopic stress	$\delta_{ij}$	Kronecker delta
$\Omega$	volume of the RVE	$\varepsilon_c$	total strain
$\partial\Omega$	boundary of the RVE	$\varepsilon_{c,\text{creep}}$	creep strain
$\alpha$	correction factor	$\varepsilon_{c,\text{elastic}}$	elastic strain
$\alpha_a$	air void content	$\varepsilon$	second-order strain tensor
$\beta$	power-law exponent	$\varepsilon_j$	second-order strain tensor of phase $j$
$\beta_j$	power-law creep exponent of phase $j$		
$\gamma$	power-law exponent	$\vartheta$	zenith angle

$\kappa$	exponent for reaction order	$\sigma_X$	parameter uncertainty
$\mu_j$	shear modulus of phase $j$	$\sigma_{X_i}$	standard uncertainty of input parameter $X_i$
$\mu_{c,j}$	shear creep modulus of phase $j$		
$\xi$	degree of hydration	$\sigma_y$	tensile strength
$\underline{\xi}$	displacement vector	$\tau$	time instant of loading
$\nu$	Poisson's ratio	$\tau_i$	characteristic time
$\rho$	particle density	$\tau_s$	shear strength
$\rho_{\text{bulk}}$	bulk density	$\varphi$	azimuth angle
$\rho_c$	aging coefficient	$\varphi_c$	creep coefficient
$\boldsymbol{\sigma}$	second-order stress tensor	$\varphi_{c,\infty}$	ultimate creep coefficient
$\boldsymbol{\sigma}_j$	second-order stress tensor of phase $j$	$\psi_c$	relaxation coefficient
$\sigma_c$	applied constant stress		

## Mathematical operators

$\mathbf{1}$	second-order identity tensor	div	divergence operator
$\cdot$	inner product	$\Delta$	increment
$:$	second-order tensor concentration	$\nabla$	nabla operator
$(..)^*$	Laplace-Carson transform of quantity (..)	$\otimes$	dyadic product



# 1 | Introduction

## 1.1 Motivation

Civil engineering structures are increasingly required to be economical and resource friendly. However, more slender and durable constructions call for the development of new generations of building materials as well as reliable methods for the assessment of the lifetime, serviceability, and load-bearing capacity.

Much research has been carried out to improve the performance of concrete, which is the most-used man-made material on Earth. Globally, about 25 billion tons of concrete are produced every year [1]. This building material is being continuously optimized to improve its resistance to the conditions to which it is subjected. Thus, more complex mixture designs are replacing the classical three-component-system consisting of cement, water, and aggregates.

One approach to optimizing concrete performance is the modification of the binder matrix. Several admixtures and additives are available that influence the fresh and hardened concrete properties. Polymer-modified cement mortars and concretes (PCC), in which cementitious and polymer components together form the binder matrix, are well established in repair and restoration. The importance of these materials in construction is nowadays also increased considerably. PCC are mainly applied in conditions that are chemically and mechanically demanding due to their improved chemical resistance, adhesion to substrates, and impermeability [2]. Still, these favorable properties go hand in hand with both a reduced elastic stiffness and a more pronounced creep activity.

For the efficient use of polymer-modified concrete in construction, its mechanical behavior must be well understood, and, furthermore, it must be predictable. For this, the establishment of a relation between the microscopic properties and the macroscopic material behavior is essential. Prediction models that take into account the different length scales of the material are helpful for providing a more general description of the influences of

polymers in cement-based materials. The models are also fundamental for the development of guidelines for new building materials and represent an important step towards the use of PCC in construction.

First approaches aimed at the prediction of the mechanical properties of PCC have already been proposed [3, 4, 5]. However, these models are not generally applicable to different mixture compositions and different polymer types. The models are empirical and often require model calibration using experimental data. The significantly different creep behavior of PCC compared with conventional concrete does also not allow for the simple application of macroscopic creep prediction models, which were originally developed for conventional concretes [6, 7]. A suitable microstructure-based method for estimating the mechanical behavior of polymer-modified cement-based materials is not available.

## 1.2 Objective and approach

Heterogeneous materials, such as concrete, represent multi-phase materials. To characterize the behavior of these materials, complex constitutive formulations are usually derived. Corresponding model calibration is often costly and requires several iterative steps. In contrast, multiscale models represent the material behavior across different length scales in a detailed way. By means of analytical or numerical homogenization methods, models defined at the micro-, meso-, or macroscale can be coupled.

Multiscale models based on the principles of continuum micromechanics appear to be promising for polymer-modified cement-based materials because they explicitly consider microstructural specifics as well as hydration-induced changes of the volume fractions of the constituents. Furthermore, a minimum number of material constants having a physical meaning instead of fitted parameters is employed. The properties of the compound material on the macroscopic scale are derived from the properties of the microstructural constituents by means of a bottom-up approach. This work aims to extend existing multiscale methods, originally developed for conventional cement-based materials, to use for PCC. The applicability of these models for polymer-modified cement-based materials needs to be proved. One relevant aspect concerns the implementation of the polymer phase into the model.

The strength, elasticity, and creep are the major mechanical properties characterizing cement-based materials. The elastic stiffness and the creep behavior of PCC, particularly their experimental quantification and microstructure-based prediction, are the main focuses of this thesis. To this end, continuum micromechanics approaches are applied.

To obtain a reliable multiscale model for polymer-modified cement-based materials, experimental data for the model calibration and validation are required. The intrinsic elastic and creep properties of the constituents, particularly of the polymers, were quantified using the nanoindentation technique. An experimental multiscale study with cement pastes, mortars, and concretes was conducted to characterize their mechanical behavior. Of particular importance was the early-age behavior of PCC because long-term durability is only achievable, if the materials remain undamaged at early ages. An experimental campaign aimed at the quasi-continuous quantification of the elastic and creep properties of young cement pastes and concretes was carried out. As regards to the polymer modification, three different polymers were used: one re-dispersible powder and two dispersions. Varying polymer contents were considered to provide a broad overview of the properties of PCC.

The experimental data, and correspondingly, the model input parameters exhibit stochastic variations that entail a scattering model response. The influences of the uncertain parameters on the multiscale model output were evaluated using probabilistic methods. The concepts of sensitivity and uncertainty analyses were used to identify influential input parameters across the scales of the model. Sensitivity indices quantified the influences of the input parameters on the model-predicted Young's moduli of cement-based materials. Within the analysis, two aspects deserve particular attention: the mixture composition and the hydration time. The microstructure of concrete does not remain constant over time. The hydration process, i.e. the continuous reaction between clinker minerals and water leading to the precipitation of hydration products, goes along with evolving volume fractions of the reactants. Different hydration models have been developed to predict the evolution of the material phases with time. The hydration models are combined with the semi-analytical multiscale models to account for the time-variant nature of concrete. However, the influence of the choice of the hydration model within the multiscale modeling procedure has not yet been investigated. In this thesis, the concept of total uncertainty was used to rank two hydration models regarding the uncertainty that the model responses show. The total uncertainty was determined based on the adjustment factor approach.

The responses of different empirical models predicting the elastic modulus of concrete were compared with the experimental data of different PCC. A comparison between phenomenological and multiscale model responses was also carried out for the creep phenomenon. Long-term creep tests of polymer-modified concrete reported in the literature were used as a reference. With that, the question has to be answered as to whether or not the multiscale models, which directly account for microstructural specifics, are more appropriate for predicting the elastic and creep behavior of PCC compared with empirical models that are solely defined on the macroscopic scale.

## 1.3 Outline of the thesis

**Chapter 2** presents the state of the art of polymer-modified cement-based materials with particular emphasis on the influences of polymers on the microstructure, the hydration kinetics, and the mechanical properties. Furthermore, basic aspects of multiscale modeling are summarized, covering the introduction of representative volume elements and the principles of continuum micromechanics, as well as the fundamentals of the creep behavior of cement-based materials.

In **Chapter 3**, the evaluation of a semi-analytical multiscale model by means of probabilistic analyses is carried out. In detail, sensitivity and uncertainty analyses are explained and applied within the context of multiscale modeling based on the principles of continuum micromechanics. Two different hydration models are compared with respect to their influences on the uncertainties of the multiscale model responses on the scales of cement paste, mortar, and concrete.

**Chapter 4** presents an experimental multiscale study carried out with polymer-modified cement pastes, mortars, and concretes. Besides macroscopic quantities, the elastic and viscoelastic micromechanical properties of solid polymer specimens and cement pastes are investigated.

The focus of **Chapter 5** is the early-age elastic and creep behavior of polymer-modified cement pastes and concretes. An experimental campaign is presented with the aim of achieving the quasi-continuous quantification of early-age mechanical properties. The experimental data are exploited in the form of multiscale modeling based on continuum micromechanics. Existing multiscale models are extended to the application to PCC. Experimental data reported in Chapter 4 are used as both input and validation parameters for the model.

In **Chapter 6**, the responses of empirical and semi-analytical multiscale models are compared with respect to the predictive capability for polymer-modified cement-based materials. Empirical models, which are defined on the macroscopic material scale, are compared with experimental data concerning the elastic and creep behavior of PCC, and the goodness-of-fit is evaluated.

**Chapter 7** summarizes the results of the thesis.

**Chapter 8** provides an outlook regarding further research possibilities in the areas of semi-analytical multiscale modeling and polymer-modified cement-based materials.

## 2 | State of the art

### 2.1 Polymer-modified cement-based materials

The demand for durable, economic, and stable constructions is growing continuously, which requires the development of new generations of building materials. Since the 1950s, cement-based materials modified with polymers have experienced a steady boom. Particularly in repair and restoration as well as in surface protection systems, polymer-modified mortars and concretes have been established, e.g. [2, 8, 9]. During the past few years, these materials have been increasingly applied in construction [10, 11, 12, 13, 14].

#### 2.1.1 Polymers in cement-based systems

In polymer-modified cement mortars and concretes (PCC), cementitious and polymer components together form the matrix and perform the binder function [15]. Commonly, the polymer-to-cement mass ratio ( $p/c$ ) is between 5 % and 20 %, depending on the advice of the manufacturer and the required material properties [16].

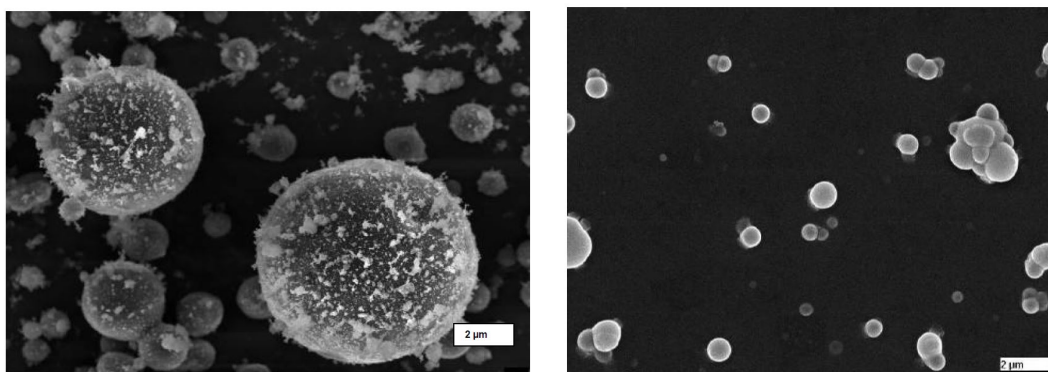
The polymers are macromolecular compounds, produced with a polymerization reaction between monomers of the same or different compositions. The product of the first reaction type is a homopolymer, of the latter a copolymer. Typical monomers are vinyl acetate, styrene, butadiene, and acrylic acid ester<sup>1</sup>. The most important requirement for the use of polymers in cement-based materials is the compatibility with the cement. In particular, the polymers need to be alkali-resistant, stable against saponification, and resistant to the ions delivered during the hydration reaction. They should not coagulate during mixing, and they should not impair the cement hydration [17, 18].

---

<sup>1</sup>Epoxy-modified cement concretes (ECC), where water-emulsified epoxy resins, hardeners, and / or curing agents are added to the fresh mortar or concrete, are beyond the scope of this thesis.

Polymers in the form of aqueous dispersions and redispersible powders are used for the modification of cement-based systems. The aqueous dispersions (or latices) contain thermoplastic polymers and have usually a solid content between 35 % and 55 %. The liquid phase of common polymer dispersions is water. The latices exhibit a high interfacial energy, entailing a thermodynamic instability. Small dispersed particles tend to coagulate in order to achieve a state of minimal energy [17]. The phase separation in polymer dispersions is called demulsification. For the stabilization of the polymer dispersions, protective colloids (macromolecules) and / or emulsifiers (surfactants) are added. [19, 20, 21]

Redispersible powders are produced by spray drying. The production is a two-step process: At first, polymer dispersions are obtained from the emulsion polymerization. This is followed by the spray drying of the dispersion under the addition of water-soluble protective colloids, spray-drying aids, and anti-blocking agents. In contact with water, the polymer powder redisperses, and the initial polymer dispersion is obtained ideally. Effectively, particles of the dispersion partially coagulate during the spray drying so that the particle size distribution of the powder is slightly larger than that of the dispersion. Besides, the anti-blocking agents coarsen the particle size distribution in comparison to the polymer dispersion. Nowadays, redispersible powders are increasingly favored over dispersions because application errors are minimized. Dimmig et al. [22] observed the polymer particles in redispersible powders after spray drying and the redispersion due to water addition with a scanning electron microscope, see Figure 2.1. The powder particles represent hollow spheres with craters on their surfaces initially. After redispersion, small dispersed particles are visible, which are partially strongly agglomerated.



(a)

(b)

**Figure 2.1:** Polymer powder particles after spray drying (a) and after redispersion (b) [22].

The removal of water increases the viscosity of the dispersions. Several studies on the film forming process of polymer dispersions have already been performed, e.g. [23, 24]. With

the removal of water from the dispersion, arranging and packing of the polymer particles start. The particles come into contact one another as water evaporation progresses. Due to particle coalescence, a polymer film might be formed. The minimum temperature at which the polymer particles are able to coalesce into continuous polymer films is called the minimum film forming temperature (MFT) [18]. However, the film formation of latices is not only governed by the curing temperature, but also by the particle size, the relative humidity, the type of monomers, the rate of drying, and the additives stemming from the polymerization process [15, 25, 26].

The mechanisms of the film formation of polymer coatings on substrates are not directly applicable to the processes taking place in mortars and concretes. In such systems, the polymer film formation is influenced by the alkaline environment, the interactions between the polymer, the additives, and the cement particles, and by the lower polymer concentration [21]. The water removal is mainly determined by the cement hydration.

## **2.1.2 Microstructure of PCC**

The polymer modification influences the microstructure of the cementitious matrix, and it entails changes concerning the hydration process. Both aspects have been intensively investigated and reported in the literature. However, neither generalized conclusions nor consistent findings have been revealed due to the complex nature of the polymer systems. The latter may differ regarding their chemical composition, the degree of polymerization, and the proportion of monomers in the copolymer. Further interactions between the constituents of the diverse cements and the additives of the polymer dispersions and powders, e.g. anti-foaming agents, demulsifiers, preservatives, stabilizers, and surfactants, may influence the performance of the modified materials. The huge variability of the polymers in combination with different additives renders the estimation of the mechanical behavior of polymer-modified mortars and concretes challenging. Thus, the comprehensive understanding of the processes and interactions taking place between the polymers and the cement particles is relevant for the durable design of PCC structures. [19, 21]

### **2.1.2.1 Influences of polymers on the cement hydration**

Several macroscopic properties of cement-based materials are strongly related to the hydration kinetics, particularly so at early ages. The workability, the setting time, and the strength evolution are determined based on the processes taking place during cement hydration. It is well accepted that the polymer particles are partially adsorbed by the cement particles directly after mixing. The degree of adsorption depends on the type and particle size of the polymers, the admixtures, and the cement type [27, 28, 29]. Detailed

studies on the chemical and physical interactions between cementitious and polymer components can be found in the literature, e.g. [20, 30, 31, 32, 33].

Clearly, the polymer modification influences the progress of the hydration reaction between water and clinker particles. The effects of polymers on the cement hydration have been explicitly investigated since the late 1980s. Larbi and Bijen [34] determined the chemistry of the pore solution in polymer-modified cement pastes for a period of 28 days. Polystyrene acrylate and polyvinylidene chloride were used. It was found that the polymers – more precisely, their functional groups – interact with ions released during cement hydration.

Su et al. [35, 36] investigated the evolution of the hydration degree, which is a measure of the progress of the hydration reaction, in plain and polymer-modified cement pastes comparatively. The hydration degree was determined from the non-evaporable water content in the cement pastes. It was shown that the hydration rate decreases with increasing quantity of styrene acrylate copolymer added. The restricted access of water to the clinker particles, which a “polymer skin” cover, explained the experimental results. In addition, the higher fineness of the polymers in comparison with the cement and the adsorption of surfactants onto cement grains were itemized [36]. On the contrary, cement pastes modified with the copolymers of vinylpropionate and vinylidene chloride tended to accelerate the cement hydration. The hastening was considered to be due to the presence of chloride ions in the pore solution because many chloride salts are known to accelerate the hydration [37]. However, throughout the study, different water-to-cement ratios were used, prohibiting the sufficient comparability of the results.

Atkins et al. [38] studied the hydration kinetics of six polymer-modified cement pastes by means of conduction calorimetry, X-ray diffraction, and infrared spectroscopy. The results revealed that varying types of polymer dispersions interact differently with the cement. By way of example, polyvinyl alcohol (PVA) increased the hydration rate slightly, whereas other polymers, such as polyvinyl acetate (PVAc), polystyrene acrylic ester (SA), and polystyrene butadiene rubber (SBR), retarded the hydration process. The cement pastes modified with PVAc, SA, and SBR exhibited higher amounts of alite after one week and a lower heat output at 48 hours after the production compared with the plain paste.

Quasi-isothermal calorimetry is a powerful and widely used technique to get quantitative access to the reaction kinetics between clinker particles and water. Zeng et al. [39] also used this method to study the hydration kinetics of SBR-modified cement pastes. It was found out that the polymer retards the hydration process by increasing the duration of the induction period, on the one hand, and by restraining the growth of the hydration products, on the other hand. Furthermore, an influence of the polymer content on the



hydration kinetics was revealed. Accordingly, low  $p/c$ -ratios up to 0.05 did not change the intrinsic hydration mechanisms, whereas higher  $p/c$ -ratios affected them. For low polymer contents, the diffusion of ions through a reacted layer is the mechanism controlling the hydration rate. For high polymer contents, the movement of water to hydration sites is supposed to be the rate-controlling step.

Silva and Monteiro [40, 41] investigated the influence of polyethylene co-vinyl acetate (EVA) on the hydration of cement paste using the soft X-ray transmission microscopy. This technique permits observations of the nucleation and growth of crystals. It was shown that directly after mixing, the EVA particles tend to concentrate around the hydrating  $C_3S$  and  $C_3A$  grains. The alite dissolution was retarded, and also, the morphology of the hydration products was affected. The hydrate needles seemed to be thicker in the presence of EVA. Furthermore, the formation of Portlandite and ettringite crystals was inhibited.

Jansen et al. [42] performed *in-situ* X-ray diffractometry (XRD) measurements. The focus was on the crystallography of the ettringite crystals. The investigations revealed that the crystal structure of the ettringite is influenced by the polymers, though the integration of polymer particles into the ettringite crystals was excluded.

Wang et al. performed a series of experiments to analyze the influences of polymers on the cement hydration [43, 44, 45]. Several measurement technologies, such as differential scanning calorimetry, XRD, and  $^{29}Si$  NMR analysis, were used to characterize the hydration behavior of SBR- and SA-modified cement pastes. It was observed that the degree of hydration increased with the polymer-to-cement ratio first, and it decreased for polymer-to-cement ratios higher than 0.10. The results were explained by the formation of polymer films around cementitious constituents. In cement pastes modified with less than 10% polymers, the polymer accumulation is low, allowing the polymer phase to keep water that is successively provided for the cement hydration. For higher  $p/c$ -ratios, the polymer films are thicker, hinder a free ion transfer, and retard the hydration [43]. The same trend was observed for the  $Ca(OH)_2$  content. It increased with the  $p/c$ -ratio first and decreased afterward. By means of XRD patterns, it was additionally found out that both SBR latex and SA powder support the reaction of calcium aluminate with gypsum, leading to more stable ettringite crystals [43, 44].

Recently, Kong et al. [46, 47] investigated the retardation mechanisms of styrene acrylate latexes in detail. Calorimetry and adsorption measurements as well as investigations using confocal laser scanning microscopy and cryo scanning electron microscopy were performed. As a result, two types of retardation mechanisms were declared: The chemical retardation involves the calcium complexation by the carboxyl groups of the polymers so that the

concentration of free calcium ions in the aqueous phase is decreased and the induction period is prolonged. Thus, the content of R-COO<sup>-</sup> in the polymer latex mainly determines the extent of the retardation; a finding that Zeng et al. [39] also reported. The physical retardation comprises the formation of a polymer layer around hydrating cement surfaces due to adsorption. The polymer layer inhibits the nucleation and growth processes of hydration crystals and restricts the accessibility of water and ions at the hydrating cement surfaces. This reduces the hydration rate during the acceleration period as well as the total heat. Wang et al. [45] also distinguished physical and chemical retardation aspects.

Schirmer [21] correlated the hydration kinetics of polymer-modified cement pastes with the adsorption mechanisms of polymer particles and their additives on cementitious phases. Four different polymer dispersions containing copolymers on the basis of vinyl acetate ethylene, vinyl chloride ethylene, and styrene-acrylate were investigated. By means of calorimetry measurements, a delayed acceleration period was observed for all investigated pastes. This effect was traced back to altered solvating and precipitation processes and, consequently, a retarded nucleation reaction of the hydrates. The retardation is not mainly caused by the adsorption of dispersed particles, but by the adsorption of protective colloids. Another aspect is that solvated calcium ions form complexes with the protective colloids so that they are not available for the growth of hydrate phases. The main silicate reaction starts when the saturation concentration of Ca<sup>2+</sup> is reached by further solvated ions.

Baueregger et al. [48] investigated the influence of SBR on both the hydration kinetics of Portland cement and a ternary binder system (TBS) consisting of Portland cement, calcium alumina cement, and anhydrite using isothermal heat flow calorimetry and *in situ* X-ray diffraction. A significant retardation effect of the polymer on the hydration process of the Portland cement was evidenced. Again, the complexation of Ca<sup>2+</sup> of the cement paste pore solution and the adsorption of the SBR particles onto cementitious phases explained the results. On the contrary, the SBR latex accelerated the hydration reaction in the TBS. The ettringite formation and the silicate reaction were promoted.

### 2.1.2.2 Microstructure formation

Microstructural specifics govern the macroscopic properties of polymer-modified cement pastes, mortars, and concretes. The binder matrix consists of cementitious and polymer components, which interpenetrate each other. Thus, the research on the microstructure and the corresponding macroscopic properties is of interest. Essential contributions to this topic have been reported since the 1980s. Several models illustrating the microstructural formation in PCC have already been developed. Among them, the most important models are chronologically described in the following, showing the increasing understanding of

the microstructural formation. The improved knowledge about the morphology and the formation of the polymer phase within the cementitious structure was enabled by enhanced scanning electron microscopy (SEM) resolution and the integration of the ESEM technique in the studies [49]. It represents a fundamental basis for the follow-up success of multiscale modeling activities, see Section 5.3.

Ohama [2, 50] described the formation of a co-matrix phase consisting of cement gel and polymer films with a three-step process as follows. (i) Immediately after mixing, the polymers are uniformly dispersed in the cement paste. A cementitious gel is formed, on which polymer particles deposit. (ii) With ongoing hydration and densification of the cement gel structure, the polymer particles are increasingly confined in the capillary pores. Water is withdrawn continuously so that the polymer particles flocculate. They form continuous films on unhydrated and hydrated cementitious phases as well as on aggregates due to inter-molecular attraction forces. (iii) A monolithic network is obtained in which the polymer phase interpenetrates the cementitious hydration products. For  $p/c$ -ratios lower than 0.05, the polymer compounds are isolated, and the films are discontinuous.

Experimental investigations using the SEM and the ESEM techniques by Su and co-workers [36, 51] revealed similar results. Additionally, the authors quantified the amount of polymer particles adsorbed onto the cement surface directly after mixing. It amounts to 50 %. Those polymers act as barriers, delaying the hydration process. The other part of the polymers remains dispersed in the mixing water. Furthermore, the authors found out that the polymer particles are not uniformly distributed in the hardened cement paste matrix. They are mainly deposited on areas with high capillary forces, e.g. in the contact zones between cementitious particles.

The composite mechanisms in EVA-modified mortars and concretes taking place after mixing were investigated by means of the cryo-SEM technique by Sakai and Sugita [52]. It was observed that one part of the spheroidal polymer particles fills the interface between unhydrated cement grains and hydration products, and the other part forms layers around aggregates.

Puterman and Malorny [53] improved the three-step-model of Ohama by considering the minimum film forming temperature as the essential parameter that controls the polymer film formation. The authors claimed that if the MFT is below the curing temperature, the closely packed polymers are able to form a continuous film. Otherwise, the polymer particles remain as stacked droplets on the surface of the cementitious particles. The ideas were supported by ESEM observations of Schorn and Schiekkel [54].

Afridi [55] investigated the coalescence of polymer particles (SBR and EVA) in mortars by means of SEM investigations. In contrast to unmodified mortars, where hydration products and sand grains are loosely joined with each other, polymer-modified mortars exhibit an improved adhesion among the components. The reinforcing effects of coherent “interweaving” polymer films on the cementitious network were claimed. The form of the polymer films was observed to be either mesh-like, dense, fibrous, or rugged, depending on the type of polymer used. For mortars modified with latices, a better coalescence of the polymer particles was observed in comparison with powdered polymers. A monolithic network with continuous polymer films was reported for  $p/c$ -ratios higher than 0.10.

Beeldens et al. [56] picked up the idea of incorporating the minimum film forming temperature as a decisive aspect into a model illustrating the microstructure formation in PCC. The three-step model of Ohama was extended with respect to the consideration of curing conditions related to a time scale and the formation of an interstitial phase as follows. (i) The cement and polymer particles are dispersed in water after mixing; cement hydration starts. (ii) The polymers interact with the clinker grains and the aggregates. The polymer particles may partly coalesce into continuous films, particularly if a dry curing period is enabled. The polymer films envelope the cement particles either partly or completely. (iii) Cement hydration and further polymer flocculation and coalescence take place. The processes depend on the curing conditions. If a drying period is included, the polymer film formation takes place, influencing the cement hydration progress. If no drying period exists, the film formation is retarded. An interstitial phase consisting of organic and cementitious components is formed. (iv) Further cement hydration and polymer film formation on and in between the cement hydrates take place. Polymer particles not deposited yet, concentrate in capillary pores and at the interfacial transition zone. The authors point out that optimal curing conditions for achieving a high strength evolution comprise a wet curing period, followed by a dry curing period.

However, most of the proposed theories and models describe the microstructural formation of PCC generally, neither considering different polymer systems nor the various additives included. Therefore, the resulting differences of the microstructures, leading to contradictory properties of the fresh and hardened mortars and concretes, are not satisfactorily explained. Dimmig-Osburg [27, 57, 58] claimed that a successful microstructural model should incorporate the interactions of all components, considering adsorption, agglomeration, and the retardation of the cement hydration. She proposed a model including the following steps. (i) The polymers are adsorbed on cementitious particles directly after mixing. The occupied surface depends on the size of the dispersed particles. Small polymer particles deposit on the clinker grains densely. (ii) If the minimum film forming temperature is lower

than the processing temperature is, the polymers form films, and a monolithic network together with the cementitious components is built. The films are formed out of the non-adsorbed polymers in pores and are arranged between the cementitious particles or inside the pores. For polymers with an MFT higher than the environmental temperature, the particles are stored to one another, but they are not coalesced. (iii) The microstructure is continuously densified along with the hydration process. Hydrates grow through polymer compounds. The organic and inorganic matrix interpenetrate each other. The finer the polymer particles are, the more homogeneous is the structure. (iv) The microstructural formation takes mainly place during the first 24 hours. Furthermore, experiments have shown that the pore solution of a polymer-modified cement paste corresponds to that of conventional cement paste after three days of hydration.

Tian et al. [59] further improved the microstructural knowledge, integrating the processes of flocculation and coagulation of polyacrylate polymer in fresh mortars. Accordingly, a four-step microstructural formation is proposed. (i) The components (polymer particles, water, cement, sand) are mixed, whereby neither chemical nor physical reactions are considered. (ii) Cement hydration starts. The polymer particles are partly adsorbed on clinker phases, hydrates, or sand grains, whereas the other part flocculates due to calcium complexation. The polymers are concentrated on the mineral surfaces, referred to as localization. (iii) The hydration products break through the adsorbed polymer layers, disaggregating the polymer layer. With ongoing hydration process, the hydrates further grow and embed the flocculated polymers. The polymer particles partially coalesce. (iv) The hydration reactions slows down, and the microstructural formations finishes. The polymer particles further coalesce.

Ma and Li [60] investigated the influences of acrylic latexes on the microstructural formation of mortars by means of experimentally observed and computed microstructures. Based on the known interaction mechanisms between the polymers and the cementitious components, the microstructural evolution of polymer-modified cement pastes was simulated. Accordingly, the initial cement paste microstructure consists of unhydrated clinker grains, inner and outer hydrate layers, and capillary pores. For the polymer-modified cement pastes, capillary water voxels are randomly replaced with polymer voxels. It is assumed that the addition of polymers does not influence the inner layer of the hydrates but has significant effects on the outer hydrate layer due to the adsorption of polymer particles onto the latter. As a result, a cementitious structure interpenetrated by polymer films is described. With the simulated microstructures, the characteristic mechanical behavior of polymer-modified cement pastes can be explained realistically, e.g. the increase of the flexural strength due to the polymer modification is predicted [60].

The interfacial transition zone (ITZ) between the cement paste and the aggregates is a critical factor concerning the strength and ductility of concretes. Commonly, the ITZ is more porous than the surrounding matrix. Thus, it is considered to be a weakening link [61]. The origin of the ITZ is the so-called wall effect disrupting the packing of cement grains [61]. Wei et al. [62] investigated the ITZ in steel fiber reinforced polymer cement concrete and observed a strengthened and thinner interfacial layer between fibers and the cement matrix compared with mixtures that did not contain polymers. The particle size and the enrichment of Portlandite crystals in the ITZ were reduced with increasing content of polyacrylate ethyl ester. Bijen [63] and Xu et al. [64] reported that polymers fill the interspaces between cement grains in the interfacial transition zone, improving the contact adhesion between aggregates and matrix. Bode [65] investigated the increase of the specific adhesion between the cementitious matrix and aggregates in polymer-modified mortars. By means of SEM-observations, Bode found out that non-adsorbed polymer particles, which remain in the liquid phase after mixing, fill the interspace between hydrating cement grains and aggregates. This increases the compactness of the ITZ and improves the mechanical adhesion, see Figure 2.2. Furthermore, the delayed hydration reaction in PCC inhibits the formation of preferably oriented Portlandite crystals. Thus, the packing density in the interfacial transition zone increases [65].

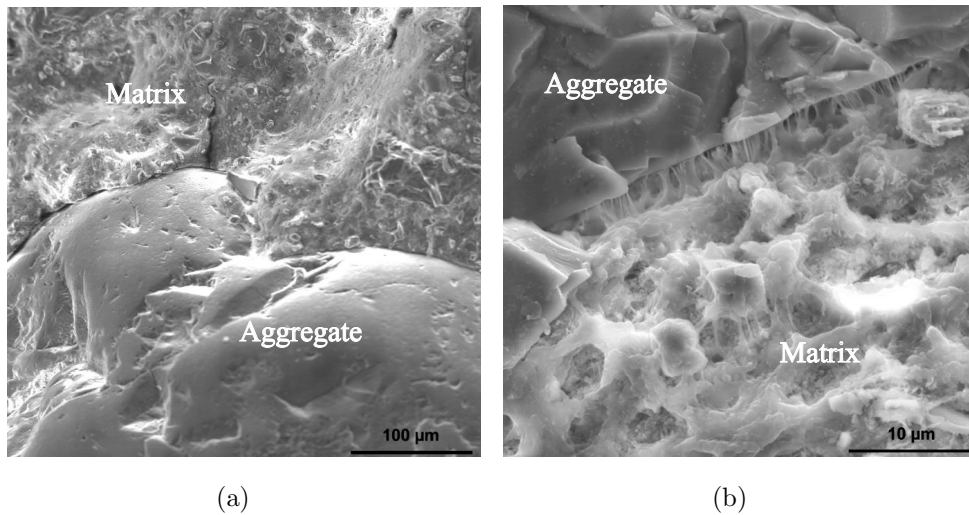


**Figure 2.2:** SEM images of the ITZ in unmodified (a) and polymer-modified mortar (b) [65].

The pore structure in cementitious materials greatly influences the permeability and durability. It appears that the pore structure in PCC differs with the type of polymer and the polymer content. Ohama et al. [66, 67] stated that for PCC having a comparable workability, the polymers reduce the total porosity and the fraction of large pores, whereas the volume of smaller pores is increased. Ray et al. [68] performed mercury intrusion

porosimetry tests with polymer-modified cement pastes and found out that the polymers do not affect the total porosity significantly; a more homogeneous pore size distribution was reported instead. The pore size distribution in polymer-modified mortars was also investigated by Ramli and Tabassi [69], who observed that the maximum pore size is reduced due to the polymer modification. Barluenga and Hernández-Olivares [70] stated that the polymer modification increases the total and the closed porosity but decreases the open porosity. The contradictory results reported in the literature are related to the variable use of defoamers. Often, the defoamers are additives of the polymer dispersions, or they are added during the mixing. Therefore, uniform conclusions about the influences of polymers on the pore size distribution of cementitious materials cannot be drawn.

### 2.1.3 Fresh concrete properties

Typically, polymers improve the **workability** of cement-based materials with increasing  $p/c$ -ratio [2, 65, 71]. Reasons for this are the ball-bearing action of the polymer particles, entrapped air, and the dispersing effect of surfactants added to the dispersions [2]. Barluenga and Hernández-Olivares [70] investigated the rheology of SBR-modified mortar, illustrating the improved consistency along with the polymer quantity added. Similar results were reported by Kubens and Wallevik [72] who observed that the polymer modification leads to a reduced viscosity and yield stress of cement mortars.

**Setting times** are influenced by the polymers differently, depending on the type of cement and the chemical basis of the polymer. In [70], reduced initial and final setting times were reported, whereas more commonly a delayed setting of polymer-modified mortars and concretes is noticed [2, 73]. The delay of the setting times is related to surfactants in the dispersions and the retarded hydration [36].

Mostly, PCC exhibit higher **air void contents** in comparison with conventional fresh mortars and concretes because the admixtures often act as air-entraining agents and emulsifiers [15, 74]. For polymer dispersions that remarkably increase the viscosity of a mixture, less entrapped air voids occur because the mixtures are able to deaerate. The **density** of fresh polymer-modified mortars and concretes is reduced with increasing polymer content due to the low density of the polymers and the entrapped air. However, excessive air entrainment should be prevented by the addition of antifoaming agents in order to avoid a pronounced loss of strength.

Polymer-modified mortars and concretes show an improved **water retention** which increases – depending on the type of the polymer – with the  $p/c$ -ratio [75]. Ohama [2] found the reason for that in the polymers, which inhibit the water evaporation by sealing

the cementitious particles. Although the PCC exhibit a larger flowability, **bleeding and segregation** are not worse than in conventional mortars and concretes [2, 76, 77]. Su [36] even reported considerably less bleeding and segregation in PCC due to the better dispersion of the cement particles and the entrained air.

**Curing conditions** play a significant role for the strength development in polymer-modified mortars and concretes. They have often been varied within experimental campaigns in order to propose the ideal curing regime, e.g. [15, 65, 78]. Most preferably, PCC are cured under water during the first few days of hydration to allow for a satisfactory cementitious hydration reaction. This should be followed by the storage exposed to air to support the polymer film formation and the water evaporation.

#### 2.1.4 Hardened concrete properties

The variability of polymers, their admixtures, the mixture design, and the curing conditions entail different influences of the polymers on the engineering properties of mortars and concretes. To evaluate the influences of polymers on the hardened concrete properties, the knowledge of the microstructure formation in dependence on the polymer type, polymer content, temperature, storage conditions, and mixture design is fundamental.

One important differentiating factor of the polymers, which affects the microstructure of the compound material, is the minimum film forming temperature (MFT). Konietzko [79] distinguished film-forming polymers and polymers which are not able to form continuous films in the cement matrix. He proposed that the polymers without the capability to form films only act as filler materials which do not contribute to the load transfer. This assumption was disproved by Bode [65]. Bode evidenced an increase of the adhesive bond between the aggregates and the cement paste matrix as a consequence of the polymer modification. He showed that also polymers that do not form films in the matrix effectively increase the tensile strength [65].

Lohaus and Anders [80] described the influence of the polymer modification on the mechanical properties of high and ultra-high strength concrete. Properties of fresh and hardened mixtures as well as the **stress-strain relationship** were investigated. In dependence on the type of polymer used, the mechanical and fracture behavior significantly differed from conventional concrete. A decreased fracture energy was noticed. Several contradictory explanations for the experimental results were given. However, a more detailed experimental study on the microstructure formation and the interactions between polymer and cementitious components was recommended to get a more fundamental insight into the mechanisms affecting the mechanical behavior of PCC.



The polymers tend to decrease the **compressive strength** of cement-based mortars and concretes at given time instants, as it was confirmed by experimental investigations of e.g. Gierloff [73], Konietzko [79], and Flohr [76]. On the contrary, an increase of the compressive strength for low polymer-to-cement ratios (up to 0.08) was reported in some publications [78, 81].

The central **tensile strength** of PCC is commonly characterized by an increase or at least a constant evolution with increasing  $p/c$ -ratio e.g. [65, 74, 79]. Reasons for that behavior were studied in Flohr [76] by means of the SEM technique. In polymer-modified mortar specimens subjected to tensile loads, stretched polymers bridging the crack between matrix and aggregate are visible, see Figure 2.3. Microcrack edges are connected by the polymer, leading to a higher energy consumption for the generation of macrocracks. The crack bridging ability depends on the polymer quantity added and the type of polymer, especially on its MFT. Also, the adhesive bonding of the polymers to the aggregates and cementitious grains improves the tensile strength [76]. This effect is supported by a film formation of some polymers [65]. Analogously, the **bending tensile strength** of PCC is increased in comparison with conventional concrete, e.g. [81, 82].

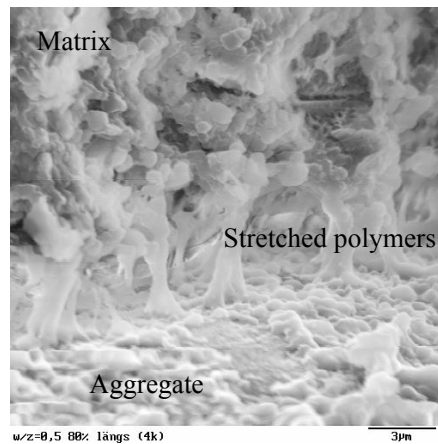


**Figure 2.3:** Crack between matrix and aggregate, bridged by stretched polymers [76]

The embedment of polymers in the cement matrix entails a flexibilized microstructure resulting in lower **elastic moduli** and a more pronounced **ductility**. In particular, the polymers coat crystalline cementitious phases and act as “lubricants” that represent sliding planes inside the material [76]. Bureau et al. [82] investigated the ductility of SBR-modified concretes. Several  $p/c$ -ratios were considered and a continuous decrease of the Young’s modulus along with the increasing polymer content was shown, whereas the Poisson’s ratio remained constant. The inelastic behavior of the polymer-modified mortars was explained with two mechanisms: the development of cracks causing damage and the viscous dissipation in the polymer phase. Flohr [76] also found out that the addition of polymers

improves the ductility of concrete. The lower elastic moduli of PCC in comparison with conventional concrete have already been widely reported, e.g. [15, 81, 83].

The mechanical behavior of polymer-modified mortars and concretes is dependent on the **temperature** [84]. The residual compressive strength of PCC subjected to temperatures between 200 °C and 800 °C was investigated in [85, 86]. It was found that the strength loss is slightly more pronounced for the PCC compared with the unmodified reference.

### 2.1.5 Deformation behavior

Similarly to conventional concretes, PCC exhibit a **viscoelastic deformation behavior** (creep). Konietzko [79] investigated the creep behavior of PCC for varying  $p/c$ -ratios. With increasing polymer quantity added, a more pronounced creep deformation was noticed, which the formation of polymeric sliding planes inside the matrix explained. Experiments reported in [87, 84] also revealed that the strains that PCC show are commonly larger than in conventional concretes.

Bokan-Bosiljkov and Saje [88] reported long-term mechanical tests with SA-modified concrete at ambient and elevated temperatures up to 150 °C. At 20 °C, the PCC only exhibited larger strains than the unmodified concrete at sample ages up to five days did. After that, the deformations of the PCC developed more slowly. Uncoiling processes in the polymers explained this. However, proof for this theory was not achieved. At elevated temperatures, the intensifying effect of the polymers on the creep strains was shown, which the softening of polymers at temperatures higher than 50 °C caused [88].

Mangat et al. [3] investigated PCC with a  $p/c$ -ratio of 0.25, modified with acrylic, styrene acrylic, and styrene butadiene polymers. The samples were loaded with 25% of the compressive strength at material ages ranging from 28 days to 118 days. An increase of the creep strain and the creep recovery with the polymer content was found. The higher creep strains were related to the presence of emulsifiers and stabilizers in the polymer dispersions that retard the hydration process and thereby lead to lower strength. With higher polymer contents, more water is retained via the polymer phase [3]. Furthermore, SA-based polymers cause larger creep strains than polymers based on SBR.

Heidolf [5, 89] investigated the time-variant behavior of PCC under repeated stress considering damage. Accordingly, the stiffness degradation of PCC was much more pronounced than that of conventional concrete. The polymer-modified concrete exhibited remarkably high creep strains. It was observed that the range of linear creep is very small compared with nonlinear creep. Therefore, the nonlinear creep should not be neglected in the design and computations of structures. A linear relation between the creep-generating

stresses and the creep deformation was not recognized. Therewith, the prediction of the long-term behavior of PCC on the basis of linear creep theories is not sufficient [89]. Furthermore, it was found that preloadings can anticipate structural changes so that during a reloading below the preloading level, an almost linear stress-strain relation is observed.

Flohr [90] also investigated the long-term creep behavior of PCC. Two SA-modified concretes with a  $p/c$ -ratio of 0.15 were tested. The first test started at a sample age of 75 days, and the loading duration was 28 days. The second test series was conducted with a 265-day-old concrete and a loading duration of 154 days. A differing creep behavior of the PCC in comparison with conventional concrete was found; significantly larger creep strains were measured.

The **shrinkage behavior** of polymer-modified mortars and concretes was also investigated experimentally. Several contradictory effects of the polymers on the shrinkage behavior of mortars and concretes were published in the literature. Wang et al. [75] observed that the addition of 10 % SA latex decreases the shrinkage rate of mortars remarkably. In contrast, the experimental results of Bishara et al. [87] showed that SBR-modified mortars exhibit significantly higher shrinkage strains than unmodified mortars do. Bode [65] investigated mortars modified with styrene acrylate dispersions. He found out that the shrinkage strains of PCC were much more pronounced compared with those of the reference mortar without polymer addition. The higher the polymer content, the larger the load-independent length changes are. Bode claimed that the extended length changes do not result from an increased drying shrinkage but from the retarded hydration process. Therewith, shrinkage strains are not released within plastic but within already hardened stages, thus worsening the cohesion within the mortar. An extension of the shrinkage measurement duration according to codes up to 90 days was recommended because shrinkage measurements up to 28 days are not sufficient [65]. Furthermore, the importance of the storage conditions for the shrinkage strains was illustrated. Particularly air-dried polymer-modified mortars exhibited large shrinkage strains, which experiments that Dimmig [15] reported also confirmed. She found out that polymer-modified mortars with a  $p/c$ -ratio of 0.15 exhibit larger shrinkage strains than mortars with a  $p/c$ -ratio of 0.05 do.

### 2.1.6 Modeling the mechanical behavior of PCC

The model-based prediction of the mechanical properties of polymer-modified mortars and concretes has been rarely investigated so far. Some empirical models based on experimental data have been developed. Bishara et al. [87] proposed empirical equations for predicting the shrinkage and creep strains. Accordingly, the creep coefficient  $C$  depending on the time  $t$  was described by  $C = d \cdot t^{0.60} / (10 + t^{0.60})$  with the constant  $d$  to be determined based on experimental data.

Mangat [3] proposed a hyperbolic creep expression of the form  $c = t / (a + bt)$ , linking creep strains  $c$  and time  $t$  via two fitted parameters,  $a$  and  $b$ . The comparison of model-predicted and experimentally determined creep strains revealed the validity of the approach for one certain type of PCC. However, for both models, the generation of experimental data is required to identify the fitted parameters. Also, the applicability to different mixture designs was not proven.

Heidolf [5] developed a rheological model describing the creep behavior of polymer-modified concrete subjected to cyclic loading. A time-invariant material model is combined with a time-variant creep model consisting of Kelvin and Bingham elements, see Figure 2.4. The Kelvin elements represent the reversible visco-elastic strains, whereas the Bingham elements characterize the irreversible visco-plastic strains. In this approach, nonlinear creep, stiffness degradation, the strength reduction due to the creep process, and the post-hardening of concrete are considered. Nevertheless, this model requires the back-calculation of experimental tests to identify model input parameters.

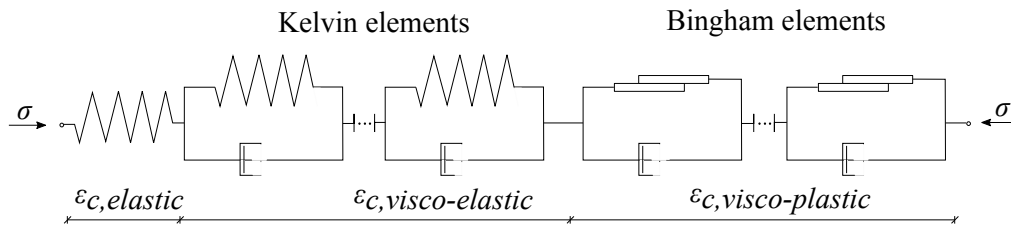


Figure 2.4: Rheological model of Heidolf [5].

Keitel and Dimmig-Osburg [6, 7, 91] studied the applicability of existing phenomenological creep models, which were originally developed for conventional concrete, to PCC. The comparison of six different creep models with experimental creep strains determined by Flohr [76] revealed significant deviations. Mostly, the models underestimated the creep strains that the SA-modified concrete exhibited. By means of parameter optimization, the input parameters of the creep models were adapted for the application to PCC. With this procedure, the differences between model-predicted and experimental creep strains were

reduced. However, a general applicability of the chosen creep models for polymer-modified concrete was not proved because the optimized parameters depend on the test boundary conditions and the duration of the loading.

Eden et al. [92] developed a model for the tensile strength of Portland cement paste with and without polymer modification. The model is based upon the idea that tensile failure occurs by pulling fibrills made of calcium silicate hydrates (C-S-H). The model is of the form

$$\sigma_y \approx \pi l d \tau_s N \quad (2.1)$$

with	$\sigma_y$	tensile strength
	$l, d$	length and diameter of C-S-H fibrill
	$\tau_s$	shear strength
	$N$	number of fibrils per unit area of failure surface.

By means of this model, Eden et al. [92] explained the origin of mechanical features of PCC. In particular, the principal effect of the polymers as an adhesive between fibrils made of calcium silicate hydrate was shown.

The prediction of the stress-strain relation in polymer-modified concretes was the focus of studies by Çolak [4]. Several mathematical formulations based on a stress-strain relation of the form  $\sigma = a\varepsilon/(1 + b\varepsilon)^n$  were proposed in which the parameters  $a, b, n$  are to be determined.  $\sigma$  and  $\varepsilon$  denote the stress and strain respectively. A satisfactory approximation of experimental data was obtained [4]. Still, within this investigation only polymer-to-cement ratios up to 3% were considered. Thus, the model is not approved for practical applications in which higher  $p/c$ -ratios are applied commonly.

Göbel et al. [93] investigated if existing analytical models for the quantification of the elastic modulus, which were originally developed for conventional concretes and are commonly used in design codes, are also valid for PCC. By means of an extended database comprising experimental data of more than 25 publications, it was shown that the models are applicable to polymer-modified concretes, although the predictions exhibit slightly worse performance compared with conventional concretes.

## 2.2 Multiscale modeling of cement-based materials

Both cementitious and polymer components govern the macroscopic properties of polymer-modified cement-based materials. The polymer modification causes microstructural changes in the binder matrix where polymers are intermingled with the cementitious constituents [15, 36]. Thus, quantifying the influences of the microstructural modifications on the macroscopic effective properties is of particular importance. Multiscale models considering microstructural specifics are promising methods for predicting the mechanical behavior of polymer-modified cement-based materials.

In the sequel, fundamentals of multiscale models and different multiscale approaches are presented. Afterward, the multiscale modeling based on the principles of continuum micromechanics is introduced with particular emphasis on the upscaling of elasticity and creep properties from microscopic scales up to the concrete level.

### 2.2.1 Fundamentals of multiscale modeling

From the design perspective, concrete is considered as homogeneous [94]. However, a closer look reveals that it is a heterogeneous material spanning several length scales of observation. Concrete can be seen as a hierarchically organized material incorporating material phases that are significantly smaller than the structural dimensions, see Figure 2.5. On the length scale of a few centimeters, aggregates embedded in a matrix (cement paste) are visible. On the smaller length scale of a few micrometers or nanometers, the microstructure appears more complex, which renders the modeling of cementitious materials difficult.

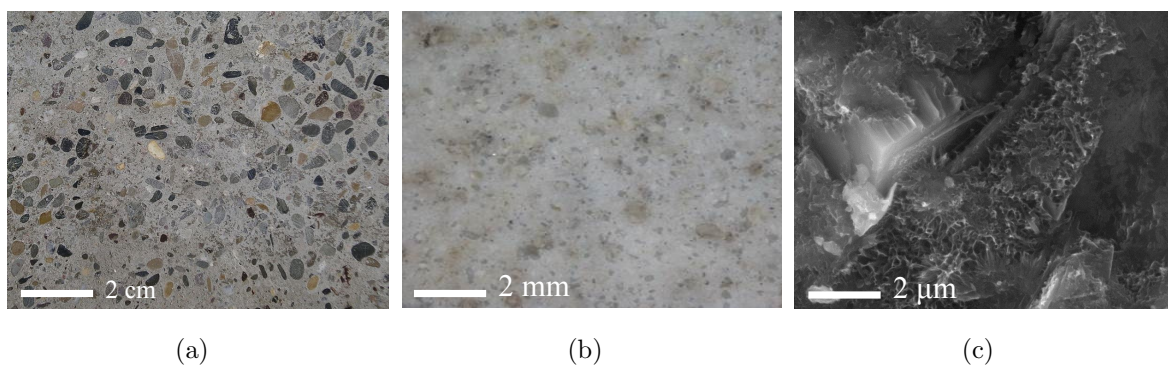


**Figure 2.5:** Hierarchical multiscale nature of concrete: aggregates embedded in a matrix of cement paste (a), cement paste distinguishing clinker grains inside a dense matrix (b), hydrates on the scale of a few microns observed with an environmental scanning electron microscope (XL30 ESEM, Philipps) (c), [own figure].

Several macroscopic phenomena of concrete can be traced back to processes taking place at microscopic scales. By way of example, the creep behavior of concrete is most likely determined via sliding processes at viscous interfaces within the C-S-H phases [95]. In addition, the stress-strain relationship of concrete and the elastic limit refer to microcracks between the aggregates and the cement paste matrix as well as to cracking within the matrix.

Thus, understanding and predicting the macroscopic material behavior requires the consideration of smaller observation scales. A model that solely takes into account concrete as a macro-homogeneous material will not be able to sufficiently describe and capture all complex material phenomena; it only provides the prediction of a homogenized response. Along with the increasing quantity of macroscopically observable phenomena, the complexity of such empirical models increases. The phenomenological formulation of constitutive models describing the overall material behavior is challenging and often requires the implementation of a large number of input parameters. Mostly, the input parameters do not rely on a physical meaning and need to be determined experimentally, which might be a difficult and time-consuming task. Also, the material properties may vary between the stages of production and application, rendering integrated measurements prohibitive. [94]

On the contrary, in microscale models, which explicitly consider micro-heterogeneous components, rather simple constitutive equations can be assigned to single material phases. However, these models are too computationally expensive for the modeling of whole structures.

Multiscale models combine features of several observation scales. Information of different scales are used to provide the macroscopic material behavior considering structure-property relationships. Macroscopic material properties are related to chemical and physical processes at the scale of their origin [96]. Multiscale models also allow for the probabilistic prediction of material properties because random heterogeneous and varying microstructures can be considered [94].

### **2.2.2 Multiscale modeling approaches**

Two types of multiscale modeling approaches are commonly distinguished. The key difference is the methodology for bridging the scales [97]. Within the first approach, referred to as concurrent or integrated multiscale modeling, the structure is subdivided into subdomains. These subdomains are local zones of particular interest such as connections between concrete and the reinforcement or regions in which microcracks evolve. The

local zones are modeled at a lower scale resolving the heterogeneous microstructure of the material. Thus, the discretization must be adapted taking the internal material structure into account, see Figure 2.6 (a). The nature of the bridging methodology is numerical [97].

The hierarchical or sequential multiscale modeling requires the definition of representative volume elements (RVE) on the scales of interest. The structural response of the RVE at the lower scale is transmitted to a higher scale. Constitutive equations on the macroscale are derived using homogenization techniques, see Figure 2.6 (b). The material properties are determined independently of the actual stress and deformation state in the structure [96].

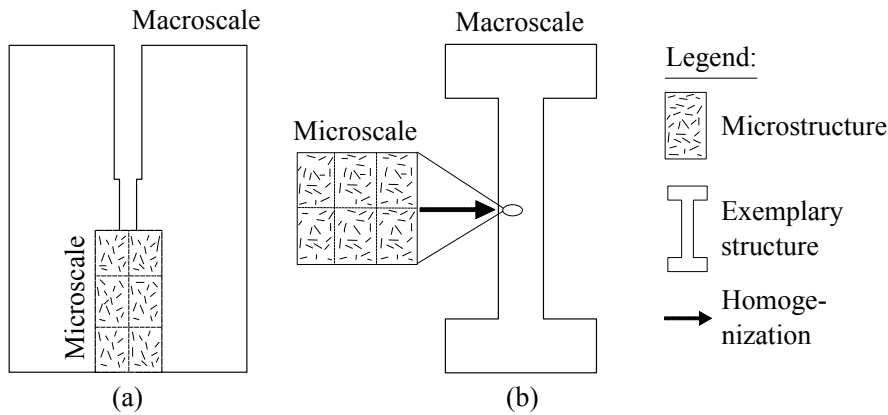


**Figure 2.6:** Approaches for the multiscale modeling of structures: concurrent (a) and hierarchical (b) multiscale modeling, [own figure].

The development of homogenization techniques providing relations between microstructural specifics and the effective macroscopic behavior is still a field of ongoing research [98]. For materials characterized by spatial fluctuations of physical quantities, homogenization methods within the periodic media theory may be employed [99, 100]. The response of a composite material, which incorporates randomly distributed heterogeneities, is commonly determined within the context of the effective media theory [101]. Homogenization is performed using mean-field methods, which are characterized by the application of displacements (forces) in terms of strains (stresses) at the boundary of an RVE [96]. Two different approaches for the homogenization of composite materials are commonly distinguished:

- Numerical techniques using the finite element method (FEM), the discrete element method (DEM) and others, e.g. [102, 103, 104].
- Analytical techniques based on continuum micromechanics, which are derived from the solution for ellipsoidal inclusions from Eshelby [105].



The numerical methods require the generation of detailed microstructures, which renders them computationally demanding. Within this thesis, semi-analytical multiscale methods based on the principles of continuum micromechanics are applied due to their ease of use and their low computational costs. These approaches have been applied successfully to the prediction of macroscopic properties of conventional cement-based materials, such as strength [106, 107, 108, 109, 110], elasticity [111, 112, 113, 114], and creep [95, 115, 116, 117, 118, 119, 120, 121]. Continuum micromechanics accounts for key features of the individual constituents, i.e. for their elastic stiffness properties, their characteristic shapes, their volume fractions, and the characteristic mode of their mutual interaction.

### **2.2.3 Multiscale modeling based on the principles of continuum micromechanics**

Multiscale modeling within the context of continuum micromechanics comprises three elements, namely [111, 122]:

- Representation: Geometrical description of the heterogeneous material, including the identification of material phases in the RVE and the morphology.
- Localization: Mechanical modeling of the interactions between the material phases linking the local strain (or stress) fields within the RVE and the macroscopic quantities of strain and stress.
- Homogenization: Volume averaging of the constitutive formulations defined on the scales of interest over the RVE so that macroscopic properties are obtained.

#### **2.2.3.1 Concept of representative volume elements**

Theoretical fundamentals on micromechanics and the homogenization theory in linear elasticity were reported in [105, 122, 123, 124, 125, 126]. In continuum micromechanics, the concept of representative volume elements [127] is considered because the complex microstructure of concrete cannot be resolved in every detail. Each RVE consists of quasi-homogeneous subdomains referred to as material phases. This entails the validity of the principle of scale separation. On the one hand, the structural dimensions and the dimensions of external loading  $L$  should be significantly larger than the characteristic size of the RVE  $l$ . On the other hand, the characteristic size of the RVE  $l$  is supposed to be considerably larger than the characteristic dimensions of heterogeneities  $d$  within the RVE, see Figure 2.7. It holds that  $L \gg l \gg d$ .

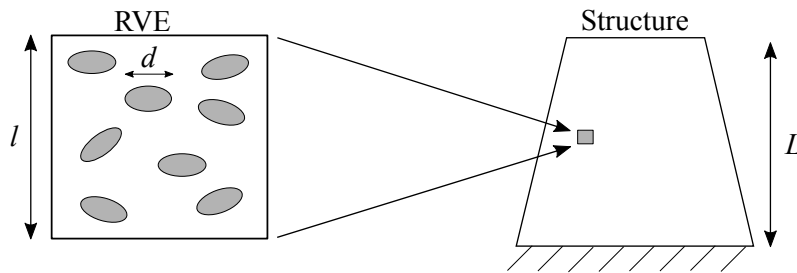


**Figure 2.7:** Scale of separation principle: The size of the RVE  $l$  is considerably larger than the dimensions of heterogeneities  $d$ , and also significantly smaller when compared with the structure with dimension  $L$  that the RVE has built up, adapted from [113].

### 2.2.3.2 Micromechanical representation of cement-based materials

Continuum micromechanics provides a powerful framework for the homogenization of cement-based materials, provided that their hierarchical organization is appropriately considered. The quest for the most realistic representation of cement pastes dates back to the early 2000s, see also [128] for a short overview about the most important models. The first three types of models were developed for estimating the stiffness properties of cement pastes as functions of the progressing hydration reaction.

- Bernard et al. [111] considered cement paste consisting of five spherical phases, which are highly disordered: unhydrated clinker grains, capillary pores, C-S-H gel, Portlandite crystals, and aluminate. The C-S-H gel is resolved at the next smaller scale. This RVE exhibits a matrix-inclusion morphology with a matrix made of outer low-density C-S-H gel and spherical inner high-density C-S-H gel.
- Constantinides and Ulm [112] improved the morphological representation by considering a matrix-inclusion composite at the scale of cement paste with a C-S-H gel matrix, in which spherical inclusions of unhydrated cement particles, pores, and Portlandite are embedded. At the next smaller scale of the C-S-H gel, they followed the representation of Bernard et al.
- Sanahuja et al. [113] modeled cement paste as a matrix-inclusion composite with an outer low-density C-S-H gel matrix. Therein, spherical composite inclusions consisting of an unhydrated clinker core and inner high-density C-S-H are considered. Sanahuja et al. improved the next smaller scale by introducing oblate solid C-S-H particles in direct mutual interaction with gel and capillary pores. The newly considered non-spherical shape of the C-S-H phases allowed for estimating the percolation threshold, i.e. hydration degrees at which nonzero elastic stiffness evolves.

The percolation threshold represents the hydration degree at which a connected network of solid particles is formed.

For modeling the hydration-induced stiffness evolution and the uniaxial compressive strength, the following two types of models were developed.

- Pichler et al. [106, 129] considered that the cement paste scale consists of highly disordered spherical unhydrated clinker particles, spherical water and air pores, and needle-shaped hydrates that are isotropically oriented in all spatial directions. The needle shape was essential for successfully predicting the strength. The stress concentration into a hydrate needle is more realistic for quantifying strength-related stress peaks compared to the stress concentration into spherical hydrates.
- Pichler and Hellmich [107] considered that the unhydrated cement particles are significantly larger than the capillary pores and the needle-shaped hydrates. Cement paste is modeled as a matrix-inclusion composite with spherical clinker grains embedded in a matrix referred to as “hydrate foam”. This matrix consists of spherical capillary pores and hydrate gel needles, which are highly disordered and isotropically oriented in all space directions, see Figure 2.8. The scale separation between the hydrates and the pores on the one hand and the clinker grains on the other hand also allowed to predict a stiffness evolution that starts with upward concavity.

For the sake of completeness, aggregate inclusions inside a cement paste matrix represent mortar and concrete. Within this thesis, the particle size of the aggregates distinguishes the scales of mortar and concrete. For aggregates with particle sizes smaller than 2 mm, the RVE refers to mortar. In case of concrete, also larger aggregates are considered.

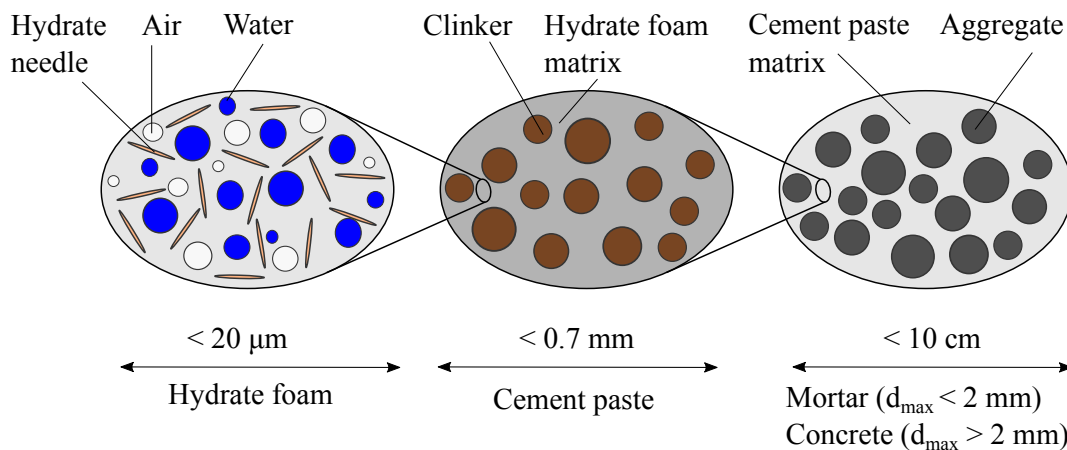


**Figure 2.8:** Micromechanical representation of cement-based materials, resolving three scales of observation [107]. Two-dimensional sketches refer to three-dimensional RVEs.

### 2.2.3.3 Influence of the shape of the hydrates on the elastic stiffness properties

The discussion about the shape of the hydration products was controversial. Sanahuja et al. [113] modeled the hydrates as flat spheroids (oblates) with an aspect ratio smaller than 1. The predictive capability of the model can be improved by adjusting the aspect ratio of the hydrates [113]. In this context, the question was addressed of how relevant the morphology of the hydrates for cement-based materials is [130]. It was claimed that the particle shape affects the percolation threshold. On the contrary, it has a less important influence on the mechanical properties, particularly at later hydration stages [130]. However, Sanahuja et al. [131] replied and showed that the particle shape can have a notable influence, in particular for modeling the setting of cement pastes.

Stora et al. [132] investigated the influence of the inclusion shapes on the linear elastic properties of cement pastes. For the modeling of the inclusions, the authors introduced a factor quantifying the asphericity of a particle. Accordingly, the hydration products were modeled as spheroids, whose shapes are needle-like or disk-like, see Figure 2.9. The appropriate modeling of the inclusion shape was found to be of particular importance for explaining leaching processes in cement pastes.

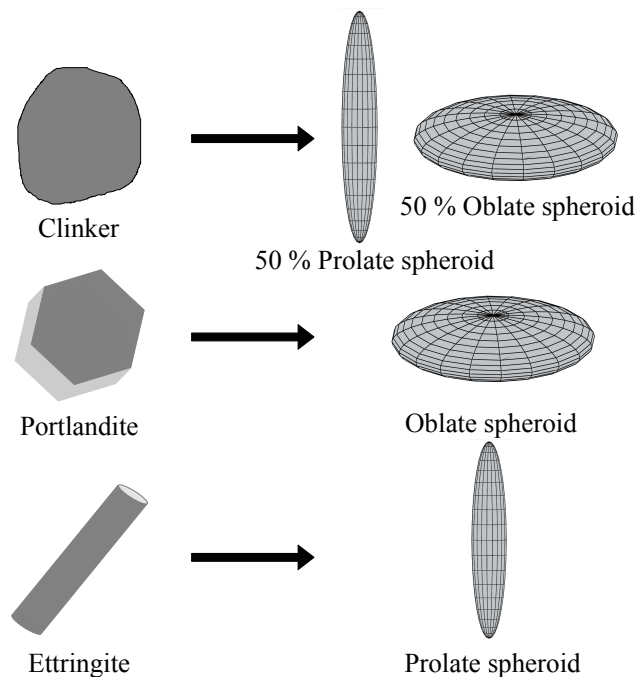


**Figure 2.9:** Approximation of realistic particle shapes in cement pastes by spheroids according to [132].

From ESEM investigations, it is known that the C-S-H phases exhibit a needle-shaped form [133]. The C-S-H phases do not have a preferred growth direction; instead, they are isotropically oriented. Therefore, Pichler et al. [106, 107, 129] and Termkhajornkit et al. [134] modeled the hydrates as cylindrical inclusions with an infinite aspect ratio. Figure 2.10 illustrates the significant role of modeling the hydrates. By means of the micromechanical model that Pichler et al. [106, 107, 129] proposed, the stiffness evolution in cement pastes is shown under the consideration of hydrates as spherical and as needle-shaped inclusions. Apparently, the modeling of spherical hydrates yields a smaller elastic stiffness of cement pastes than the modeling of needle-shaped hydrates does. Also, the onset of the stiffness evolution is remarkably different. The effect is more pronounced for low hydration degrees because needle-shaped hydrates build up a connected network more effectively than solely spherical hydrates. At higher hydration degrees, the differences between the curves for different shapes of the hydrates diminish. This result indicates that the effect of the morphological representation on the elasticity is less pronounced when the remaining space for the ongoing growth of the hydrates becomes limited [135]. The higher the  $w/c$ -ratio, the larger is the difference between the model response using needle-shaped and spherical hydrates. This observation is related to the smaller volume fraction of solid particles with increasing  $w/c$ -ratio.

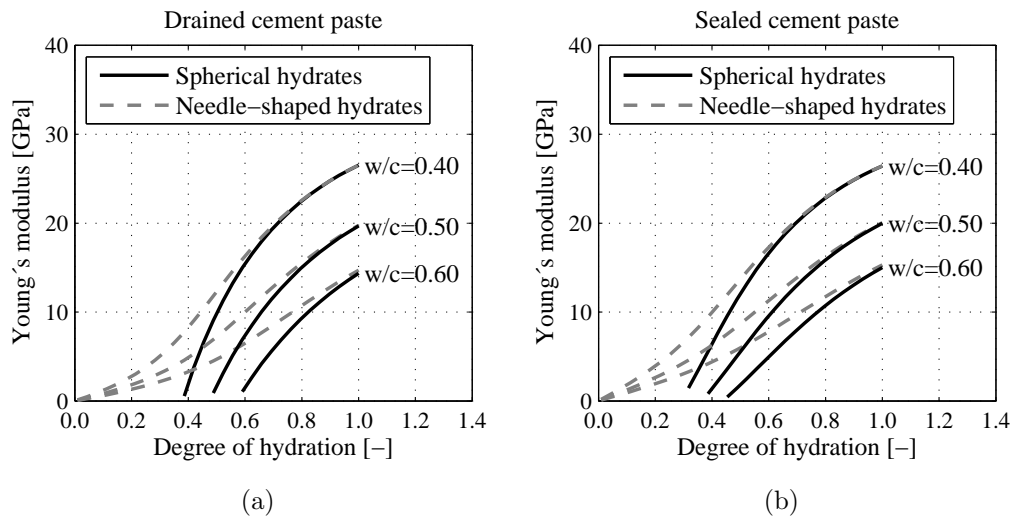


**Figure 2.10:** Stiffness evolution of cement pastes as a function of the degree of hydration under drained (a) and sealed (b) conditions compared for three different  $w/c$ -ratios and for two inclusion shapes of the hydrates, [own figure].

Furthermore, the model of Pichler et al. [106, 129] is able to capture two limit cases of macroscopic poromechanical boundary conditions of the RVE. The first case refers to drained conditions, which means that water can freely flow through the porous network.

Significant pore pressures are not activated due to loading, which requires the modeling of water as a phase with a vanishing elastic stiffness [136]. The second case refers to sealed conditions, which means that water cannot leave the RVE, causing pore pressures as a consequence of macroscopic loading. Then, water is introduced as a phase with vanishing shear stiffness but a bulk modulus of 2.3 GPa [137]. The consideration of drained conditions yields a slightly smaller stiffness than for sealed conditions. In the latter case, the stiffness of water contributes to the overall stiffness of cement paste, whereas under drained conditions water acts like air pores with a vanishing stiffness.

### 2.2.3.4 Field equations and boundary conditions

The underlying equations and boundary conditions required for multiscale modeling in the framework of continuum micromechanics are described next. Within the RVE of volume  $\Omega$ , field equations of linear elasticity are considered. The generalized Hooke's law reads as

$$\boldsymbol{\sigma}(\underline{x}) = \mathbb{C}(\underline{x}) : \boldsymbol{\varepsilon}(\underline{x}). \quad (2.2)$$

The static equilibrium conditions disregarding volume forces are given as

$$\operatorname{div} \boldsymbol{\sigma}(\underline{x}) = 0. \quad (2.3)$$

Linear strain-displacement relations are considered as

$$\boldsymbol{\varepsilon}(\underline{x}) = \frac{1}{2} \left[ \nabla \underline{\xi} + (\nabla \underline{\xi})^T \right] \quad (2.4)$$

with

$\boldsymbol{\sigma}$	second-order stress tensor
$\underline{x}$	location vector comprising positions within and on the boundary of the RVE
$\mathbb{C}$	fourth-order elastic stiffness tensor
$\boldsymbol{\varepsilon}$	second-order strain tensor
$\underline{\xi}$	displacement vector
$\nabla \underline{\xi}$	gradient of displacement vector.

In continuum micromechanics, each scale is considered to be subjected to a macroscopic strain  $\mathbf{E}$  prescribed at the boundary  $\partial\Omega$  of the RVE (Hashin-type boundary condition) [138]. The macroscopic strains are applied in terms of microscopic displacements  $\underline{\xi}$  as

$$\underline{\xi}(\underline{x}) = \mathbf{E} \cdot \underline{x} \quad \forall \underline{x} \in \partial\Omega. \quad (2.5)$$

### 2.2.3.5 Homogenization of elasticity

The macroscopic strain tensor  $\mathbf{E}$  is related to the kinematically admissible microscopic strain  $\boldsymbol{\varepsilon}(\underline{x})$  by means of a volume-averaging relation [122, 138, 139]

$$\mathbf{E} = \frac{1}{\Omega} \int_{\Omega} \boldsymbol{\varepsilon}(\underline{x}) \, dV = \sum_j f_j \boldsymbol{\varepsilon}_j. \quad (2.6)$$

The index  $j$  runs over all phases defined within the RVE. The volume fraction  $f_j$  is equal to the subvolume  $\Omega_j$  occupied by phase  $j$ , divided by the total RVE volume as  $f_j = \Omega_j/\Omega$ . The tensor of average phase strains  $\boldsymbol{\varepsilon}_j$  reads as

$$\boldsymbol{\varepsilon}_j = \frac{1}{\Omega_j} \int_{\Omega_j} \boldsymbol{\varepsilon}(\underline{x}) \, dV. \quad (2.7)$$

Analogously, the spatial average of the microstresses  $\boldsymbol{\sigma}(\underline{x})$  is equal to the macroscopic stresses  $\boldsymbol{\Sigma}$  defined as

$$\boldsymbol{\Sigma} = \frac{1}{\Omega} \int_{\Omega} \boldsymbol{\sigma}(\underline{x}) \, dV = \sum_j f_j \boldsymbol{\sigma}_j. \quad (2.8)$$

The second-order tensor of average phase stresses  $\boldsymbol{\sigma}_j$  is defined in analogy to Eq. (2.7). Microscopic and macroscopic quantities are linearly linked due to the linearity of Eqs. (2.2) – (2.4) and the geometric compatibility of the microscopic strain field with the boundary condition. Accordingly, the linear strain concentration rule reads as [140]

$$\boldsymbol{\varepsilon}(\underline{x}) = \mathbb{A}(\underline{x}) : \mathbf{E}. \quad (2.9)$$

$\mathbb{A}$  denotes the fourth-order strain concentration tensor, which quantifies the concentration of macrostrains into microstrains [141]. The strain concentration tensor provides access to the stiffness homogenization, i.e. the upscaling of the local phase stiffness  $\mathbb{C}_j$  to the homogenized elasticity tensor of the RVE  $\mathbb{C}^{\text{hom}}$ . To this end, Eq. (2.9) is inserted into the elastic constitutive law, Eq. (2.2), and the resulting formulation is further inserted into the stress average rule, Eq. (2.8), deriving the following expression

$$\boldsymbol{\Sigma} = \frac{1}{\Omega} \int_{\Omega} \mathbb{C}(\underline{x}) : \mathbb{A}(\underline{x}) \, dV : \mathbf{E}. \quad (2.10)$$

Comparing Eq. (2.10) with the macroscopic elastic law

$$\boldsymbol{\Sigma} = \mathbb{C}^{\text{hom}} : \mathbf{E} \quad (2.11)$$

yields an expression for the homogenized elasticity tensor as [122]

$$\mathbb{C}^{\text{hom}} = \frac{1}{\Omega} \int_{\Omega} \mathbb{C}(\underline{x}) : \mathbb{A}(\underline{x}) \, dV. \quad (2.12)$$

Specification of Eq. (2.9) and the elastic constitutive law for phase  $j$  reads as

$$\boldsymbol{\varepsilon}_j = \mathbb{A}_j : \mathbf{E}, \quad (2.13)$$

$$\boldsymbol{\sigma}_j = \mathbb{C}_j : \boldsymbol{\varepsilon}_j. \quad (2.14)$$

By analogy to the aforementioned steps, Eq. (2.13) is inserted into Eq. (2.14). The resulting expression is inserted into Eq. (2.6) and compared with Eq. (2.11), which yields the formulation of the homogenized elasticity tensor of a micro-heterogeneous material as [124]

$$\mathbb{C}^{\text{hom}} = \sum_j f_j \mathbb{C}_j : \mathbb{A}_j. \quad (2.15)$$

Microstructures of cementitious materials are commonly so complex that analytical access to the strain concentration tensors is out of reach. Estimations for strain concentration tensors were derived based on matrix inclusion problems of Eshelby [105] and Laws [142]. Accordingly, a single ellipsoidal inclusion having the phase stiffness  $\mathbb{C}_j$  is embedded in an infinite matrix of the stiffness  $\mathbb{C}_0$  whose boundary is subjected to homogeneous strains, see Figure 2.11. The strain localization tensors  $\mathbb{A}_j$  are derived as [107]

$$\mathbb{A}_j = [\mathbb{I} + \mathbb{P}_j : (\mathbb{C}_j - \mathbb{C}_\infty)]^{-1} : \left\{ \sum_j f_j [\mathbb{I} + \mathbb{P}_j : (\mathbb{C}_j - \mathbb{C}_\infty)]^{-1} \right\}^{-1}. \quad (2.16)$$

In Eq. (2.16),  $\mathbb{I}$  denotes the fourth-order identity tensor with the components  $I_{ijkl} = \frac{1}{2} \delta_{ik} \delta_{jl} + \delta_{il} \delta_{kj}$ . The Kronecker delta  $\delta_{ij}$  is 1 for  $i = j$  and 0, otherwise.  $\mathbb{P}_j$  is the fourth-order Hill tensor which depends on the shape of the inclusion embedded in a matrix with stiffness  $\mathbb{C}_\infty$ . The choice for  $\mathbb{C}_\infty$  characterizes the interactions between the material phases inside the RVE.

Insertion of Eq. (2.16) into Eq. (2.15) delivers an estimate for the homogenized elasticity tensor as

$$\mathbb{C}^{\text{hom}} = \sum_j f_j \mathbb{C}_j [\mathbb{I} + \mathbb{P}_j : (\mathbb{C}_j - \mathbb{C}_\infty)]^{-1} : \left\{ \sum_j f_j [\mathbb{I} + \mathbb{P}_j : (\mathbb{C}_j - \mathbb{C}_\infty)]^{-1} \right\}^{-1}. \quad (2.17)$$



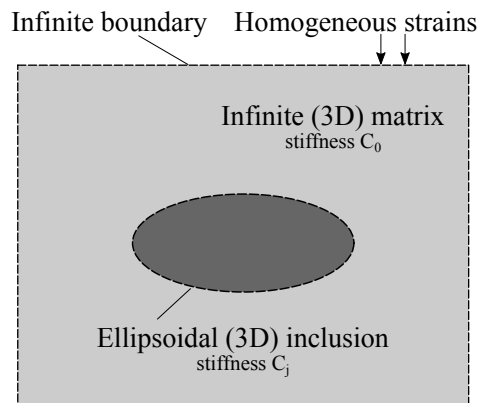


**Figure 2.11:** Ellipsoidal inclusion embedded in an infinite matrix according to the Eshelby problem, adapted from [141].

Depending on the morphology of the considered RVE,  $C_\infty$  is chosen according to the characteristic mode of interaction between the material phases. As for homogenization of matrix-inclusion composites, see Figure 2.12 (a),  $C_\infty$  is set equal to the stiffness of the matrix of the composite. This results in the so-called Mori-Tanaka scheme [143, 144]. For a RVE which exhibits a polycrystalline, highly disordered microstructure, i.e. the material phases are equally dispersed, see Figure 2.12 (b),  $C_\infty$  is set equal to the homogenized stiffness of the composite  $C^{\text{hom}}$ . This procedure results in the so-called self-consistent scheme [123, 125], which requires the iterative computation of the homogenized stiffness.

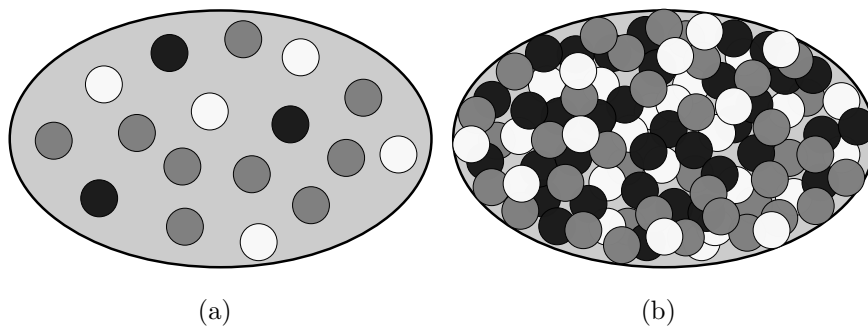


**Figure 2.12:** Types of microstructures in RVEs: matrix-inclusion-type morphology (a) and polycrystalline morphology (b), [own figure].

### 2.2.3.6 Homogenization of isotropic elastic stiffness properties

Based on the micromechanical representation of cement-based materials, shown in Figure 2.8, Pichler et al. [106, 107, 129] provided the formulations required for the upscaling of the elastic stiffness tensor from the hydrate foam scale up to the scales of mortar and concrete, respectively. On the scale of hydrate foam, the self-consistent scheme is employed,

yielding the homogenized stiffness tensor for hydrate foam,  $\mathbb{C}_{hf}^{\text{hom}}$ , as follows

$$\begin{aligned}
 \mathbb{C}_{hf}^{\text{hom}} = & \left\{ \sum_j f_j^{hf} \mathbb{C}_j : \left[ \mathbb{I} + \mathbb{P}_{\text{sph}}^{hf} : (\mathbb{C}_j - \mathbb{C}_{hf}^{\text{hom}}) \right]^{-1} + f_{\text{hyd}}^{hf} \mathbb{C}_{\text{hyd}} \right. \\
 & : \left. \int_0^{2\pi} \int_0^\pi \left[ \mathbb{I} + \mathbb{P}_{\text{cyl}}^{hf}(\varphi, \vartheta) : (\mathbb{C}_{\text{hyd}} - \mathbb{C}_{hf}^{\text{hom}}) \right]^{-1} \frac{\sin\vartheta d\vartheta d\varphi}{4\pi} \right\} \\
 & : \left\{ \sum_j f_j^{hf} : \left[ \mathbb{I} + \mathbb{P}_{\text{sph}}^{hf} : (\mathbb{C}_j - \mathbb{C}_{hf}^{\text{hom}}) \right]^{-1} + f_{\text{hyd}}^{hf} \right. \\
 & : \left. \int_0^{2\pi} \int_0^\pi \left[ \mathbb{I} + \mathbb{P}_{\text{cyl}}^{hf}(\varphi, \vartheta) : (\mathbb{C}_{\text{hyd}} - \mathbb{C}_{hf}^{\text{hom}}) \right]^{-1} \frac{\sin\vartheta d\vartheta d\varphi}{4\pi} \right\}^{-1}.
 \end{aligned} \tag{2.18}$$

In Eq. (2.18),  $j$  comprises the phases air and water with the hydrate foam-related volume fractions  $f_j^{hf}$ . For the computation of the latter, see Section 3.3.1. The Hill tensor  $\mathbb{P}_{\text{sph}}^{hf}$  takes into account the spherical shapes of the air and water inclusions. On the contrary, the Hill tensor  $\mathbb{P}_{\text{cyl}}^{hf}$  refers to the needle-shaped hydration products with the stiffness  $\mathbb{C}_{\text{hyd}}$  and the spatial orientations described by the angles  $\varphi$  and  $\vartheta$ . For computational details of the Hill tensors as well as the numerical evaluation of Eq. (2.18), see [106, 129] and the Appendix A.1.

The RVEs of cement paste, mortar, and concrete exhibit a matrix-inclusion-type morphology, rendering the application of the Mori-Tanaka scheme appropriate [143, 144]. On the scale of cement paste,  $\mathbb{C}_\infty$  is set to be equal to the homogenized stiffness of the hydrate foam. Therefore, the homogenized stiffness of cement paste,  $\mathbb{C}_{cp}^{\text{hom}}$ , reads as

$$\begin{aligned}
 \mathbb{C}_{cp}^{\text{hom}} = & \left\{ (1 - f_{\text{clin}}^{cp}) \mathbb{C}_{hf}^{\text{hom}} + f_{\text{clin}}^{cp} \mathbb{C}_{\text{clin}} : \left[ \mathbb{I} + \mathbb{P}_{\text{sph}}^{hf} : (\mathbb{C}_{\text{clin}} - \mathbb{C}_{hf}^{\text{hom}}) \right]^{-1} \right\} \\
 & : \left\{ (1 - f_{\text{clin}}^{cp}) \mathbb{I} + f_{\text{clin}}^{cp} : \left[ \mathbb{I} + \mathbb{P}_{\text{sph}}^{hf} : (\mathbb{C}_{\text{clin}} - \mathbb{C}_{hf}^{\text{hom}}) \right]^{-1} \right\}^{-1},
 \end{aligned} \tag{2.19}$$

with the cement paste-related volume fractions of clinker  $f_{\text{clin}}^{cp}$  and of the hydrate foam matrix  $(1 - f_{\text{clin}}^{cp})$ , see Section 3.3.1. For deriving the homogenized stiffness tensors of mortar,  $\mathbb{C}_{\text{mortar}}^{\text{hom}}$ , and concrete,  $\mathbb{C}_{\text{concrete}}^{\text{hom}}$ ,  $\mathbb{C}_\infty$  is set equal to the homogenized stiffness of cement paste, which reveals the following expressions

$$\begin{aligned}
 \mathbb{C}_{\text{mortar}}^{\text{hom}} = & \left\{ (1 - f_{\text{san}}^{\text{mortar}}) \mathbb{C}_{cp}^{\text{hom}} + f_{\text{san}}^{\text{mortar}} \mathbb{C}_{\text{san}} : \left[ \mathbb{I} + \mathbb{P}_{\text{sph}}^{cp} : (\mathbb{C}_{\text{san}} - \mathbb{C}_{cp}^{\text{hom}}) \right]^{-1} \right\} : \\
 & \left\{ (1 - f_{\text{san}}^{\text{mortar}}) \mathbb{I} + f_{\text{san}}^{\text{mortar}} : \left[ \mathbb{I} + \mathbb{P}_{\text{sph}}^{cp} : (\mathbb{C}_{\text{san}} - \mathbb{C}_{cp}^{\text{hom}}) \right]^{-1} \right\}^{-1},
 \end{aligned} \tag{2.20}$$

$$\mathbb{C}_{concrete}^{hom} = \left\{ \left(1 - f_{agg}^{concrete}\right) \mathbb{C}_{cp}^{hom} + f_{agg}^{concrete} \mathbb{C}_{agg} : \left[ \mathbb{I} + \mathbb{P}_{sph}^{cp} : \left( \mathbb{C}_{agg} - \mathbb{C}_{cp}^{hom} \right) \right]^{-1} \right\} : \quad (2.21)$$

$$\left\{ \left(1 - f_{agg}^{concrete}\right) \mathbb{I} + f_{agg}^{concrete} : \left[ \mathbb{I} + \mathbb{P}_{sph}^{cp} : \left( \mathbb{C}_{agg} - \mathbb{C}_{cp}^{hom} \right) \right]^{-1} \right\}^{-1}.$$

$f_{san}^{mortar}$  denotes the volume fraction of sand at the mortar scale. Correspondingly,  $f_{agg}^{concrete}$  is the volume fraction of the aggregates on the scale of concrete.

## 2.2.4 Experimental calibration and validation

The fundament for successful multiscale modeling is the interaction between theoretical and experimental investigations. Two types of experimental studies need to be performed in the context of multiscale modeling: calibration and validation experiments, see Figure 2.13. For the characterization of the material phases, particularly for their elastic properties and their morphology, experimental microscale investigations are required. Techniques such as microscopy or nanoindentation are commonly employed. Additionally, validation experiments need to be performed to evaluate the homogenization approach across the scales. Such experiments may be mechanical testing methods.

In exceptional cases, experimental techniques are not feasible or inadequate so that the identification of required (input) parameters fails. Then, the properties of the material phases can be identified by means of validation experiments via inverse analysis. A top-down approach is applied instead of bottom-up modeling, see e.g. [120, 145]. That means, a finer-scale model is iteratively adapted aimed at the correct representation of macroscopic test data.

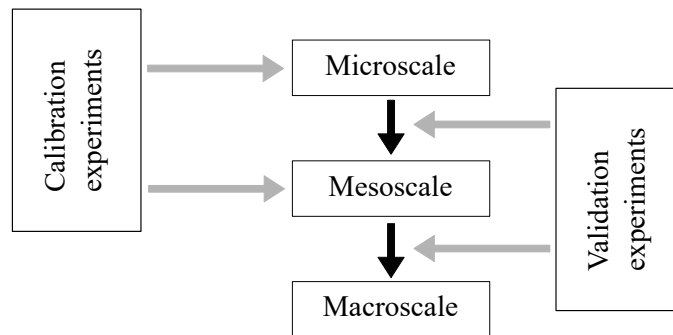


**Figure 2.13:** Experiments required in the context of multiscale modeling, adapted from [116].

Since the beginning of the 20<sup>th</sup> century, the indentation method has been used to measure mechanical properties of materials. By way of example, Brinell and Rockwell [146] employed metal balls as indenters. During the past few decades, advances in experimental micromechanics extended the scope of indentation testing down to the nanometer range [147].

Nanoindentation turned out to be a powerful and reliable experimental technique for the determination of mechanical properties such as elastic modulus, hardness, and viscous parameters within the nano- and micrometer range. The quantities are obtained from information about the loading, introduced via a small tip that is pushed into a sample, and the corresponding response of the tip in terms of the penetration depth, see Figure 2.14.

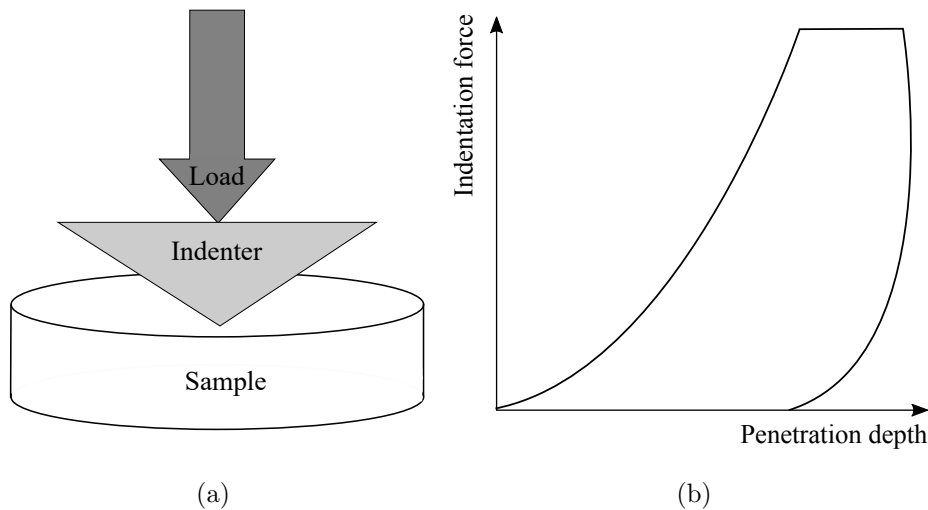


**Figure 2.14:** Principle of nanoindentation testing (a) and exemplary corresponding force–penetration diagram (b) according to [148].

Since 2001, several efforts have been directed towards characterizing the intrinsic elastic properties of the cement constituents. Velez et al. [149] determined the elastic modulus and hardness of the clinker phases in Portland cement. It was found that the elastic moduli of  $C_3S$ ,  $C_2S$ ,  $C_3A$ , and  $C_4AF$  are in the range between 125 and 145 GPa. Furthermore, statistical methods to evaluate a large number of indentations have been applied [150, 151]. Indents are performed over a large area of the sample to capture the heterogeneity of the material, see Figure 2.15 (a). Information about the mechanical properties and the volume fractions of the phases are obtained by means of property histograms and deconvolution techniques [112, 150, 151, 152], see Figure 2.15 (b). The concept of statistical grid nanoindentation has been refined and applied to hydrated cement pastes successfully, e.g. [153, 154].

In several studies, the existence of two types of C-S-H phases, often referred to as low-density C-S-H and high-density C-S-H, exhibiting different elastic properties has been observed due to the bimodal response in the frequency plots of the elastic modulus [112, 155, 136]. A third phase, the so-called ultra-high density (UHD) phase, exists, with an elastic modulus larger than the other two C-S-H phases [153, 156]. The UHD phase was observed for

cement pastes with water-to-cement ratios lower than 0.40. However, Chen et al. [157] recognized that the UHD phase is rather a mix of Portlandite and C-S-H phases, referred to as C-S-H/CH nanocomposites.

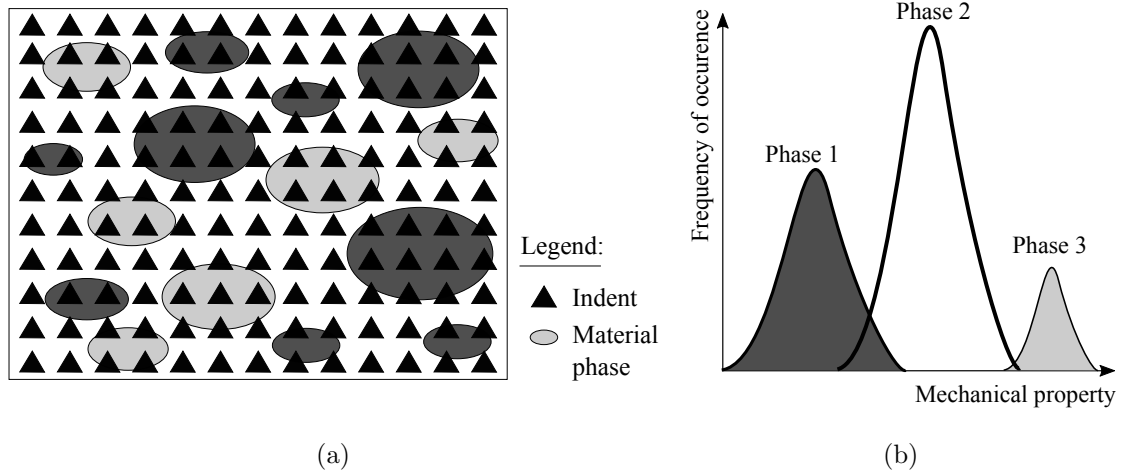


**Figure 2.15:** Statistical nanoindentation (a) and corresponding data evaluation using the deconvolution technique (b) according to [148].

The accuracy of the nanoindentation results significantly depends on the surface roughness of the cement paste specimens as well as on the size of the individual homogeneous phases [158, 159]. For a high surface roughness, an increased scatter and reduced indentation moduli have been reported [160, 161]. According to Trtik et al. [158], the homogeneous domains of the single phases should be at least three times larger than the size of the nanoindentation interaction volume; otherwise, the measured responses correspond to the average moduli of different phases. Miller et al. [159] suggest a surface roughness criterion of  $h_{max} \geq 5R_q$ , where  $h_{max}$  denotes the maximum penetration depth and  $R_q$  the root-mean-squared (RMS) roughness.

Recent activities aimed at coupling the mechanical nanoindentation tests with chemical measurements to obtain improved information on the phase identity, e.g. [157, 162, 163]. By way of example, scanning electron microscope/energy dispersive X-ray spectra (SEM-EDS) were combined with grid nanoindentation. One further important capability of nanoindentation testing is the measurement of basic creep properties. It was observed that the logarithmic kinetics of the long-term creep of concrete can be quantitatively estimated based on minutes-long microindentations on cement paste [164, 165, 166].

Hitherto, the focus has been mainly on Portland cement pastes. However, admixtures may significantly influence the (micromechanical) properties of cement-based materials, requiring nanoindentation tests on blended and modified cements. The technique was applied

to alkali-activated cementitious materials [167, 168] as well as to blended cement pastes containing fly ash [169, 170], slag [169, 171], and silica fume [170, 172]. The nanoindentation investigations revealed morphological changes of the hydration products and significant influences of the additives on the micromechanical properties of the cementitious phases.

A comprehensive study of the micromechanical properties of polymer-modified cement pastes is missing, although a few attempts can be found. Wang et al. [173] investigated SBR-modified cement pastes with varying polymer-to-cement ratios within the range of 0% to 20%. They determined the mean indentation modulus, i.e. the average value of 225 indents per sample, of the cement pastes as a function of the polymer content in order to identify the finer-scale origin of the macroscopic properties. It was observed that the average indentation modulus of the cement pastes decreases with increasing  $p/c$ -ratio.

Nanoindentation has also been employed to characterize the viscoelastic properties of polymers, see e.g. [174, 175, 176, 177, 178]. For polymers having a large modulus ( $\approx 1$  GPa), a good agreement between results from dynamic nanoindentation and standard dynamical mechanical analyses was found [176, 177], although a perfect match between macroscopic techniques and nanoindentation testing cannot be expected [174]. Reasons for that are differences in the stress and strain levels, the probed volume, and modes of deformation during the testing. Odegard et al. [176] presented a study on the influences of test parameters on the measured quantities and revealed that varying the frequency of the oscillation in nanoindentation testing does not have a significant effect on the measured viscoelastic properties of the polymers. In contrast, it was found that the amplitude may significantly influence the storage and loss moduli.

## 2.3 Creep behavior of cement-based materials

### 2.3.1 Long-term deformations in cement-based materials

Cement-based materials exhibit several deformations due to their aging and hygroscopic nature, see Figure 2.16. Three types of deformations are commonly distinguished: the instantaneous elastic response upon loading, shrinkage, and creep. Shrinkage is the volume change of concrete without external mechanical loading and comprises two categories, autogenous and drying shrinkage. There are many influences governing the shrinkage behavior of concrete such as the  $w/c$ -ratio, the type of aggregates and the shape of the structure. This renders the prediction of shrinkage strains difficult. Several prediction models were proposed, e.g. [179, 180, 181, 182, 183]. Still, huge discrepancies between the model predictions and experimental shrinkage measurements are reported [184].

### 2.3.2 Definition and origin of creep in cement-based materials

Viscous materials are characterized by an increase of deformations during constant loading, commonly referred to as creep, and a decrease of stress during constant deformation, the so-called relaxation. Also concrete exhibits creep and relaxation. In the past, concrete creep phenomena caused severe damage, for example at the Koror-Babeldaob Bridge in Palau [185]. Creep effects on reinforced concrete structures are rather complex. Often, a reduced stiffness of concrete is registered, which causes larger displacements and crack widths. For slender structures, creep has major influences on the load-bearing capacity. The time-dependent creep deformations cause a redistribution of stress within the cross-section, which decreases the compressive stress in concrete and increases the stresses in steel bars [91]. On the contrary, creep deformations may also reduce undesirable stresses [186, 187]. It has also been widely reported that creep deformations cause a loss of prestress [188]. Therefore, besides the short-term mechanical properties such as the compressive strength and the elastic modulus, the long-term time-dependent deformations of concrete should be evaluated and considered during the design process.

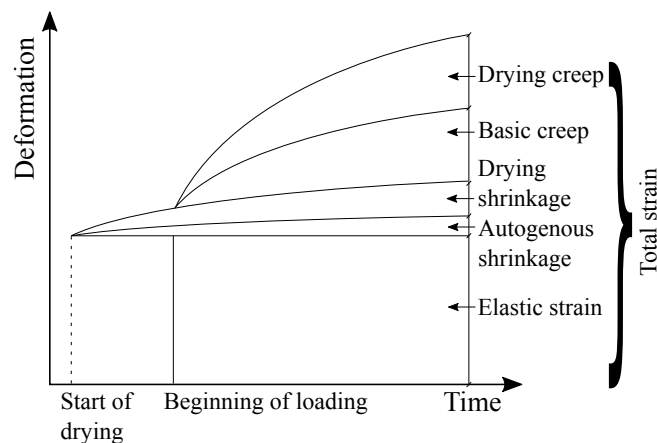


**Figure 2.16:** Time-dependent deformations in concrete according to [189].

Commonly, two different parts of occurring creep strains are distinguished: basic and drying creep. The basic creep occurs under conditions where moisture movement to or from the environment is prohibited. Drying creep, also known as Pickett-effect, is the additional creep deformation that concrete undergoes when it is exposed to drying during sustained loading [190]. Another categorization classifies the creep with respect to the load level into linear and nonlinear creep. Within the linear creep, the creep deformations and the applied stress are proportional. This is valid for stresses up to 25 % . . . 40 % of the concrete compressive strength [191]. Beyond this range, the creep deformations increase overlinearly with increasing stress due to the growth of microcracks (nonlinear creep).

Until recently, numerous theories have been developed to explain the physical origins of creep in concrete. Therein, it was suggested that the creep of concrete stems from crystalline flow, just as in metals [192], or that creep is caused by the loss of physically adsorbed water from the C-S-H gel into capillary pores [193]. Other theories such as the solidification theory [194] and the microprestress-solidification theory [190] are capable to explain the aging behavior of creep as well as the role of water. Still, the creep of concrete is a field of ongoing research [195]. Reasons for this are manifold: (i) Creep is observed on different length scales bridging phenomena inside the hydration products up to the concrete scale. (ii) The creep phenomenon in cement-based materials is coupled with the hydration process, which lasts months to years. Thus, the creep properties are dependent on the maturity of the material. (iii) Several factors determine the creep of concrete, rendering the experimental determination difficult. The material age, water and cement content, curing and storage conditions, types and amount of aggregates, temperature, concrete strength, and humidity influence the creep.

However, nowadays, it is accepted that the delayed deformations under time-invariant stresses stem from the hydrates; most aggregates and the unhydrated clinker particles do not exhibit creep [194, 196]. Thus, creep is almost completely related to the cementitious matrix. The aging (time-variant) creep properties of cement-based materials are related to the continuous formation of larger amounts of hydration products as a consequence of ongoing hydration. The hydrates exhibit nonaging (time-invariant) creep properties [118, 120].

#### **2.3.3 Short-term creep testing**

The creep of concrete has already been the focus of research for more than 100 years [197, 198]. The duration of classical creep tests on concretes as summarized in the database of laboratory creep and shrinkage experiments by Bažant and Li [199] typically ranges from several days to even years. One limitation of such long-term creep testing is that the creep response of the material might be influenced by environmental parameters, such as the humidity and the temperature, which may vary during the tests. Furthermore, long-lasting creep tests entail that the hydration and the creep response of the material are closely coupled. That means, such “aging” creep tests refer to material microstructures that undergo changes during the loading.

For practical civil engineering, the material behavior at early ages is of high relevance. The cracking in concrete, which represents a decisive control parameter for the design of structures, is considerably dependent on the age of the material [200, 201]. The effects of loading on young concrete are also significant for estimating the deformations that particularly occur in high-rise buildings and bridge towers [202]. Rather recently, short-



term early-age creep testing protocols were developed [203, 204, 205, 206, 207, 208]. They include regularly-repeated sequences of loading and unloading steps with a duration of a few minutes only, so that the hydration reaction does not progress significantly within one single test. Therefore, such short-term creep testing regimes provide insight into the hydration-induced evolutions of the elastic stiffness and the non-aging creep properties of cement-based materials. It was also elaborated that creep strains do not only develop during constant loads; instead, time-dependent deformations occur already during the loading process [207, 208]. This observation extends traditional definitions of concrete creep, which rather consider creep deformations starting at the onset of the loading plateau, e.g. [209, 210]

### 2.3.4 Fundamental formulations of creep

Within the range of linear creep, the creep strains of concrete  $\varepsilon_{c,\text{creep}}(t, \tau)$  can be described by means of the dimensionless creep coefficient  $\varphi_c$ . The creep coefficient is popular in design codes for quantifying creep deformations and links the elastic and creep strains as

$$\varepsilon_{c,\text{creep}}(t, \tau) = \varphi_c(t, \tau) \cdot \varepsilon_{c,\text{elastic}}(\tau) \quad (2.22)$$

with

- $\varepsilon_{c,\text{creep}}$  creep strain
- $t$  time instant of observation (age of concrete)
- $\tau$  time instant of loading
- $\varepsilon_{c,\text{elastic}}$  elastic strain.

Accordingly, the creep displacement depends on the time at which it is determined and the time at which the stress is applied. The reference elastic strain  $\varepsilon_{c,\text{elastic}}$  can either be determined at a concrete age of 28 days, as it is defined in Eurocode 2 [211], or more commonly at the time instant of loading  $\tau$ . The latter definition is considered in the sequel, reading as

$$\varepsilon_{c,\text{elastic}}(\tau) = \frac{\sigma_c(\tau)}{E(\tau)} \quad (2.23)$$

with

- $\sigma_c$  applied constant stress
- $E(\tau)$  elastic modulus at time  $\tau$ .

The load-dependent total strain  $\varepsilon_c$  is obtained as the sum of the elastic and the creep deformations and reads as

$$\varepsilon_c(t, \tau) = \varepsilon_{c,\text{elastic}}(\tau) + \varepsilon_{c,\text{creep}}(t, \tau) = \sigma_c(\tau) \left[ \frac{1}{E(\tau)} + \frac{\varphi_c(t, \tau)}{E(\tau)} \right]. \quad (2.24)$$

Eq. (2.24) provides access to the creep compliance  $C(t, \tau)$  and the creep compliance function  $J(t, \tau)$  as follows

$$\varepsilon_c(t, \tau) = \sigma_c(\tau) \left[ \frac{1}{E(\tau)} + C(t, \tau) \right] = \sigma_c(\tau) J(t, \tau). \quad (2.25)$$

In the case of nonlinear creep, the creep coefficient  $\varphi_c$  is also dependent on the concrete stress so that the variables  $\varphi_c(t, \tau)$ ,  $C(t, \tau)$ , and  $J(t, \tau)$  should be replaced with  $\varphi_c(\sigma_c, t, \tau)$ ,  $C(\sigma_c, t, \tau)$ , and  $J(\sigma_c, t, \tau)$ , respectively [212].

Relaxation is a conjugate property of the creep phenomenon. Equivalent to the creep coefficient  $\varphi_c$ , the dimensionless relaxation coefficient  $\psi_c$  describes the time-dependent decrease of stresses  $\Delta\sigma_c(t, \tau)$  under constant deformation:

$$\Delta\sigma_c(t, \tau) = \psi_c(t, \tau) \cdot \sigma_c(\tau). \quad (2.26)$$

Between the creep coefficient and the relaxation coefficient, the following relation holds.

$$\psi_c(t, \tau) = \frac{\varphi_c(t, \tau)}{1 + \rho_c \cdot \varphi_c(t, \tau)}. \quad (2.27)$$

$\rho_c$  is the aging coefficient taking into account the influence of aging concrete on the creep.

The previous equations hold for creep under constant stress and relaxation under constant deformation. However, commonly time-variant stresses occur in reinforced and prestressed concrete stemming from the bond between concrete and steel. This requires the modification and extension of the creep formulations by integral or differential equations to consider variable stresses and displacements.

Within the range of linear creep, the superposition principle of Boltzmann [213] for linear viscous-elastic materials can be applied. The explicit loading history, including different loading durations and onsets, is taken into account. The stress history is divided into  $n$  stress increments  $\Delta\sigma_c$  (Figure 2.17 (a)), providing access to the total displacement at time  $t$ :

$$\varepsilon_c(t, \tau) = \sigma_c(\tau) J(t, \tau) + \sum_{i=1}^n \Delta\sigma_c(\tau_i) J(t, \tau_i). \quad (2.28)$$

For a continuous and differentiable stress history, Eq. (2.28) turns into

$$\varepsilon_c(t, \tau) = \sigma_c(\tau) J(t, \tau) + \int_t^\tau \frac{\partial \sigma_c(\tau)}{\partial \tau} J(t, \tau) d\tau. \quad (2.29)$$

Partial integration of Eq. (2.29) delivers

$$\varepsilon_c(t, \tau) = \frac{\sigma_c(\tau)}{E_c(\tau)} - \int_t^\tau \sigma_c(\tau) \frac{\partial J(t, \tau)}{\partial \tau} d\tau. \quad (2.30)$$

Eq. (2.30) can also be obtained by dividing the time-dependent stress history into vertical intervals (impulse-type stress) and superposing the resulting strain changes. The stresses are discretized into stress impulses, see Figure 2.17 (b). Both formulations are equivalent.

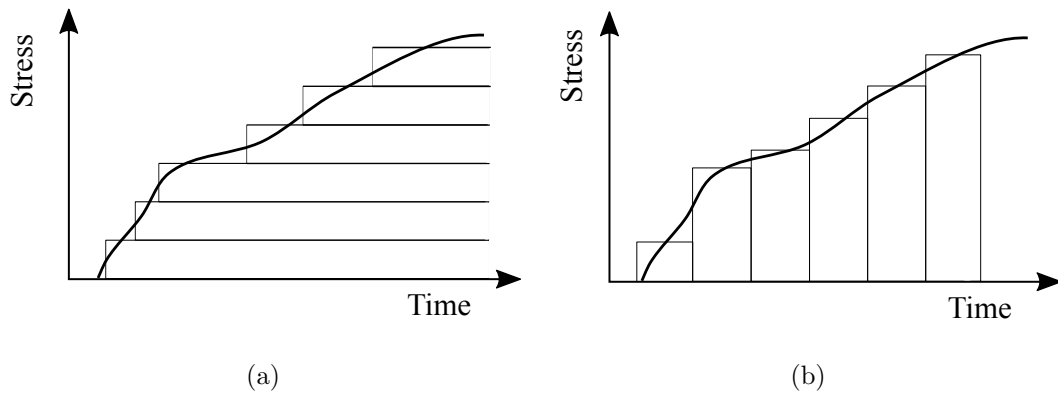


**Figure 2.17:** Discretization of the stress history into stress increments (a) and into stress impulses (b).

In the context of determining the long-term deformations at varying stresses, several definitions of the creep compliance  $C(t, \tau)$  and the creep compliance function  $J(t, \tau)$  exist, such as the theory of elastic creep, the theory of aging, and the theory of delayed creep recovery. For a detailed description of the theories, the reader is referred to [212].

The formulations mentioned above are only applicable for linear creep, where the stresses and the creep strains are proportional. If the stresses exceed a threshold of approximately 40 % of the short-term compressive strength of concrete, microcracks are formed increasingly and the creep strains increase overlinearly with the stresses. The nonlinear creep should not be neglected; otherwise, the creep deformation might be considerably underestimated.

The assessment of the nonlinear creep has been the focus of research during the past few years. Diener [212] summarized the approaches for considering the nonlinearity of creep during large stresses as follows, see [91, 212] for more details.

- Developing nonlinear spring–damper–models, which are formulated in terms of nonlinear differential equations.

- Assuming proportionality between creep deformations and short-term deformations considering inelastic deformations; the linear creep coefficient is coupled with strains of the nonlinear stress-strain relation of concrete subjected to short-term loading.
- Splitting the creep function into a linear (stress-independent) and a nonlinear (stress-dependent) part.
- Increasing the linear creep coefficient with an empirically determined over-proportionality factor.

#### 2.3.5 Multiscale prediction models for creep

Several phenomenological models predicting the creep compliance have been developed, e.g. [179, 181, 182]. Besides, the microscopic origin of shrinkage and creep in concrete motivated also the development of multiscale approaches. Hua et al. [214, 215] proposed the first approaches taking the macroscopic and the microscopic scales separately into account. Havlásek and Jirásek [216] performed numerical multiscale simulations. By means of finite element simulations at the mesoscale of concrete, sources for the nonlinear behavior of the drying shrinkage were investigated. Honorio et al. [217] combined analytical and numerical multiscale approaches to predict the aging viscoelastic behavior of cement-based materials at early age.

Within the framework of continuum micromechanics, several approaches to predict the cementitious creep properties have been developed. One common approach follows Laws and McLaughlin [218]. The homogenized material properties across the scales of cement-based materials are obtained based on the viscoelastic correspondence principle. Accordingly, the viscoelastic constitutive laws from the time domain are transferred to the Laplace-Carson (LC) domain, which yields mathematical formulations that are identical to the elastic equations used in the time domain. This allows the application of the same mathematical procedure for the homogenization of the LC-transformed viscoelastic properties as for the homogenization of elastic properties. The material properties in the time domain are obtained via analytical or numerical back-transformation of the LC-transformed homogenized material properties.

However, one cannot apply the Laplace-Carson transform in case of local aging linear viscoelastic behavior, where time is considered in both morphological evolutions and the mechanical behavior of the material phases [119]. Commonly, it is then assumed that the microstructure does not evolve anymore once it is subjected to macroscopic loading, e.g. [219, 220], which restricts this approach to fully hydrated concrete. Furthermore, innovative homogenization methods operate in the time domain and therefore avoid the

back-transformation of the Laplace-Carson transform. Several techniques to upscale non-aging linear viscoelastic behavior were derived [221, 222] and extended towards aging linear viscoelasticity [119, 223, 224]. Another approach has been proposed by Scheiner and Hellmich [118]. Accordingly, non-aging linear viscoelastic material phases are homogenized considering volume fractions that evolve with the time.

Shahidi et al. [95, 115] applied a continuum micromechanics-based approach to justify viscous surfaces as a source of material creep. Matrix-interface composites, including a linear elastic solid matrix and parallel viscous interfaces, were proposed. It was found out that the creep behavior of such composites is a result of micro-sliding processes within adsorbed fluid layers that fill the interfaces [115]. The fluids may be lubricating thin layers of adsorbed water. As regards cement-based materials, creep was related to the nanoscale of cement hydrates [225], see Figure 2.18.

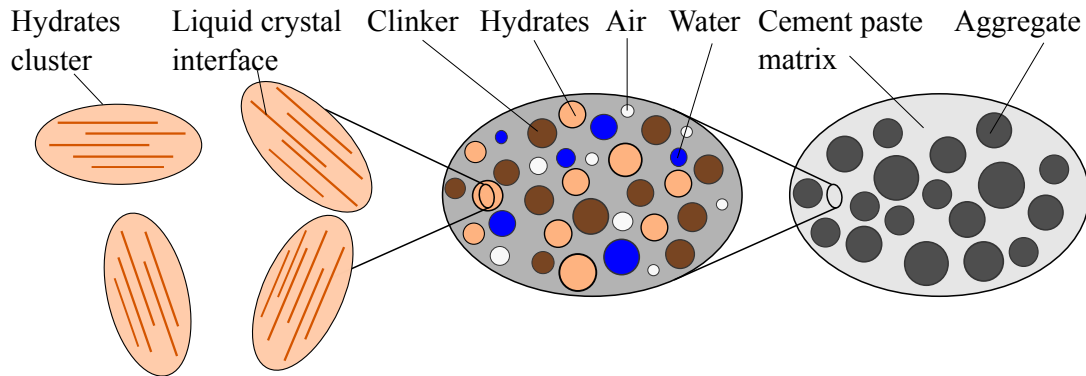


**Figure 2.18:** Morphological representation of concrete illustrating the microstructure of the hydrates as isotropically oriented matrix-interface composites according to [225].

The viscoelastic behavior of the hydrates can also be identified by means of a top-down approach using experimental data obtained at the cement paste scale. Königsberger et al. [120] identified two creep constants of the hydrate needles by means of a top-down analysis considering more than 500 non-aging creep functions of cement paste [207]. In particular, the cement paste microstructure was resolved down to the scale of hydrate foam. The universal, i.e. age- und composition-independent, creep properties of the hydrates, were shown to be the origin of the age- and composition-dependent macroscopic material behavior of cement-based materials. The significance of the newly identified quantities was illustrated by comparing model-predicted creep functions with results from independent creep tests of Tamtsia and Beaudoin [226], who performed 30-days-long creep tests on 30-years-old Portland cement pastes.

Irfan-ul-Hassan et al. [227] extended the homogenization of creep properties up to the scales of mortar and concrete. The computations revealed that two internal effects need to be integrated, namely the initial water uptake through the water-absorbing aggregates and the subsequent backsuction of this water from the aggregates to the hydrating cement paste. An improved hydration model based on that of Powers was developed, introducing two new quantities: the water uptake capacity of the aggregates and the water-filling extent of the cement paste voids. The water uptake capacity reveals how much water (in gram per kilogram) is taken up by the aggregates during mixing the raw materials. The water-filling extent implies the extent to which the shrinkage-induced voids of the cement pastes are filled by water that is sucked back from the open porosity of the aggregates. The newly computed volume fractions were used for upscaling the cement paste creep behavior up to the levels of mortar and concrete.

## **2.4 Summary and scientific questions**

Polymer-modified cement mortars and concretes have been mainly used in the repair and restoration. With the increasing application of PCC in construction, methods to estimate their mechanical behavior are required. One further aspect is that there is a large variability of polymers used to modify mortars and concretes. The experimental investigation of different combinations of cementitious systems and the polymers with varying technical additives and polymer contents is time-consuming. In order to provide a more general description of the influence of polymers in cement-based materials and to establish guidelines for the practical application in constructions, the reliable computer-based prediction of the elastic and creep behavior of polymer-modified mortars and concrete is necessary.

The basis for the development of prediction models is the knowledge about the hydration kinetics and the microstructure formation in polymer-modified cement-based materials. Both aspects have already been investigated intensively. In the literature, it was found out that the polymers slow down the hydration process. Reasons for the delayed hydration reaction are the adsorption of polymer layers on hydrating clinker particles and the complexation of calcium ions via functional groups of the polymers.

The properties of fresh and hardened PCC have been another field of research. Experimental tests revealed a lower elastic stiffness and a more pronounced creep activity in comparison with conventional concretes. However, the experiments have mainly been performed with mature materials. Much less is known about the mechanical behavior of polymer-modified cement-based materials at early ages. The properties of young concrete change continuously due to the ongoing hydration. In laboratories, the experimental determination of the strength and the Young's modulus is commonly performed with unstressed specimens. On the contrary, the concrete is often subjected to continuous preloadings since very early ages in constructions. Thus, the assessment of possible influences of such loadings on the material properties of young concrete is of importance for the precise prediction of the stress and strain development inside the hardening material as well as for further consequences such as the formation of cracks. The early-age elastic and creep behavior of polymer-modified cement-based materials is one focus of this work. Experimental and modeling approaches are pursued.

A few approaches have already been proposed to predict mechanical quantities that polymer-modified cement-based materials exhibit. However, the models are empirical and require the experimental identification of input parameters. Furthermore, the models have in most cases been developed for only one specific mixture of a PCC. Every other mixture

design requires another calibration of the model using experimental data. The general applicability of the prediction models to PCC containing different polymer modifications has not been proven yet. The empirical models do not consider microstructural characteristics of the material. Particularly for polymer-modified cement-based materials, where the polymers are effective at the microscale, this is unfavorable. Multiscale models overcome this limitation since they relate macroscopic material properties to chemical and physical processes at their scale of origin.

Multiscale models based on the principles of continuum micromechanics are able to predict mechanical properties of conventional concretes such as elasticity, strength, and creep. These models are also promising to be applied for polymer-modified cement-based materials. Still, the correct transferability of such models to PCC requires research. It has to be answered on which scale and with which inclusion shape the polymers need to be introduced into the micromechanical model. It is also of interest if the extended multiscale model is able to reliably predict mechanical quantities of PCC with differing polymer modifications.

The extension of existing multiscale models in the context of continuum micromechanics to include polymer-modified cement-based materials requires additional experimental investigations. On the one hand, the micromechanical properties of the polymers are essential input parameters for the model. On the other hand, validation experiments are needed to evaluate the homogenization procedure across the scales. The multiscale model developed within this thesis aims at predicting the mechanical properties on the scales of cement paste, mortar, and concrete. Thus, experimental data at each observation scale are demanded. Experimental results that allow the comparison of mechanical properties between several scales are not sufficiently given in the literature. For this purpose, an experimental multiscale study is performed with polymer-modified cement pastes, mortars, and concretes having a comparable mixture design. Different polymer modifications are used to show that the application of the multiscale model is not restricted to one specific PCC. The macroscopic mechanical properties are compared with the micromechanical properties of polymer-modified cement pastes, which also have not been thoroughly investigated yet. This allows the accentuation of structure-property relationships of polymer-modified cement-based materials.

The input parameters for the multiscale model need to be determined experimentally. Experimental data exhibit a stochastic scatter stemming from variations in the measurements and the material resources. This motivates the extension of common deterministic multiscale approaches via probabilistic analyses, which is one further focus of this thesis.



# 3 | Evaluation of semi-analytical multiscale models

The evaluation of models in the field of structural engineering has gained much attention during the past few years. A lot of research on this topic has been performed within the framework of the Training Research Group “Evaluation of Coupled Numerical and Experimental Partial Models in Structural Engineering”. Generic methods aimed at the quantitative evaluation of models considering different aspects of uncertainty within models and input parameters as well as coupling effects between partial models have been developed (see e.g. [228, 229, 230, 231, 232]). The proposed assessment methodologies have been applied to models in various fields of structural engineering, e.g. in wind engineering [233, 234] and in geotechnics [235]. Also, experimental models [236] and concrete material models [91, 237, 238] have been investigated. The evaluation of the model performance, i.e. the assessment of how closely a model describes the actual behavior, is not only a matter of comparing the model response and empirical data [239]. Rather, it is necessary to identify and evaluate the uncertainties inherent in the modeling process and to further incorporate them in the simulation and design process [240].

In Section 3.1, basics of probabilistic analyses are explained. Section 3.2 presents a review of uncertainty and sensitivity analyses applied to material models. In Section 3.3, a multiscale model for cement-based materials is evaluated using the probabilistic methods.

## 3.1 Fundamentals of probabilistic evaluation analyses

### 3.1.1 Introduction

There are several reasons to evaluate models by means of probabilistic analyses. One important factor is the heterogeneity of materials. Irregularities concerning the resources as well as the randomness of the microstructure can be taken into account using these methods. Additionally, uncertainties exhibited by the model input parameters and the model itself

can be studied. In this context, evaluation methods based on sensitivity and uncertainty analyses have been widely accepted because they are generic in their applications. The approaches are employed to study the effects of uncertain input parameters on the model response, to investigate the uncertainty propagation through a model, and to rank input parameters according to their contributions to the uncertainty of the model.

The evaluation of models with probabilistic analyses requires four consecutive steps, which are shown in Figure 3.1 and explained in the following.

1. For every input parameter  $x_i$  with  $i = 1, \dots, k$  of a model  $\mathcal{M}$ , the probability distributions, including all stochastic parameters, are defined to characterize the uncertainties inherent in the input parameters. The probability distributions have to be chosen carefully since the selection may introduce bias to the results of the evaluation analysis.
2. Input parameter samples  $\mathbf{X} = X_1, X_2, \dots, X_k$  are generated using the predefined distributions and probabilistic parameters. A matrix  $\mathbf{X}$  comprising  $k$  input parameters and  $N$  sample sets is obtained as

$$\mathbf{X} = \begin{bmatrix} x_{11} & x_{12} & \dots & x_{1k} \\ x_{21} & x_{22} & \dots & x_{2k} \\ \vdots & \vdots & \ddots & \vdots \\ x_{N1} & x_{N2} & \dots & x_{Nk} \end{bmatrix}$$

3. For each sample set, the model is evaluated. The model response  $\mathbf{Y}$  is produced as follows:  $\mathbf{Y} = \mathcal{M}(X_1, X_2, \dots, X_k)$ .
4. Probabilistic analyses of the model response are performed. Sensitivity and uncertainty analyses are carried out to study the influences of the uncertain input parameters on the model output.

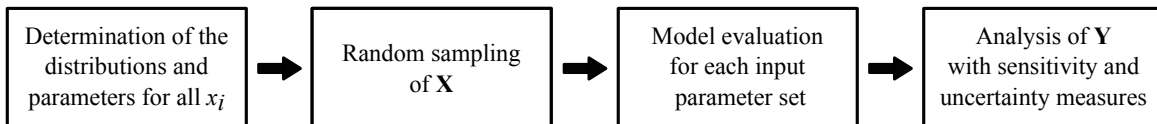


**Figure 3.1:** Workflow of the probabilistic model evaluation.

### 3.1.2 Sampling techniques

Sampling techniques aimed at the generation of large numbers of input parameter sets are fundamental for probabilistic analyses. A large amount of samples is required to represent the engineering problems with sufficient accuracy. The necessary number of samples depends on the parameter space; with increasing number of input parameters, more samples are demanded. The model behavior also plays an important role, particularly whether it behaves linearly or not with respect to the input parameters. Nonlinear models commonly require a larger amount of samples.

There is a variety of sampling techniques. The simple and robust Monte Carlo Simulation (MCS) is used frequently to perform probabilistic analyses. The MCS assumes a uniform distribution of the parameters, having lower and upper bounds given. The input parameters are sampled independently with their attributed probability density functions (PDF). One drawback of this method is that a large number of samples is required to ensure unbiased results. Otherwise, clusters and gaps might occur when only a low number of parameter sets is sampled, see Figure 3.2. Depending on the complexity of the respective model, the probabilistic analyses might become time-consuming.

In the present study, Latin Hypercube Sampling (LHS) is used. With this technique, less sample sets need to be generated to ensure sufficient accuracy of the approximated stochastic properties. The underlying idea is the subdivision of the parameter space into  $N$  intervals with equal marginal probabilities [241]. Each subdivision is only used once over all samples. LHS is independent of the dimension of the parameter space.

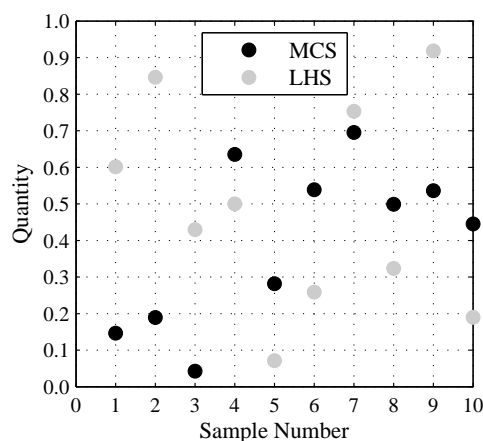


**Figure 3.2:** Comparison of a parameter set ( $N = 10$ ) sampled by means of the Monte Carlo Simulation (MCS) and the Latin Hypercube Sampling (LHS).

### 3.1.3 Sensitivity analysis

Sensitivity analysis is the study of how the (uncertain) input parameters influence the model output qualitatively and quantitatively. It is investigated how the uncertainty in the model response can be traced back to the uncertainties inherent in the model input parameters [242]. The main objective of performing a sensitivity analysis is the identification of key contributors with respect to the variance of the model output. Changes in the model output resulting from changes in the model input parameters are quantified. Insignificant input parameters can be considered as fixed in subsequent analyses, which simplifies the model evaluation process. In contrast, the precise determination of input parameters which substantially influence the model output may reduce the uncertainty of the model response and increase the model accuracy eventually.

There are several approaches for sensitivity analyses, such as local methods using partial derivatives, scatter plots, and global sensitivity analyses. For a review on these methods, the reader is referred to [243]. Local sensitivity analyses focus on the local influence of input parameters on the model response. The model is run for a few times with different parameter combinations varying one parameter at a time. In contrast, global sensitivity analyses consider the simultaneous variation of all stochastic input parameters.

Among the global approaches, variance-based sensitivity analyses have gained much attention. These methods are based on the decomposition of the variance of the model output as a sum of contributions from single and combinations of input parameters [244]. In the present study, the variance-based global sensitivity analysis of Sobol [245] and Homma and Saltelli [242], who introduced the total order sensitivity indices, is employed.

The main idea of the variance-based methods is to quantify the variance that would vanish if the true value of the input parameter  $X_i$  is known [246]. However, in structural engineering the exact value of  $X_i$  is mostly unknown. This can be represented by the conditional variance of the scalar model output  $Y$  fixing  $X_i$  at a certain value,  $V(Y | X_i)$ , and by varying over all parameters except  $X_i$ . The direct measure of the sensitivity for a factor  $X_i$ , the first order sensitivity index  $S_i$ , is defined as [245, 247]

$$S_i = \frac{V_{X_i}(E_{\mathbf{X}_{\sim i}}(Y | X_i))}{V(Y)} = 1 - \frac{E_{X_i}(V_{\mathbf{X}_{\sim i}}(Y | X_i))}{V(Y)}, \quad \sum_{i=1}^k S_i \leq 1 \quad (3.1)$$

with

- $V_{X_i}$  unconditional variance of argument  $(\cdot)$  over  $X_i$
- $\mathbf{X}_{\sim i}$  matrix of all factors but  $X_i$
- $E_{\mathbf{X}_{\sim i}}$  mean of argument  $(\cdot)$  over all factors but  $X_i$ .

$V_{X_i}(E_{\mathbf{X}_{\sim i}}(Y | X_i))$  is called the variance of conditional expectation and measures the first order effect of  $X_i$ . The larger the sensitivity index  $S_i$ , the larger is the influence of the input parameter  $X_i$  on the uncertainty of the model response. The sum over all  $S_i$  indicates the degree of correlation between the input parameters. For a sum that amounts to 1, the input parameters are uncorrelated. Then, the model is supposed to be non-additive.

The first order sensitivity indices measure the first order effects of  $X_i$  on the model response, i.e. the influence of every single variable in a decoupled sense. In order to take into account interaction effects of  $X_i$  with all other parameters  $\mathbf{X}_{\sim i}$ , higher order terms are introduced, referred to as total order sensitivity indices  $S_{T_i}$  [248] as

$$S_{T_i} = \frac{E_{\mathbf{X}_{\sim i}}(V_{X_i}(Y | \mathbf{X}_{\sim i}))}{V(Y)} = 1 - \frac{V_{\mathbf{X}_{\sim i}}(E_{X_i}(Y | \mathbf{X}_{\sim i}))}{V(Y)}, \quad \sum_{i=1}^k S_{T_i} \geq 1. \quad (3.2)$$

$V(Y | \mathbf{X}_{\sim i})$  describes the variance of the conditioned model response  $Y$  over all parameters except  $X_i$ .  $E_{X_i}(Y | \mathbf{X}_{\sim i})$  is the average of the variances over the  $X_i$ .

For the computation of the full sets of the first and total order sensitivity indices, a more economical implementation based on a matrix combination approach was proposed by Saltelli [242, 249]. Accordingly, the sensitivity indices are estimated as correlation coefficients, which requires the following steps:

- For  $k$  probabilistic input parameter, two matrices are generated, including  $N$  sample sets. The matrices  $\mathbf{X}_A$  and  $\mathbf{X}_B$  are called base matrices.

$$\mathbf{X}_A = \begin{bmatrix} x_A^{11} & x_A^{12} & \dots & x_A^{1i} & \dots & x_A^{1k} \\ x_A^{21} & x_A^{22} & \dots & x_A^{2i} & \dots & x_A^{2k} \\ \vdots & \vdots & \ddots & \vdots & \ddots & \vdots \\ x_A^{N1} & x_A^{N2} & \dots & x_A^{Ni} & \dots & x_A^{Nk} \end{bmatrix}$$

$$\mathbf{X}_B = \begin{bmatrix} x_B^{11} & x_B^{12} & \dots & x_B^{1i} & \dots & x_B^{1k} \\ x_B^{21} & x_B^{22} & \dots & x_B^{2i} & \dots & x_B^{2k} \\ \vdots & \vdots & \ddots & \vdots & \ddots & \vdots \\ x_B^{N1} & x_B^{N2} & \dots & x_B^{Ni} & \dots & x_B^{Nk} \end{bmatrix}$$

- A matrix  $\mathbf{X}_C$  is built from the base matrices such that all columns are kept from  $\mathbf{X}_A$  except the  $i$ -th column, which is retrieved from  $\mathbf{X}_B$  as follows

$$\mathbf{X}_{C_i} = \begin{bmatrix} x_A^{11} & x_A^{12} & \dots & x_B^{1i} & \dots & x_A^{1k} \\ x_A^{21} & x_A^{22} & \dots & x_B^{2i} & \dots & x_A^{2k} \\ \vdots & \vdots & \ddots & \vdots & \ddots & \vdots \\ x_A^{N1} & x_A^{N2} & \dots & x_B^{Ni} & \dots & x_A^{Nk} \end{bmatrix}$$

- The model output vectors  $\mathbf{Y}_A$ ,  $\mathbf{Y}_B$ , and  $\mathbf{Y}_{C_i}$  are obtained by evaluating the model with the input parameters collected in  $\mathbf{X}_A$ ,  $\mathbf{X}_B$ , and  $\mathbf{X}_{C_i}$  respectively.
- Finally, the first order sensitivity indices  $S_i$  and the total order sensitivity indices  $S_{T_i}$  are computed as

$$\begin{aligned} S_i &= \frac{\mathbf{Y}_A^T \mathbf{Y}_{C_i} - N(\bar{Y}_A \bar{Y}_{C_i})}{\mathbf{Y}_A^T \mathbf{Y}_A - N(\bar{Y}_A)^2}, \\ S_{T_i} &= 1 - \frac{\mathbf{Y}_B^T \mathbf{Y}_{C_i} - N(\bar{Y}_B \bar{Y}_{C_i})}{\mathbf{Y}_B^T \mathbf{Y}_B - N(\bar{Y}_B)^2} \end{aligned} \quad (3.3)$$

with  $\bar{Y}_x$  mean value of the output  $Y_x$  with  $x \in \{A, B, C_i\}$   
 $\mathbf{Y}_x$  output vectors obtained by evaluating the model for the sample matrices  $\mathbf{X}_x$  with  $x \in \{A, B, C_i\}$   
 $N$  number of sample sets.

Recently, the approach was improved by Marzban et al. [232] who introduced subdivisions of the parameter space with equal probability, requiring even less model evaluations.

### 3.1.4 Uncertainty analysis

Uncertainty analysis is used to study the propagation of the variations in the input parameters through the model, quantifying the uncertainty in the model response resulting from the uncertain input parameters. The model response and its stochastic properties can be evaluated. The uncertainties inherent in models can be classified into two categories [239]:

- parameter uncertainty (or model input uncertainty), which results from measurement inaccuracies or natural variations in the data.
- model uncertainty (or model framework uncertainty), which is caused by incomplete scientific background, lack of knowledge about mechanisms affecting the modeled system or modeling simplifications.

Uncertainty and complexity of a model are closely correlated [239], see Figure 3.3. A sophisticated model description can reduce the model uncertainty because most likely more physical phenomena are taken into account accurately. Therewith, the number of input parameters increases, which leads to a larger parameter uncertainty. The most adequate model is the one with the best trade-off between model uncertainty and parameter uncertainty. For the evaluation of the model response, both types of uncertainty are combined into the total uncertainty. With the parameter, model, and total uncertainty at hand, the model quality can be quantified [91, 250]. The model with the largest quality of the prediction and the lowest total uncertainty should be used for further analyses.

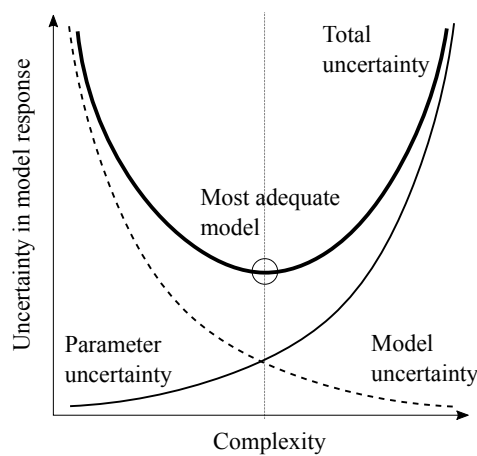


**Figure 3.3:** Relation between model complexity and uncertainty, hypothesis based on [239].

In the present study, the parameter uncertainty  $\sigma_X$  is investigated by propagating the variations in the uncertain input parameters through a multiscale model of concrete. If the input parameters are independent of each other, the parameter uncertainty  $\sigma_X$  might be determined as follows [234]

$$\sigma_X = \sqrt{\sum_{i=1}^N S_i^2 \sigma_{X_i}^2} \quad (3.4)$$

with

$N$	number of input parameters
$S_i$	first order sensitivity indices
$\sigma_{X_i}$	standard uncertainty of input parameter $X_i$ .

The model uncertainty describes the difference between the “true value”, i.e. the physical phenomenon for which the model has been developed, and the model prediction. Thus, the assessment of the model uncertainty requires the comparison between the model response and experimental data or a more complex model. For determining the model uncertainty, the adjustment factor approach is appropriate. It was developed by Zio and Apostolakis [251] and adapted by Riley [252].

The evaluation of the model uncertainty is performed by assigning model probabilities to each model based on expert judgment. For  $N_m$  considered models it holds that

$$\sum_{i=1}^{N_m} P(\mathcal{M}_i) = 1, \quad 0 \leq P(\mathcal{M}_i) \leq 1, \quad (3.5)$$

where  $P(\mathcal{M}_i)$  denotes the probability of model  $\mathcal{M}_i$ . Fundamental for estimating the model uncertainty is the choice of an appropriate reference model. Experimental data could be used for this purpose; however, in early design stages often no specific measurements are feasible. A common approach is to set the most complex model as a benchmark, which ensures that the physical phenomena are most accurately represented [228]. If no model is favored over the others or if there are no information about the model accuracy available, the model probabilities may be divided equally. Then, any model can be seen as the best model.

The adjustment factor approach is used to propagate the model uncertainty into the model prediction. Therein, an adjustment factor is assigned to the best model from a set of considered models so that an adjusted system response is obtained as

$$Y_p = Y^* + E_a^* \quad (3.6)$$

with

$Y_p$	response of an adjusted model
$Y^*$	prediction of the best model
$E_a^*$	adjustment factor.

The adjustment factor is used for taking the uncertainty concerning the best model into account.  $E_a^*$  is presumed to be a random normal variable. The expected value  $E(Y_p)$  and the variance  $V(Y_p)$  of the adjusted model are given in [251] as:

$$\begin{aligned} E(Y_p) &= Y^* + E(E_a^*) = Y^* + \sum_{i=1}^{N_m} P_{\mathcal{M}_i} (Y^{\mathcal{M}_i} - Y^*), \\ V(Y_p) &= V(E_a^*) = \sum_{i=1}^{N_m} P_{\mathcal{M}_i} (Y^{\mathcal{M}_i} - E(Y_p))^2. \end{aligned} \quad (3.7)$$

$Y^{\mathcal{M}_i}$  represents the prediction of model  $\mathcal{M}_i$ , which is deterministic as the parameter uncertainty is neglected.

According to Eq. (3.5), the model probabilities sum up to one. Thus, the following relations hold:

$$E(Y_p) = \sum_{i=1}^{N_m} P_{\mathcal{M}_i} Y^{\mathcal{M}_i} \quad \text{and} \quad V(Y_p) = \sum_{i=1}^{N_m} P_{\mathcal{M}_i} (Y^{\mathcal{M}_i} - E(Y_p))^2. \quad (3.8)$$



If the parameter uncertainty is considered, the expected value and the variance read as

$$E(Y_p) = \sum_{i=1}^{N_m} P_{\mathcal{M}_i} E(Y^{\mathcal{M}_i}) \quad \text{and} \quad V(Y_p) = \sum_{i=1}^{N_m} P_{\mathcal{M}_i} E\left(Y^{\mathcal{M}_i} - E(Y_p)\right)^2. \quad (3.9)$$

The contribution of a single model to the total variance reads as

$$V_{\mathcal{M}_i}(Y_p) = E\left[\left(Y^{\mathcal{M}_i} - E(Y_p)\right)^2\right] = V(Y^{\mathcal{M}_i}) + \left[E(Y^{\mathcal{M}_i}) - E(Y_p)\right]^2. \quad (3.10)$$

$V(Y^{\mathcal{M}_i})$  is the variation of a single model resulting from the parameter uncertainty.  $\left[E(Y^{\mathcal{M}_i}) - E(Y_p)\right]^2$  is the additive model framework uncertainty, that is the difference between the averaged response of model  $\mathcal{M}_i$  and the averaged response of the adjusted model. In complex problems of structural engineering,  $E(Y_p)$  might be unknown. Instead, the best model  $Y^{\mathcal{M}_{\text{ref}}}$  is used to compute the total variance of a single model within the concept of additive model framework uncertainty [228], where both parameter and model uncertainty are combined. Accordingly, the additive total uncertainty of a model,  $V^{\mathcal{M}_i}(Y)$ , expressed in terms of variances, is given by

$$V^{\mathcal{M}_i}(Y) \approx V(Y^{\mathcal{M}_i}) + V(\varepsilon_{\Delta}^{\mathcal{M}_i}) + V(\varepsilon^{\mathcal{M}_{\text{ref}}}). \quad (3.11)$$

The term  $V(Y^{\mathcal{M}_i})$  accounts for the parameter uncertainty that is computed using Eq. (3.4).  $V(\varepsilon_{\Delta}^{\mathcal{M}_i})$  denotes the model uncertainty with respect to the reference model as follows

$$V(\varepsilon_{\Delta}^{\mathcal{M}_i}) = \left[E(Y^{\mathcal{M}_i}) - E(Y^{\mathcal{M}_{\text{ref}}})\right]^2. \quad (3.12)$$

$V(\varepsilon^{\mathcal{M}_{\text{ref}}})$  is the uncertainty considering the shortcomings and uncertainties of the reference model itself. The values of  $V(\varepsilon^{\mathcal{M}_{\text{ref}}})$  are unknown; they are assumed to be a constant term for each model [228]. The tested values of  $V(\varepsilon^{\mathcal{M}_{\text{ref}}})$  influence the quantitative evaluations of  $V^{\mathcal{M}_i}(Y)$ ; however, they do not change the ranking of the single models.

## 3.2 Uncertainty and sensitivity analysis in material models

### 3.2.1 Uncertainty and sensitivity analysis in concrete creep models

Uncertainty and sensitivity analyses have already been employed to quantify the stochastic variations in concrete creep models. Madsen and Bažant [253] were the first who investigated the influence of input parameters exhibiting a scatter and the effect of the model

uncertainty for the creep model BP by Bažant, Kim and Panula [254]. Howells et al. [255] studied the influences of input parameters on the responses of common creep models by means of deterministic parameter studies. The authors found that the compressive strength of concrete and the relative humidity of the environment are significant factors for the concrete shrinkage and creep, whereas other parameters have an insignificant influence on the model output [255]. Several further approaches were proposed for considering material and external uncertainties in the context of time-dependent deformations of reinforced concrete structures [256, 257, 258]. Teplý et al. [259] analyzed the uncertainties of the outputs of the creep models BP-KX [260] and B3 [182, 261, 262] with respect to the influences of the input parameters. The approach was extended to the models ACI209 [179] and MC90 according to CEB-FIP Model Code 1990 [180] by Yang [263]. Yang also illustrated the influences of uncertainties in shrinkage and creep predictions on the loss of pretension force exemplary for a girder bridge [264]. Keitel et al. investigated the sources of uncertainties in creep models for correlated and uncorrelated parameters [265, 266] and elaborated the importance of the appropriate creep model selection [267]. In particular, the uncertainties of creep predictions under varying stresses were studied [266].

### **3.2.2 Uncertainty and sensitivity analysis in multiscale models**

Commonly, multiscale analyses are performed in a deterministic manner with fixed input parameters. Still, the input parameters include uncertainties inherently, which influence the predicted model responses. Computations considering uncertain input parameters result in probabilistic multiscale analyses where the model output represents a probabilistic variable as a function of the parameter variation. This motivates the investigation of the uncertainty propagation through the scales of the multiscale model.

Clément et al. [268] investigated the uncertain nature of hyperelastic heterogeneous materials at the microscopic scale and proposed a methodology for the uncertainty quantification based on polynomial chaos representation. A stochastic multiscale approach was also used to characterize the uncertainty propagation across the length scales of polycrystalline alloys [269] and of nanocrystalline membranes in metals [270]. Vu-Bac et al. proposed stochastic multiscale methods for amorphous polyethylene [271] as well as for polymer nanocomposites [272], aiming at the identification of key parameters influencing the macroscopic Young's modulus and Poisson's ratio. The uncertainty propagation across four length scales under consideration of correlated input parameters was studied [272]. Reisinger et al. [273] performed parametric studies and sensitivity analyses for a multiscale model of bone using mean field methods. Important parameters for the stiffness were identified.

Uncertainties in the multiscale modeling of concrete have been rarely investigated so far. The stochastic sensitivity of input parameters for a numerical model of cement paste was studied by Šmilauer et al. [274]. The focus was on the model-predicted hydration heat and the Young's modulus. Contradictory effects of the input parameters on the hydration heat and the governing role of the water-to-cement ratio for the Young's modulus were reported.

Unger [275] introduced the stochastic scatter of experiments into a mesoscale model of concrete. For that, spatially variable material parameters were considered. Also, a random character of the aggregate particle distribution was assumed [275].

Venkovic et al. [276] investigated the uncertainty propagation of a multiscale poromechanics-hydration model for concrete by means of stochastic meta-models (polynomial chaos expansion). The sensitivity indices of the input parameters were computed as functions of the time. The dominant roles of the apparent activation energy of calcium aluminate and the elastic modulus of the low-density calcium silicate hydrate (C-S-H) phase for the percolation threshold and the poroelastic properties in early-age stages at the cement paste scale were revealed. Berveiller et al. [277] discussed the influences of uncertain input parameters on the variability of the Young's modulus and the Poisson's ratio of cement paste. By means of a multiscale sensitivity analysis based on polynomial chaos expansions, the importance of the volume fraction of the high-density C-S-H phase was reported.

### **3.3 Evaluation of a semi-analytical multiscale model for cement-based materials**

A detailed study on the uncertainty propagation across the length scales of cement-based materials (cement paste, mortar, and concrete) is presented in the following, based on own previous investigations [278, 238]. Hitherto, it has not been thoroughly answered if and how the uncertainty in the model is magnified during the upscaling process. It also of interest to investigate which input parameters entail the largest uncertainties in the model response considering different scales of observation.

The following section is devoted to a comprehensive probabilistic study of a semi-analytical multiscale model, investigating the uncertainties throughout the upscaling process. Uncertainty and sensitivity analyses are performed at varying hydration stages and for two different water-to-cement ratios. The aims are twofold: (i) By means of sensitivity analyses, the input parameters contributing most to the uncertainties of the model responses on the scales of cement paste, mortar and concrete are identified. (ii) The question is

addressed if the choice of the hydration model also influences the uncertainties of the model responses. With the total uncertainty at hand, the hydration model that entails the lowest uncertainties in the model response can be identified.

### 3.3.1 Hydration models

In multiscale models based on the principles of continuum micromechanics (see Section 2.2.3), two consecutive steps are performed. First, the time-dependent evolutions of the phase volume fractions are computed, followed by an upscaling procedure. Hydration models allow for the quantitative description of the hydration-driven evolution of the microstructure. In particular, the volume fractions of the evolving material phases during the hydration reaction between clinker phases and water are determined. During the past decades, various hydration models have been developed with different theories and concepts behind, e.g. [279, 280, 281]. A novel hydration model based on data from nuclear magnetic resonance measurements was proposed by Königsberger et al. [282]. The model provides unprecedented access to the processes taking place in the C-S-H gel during the hydration reaction.

In the present study, two different hydration models were chosen for the probabilistic study of semi-analytical multiscale models, namely:

- the Powers-Acker hydration model [283, 284], *Powers model*.
- the hydration model proposed by Bernard et al. [111] and refined by Pichler et al. [116], *Bernard model*.

According to the literature, the Powers model and the Bernard model are the most frequently used hydration models for multiscale modeling based on the principles of continuum micromechanics.

#### 3.3.1.1 The Powers model

The Powers model, often denoted as the “engineering model”, provides the volume fractions of unhydrated clinker  $f_{\text{clin}}$ , water  $f_{\text{water}}$ , hydration products  $f_{\text{hyd}}$ , and air pores  $f_{\text{air}}$  in cement pastes; individual hydration products are not explicitly distinguished. The phase volume fractions are linear functions of the initial water-to-cement mass ratio  $w/c$  and the degree of hydration  $\xi$ , which accounts for the material maturity. Accordingly, the cement

paste-related volume fractions  $f_j^{cp}$  of the material phases  $j$  are determined as

$$\begin{aligned}
 f_{\text{clin}}^{cp} &= \frac{1 - \xi}{1 + \frac{\rho_{\text{clin}}}{\rho_{\text{water}}}(w/c)} = \frac{20(1 - \xi)}{20 + 63(w/c)} \geq 0, \\
 f_{\text{water}}^{cp} &= \frac{\rho_{\text{clin}} [(w/c) - 0.42\xi]}{\rho_{\text{water}} \left[ 1 + \frac{\rho_{\text{clin}}}{\rho_{\text{water}}}(w/c) \right]} = \frac{63 [(w/c) - 0.42\xi]}{20 + 63(w/c)} \geq 0, \\
 f_{\text{hyd}}^{cp} &= \frac{1.42\rho_{\text{clin}}\xi}{\rho_{\text{hyd}} \left[ 1 + \frac{\rho_{\text{clin}}}{\rho_{\text{water}}}(w/c) \right]} = \frac{43.15\xi}{20 + 63(w/c)} \geq 0, \\
 f_{\text{air}}^{cp} &= 1 - f_{\text{water}}^{cp} - f_{\text{hyd}}^{cp} - f_{\text{clin}}^{cp} = \frac{3.31\xi}{20\xi + 63(w/c)} \geq 0.
 \end{aligned} \tag{3.13}$$

In Eq. (3.13),  $\rho_{\text{clin}}$ ,  $\rho_{\text{water}}$ , and  $\rho_{\text{hyd}}$  are the mass densities of clinker, water, and the combined hydration products respectively. Figure 3.4 shows the evolution of the cement paste-related phase volume fractions for two different  $w/c$ -ratios, relying on the morphological model presented in Figure 2.8. On the scale of hydrate foam, the volume fractions  $f_j^{hf}$  follow from the phase volume fractions at the cement paste scale [107]

$$f_j^{hf} = \frac{f_j^{cp}}{1 - f_{\text{clin}}^{cp}}, \quad j \in \{\text{hyd}, \text{water}, \text{air}\}. \tag{3.14}$$

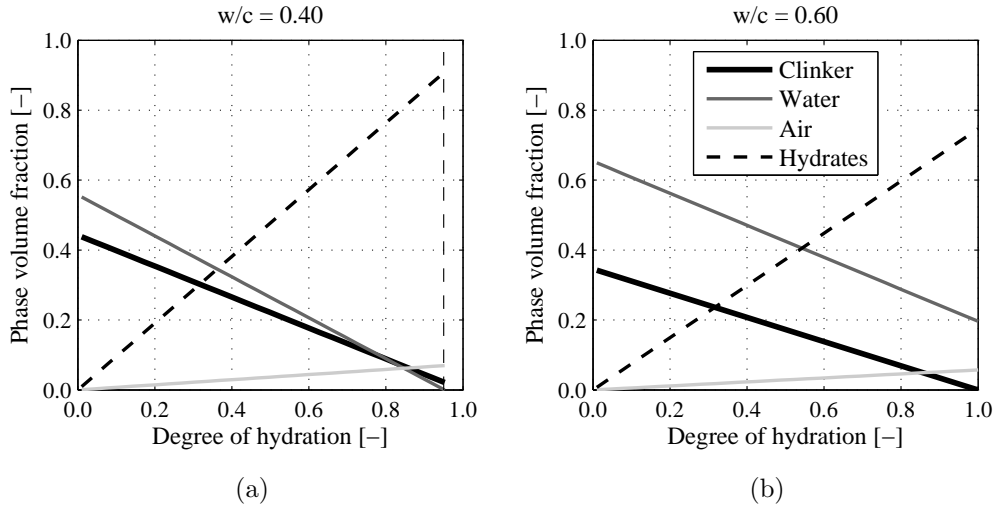


**Figure 3.4:** Evolution of the cement paste-related phase volume fractions using the Powers model for  $w/c = 0.40$  (a) and  $w/c = 0.60$  (b) as functions of the degree of hydration. The vertical dashed line in (a) refers to the maximum possible degree of hydration, which can be estimated with  $\xi_{\text{max}} = \min \left\{ \frac{w/c}{0.42}; 1 \right\}$ .

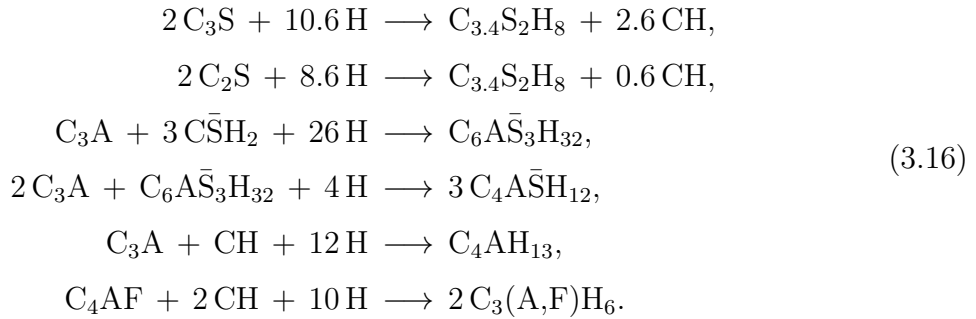
The mortar-related and concrete-related phase volume fractions,  $f_j^{mortar}$  and  $f_j^{concrete}$ , mainly depend on the mix design and read as

$$\begin{aligned}
 f_{\text{san}}^{mortar} &= \frac{\frac{s/c}{\rho_{\text{san}}}}{\frac{1}{\rho_{\text{clin}}} + \frac{w/c}{\rho_{\text{water}}} + \frac{s/c}{\rho_{\text{san}}}}, & f_{\text{cp}}^{mortar} &= 1 - f_{\text{san}}^{mortar}, \\
 f_{\text{agg}}^{concrete} &= \frac{\frac{a/c}{\rho_{\text{agg}}}}{\frac{1}{\rho_{\text{clin}}} + \frac{w/c}{\rho_{\text{water}}} + \frac{a/c}{\rho_{\text{agg}}}}, & f_{\text{cp}}^{concrete} &= 1 - f_{\text{agg}}^{concrete}.
 \end{aligned} \tag{3.15}$$

In Eq. (3.15),  $s/c$  and  $a/c$  denote the sand-to-cement mass ratio and the aggregate-to-cement mass ratio respectively.

### 3.3.1.2 The Bernard model

The Bernard model comprises stoichiometric and kinetic equations for computing the time-dependent volume fractions of the clinker phases and the hydration products. For the reactions between the unhydrated components ( $C_3S$ ,  $C_2S$ ,  $C_3A$ ,  $C_4AF$ ) and water, the stoichiometric relations according to Tennis and Jennings [285] are employed



In the Bernard model, the degree of hydration  $\xi_x$  for each clinker phase is determined as the relative amount of the reactant consumed  $m_x$  at a particular time  $t$  compared with the initial amount of anhydrous components  $m_{x,i}$ , see Eq. (3.17). The overall degree of hydration  $\xi$  is the sum of the individual hydration degrees of the clinker phases weighted by their corresponding initial weight fractions

$$\begin{aligned}
 \xi_x(t) &= 1 - \frac{m_x(t)}{m_{x,i}}, \\
 \xi(t) &= \frac{\sum_x m_{x,i} \xi_x(t)}{\sum_x m_{x,i}}.
 \end{aligned} \tag{3.17}$$

The kinetics of the hydration are described by kinetic laws linking the reaction rate  $d\xi/dt$  to the affinity  $A(\xi_x)$ . The affinity is the driving force of the reaction. The normalized affinity  $\tilde{A}(\xi_x)$  reads as

$$\tilde{A}(\xi_x) = \tau_{x,0} \exp \left[ \frac{E_{a,x}}{\mathcal{R}} \left( \frac{1}{T_0} - \frac{1}{T} \right) \right] \frac{d\xi_x}{dt} \quad (3.18)$$

with

$\tau_{x,0}$	characteristic time, depends on the hydration process
$E_{a,x}$	apparent activation energy for the hydration of phase $x$
$\mathcal{R}$	universal gas constant
$T_0$	reference temperature, typically $T_0 = 273$ K.

Three hydration stages are distinguished: dissolution, growth and nucleation, and diffusion. The hydration kinetic laws underlying the Bernard model are summarized in Appendix A.2. For a detailed explanation of all governing equations, see [111, 116]. The dissolution of the clinker particles is characterized by a normal affinity amounting to 1 and the characteristic time being equal to  $\tau_{x,0} = t_{x,0}/\xi_{x,0}$ , where  $t_{x,0}$  and  $\xi_{x,0}$  are the duration of the induction period and the hydration degree threshold at the end of the induction period respectively.

During the growth and nucleation, the characteristic time is equal to  $\tau_{x,0} = 1/(k_x \kappa_x)$  and the Avrami law [286] is employed:

$$-\ln[1 - (\xi - \xi_0)] = [k(t - t_0)]^\kappa \quad (3.19)$$

with

$k$	rate constant
$\kappa$	exponent defining the reaction order
$\xi_0, t_0$	degree of hydration and time at which the nucleation and growth reactions begin.

Afterward, the diffusion limited kinetics start, in which the Fuji and Kondo model is employed [287]. The characteristic time is described as  $\tau_{x,0} = R^2/(3D_x)$  where  $R$  is the average initial radius of the unhydrated clinker grains and  $D$  is the coefficient of diffusion of dissolved ions through formed hydration products.

The chemical and kinetic equations are fundamental for the computation of the phase volumes present in the cement pastes at given time instants. The evolving volumes of the hydration products  $V_{\text{hyd}}$  can be computed as functions of the time [276]:

$$V_{\text{hyd}}(t) = \frac{M_{\text{hyd}}}{M_x} \frac{\rho_x}{\rho_{\text{hyd}}} m_x n_{\text{hyd}/x} \xi_x(t) \quad (3.20)$$

with

- $M$  molar mass
- $\rho$  density
- $m_x$  mass fraction of the clinker phase  $x$  in the cement
- $n_{\text{hyd}/x}$  number of moles of hydration product, which are formed out of one mole of the reactant  $x$ , obtained from Eq. (3.16).

The hydration degrees  $\xi_x(t)$  are obtained solving Eq. (3.18) for the corresponding kinetic process. The molar masses  $M_x$  and the densities  $\rho_x$  are given in [285].

The volume fractions of both reactants  $f_x(t)$  and hydration products  $f_{\text{hyd}}(t)$  are obtained by normalization of the respective volumes at the specific stage of hydration. The evolutions of the volume fractions at the cement paste using the Bernard model are shown in Figure 3.5. For the mortar- and concrete-related volume fractions, Eq. (3.15) can be employed.

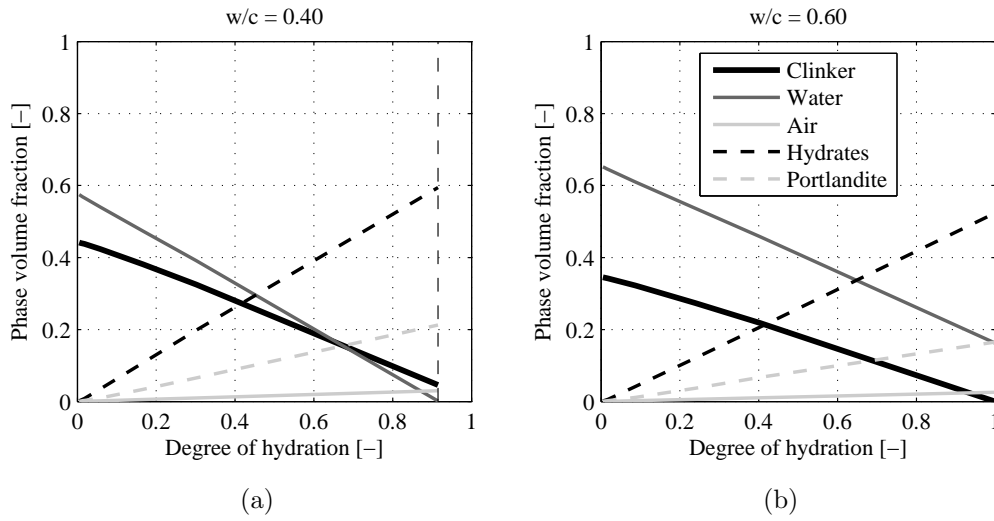


**Figure 3.5:** Evolution of the cement paste-related phase volume fractions using the Bernard model for  $w/c = 0.40$  (a) and  $w/c = 0.60$  (b) as functions of the degree of hydration. The vertical dashed line in (a) refers to the maximum possible degree of hydration, which can be estimated with  $\xi_{max} = \min \left\{ \frac{w/c}{0.42}; 1 \right\}$ .

In comparison with the model of Powers, the Bernard model explicitly distinguishes different hydration products, such as C-S-H and Portlandite. It also acts on the assumption of two types of C-S-H phases that differ according to their elastic properties. The two types are called high-density C-S-H (C-S-H HD) and low-density C-S-H (C-S-H LD), following well established proposals reported in the literature [284, 285]. It is assumed that the C-S-H



LD is mainly formed during the first hydration stages of nucleation and growth, and the C-S-H HD is formed during the stages controlled by diffusion [111]. This induces a RVE having a matrix-inclusion-type morphology, which is one scale lower than the hydrate foam depicted in Figure 2.8. The micromechanical model adapted for the use of the Bernard model is given in Figure 3.6.

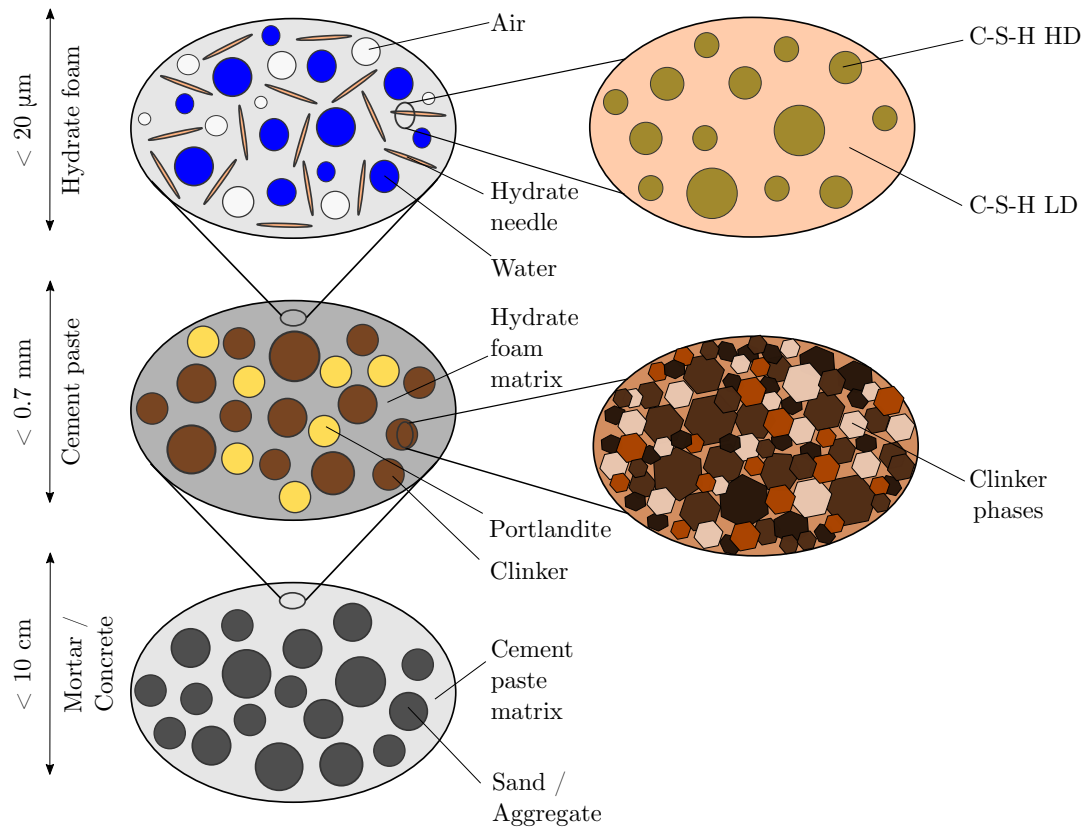


**Figure 3.6:** Adapted morphological model of concrete, including the scales of hydrate foam, cement paste and mortar or concrete as well as two types of C-S-H phases.

### 3.3.2 Probabilistic input parameters

The probabilistic evaluation methodology requires the specification of input parameters and their probabilistic properties. Within this thesis, it is assumed that the input parameters are not correlated with each other. The input parameters for the multiscale homogenization using the two hydration models are summarized in Table 3.1. The probability distributions are detailed given in Appendix A.3, sorted regarding each hydration model. For the Powers model, 14 stochastic input parameters are used. In total, 32 variables are used for implementing the Bernard model into the multiscale approach.

**Table 3.1:** Number of input parameters required for the multiscale modeling incorporating two different hydration models.

Category	Powers model	Bernard model
Elastic parameters	8	11
Mixture composition	2	2
Mass densities	4	3
Hydration kinetics	0	12
Clinker phase composition	0	4

Values for the input parameters and the corresponding probabilistic properties are reported in the literature. For some parameters, probabilistic data are not available. In these cases, missing parameters are selected by the author. A log-normal distribution is assigned to all elastic parameters, considering a coefficient of variation of 10 % around the mean value, as it was also reported in [276]. For the mass densities, a log-normal distribution with a coefficient of variation of 5 % is assumed. For the volume fractions of sand and aggregates, a uniform distribution is defined. The choice of the probabilistic properties may introduce bias into the results of both the uncertainty and the sensitivity analyses [276]. Two  $w/c$ -ratios are considered, which are handled as deterministic values.

### 3.3.3 Probabilistic model predictions

The multiscale model described in Section 2.2.3 provides predictions for the Young's moduli of cement paste, mortar, and concrete as functions of the hydration degree and the water-to-cement ratio. The probabilistic model predictions of the multiscale model incorporating both hydration models are analyzed by means of the probabilistic evaluation methodology. To this end, the model is evaluated using 5000 sample sets, which are generated by means of the LHS.

The homogenized probabilistic model predictions in terms of the Young's moduli on the scales of cement paste, mortar, and concrete, including the mean values and the standard deviations, are shown in Figure 3.7 for the use of the Powers model and the Bernard model. The curves illustrate differences in the aging elasticity at different length scales. The Young's modulus of cement paste shows an almost linear dependence on the degree of hydration. This behavior deviates on the scales of mortar and concrete. The Young's moduli of mortar and concrete increase more rapidly at early hydration stages whereas the slope of the curve diminishes with ongoing hydration. This effect is related to the development of microcracks predominantly in the interfacial transition zone of mortars and

concretes [61]. Thus, cement pastes without aggregate inclusions exhibit a more brittle elastic behavior than mortars and concretes. The elastic stiffening of mortars and concretes is more pronounced for lower  $w/c$ -ratios.

A magnification of the variability of the model responses across the scales is observed. The Young's modulus at the concrete scale exhibits a higher uncertainty than the Young's modulus at the cement paste scale, which is reasonable due to the larger number of uncertain input parameters considered at the concrete scale. The model responses for a water-to-cement ratio of 0.40 exhibit a larger variability than for a water-to-cement ratio of 0.60 at a given hydration degree. This is most likely related to the larger volume fraction of solid particles for lower water-to-cement ratios. The cementitious phases exhibit larger uncertainties than water.

Comparing the standard deviations for the multiscale model responses using the Powers model and the Bernard model does not reveal significant differences. This is surprising because the Bernard model requires a larger number of input parameters than the Powers model and a rather large scatter of the model response is expected. A more detailed investigation concerning the uncertainties within the Powers and the Bernard model is presented in Section 3.3.5.

Figure 3.7 also illustrates that the predicted Young's moduli of the cement pastes, mortars, and concretes are almost identical at final hydration stages for the multiscale model using the Powers model and the Bernard model. In contrast, at early hydration stages the stiffness of the multiscale model incorporating the Powers model increases faster. This is related to the larger volume fraction of hydrate needles in the approach using the Powers model (compare Figures 3.4 and 3.5). For the use of the Bernard model, the hydration products comprise both cylindrical hydrate needles and spherical Portlandite. With hydrate needles, a connected network of solid particles exhibiting a non-vanishing stiffness is reached at earlier hydration stages than with spherical hydrates (see Figure 2.10 and [129, 132]).

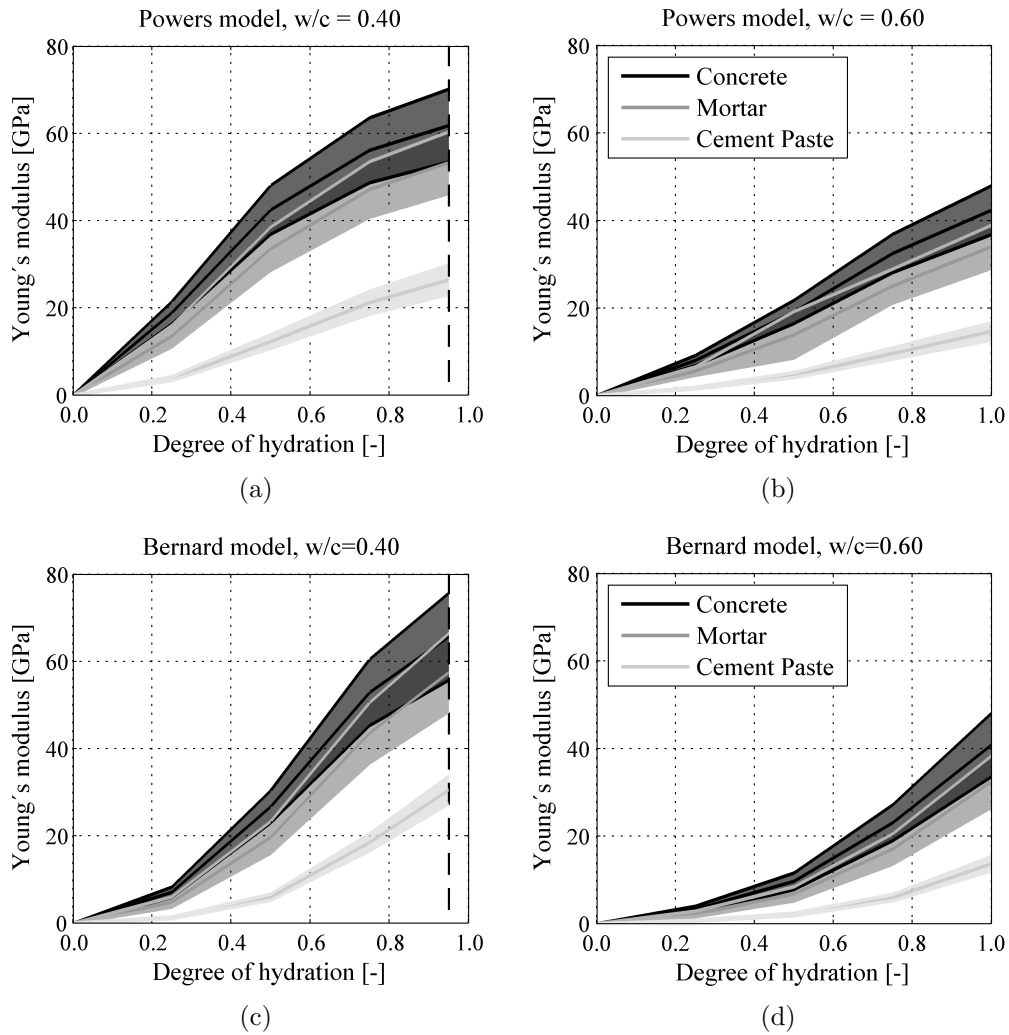


**Figure 3.7:** Stochastic model outputs (Young's moduli) of a multiscale model using the Powers model (a) and (b) and the Bernard model (c) and (d) as functions of the degree of hydration. The mean values and the standard deviations are shown. Two water-to-cement ratios are compared:  $w/c = 0.4$  [(a), (c)] and  $w/c = 0.6$  [(b), (d)].

### 3.3.4 Results of the sensitivity analysis

The results of the global sensitivity analyses with respect to the Young's moduli of cement paste, mortar, and concrete are presented in Figures 3.8 and 3.9, separately for both hydration models. The total order sensitivity indices  $S_{T_i}$  are shown as functions of the degree of hydration. For phases where both the bulk and shear moduli are given, the uncertainties are combined and only one parameter, the Young's modulus  $E$ , is specified. The other input parameters are abbreviated as  $f$  for the volume fractions and  $\rho$  for the mass densities. On each scale, the total order sensitivity indices sum up to one, which indicates that interaction effects between the input parameters are negligible.

First, the results of the multiscale model combined with the Powers model are discussed. At the cement paste scale, the greatest contributor to the uncertainty of the model response is the Young's modulus of the hydrates, which agrees well with the results of Venkovic et al. [276]. With ongoing hydration process and the corresponding densification of the microstructure, the densities of the hydrates and the clinker phases become more important. This is explained by the direct influence of the densities on the volume fractions according to Eq. (3.13). In contrast, the influence of the elastic properties of the clinker phases is negligible. At the mortar scale, the parameters related to sand influence the model results most visibly. Up to a degree of hydration of about 0.60, the volume fraction of sand is the largest contributor to the model output uncertainty. Opposed to the loss of influence of the sand volume fractions, the significance of the elastic parameters of sand increases. Analogously, the aggregates contribute most to the uncertainty of the predicted Young's modulus of concrete. With increasing degree of hydration, the influence of the Young's modulus of the aggregates grows, whereas the influence of the aggregate volume fraction decreases. For a  $w/c$ -ratio of 0.40, the role of the elastic properties of the sand and aggregates inclusions is more pronounced than for a  $w/c$  ratio of 0.60.

The results of the sensitivity analysis reveal an important feature of the multiscale model, as it was also reported by Bernard et al. [111], who described a counteracting effect of the stiffnesses of sand and aggregate inclusions as well as of their volume fractions. At early hydration stages, the volume fractions of sand and the aggregates have a stronger influence on the stiffness evolution of mortars and concretes than the Young's moduli of the inclusions. For higher degrees of hydration, the effects are inverse. At the concrete scale, the phenomenon is more pronounced because of the larger total amount of inclusions.

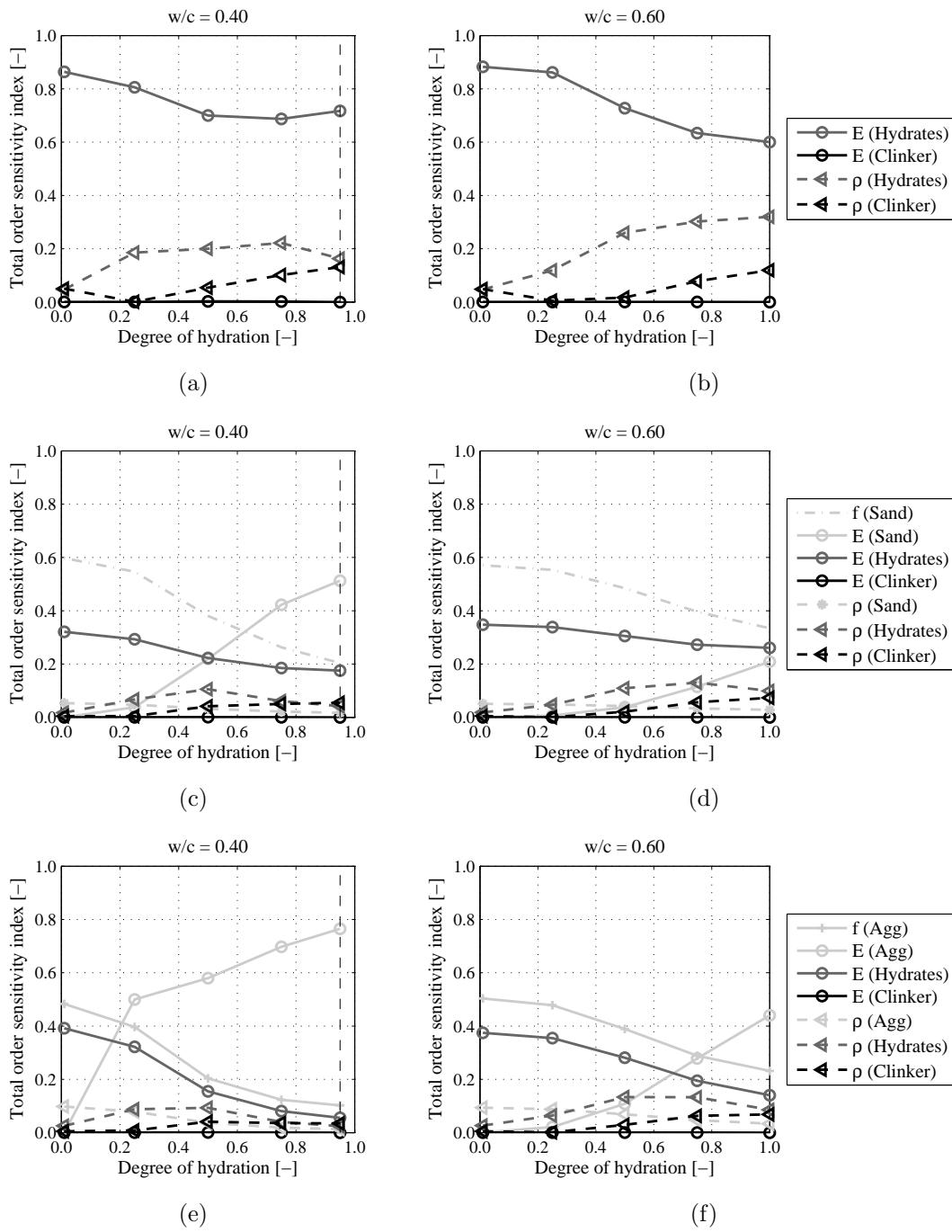


**Figure 3.8:** Evolution of total order sensitivity indices of the Powers model as functions of the degree of hydration for two different water-to-cement ratios, compared at three length scales: cement paste [(a),(b)], mortar [(c),(d)] and concrete [(e),(f)].  $f$  – Volume fraction,  $E$ – Young’s modulus,  $\rho$  – mass density.

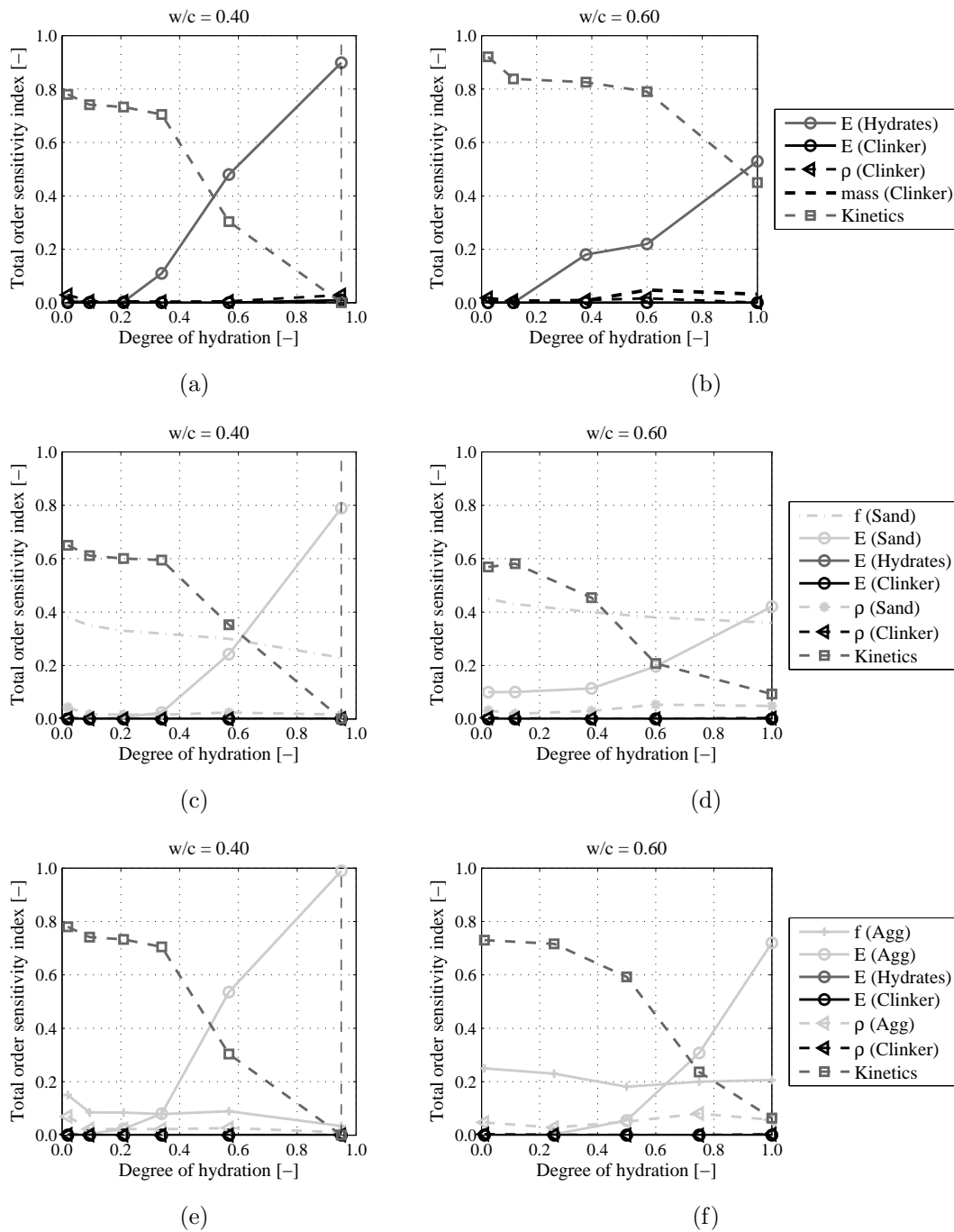


**Figure 3.9:** Evolution of total order sensitivity indices of the Bernard model as functions of the degree of hydration for two different water-to-cement ratios, compared at three length scales: cement paste [(a),(b)], mortar [(c),(d)], concrete [(e),(f)].  $f$  – Volume fraction,  $E$  – Young’s modulus,  $\rho$  – mass density.

The total order sensitivity indices related to the use of the Bernard model illustrate the importance of the kinetic factors, which are summarized into one category (“kinetics”). At early hydration stages, the kinetic parameters determine the uncertainty of the model response most dominantly. Particularly, the activation energies of the clinker particles play an important role, which agrees well with the results published by Venkovic et al. [276]. The mass composition of the clinker phases is of minor importance. With ongoing hydration and the corresponding decrease of the hydration rate, the elastic properties of the main components govern the uncertainties of the model-predicted Young’s modulus on the scales of cement paste, mortar, and concrete. The kinetic parameters are less important for later hydration stages. Again, the contradictory evolutions of the volume fractions and elastic properties of the sand and aggregate inclusions are observed.

The sand and aggregate inclusions most dominantly determine the uncertainties of the model responses on the scales of mortar and concrete respectively. However, the stochastic properties concerning their elastic moduli and their volume fractions are assumptions, chosen by the author. In reality, different scenarios might be possible. In laboratories, concretes are usually mixed with aggregates whose properties are known precisely. In contrast, the volume fraction and the Young’s modulus of the aggregates might exhibit larger uncertainties at construction sites. Thus, a study about the influences of the chosen uncertainties apportioned to the elastic parameters and the volume fractions of the aggregates is of interest.

To this end, the total order sensitivity indices are re-computed at the concrete scale using the multiscale model combined with the Powers model. Due to the similarities observed between Figures 3.8 and 3.9, the results can also be transferred to the multiscale model in combination with the Bernard model. The study is carried out as follows: One parameter at a time concerning the uncertainties of the aggregate inclusions is changed, whereas the other parameters remain fixed and take the values prescribed before (see Appendix A.3).

The variations of all uncertainties related to the aggregates are summarized in Table 3.2. First, the stochastic parameters of the probability distribution assigned to the volume fraction are varied. On the one hand, a uniform PDF with the bounds of  $\text{unif}(3,7)$  is assigned so that a large scatter of the volume fraction is assumed. On the other hand, a PDF with more narrow bounds of  $\text{unif}(4.5,5.5)$  is chosen. Previously, the bounds were  $\text{unif}(4,6)$ . Also, the stochastic properties of the elastic parameters  $k_{\text{agg}}$  and  $\mu_{\text{agg}}$  are varied. Log-normal probability distributions with standard deviations of 5 and 20 GPa are attributed to the elastic properties of the aggregates to model low and high uncertainties, respectively. In the previous section, the standard deviation was set to equal to 10 GPa.



**Table 3.2:** Variations of the stochastic parameters assigned to the volume fraction and the elastic parameters of the aggregates (SD - standard deviation, PDF - probability density function, unif( $\cdot$ ) - uniformly distributed).

Parameter to be varied	Mean	SD	PDF
Volume fractions (low uncertainty)	5	–	unif(4.5, 5.5)
Volume fractions (high uncertainty)	5	–	unif(3, 7)
Elastic parameters (low uncertainty)	$k_{\text{agg}} = 37.8$	5	logn
	$\mu_{\text{agg}} = 44.3$	5	logn
Elastic parameters (high uncertainty)	$k_{\text{agg}} = 37.8$	20	logn
	$\mu_{\text{agg}} = 44.3$	20	logn

Figures 3.10 and 3.11 show the influences of the chosen uncertainties related to the aggregates on the total order sensitivity indices at the concrete scale, obtained with a multiscale model in combination with the Powers model.

The large influence of the aggregate uncertainties can be observed. The higher the uncertainty of the volume fraction or the elastic properties, the larger are the total order sensitivity indices and the more sensitive is the model to changes of that parameter. This can be particularly well observed for the aggregate volume fractions. In Figures 3.10 (a) and (b),  $f_{\text{agg}}$  is of minor importance for the model response uncertainty because the volume fraction is afflicted with a low uncertainty. On the contrary, the volume fractions are governing for the model response when they are considered with a wider probability distribution, see Figures 3.10 (c) and (d). For the elastic properties of the aggregates, the same trends are observed. The elastic properties entail large total order sensitivity indices when they exhibit high uncertainties, and vice versa.

Hence, in dependence on where the concrete is prepared, either in the laboratory or at construction site, appropriate probabilistic parameters should be considered in probabilistic computations.

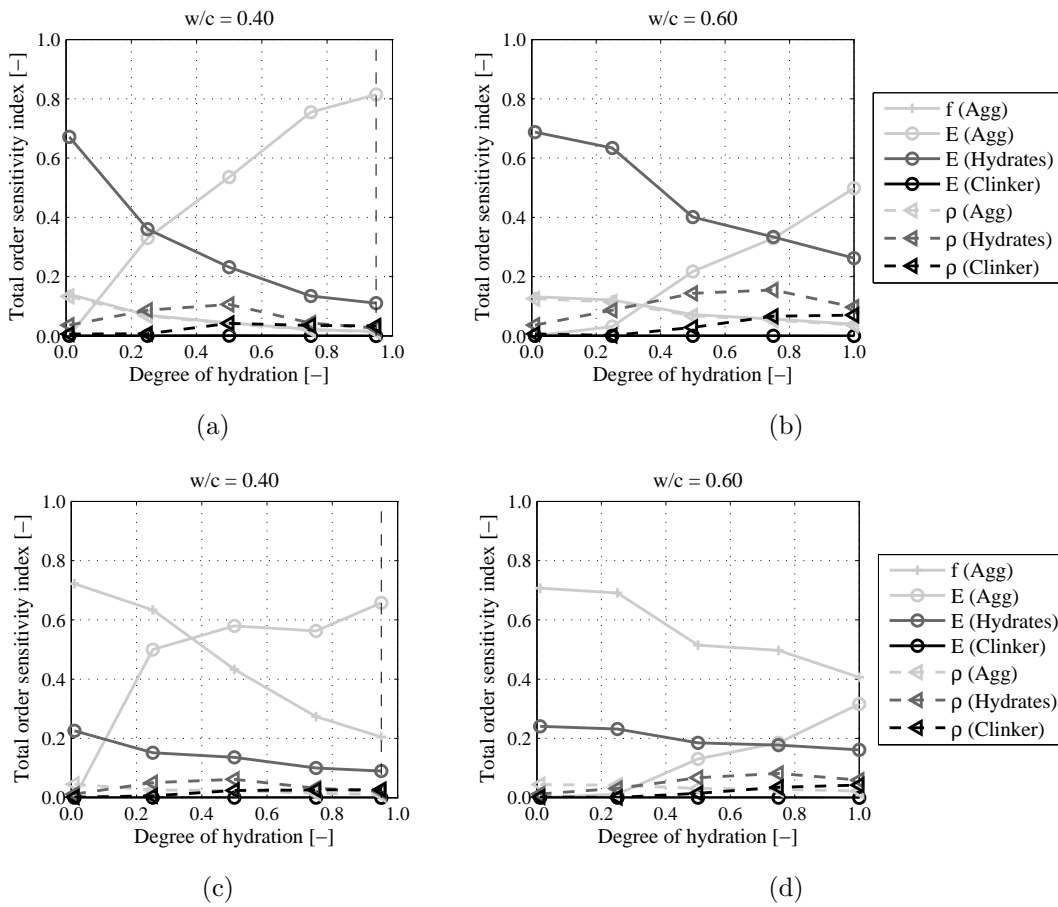


**Figure 3.10:** Total order sensitivity indices at the concrete scale resulting from varying uncertainties exhibited by the volume fraction of the aggregates for two different  $w/c$ -ratios: (a) and (b) show the total order sensitivities with a low uncertainty of the volume fraction, (c) and (d) with high uncertainties in the volume fraction, see Table 3.2 for details.

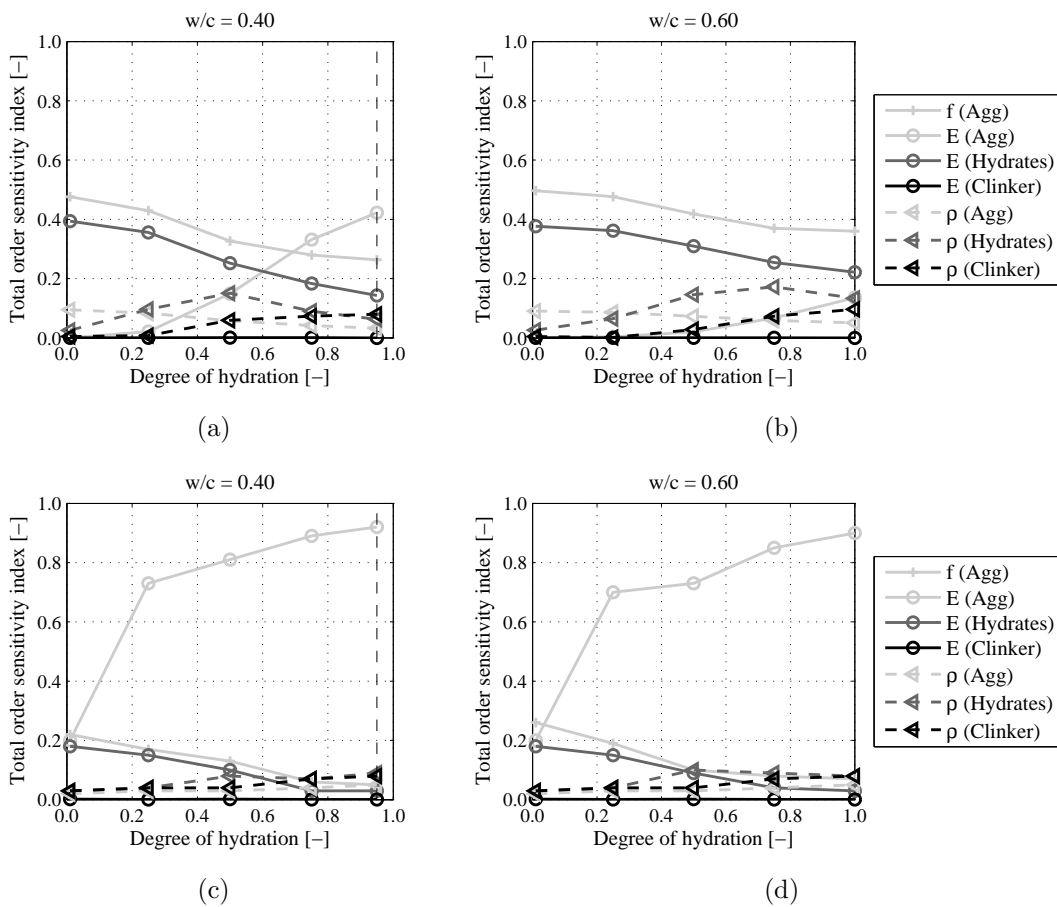


**Figure 3.11:** Total order sensitivity indices at the concrete scale resulting from varying uncertainties exhibited by the elastic properties of the aggregates for two different  $w/c$ -ratios: (a) and (b) show the total order sensitivities with a low uncertainty of the elastic parameters, (c) and (d) with high uncertainties of the elastic parameters, see Table 3.2 for details.

### 3.3.5 Results of the uncertainty analysis

#### 3.3.5.1 Parameter uncertainty

The effects of the input parameter uncertainties on the variability of the multiscale model response are investigated according to Eq. (3.4), see Figure 3.12. As expected, the parameter uncertainty is magnified during the upscaling process. The cement paste scale exhibits the lowest uncertainties and the concrete scale the largest. With ongoing hydration process, the parameter uncertainty increases significantly at the scales of mortar and concrete. This is related to the increasing sensitivity of the model response with respect to the elastic parameters of sand and the aggregates, which exhibit large variations. The parameter uncertainties of the predicted Young's moduli across the scales are larger

in case of a  $w/c$ -ratio of 0.4 than for a  $w/c$ -ratio of 0.6. There are also differences between the Powers model and the Bernard model. Up to hydration stages of about 0.6, the Powers model exhibits larger uncertainties. This is related to the faster stiffening at lower hydration degrees of the cement pastes, mortars, and concretes predicted using the Powers model, as discussed before. At later degrees of hydration, the model responses using the Bernard model exhibit larger uncertainties than for the Powers model.

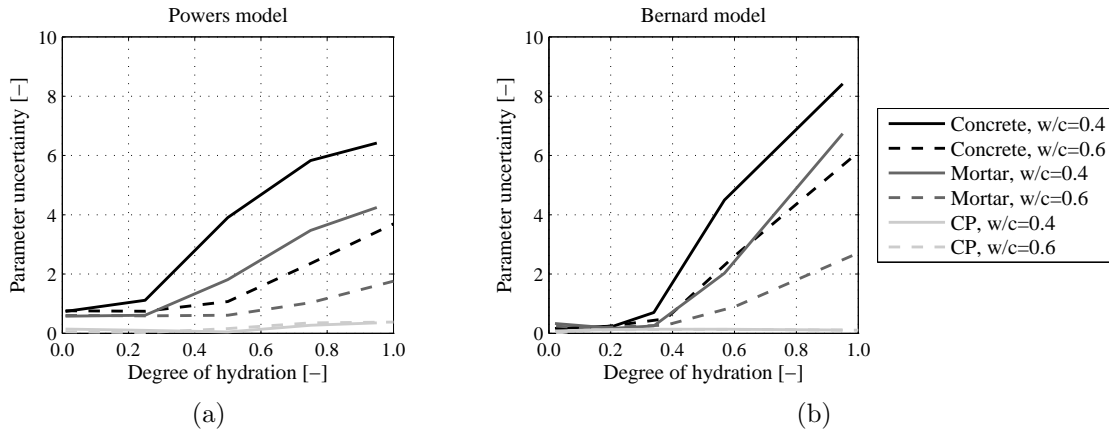


**Figure 3.12:** Evolution of the parameter uncertainty for the Powers model (a) and for the Bernard model (b) as functions of the degree of hydration for two different  $w/c$ -ratios.

### 3.3.5.2 Total uncertainty

With the evaluation methodology presented in Section 3.1, the two hydration models can be directly compared concerning the uncertainties of their model responses taking the parameter and the model uncertainty into account. To determine the latter, the average of the two model responses is taken as the reference response. The uncertainty of the reference model  $V(\varepsilon^{M_{\text{ref}}})$  is assumed to take a range of values whose influences on the total uncertainties are investigated, see Figure 3.13. The values of  $V(\varepsilon^{M_{\text{ref}}})$  affect the total uncertainties quantitatively but not the ranking of the models.

The previous findings, revealed from the sensitivity analysis and the parameter uncertainty, are confirmed by the study of the total uncertainty. An uncertainty magnification across the scales is observed, illustrating a larger uncertainty of the Young's modulus of concrete than of cement paste. Furthermore, the uncertainty increases during the hydration process due to the formation of hydration products and the densification of the microstructure. The model responses for the water-to-cement ratio of 0.40 are afflicted with larger uncertainties than for  $w/c$ -ratios of 0.60. As it has already been observed in Figure 3.12, the uncertainty of the multiscale model using the Powers model is larger for hydration degrees up to 0.6, which is also reflected in the total uncertainty. For higher degrees of hydration, the

uncertainty related to the Bernard model is larger than that of the Powers model is, particularly so at the concrete scale.

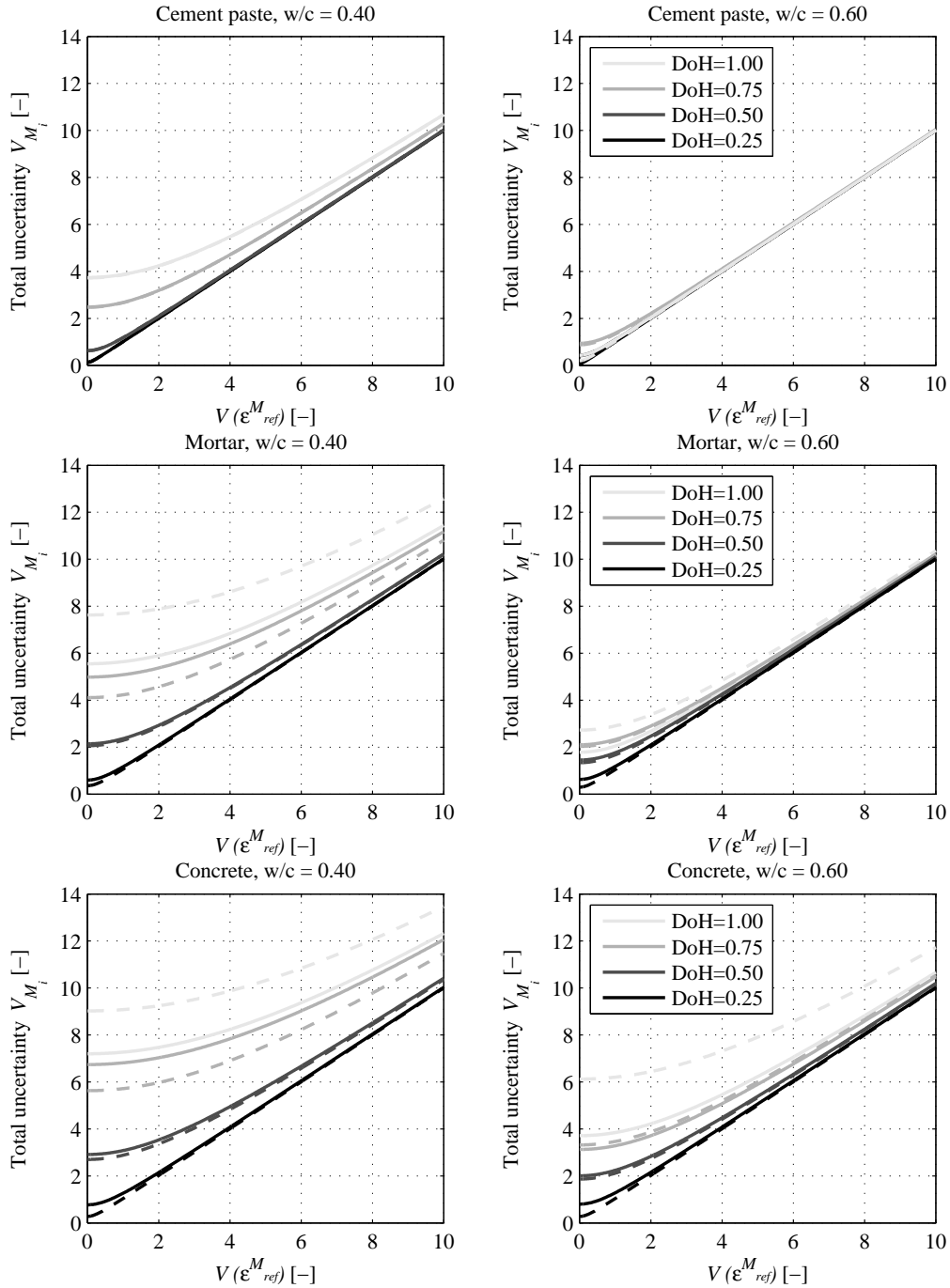


**Figure 3.13:** Total uncertainties for the Powers model (—) and the Bernard model (--) at given degrees of hydration: Cement paste (upper row), mortar (middle row), and concrete (lower row) at two different water-to-cement ratios.



## 4 | Experimental multiscale study of polymer-modified cement-based materials

For the development of multiscale models, experimental investigations aimed at the determination of input parameters, on the one hand, and the validation of modeling results, on the other hand, are prerequisite. The objective of the experimental study presented herein is the characterization of the mechanical behavior of polymer-modified cement-based materials across the scales. Special emphasis is placed on the influences of polymer modifications on the microstructure formation and the elastic properties of cement-based materials. The experiments were performed with polymer-modified cement pastes, mortars, and concretes in fresh and hardened states. Also, the polymers used for the modification were investigated separately. Table 4.1 shows an overview of the experimental investigations performed in this thesis. In the table, also information regarding the mixture design are given, in which  $w/c$  denotes the initial water-to-cement mass ratio,  $p/c$  the initial polymer-to-cement mass ratio,  $s/c$  the initial sand-to-cement mass ratio, and  $a/c$  the initial aggregate-to-cement mass ratio. The experiments are described in more detail in the sequel.

The experiments were mainly conducted at the F.A. Finger-Institute of Building Material Engineering in Weimar. Clémence Bos and Dr. Ruth Schwaiger performed and partially evaluated the investigations related to the micromechanical properties of the polymers and cement pastes, namely the nanoindentation tests, at the Karlsruhe Institute of Technology, Institute for Applied Materials.

The early-age short-term creep tests, see Section 5, were performed at the Vienna University of Technology, Institute for Mechanics of Materials and Structures, supported by the technical staff.

**Table 4.1:** Overview of the experimental multiscale study.

<b>Polymers</b>	Macroscopic solid polymer specimens; three polymers	
	<b>Mechanical behavior</b> <ul style="list-style-type: none"> <li>• Micromechanical properties</li> </ul>	
<b>Cement paste</b>	Portland cement; three polymers; $p/c = 0, 0.05, 0.10, 0.20$ ; $w/c = 0.40$	
	<b>Hydration kinetics</b> <ul style="list-style-type: none"> <li>• Hydration heat release and hydration heat rate</li> <li>• Degree of hydration</li> </ul> <b>Microstructure</b>	<b>Fresh cement paste</b> <ul style="list-style-type: none"> <li>• Consistency</li> </ul> <b>Hardened cement paste</b> <ul style="list-style-type: none"> <li>• Bulk and particle density, porosity</li> <li>• Compressive strength</li> <li>• Dynamic modulus</li> <li>• Length changes</li> <li>• Micromechanical properties</li> <li>• Early-age elastic and creep behavior (Section 5)</li> </ul>
<b>Mortar</b>	Portland cement; sand; three polymers; $p/c = 0, 0.05, 0.20$ ; $w/c = 0.40$ ; $s/c = 3.0$	
	<b>Fresh mortar</b> <ul style="list-style-type: none"> <li>• Consistency</li> <li>• Air void content</li> <li>• Fresh mortar density</li> </ul>	<b>Hardened mortar</b> <ul style="list-style-type: none"> <li>• Compressive strength</li> <li>• Static modulus</li> <li>• Dynamic modulus</li> </ul>
<b>Concrete</b>	Portland cement; aggregates; three polymers; $p/c = 0, 0.05, 0.10, 0.20$ ; $w/c = 0.40$ ; $a/c = 5.3, 5.6, 5.8$	
	<b>Fresh concrete</b> <ul style="list-style-type: none"> <li>• Consistency</li> <li>• Air void content</li> <li>• Fresh concrete density</li> <li>• Fresh concrete temperature</li> </ul>	<b>Hardened concrete</b> <ul style="list-style-type: none"> <li>• Compressive strength</li> <li>• Static modulus</li> <li>• Dynamic modulus</li> <li>• Early-age elastic and creep behavior (Section 5)</li> </ul>



## 4.1 Materials

### 4.1.1 Cement

The experimental program was conducted in laboratories at three different locations. Due to logistics reasons, three different Portland cements were used. However, all cements exhibit a clinker amount of at least 95 % so that the amount of minor components and additives, which influence the cement hydration process, is low. All specimens devoted to the macroscopic mechanical tests were produced with Portland cement (CEM I 42.5 R) from Dyckerhoff (Germany). For the nanoindentation tests, a Portland cement (CEM I 52.5 R) from HeidelbergCement (Germany) was used. The early-age creep tests were performed with Portland cement (CEM I 42.5 N) from Lafarge (Austria). The chemical and mineralogical compositions of the cements are given in Table 4.2 and Table 4.3, respectively. The used cements mainly differ regarding their specific surface, which influences their mechanical properties at early ages. However, the different specimens of one experiment were produced with the same cement so that comparability is ensured.

**Table 4.2:** Mass percentage of the chemical components of the used Portland cements [%].

Cement	CaO	SiO <sub>2</sub>	Al <sub>2</sub> O <sub>3</sub>	Fe <sub>2</sub> O <sub>3</sub>	SO <sub>3</sub>	MgO	K <sub>2</sub> O	Na <sub>2</sub> O	LOI
CEM I 42.5 R	63.2	20.3	4.8	2.4	3.3	1.4	1.3	0.2	2.7
CEM I 52.5 R	65.8	23.2	4.2	1.2	2.8	0.9	0.6	0.4	1.0
CEM I 42.5 N	64.1	20.3	3.2	4.6	2.3	1.2	0.6	0.2	3.3

**Table 4.3:** Mass percentage of the mineralogical compositions according to Bogue and specific surfaces (Blaine) of the used Portland cements.

Cement	C <sub>3</sub> S [%]	C <sub>2</sub> S [%]	C <sub>3</sub> A [%]	C <sub>4</sub> AF [%]	Specific surface [cm <sup>2</sup> g <sup>-1</sup> ]
CEM I 42.5 R	52.6	18.5	8.7	7.3	4,600
CEM I 52.5 R	53.2	26.4	9.1	3.7	5,900
CEM I 42.5 N	51.4	21.2	7.9	7.1	3,900

### 4.1.2 Polymers

Three different polymers were used: a styrene/acrylate copolymer in form of both a redispersible powder (P1) and a dispersion (P2) as well as a dispersion on the basis of a styrene/butadiene copolymer (P3), see Table 4.4. Polymer P1, produced by Wacker Chemie

AG (Germany), contains a fine mineral filler as an antiblocking agent and polyvinyl alcohol as a protective colloid. The dispersions P2, produced by Ha-Be Betonchemie (Germany), and P3, produced by BASF (Germany), are stabilized with ionic and anionic surfactants, respectively, and anti-foaming agents. All three polymers are commercially available and explicitly appropriate for the application in cement-based materials.

The comparison of the minimum film forming temperatures shows that the polymers P1 and P3 are able to form films in hardening cement pastes under given processing and storage conditions (20 °C and 65 % RH). On the contrary, the MFT of P2 is higher than the curing temperature, such that film formation is not expected. Still, the polymer particles exhibit adhesive bonds to the cementitious matrix [65]. Furthermore, it is worth mentioning that film formation has also been observed for polymers with an MFT slightly higher than the curing temperature [56], see Section 2.1.1. Two polymer-to-cement mass ratios ( $p/c$ ) were chosen, amounting to 0.05 and 0.20, because these values represent the minimum and maximum polymer quantities to be added, as proposed by the manufacturers. Notably, the  $p/c$ -ratio refers to the solid polymer content. In the following, the specimens are denominated according to the nomenclature ‘*polymer type – p/c-ratio*’.

**Table 4.4:** Characteristics of the polymers, given by the manufacturers.

Attribute	P1	P2	P3
Delivery form	powder	dispersion	dipersion
Main constituents	styrene, acrylic acid ester	styrene, acrylic acid ester	styrene, butadiene, acrylonitrile
Solid particle content [%]	99 ± 1	50 ± 1	51 ± 1
pH value	approx. 8	7 – 9	8 – 10
MFT [°C]	5	30	16
Density [g cm <sup>-3</sup> ]	approx. 1.04	approx. 1.03	approx. 1.04
Particle size [µm]	max. 400 (powder), 0.5-10 (dispersion)	0.20 (mean)	0.19 (mean)

To explicitly evaluate the effects of polymers on the properties of fresh and hardened cement-based materials, no further admixtures and additives were added to the mixtures. For concretes and mortars modified with the redispersible powder P1, the anti-foaming agent “Foammaster PD 1” was used to reduce the air void content of the mixtures.

### 4.1.3 Sand and aggregates

In this work, mortars and concretes are distinguished according to the maximum particle size of the aggregates. Mortars contain aggregates with particles sizes smaller than 2 mm. The concretes also contain larger aggregates. For the mortars, sand, according to DIN EN 196-1 [288], with a maximum particle size of 2 mm was used. For the concretes, unfractured quartz gravel with a maximum particle size of 16 mm with the three fractions 0/2, 2/8, and 8/16 was utilized.

### 4.1.4 Mixture design

The experimental study is based on the mixture designs described in the following section. For all mixtures, the  $w/c$ -ratio was kept constant at 0.40 to ensure comparability. The  $w/c$ -ratio considers both the amount of deionized water and the liquid phase (water) of the aqueous polymer dispersions.

**Cement pastes:** The cement pastes were mixed with cement, deionized (DI) water, and where required polymer powder or polymer latex respectively.

**Mortars:** The mix design of the mortars was partially based on DIN EN 196-1 [288], see Table 4.5. A constant sand-to-cement mass ratio ( $s/c$ ) of 3.0 was defined so that 450 g cement and 1350 g sand were used in every mixture.

**Table 4.5:** Mix design of polymer-modified mortars.

Sample	$w/c$	$s/c$	$p/c$	Water [g]	Polymer [g]	PD 1 [g]
Reference	0.40	3.0	0.00	180.0	0.0	0.0
P1-0.05	0.40	3.0	0.05	180.0	22.5	0.5
P1-0.20	0.40	3.0	0.20	180.0	90.0	2.0
P2-0.05	0.40	3.0	0.05	157.5	45.0	0.0
P2-0.20	0.40	3.0	0.20	90.0	180.0	0.0
P3-0.05	0.40	3.0	0.05	157.5	45.0	0.0
P3-0.20	0.40	3.0	0.20	90.0	180.0	0.0

**Concretes:** For the concretes, the aggregate-to-cement mass ratio ( $a/c$ ) varied between 5.3 and 5.8, depending on the  $p/c$ -ratio, see Table 4.6. The solid contents of the polymer modifications were considered in the volume calculation of the mix designs. The cement

content was chosen to be  $340 \text{ kg m}^{-3}$  for all mixtures. Concerning the aggregates, a grading curve between A and B was sought.

**Table 4.6:** Mix design of polymer-modified concretes.

Sample	$w/c$	$p/c$	$a/c$	Water	Polymer	Aggregates		
						0/2	2/8	8/16
				[ $\text{kg m}^{-3}$ ]	[ $\text{kg m}^{-3}$ ]	[ $\text{kg m}^{-3}$ ]	[ $\text{kg m}^{-3}$ ]	[ $\text{kg m}^{-3}$ ]
Reference	0.40	0.0	5.8	136	0	725	686	549
P1-0.05	0.40	0.05	5.6	136	17	709	671	536
P1-0.20	0.40	0.20	5.3	136	68	661	625	500
P2-0.05	0.40	0.05	5.6	119	34	719	672	537
P2-0.20	0.40	0.20	5.3	68	136	664	628	503
P3-0.05	0.40	0.05	5.6	119	34	719	672	537
P3-0.20	0.40	0.20	5.3	68	136	664	628	503

## 4.2 Experimental investigations with polymers

Both cementitious and polymer components govern the mechanical properties of polymer-modified cement-based materials. For instance, the age-dependent creep behavior does not only result from the creep activity of the cementitious hydration products but also from the viscoelastic behavior of the polymers [289]. In addition, the elastic behavior of cement-based materials is modified by adding polymers. The micromechanical properties of the polymers are of particular interest because they represent essential input parameters for the continuum micromechanics-based multiscale model presented in Section 5.3.

### 4.2.1 Sample preparation

The micromechanical properties of the polymers were determined on solid polymer films prepared of the polymer dispersions and the polymer powder, which was re-dispersed previously. The polymer dispersions were poured into  $1 \text{ cm} \times 1 \text{ cm} \times 0.1 \text{ cm}$  silicone molds (ADDV-42, R&G Faserverbundwerkstoffe GmbH, Germany), reproducing a glass surface on one face so that a low surface roughness of the specimens was ensured. The molds were stored for three days at ambient temperature of  $20^\circ\text{C}$  to enable water evaporation. For the polymers P1 and P3, polymer films were obtained. The storage temperature was lower than the MFT of polymer P2 was. Though, a compact polymer specimen was formed. Before the nanoindentation testing, the specimens were glued onto aluminum sample holders using a two-component adhesive on the basis of epoxy resins.

## 4.2.2 Nanoindentation testing

For polymers, dynamic nanoindentation testing is appropriate because of the time-dependent nature of polymers; the polymers do not solely exhibit linear elasticity. The viscoelastic properties of the polymers are described by the complex modulus  $E^*$ , which is defined as

$$E^* = E' + iE'' \quad (4.1)$$

with

$E'$	storage modulus [GPa]
$E''$	loss modulus [GPa]
$i$	complex number.

The storage modulus  $E'$  represents the capacity to store energy.  $E''$  is a measure for the energy amount dissipated in the material. It describes internal damping.

During dynamic nanoindentation testing, an oscillating, sinusoidal force is superimposed on the quasi-static loading, which allows the direct measurement of the contact stiffness as a continuous function of the indentation depth [174]. The nanoindentation testing was performed at ambient temperature of 20 °C using a Nanoindenter G200 (Keysight Technologies, Inc., CA, USA) equipped with the continuous stiffness measurement (CSM) option and a conical flat punch with a tip diameter of 100  $\mu\text{m}$  and an angle of 60°. A flat-ended indenter tip was chosen because it causes deformation that is consistent with the assumption of linear viscoelasticity [290], according to which the material structure is intact. Furthermore, the contact area is known and, in case of a conical shape, almost independent of the penetration depth.

The samples were loaded at a constant displacement rate of 30  $\text{nm s}^{-1}$  to a displacement of 2  $\mu\text{m}$ . A low magnitude oscillating force with a frequency of 45 Hz and an amplitude of 20 nm was superimposed on the quasi-static force. Then, the load was adjusted to maintain the initial displacement within a predefined range of  $\pm 10$  nm allowing the sample to exhaust intrinsic relaxation mechanisms, see Table 4.7. After stabilization, the actual measurement started at harmonic amplitude of 20 nm and frequency of 45 Hz. The average indentation depth was 3.1  $\mu\text{m}$ . The frequency of 45 Hz was chosen to ensure comparability with Berkovich tests (see Section 4.3.4.5). Between 10 and 14 tests were performed on each polymer specimen. The results for each specimen were averaged.

**Table 4.7:** Nanoindentation parameters for the viscoelastic analysis of polymer specimens.

Polymer	Number of tests	Depth during pre-loading [ $\mu\text{m}$ ]
P1	12	2
P2	14	3
P3	10	3

## 4.3 Experimental investigations with cement pastes

The hydration kinetics of the cement reaction and the formation of the microstructure in polymer-modified cement pastes were investigated first. Then, characteristic properties of fresh and hardened cement pastes were determined.

### 4.3.1 Hydration kinetics

To determine the influences of the polymers on the hydration reaction of the cement, the hydration kinetics of polymer-modified cement pastes were investigated and compared with a conventional cement paste using isothermal calorimetry (TA Instruments DSC Q200, USA). The **heat rate** and the cumulative **heat release** were recorded for 80 hours at a temperature of 20 °C. For each measurement, a test tube was filled with 10 g of cement. The cement was thoroughly mixed with the respective amount of water and, if required, with the polymer dispersions or the polymer powder.

Additionally, the **degree of hydration** was determined via the non-evaporable (chemically bounded) water content  $m_{w,\text{chem}}$  according to the procedure that Copeland and Hayes [291] described. The quantity  $m_{w,\text{chem}}$  is defined as the mass loss per gram cement paste in the temperature range between 105 °C and 1000 °C. At each predefined time step (1, 2, 7, 28, and 56 days after the production), the specimens were ground using a porcelain mortar. Isopropyl alcohol was added to stop the hydration reaction. The specimens were dried at 40 °C and ground to powders with particle sizes smaller than 63  $\mu\text{m}$  afterward. Then, the powders were dried in an oven at 105 °C for at least 24 hours until a constant mass was reached. Subsequently, the samples were stored in a furnace at a temperature of 1000 °C to determine the loss on ignition. In polymer-modified cement pastes, the weight loss on ignition results from the volatilization of the non-evaporable water and constituents of the

polymers. Accordingly, the degree of hydration  $\xi$  is computed as [76]

$$\xi = \frac{m_{w,\text{chem}}}{m_{w,\text{max}}} \cdot 100 = \frac{m_i - m_o - \frac{LOI_{\text{pol}} \cdot p/c \cdot m_o}{1 + p/c - p/c \cdot LOI_{\text{pol}}}}{m_{w,\text{max}}} \cdot 100 \quad (4.2)$$

with  $m_{w,\text{max}}$  maximum water content that can be bound at age  $t \rightarrow \infty$  [g];  
 depends on the cement composition  
 $m_i$  initial weight of the sample [g]  
 $m_o$  output weight of the ignited sample [g]  
 $LOI_{\text{pol}}$  loss on ignition of the polymer [-]  
 $p/c$  polymer-to-cement ratio.

The polymer dispersions P2 and P3 exhibit a loss on ignition of 99.5% and of 99.0% respectively. The LOI of P1 amounts to 86.0%. The remaining mass after the ignition of the powder P1 refers to heat-resisting anti-caking agents (e.g. clay), which are commonly added during the manufacturing process (spray drying).

### 4.3.2 Microstructure

Information about the microstructure are fundamental for the successful development of multiscale prediction models. For polymer-modified cement-based materials, it is of particular importance to collect knowledge about the incorporation of the polymers inside the matrix.

The environmental scanning electron microscopy (ESEM) was applied to observe the effects of the polymers on the microstructural formation of the cement pastes. The plain reference sample as well as the cement pastes with a  $p/c$ -ratio of 0.20 were investigated at material ages of 21 hours, which refers to the onset of loading of the early-age creep tests, see Section 5.1. A XL30 ESEM (Philipps, USA) with FEG source was used. The fracture areas, obtained by manually breaking small samples of the dimensions 1 cm  $\times$  1 cm  $\times$  2 cm into pieces, were investigated. The pea-sized specimens were locked in the specimen chamber. By means of the ESEM technique, a coating of the specimens with conductible films is not required. The physically and chemically bounded water remains in the structure, which enables the visualization of the original microstructure. However, influences on the specimens due to preparation processes cannot be excluded.

### 4.3.3 Fresh cement paste properties

The **consistencies** of the fresh cement pastes were determined with the slump test according to DIN EN 1015-3:2007-05 [292]. For two mixtures (P2-0.20 and P3-0.20), whose consistencies were too fluid for the slump test, the slump flow was determined instead [293].

### 4.3.4 Hardened cement paste properties

#### 4.3.4.1 Density and total porosity

The **bulk density** of the hardened cement pastes was directly determined from the prisms via the determination of the dimensions and the corresponding weights. For the determination of the **particle density**, the cement pastes were ground to powders with particles sizes smaller than 63  $\mu\text{m}$ . The measurement of the particle density was conducted using the helium pycnometer AccuPyc 1330 (Micromeritics, USA). The quantities were determined at 2, 7, and 28 days after the production of the pastes. Besides the degree of hydration, the porosity of the specimens governs mechanical properties, such as the compressive strength. With the bulk and the particle density, the **total porosity** can be calculated as follows:

$$P = \left(1 - \frac{\rho_{\text{bulk}}}{\rho}\right) \cdot 100 \quad (4.3)$$

with

$P$	total porosity [%]
$\rho_{\text{bulk}}$	bulk density [ $\text{g cm}^{-3}$ ]
$\rho$	particle density [ $\text{g cm}^{-3}$ ].

#### 4.3.4.2 Compressive strength

For the determination of the **compressive strength**, prism specimens of the dimensions 4 cm  $\times$  4 cm  $\times$  16 cm were produced. The specimens were first cured for 24 hours at 20°C and 95% RH and then stripped from the formwork. Until the testing (2, 7, and 28 days after the production), the specimens were stored immersed under water. The determination of the compressive strength followed DIN EN 1015-11 [294].

#### 4.3.4.3 Dynamic modulus

Ultrasonic measurements provide information about the stiffness of cement pastes. The **dynamic modulus** was determined using a vibration severity meter (digital vibrometer OFV-505, Polytec GmbH, Germany) with an ultrasound measurement frequency amounting to 500 kHz. For that, cement paste prisms of the dimensions 1 cm  $\times$  1 cm  $\times$  6 cm were tested. The resonance frequency of an expansion wave  $f_D$  was measured. The dynamic



modulus  $E_{\text{dyn}}$  is computed as [295]

$$E_{\text{dyn}} = 4 \cdot l^2 \cdot f_{\text{D}}^2 \cdot \rho_{\text{bulk}} \quad (4.4)$$

with

$E_{\text{dyn}}$	dynamic modulus [N mm <sup>-2</sup> ]
$l$	length of the specimen [mm]
$f_{\text{D}}$	resonance frequency of the expansion wave [kHz]
$\rho_{\text{bulk}}$	bulk density of the specimen [kg m <sup>-3</sup> ].

#### 4.3.4.4 Length changes

The load-independent **length changes** that the cement pastes exhibit were determined according to DIN EN 12617-4 [296]. Prism specimens of the dimensions 4 cm × 4 cm × 16 cm equipped with measuring pegs were produced. The specimens were demolded at 24 hours after the production and stored at 20 °C and 65 % RH. The samples were tested at ages of 2, 7, 14, 21, and 28 days. The length changes in terms of strains read as

$$\text{Strains} = \frac{\Delta L \times 1000}{L_{\text{g}}} \quad [\text{mm/m}] \quad (4.5)$$

with

$\Delta L$	length changes related to the initial measurement at 24 hours [mm]
$L_{\text{g}}$	measurement length, amounts to 160 mm herein.

#### 4.3.4.5 Micromechanical properties

Several studies have already focused on the macroscopic properties and the durability of polymer-modified cement-based materials (see Section 2.1). In contrast, less is known about the fundamental mechanisms underlying the microstructure and their influences on the macroscopic behavior. The knowledge of micromechanical properties is not only essential for the improvement of the material performance at the macroscopic scale but it is also required for the development of prediction models that incorporate microstructural information. Thus, the **micromechanical properties** of polymer-modified cement pastes were quantified by means of nanoindentation tests. First, the micromechanical elastic properties were determined. Then, nanoindentation creep tests were performed.

**Sample preparation** The cement pastes were prepared by first mixing the water with the polymer dispersions (P2 and P3) and by adding the Portland cement to the liquids. The polymer powder P1 was first mixed with the cement and then added to the water. The specimens were cast in silicone molds of the dimensions 1 cm × 1 cm × 0.1 cm. After demolding, the surface preparation included grinding with water lubrication up to P4000

grit size and three polishing steps with alcohol-based diamond paste up to a particle size of 0.25  $\mu\text{m}$ , with the goal being to achieve a flat surface. After each polishing step, the specimens were cleaned with isopropyl alcohol and put into an ultrasonic bath (deionized water) to remove dust. It is worth mentioning that surface Portlandite crystals could have been removed during the preparation steps. However, all specimens were prepared in the same way so that the influence is similar for all cement pastes. The nanoindentation tests were carried out at room temperature and ambient air, i.e. 25 °C and 50 % RH.

The surfaces of the specimens were observed using a scanning electron microscope (TM3000, HITACHI, Bruker, USA). The surface images (see Figure 4.1) illustrate an increased porosity of the cement pastes modified with polymers. The higher the  $p/c$ -ratio, the larger the inhomogeneity of the surface is. Particularly, on the specimens P1-0.20 and P3-0.20 pores of diameters up to 25  $\mu\text{m}$  are found. The high porosity is the result of entrapped air generated during the mixing process, as well as chemical reactions between the cement constituents and the additives of the polymers, particularly of surfactants, see Section 2.1.1.

**Nanoindentation testing - Micromechanical elastic properties** The cement pastes were investigated using a Nanoindenter G200 (Keysight Technologies, Inc., CA, USA). A Berkovich tip was used, for which the nanoindenter frame stiffness and the tip area function were calibrated testing on fused quartz with known mechanical properties. The nanoindentation tests were carried out 28 days after the production of the specimens. Two different types of nanoindentation tests were performed: standard continuous stiffness measurements (CSM) [147, 297] and high speed grid indentation (Express Test, ET) tests [298]. The ET indents were repeated at a material age of 56 days to observe hydration-induced changes of the phase volume fractions.

The CSM tests were conducted with a small oscillation having an amplitude of 20 nm and a frequency of 45 Hz superimposed on the loading. The samples were indented at a constant indentation strain rate of 0.05  $\text{s}^{-1}$  up to a depth of 1000 nm using a Berkovich tip. With the CSM measurement, micromechanical properties are determined as a function of the indentation depth [297]. The measurement of the contact stiffness can be carried out at any point of the loading curve [147]. In this work, the indentation moduli were evaluated at indentation depths of 200 and 900 nm. At least 17 tests were performed on each sample, lasting ten minutes each.

In contrast, up to 5000 indents can be performed within one hour using the ET method, a novel statistical high-speed indentation approach [298]. Herein, 2000–4000 indents were conducted on each specimen to account for the heterogeneity of the surfaces. The indentation depth was 1000 nm, varying for every cement paste within 100 nm. The array

size was  $2\text{ mm} \times 1\text{ mm}$ . The distance between the individual indents was  $20\text{ }\mu\text{m}$ . Not all of the performed indents could be evaluated because in some cases the machine did not record data or it was not able to maintain the preset parameters, most likely because of the high surface roughness of the specimens. By way of example, paste P3-0.20 exhibited a rather high porosity, which reduced the number of successful indents to 475 and 812 for material ages of 28 days and 56 days, respectively.

The elastic properties of the samples were evaluated based on the relation

$$E_{\text{eff}} = \frac{1}{\beta_g} \frac{\sqrt{\pi}}{2} \frac{S}{\sqrt{A_c}}, \quad (4.6)$$

with

$E_{\text{eff}}$	effective modulus, which accounts for the deformation of both the indenter tip and the sample [299]
$\beta_g$	geometrical constant
$S$	contact stiffness
$A_c$	contact area.

The effective modulus is defined as

$$\frac{1}{E_{\text{eff}}} = \frac{(1 - \nu_{\text{tip}}^2)}{E_{\text{tip}}} + \frac{(1 - \nu_{\text{sample}}^2)}{E_{\text{sample}}}. \quad (4.7)$$

$E_{\text{tip}}$ ,  $\nu_{\text{tip}}$ ,  $E_{\text{sample}}$ , and  $\nu_{\text{sample}}$  are the Young's modulus and Poisson's ratio of the tip and the sample, respectively.  $E_{\text{tip}}$  is assumed as 1141 GPa and  $\nu_{\text{tip}}$  as 0.07.

Since the Poisson's ratio is not always known, the indentation modulus  $M$  was determined as

$$M = \left( \frac{1}{E_{\text{eff}}} - \frac{(1 - \nu_{\text{tip}}^2)}{E_{\text{tip}}} \right)^{-1}. \quad (4.8)$$

The sample modulus  $E_{\text{sample}} = M \cdot (1 - \nu_{\text{sample}}^2)$  can then be estimated assuming an appropriate value for the Poisson's ratio. The latter was assumed as 0.3 in this study.

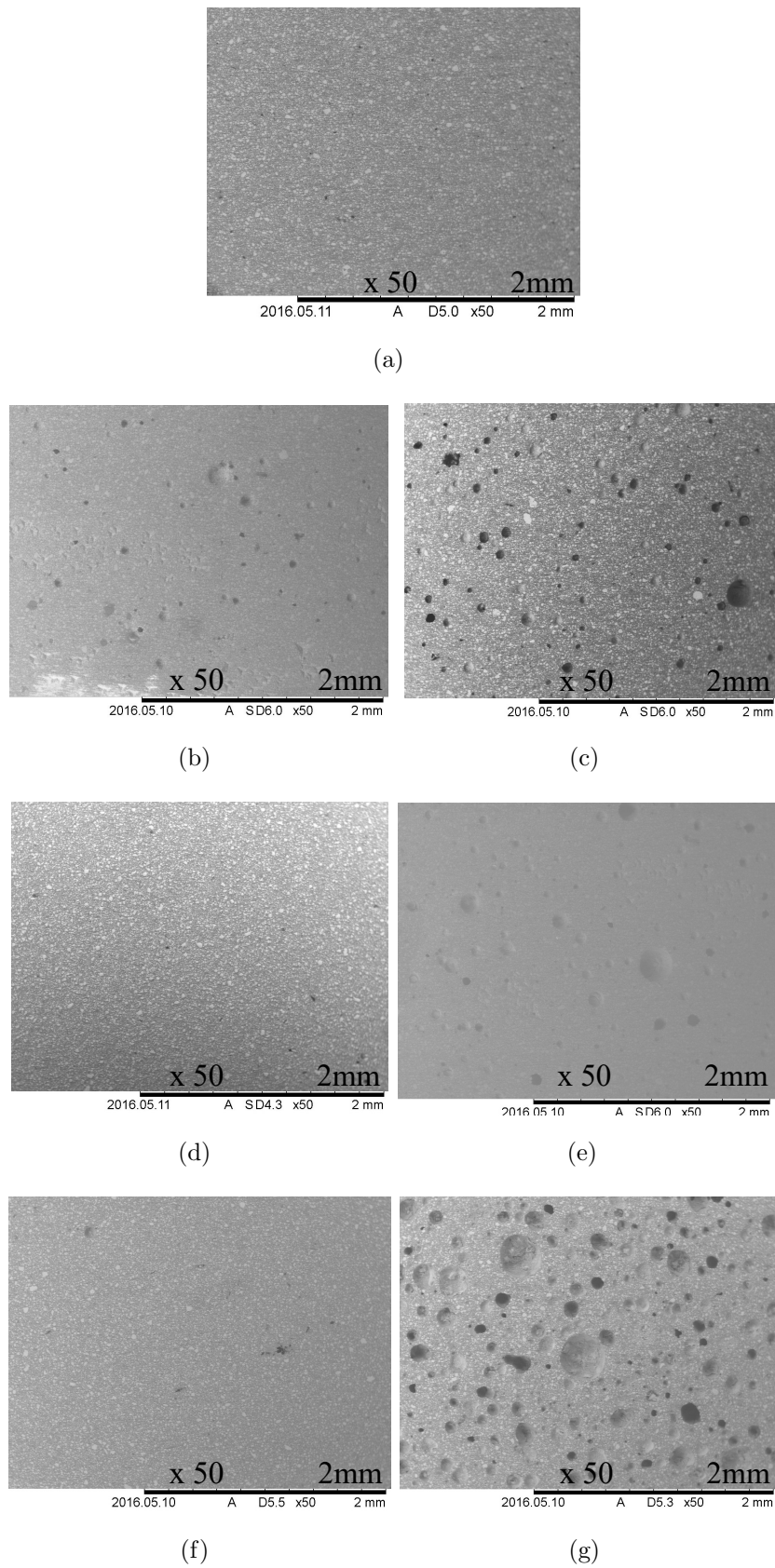


**Figure 4.1:** Surface images of cement pastes, observed using SEM (magnification 50 ×): Reference (a), P1-0.05 (b), P1-0.20 (c), P2-0.05 (d), P2-0.20 (e), P3-0.05 (f), P3-0.20 (g).

**Statistical analysis of the indentation modulus of polymer-modified cement pastes**

From the nanoindentation measurements (both ET and CSM), empirical distributions of the mechanical properties are obtained. Statistical analysis and a subsequent deconvolution of the indentation results are required to identify the mechanical phases and their corresponding properties, see Section 2.2.4. A mechanical phase represents a (virtual) part of the material with a homogeneous elastic response. The chemical composition of the material, the microstructure, and the volume tested under the indenter influence the properties of the mechanical phases [148].

Every mechanical phase is described by a modulus with its standard deviation and a phase (volume) fraction. From the cumulative distribution function (CDF), the sought parameters such as the indentation modulus of each phase, are obtained by fitting the CDF with a sum of weighted Gaussian distributions [152]. The procedure is called deconvolution. In this work, a Levenberg-Marquardt fitting algorithm (Peak Fit Analyzer, OriginLab) was used to fit the empirical CDF of the indentation modulus. It was found that a phase number of three allows for an accurate description of the experimental CDF. In addition, a good reproducibility of the deconvolution results over a large set of initial parameters was ensured using three material phases.

**Nanoindentation testing - Micromechanical creep properties** With the nanoindentation technique, creep tests were performed on the paste specimens to explore the creep behavior at the micrometer scale. During the tests, the creep responses of the specimens were measured by keeping the indentation load constant and recording the change of the indentation depth over time. For each indent, the load was increased linearly at a rate of  $1 \text{ mN s}^{-1}$  until an indentation depth of  $1 \mu\text{m}$  was reached. Then, the load was kept constant for 220 seconds and the displacement of the Berkovich indenter tip was measured. Finally, the specimen was unloaded. Between seven and eight indents were performed on each sample. One averaged curve for each cement paste was evaluated. At the time instant of testing, the specimens were three months old so that autogeneous shrinkage strains during the creep test can be neglected with respect to the strains induced by the loading.

The indentation moduli  $M$  of the cement pastes can be obtained either from the CSM or the ET measurements. Indents with a holding duration of 200 seconds additionally enable the determination of time-dependent properties of the cement pastes. A contact creep compliance  $L(t)$  is introduced to characterize the creep behavior of a material under an indented load. This quantity is neither dependent on the probe geometry nor the load magnitude [156, 166]. For a material that undergoes time-dependent plasticity upon conical indentation testing, the contact creep function  $L(t) - L(0)$ , linking the applied

load and the measured indentation depth, is defined as [164, 166]

$$L(t) - L(0) = L(t) - \frac{1}{M} = \frac{2a_u \Delta h(t)}{P_{\max}} \quad (4.9)$$

with

$L(t)$	contact creep compliance [ $10^{-6}/\text{MPa}$ ]
$L(0)$	contact creep compliance at time $t = 0$ [ $10^{-6}/\text{MPa}$ ]
$a_u$	contact radius of the projected area between indenter and indented material at the onset of unloading [nm]
$\Delta h(t)$	increment of indentation depth response [nm]
$P_{\max}$	applied load during the holding phase [mN].

The radius  $a_u$  was estimated with the method by Oliver and Pharr [300]. In Eq. (4.9), the time instant  $t = 0$  corresponds to the beginning of the holding period. The equation is based on the assumption that plastic deformations only appear during the loading period and not during the holding and unloading phase [164].

Furthermore, it was found out that the creep of cement pastes exhibited during indentation creep tests can be modeled using a logarithmic function of the time [166]. Thus, with minutes-long indentation creep experiments on cement pastes, a quantitative measurement of the long-term creep kinetics of cement pastes is provided. For describing the creep behavior of the cement pastes quantitatively, the measured contact creep compliance function is fitted as follows [166]:

$$L(t) - \frac{1}{M} = \frac{\ln(t/\tau_i + 1)}{C_i} \quad (4.10)$$

with

$\tau_i$	characteristic time [s]
$C_i$	contact creep modulus [GPa].

Eq. (4.10) yields two fitting parameters, namely the contact creep modulus  $C_i$  and the characteristic time  $\tau_i$ . The contact creep modulus is a measure of the creep rate. The higher  $C_i$ , the lower is the rate of the creep. The characteristic time describes the time at which the creep starts to exhibit logarithmic kinetics. The optimization problem in Eq. (4.10) is solved using the Nelder-Mead Simplex algorithm, which is implemented in the software Matlab (MathWorks, USA).

## 4.4 Experimental investigations with mortars

### 4.4.1 Fresh mortar properties

Analogously to the fresh cement pastes, the **consistency** of the fresh mortars was determined with the slump test according to DIN EN 1015-3:2007-05 [292].

The **air void content** was determined directly after mixing, following DIN EN 1015-7:1998 [301].

The determination of the **fresh bulk density** of the mortars was performed according to DIN EN 1015-6:2007-05 [302].

### 4.4.2 Hardened mortar properties

The **compressive strength** was determined with prism specimens ( $4\text{ cm} \times 4\text{ cm} \times 16\text{ cm}$ ) according to DIN EN 1015-11:1999+A1:2006 [294] at 2, 7, and 28 days after the production.

The **static (elastic) modulus** was determined as the secant modulus of prism specimens ( $4\text{ cm} \times 4\text{ cm} \times 16\text{ cm}$ ) following DIN EN 12390-13:2014-06 [303]. The rate of loading was  $0.5\text{ N mm}^{-1}$ . The maximum load level amounted to one third of the compressive strength of the mortar at the time of testing (at 2, 7, and 28 days).

The **dynamic (elastic) modulus** was determined with the resonant frequency measurement on prism specimens ( $4\text{ cm} \times 4\text{ cm} \times 16\text{ cm}$ ) at 2, 7, and 28 days. The testing was performed according to DIN EN 12504-4:2004 [304].

## 4.5 Experimental investigations with concretes

### 4.5.1 Fresh concrete properties

The **fresh bulk density** and the **air void content** of the fresh concretes were determined directly after mixing according to DIN EN 12350-5:2009 [305] and DIN EN 12350-6:2009 [306] respectively.

The **consistency** of the fresh concrete mixtures was determined with the slump test, ten minutes after water addition, according to DIN EN 12350-5:2009 [305].

### 4.5.2 Hardened concrete properties

For the determination of the **compressive strength** of the concretes, cubic specimens with an edge length of 10 cm were produced. At sample ages of 2, 7, and 28 days, the compressive strength was determined according to DIN EN 12390-3:2009 [307].

The **static (elastic) modulus** was determined with cylindrical specimens (height = 30 cm, diameter = 15 cm) at 2, 7, and 28 days after the production following DIN EN 12390-13:2014 [303].

For the determination of the **dynamic (elastic) modulus**, also cylindrical specimens were tested at 2, 7, and 28 days after the production. The testing was performed according to DIN EN 12504-4:2004 [304].

## 4.6 Results

The results of the experimental investigations with the polymer specimens as well as with polymer-modified cement pastes, mortars, and concretes are described in the following. Where applicable, averaged experimental data are presented with error bars spanning one standard deviation about the mean.

### 4.6.1 Micromechanical properties of the polymers

The Young's moduli  $E$  of the polymer specimens are calculated using the storage  $E'$  and the loss moduli  $E''$  according to  $E = \sqrt{E'^2 + E''^2}$ . The flat punch nanoindentation tests (CSM measurements) on polymer samples reveal that the elastic stiffness of the polymers is by one magnitude lower than those of the cementitious constituents are, which are given in the literature [149, 150]. Polymer P1 has both the largest Young's modulus and the largest storage modulus, which is most likely related to the low minimum film forming temperature of this polymer, see Figure 4.2. For polymer P2, the MFT was not reached throughout the production and testing. Indeed, a compact specimen was obtained that could not support any tension. This probably explains the difference between P1 and P2, which have the same chemical composition. The viscoelastic behavior of P3 is more pronounced than for the other polymers. It exhibits the largest loss modulus and the lowest storage modulus. The low stiffness of P3 is related to the large amount of soft butadiene. Due to their specific micromechanical properties, the three polymers are expected to modify the mechanical behavior of cement-based materials differently.



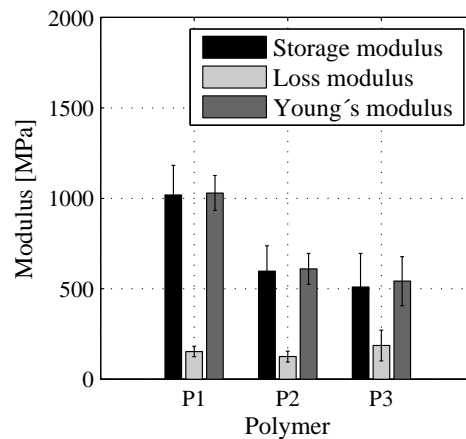


**Figure 4.2:** Storage, loss and Young's moduli of compact specimens made of polymer dispersions and powders, determined by means of flat punch nanoindentation tests with the continuous stiffness measurement.

## 4.6.2 Cement pastes

### 4.6.2.1 Hydration kinetics

The addition of polymers influences the hydration kinetics of cement pastes remarkably. The polymers retard the hydration process, as it can be quantified from the isothermal calorimetry tests, see Figure 4.3. The polymer-modified cement pastes exhibit an extended time length of the dormant period. This is particularly well visible for the sample P2-0.20. The heat rate during the acceleration period is slowed down and delayed in comparison with the reference cement paste, as e.g. Kong et al. [46] and Schirmer [21] also reported, see Section 2.1.2.1. The accumulated heat quantity is reduced with increasing polymer content. For a given time instant, the heat quantity of the unmodified cement paste is larger than those of the polymer-modified cement pastes are. Differences concerning the accumulated heat quantity between varying cement pastes having the same  $p/c$ -ratio are rather small, showing that the chemical composition has a minor effect on the hydration kinetics. The polymer quantity added is of greater importance. The larger the  $p/c$ -ratio, the more pronounced is the retardation of the hydration heat development.

The degree of hydration is a major factor governing the mechanical properties of cementitious materials. As expected from the literature review in Section 2.1.2.1, the decreased heat rates and heat quantities entail a slower temporal evolution of the degree of hydration in polymer-modified cement pastes, see Figure 4.4. For a given time instant, the unmodified reference sample exhibits a larger hydration degree than the polymer-modified cement pastes do. The cement pastes with a  $p/c$ -ratio of 0.20 have a remarkably lower hydration

degree than the cement pastes with a  $p/c$ -ratio of 0.05. Again, the chemical composition of the polymers has a minor influence on the hydration degree than the polymer content does. Only slight differences between the different polymer types are visible. At two days after the production, specimen P2-0.05 shows larger degrees of hydration than cement pastes P1-0.05 and P3-0.05 do.

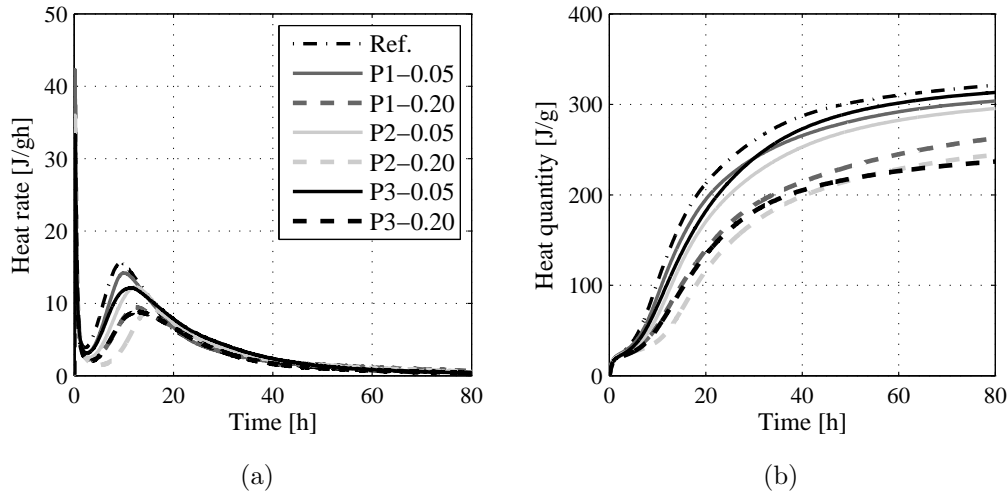


**Figure 4.3:** Time-dependent heat rate (a) and cumulative heat quantity (b) of one plain cement paste and six polymer-modified cement pastes with  $w/c = 0.40$ .

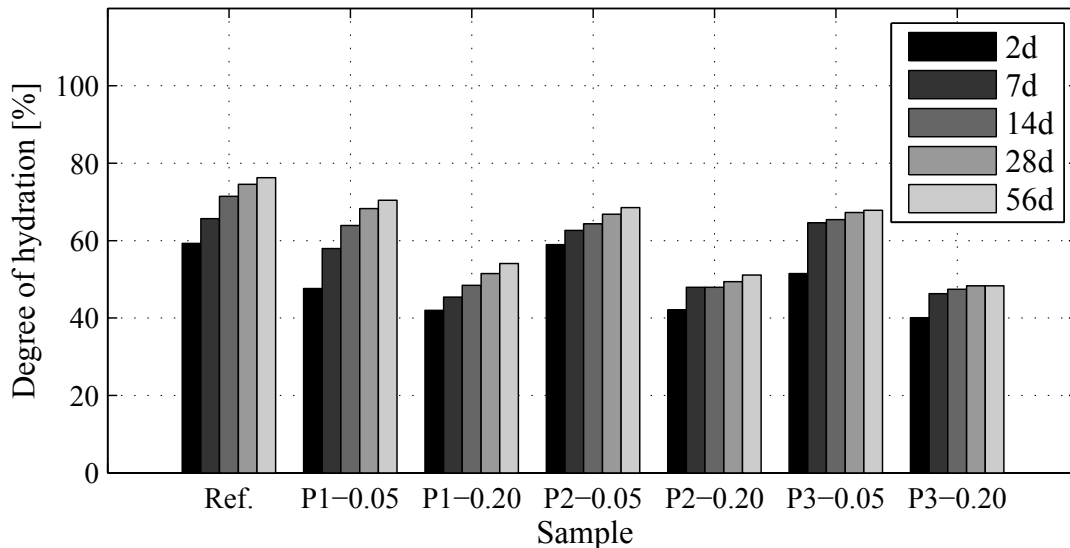


**Figure 4.4:** Temporal evolution of the degree of hydration of plain and polymer-modified cement pastes with  $w/c = 0.40$ .

#### 4.6.2.2 Microstructure formation

The microstructures of the cement pastes were investigated using the environmental scanning electron microscopy (ESEM), at material ages of 21 hours after production. This time instant refers to the start of the early-age short-term creep tests on cement pastes described in Section 5. According to Dimmig [15], the microstructure in polymer-modified cement pastes is mainly formed during the first 24 hours of the hydration process. Afterward, no significant changes are expected. The elucidation of the microstructural formation provides fundamental information for the development of a realistic micromechanical model of polymer-modified cement pastes, see Section 5.3.

The microstructure of the unmodified cement paste is characterized by a dense arrangement of hydration products. The C-S-H gel structure, rod-like ettringite, and bar-like portlandite crystals can be distinguished, see Figure 4.5.

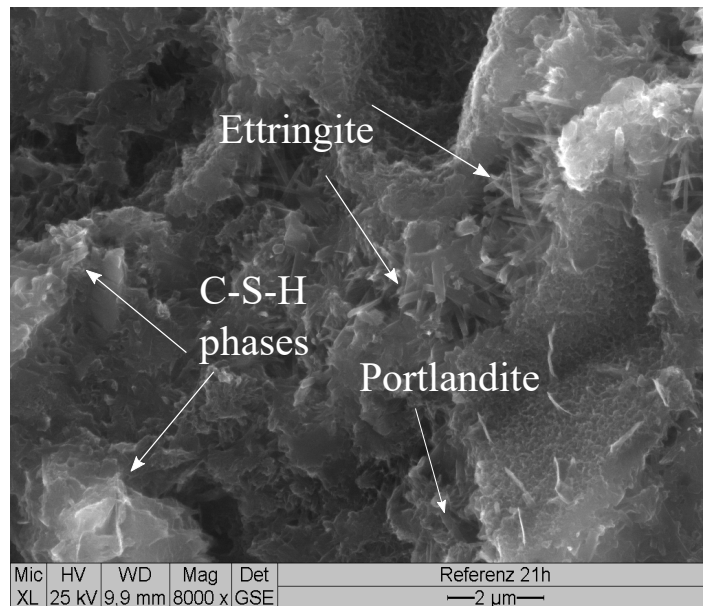


**Figure 4.5:** Microstructure of the plain cement paste with  $w/c = 0.40$  at a material age of 21 hours after production.

In comparison with the reference, the polymer-modified cement pastes exhibit microstructural changes, see Figures 4.6, 4.7, and 4.8. In cement paste P1, polymer films partially cover the cementitious matrix, including the hydration products. The polymer particles are mostly coalesced and filmed but some spherical particles with diameters of a few hundred nanometers are still visible. It seems as if the polymer spheres are glued against each other.

The retarded film formation of some polymers has been also observed by Gretz and Plank [24], who showed that anionic stabilized polymer particles exhibit a hampered coalesce at high pH-values due to the adsorption of calcium ions. The complexation of functional groups of the polymers by calcium ions retards the film formation. Polymer P2 contains polyvinyl alcohol as a protective colloid. Schirmer [21] recently elaborated that the protective colloid also forms complexes with the calcium ions of the cement paste pore solution. She investigated the microstructure formation of vinyl acetate-modified cement pastes by means of cryo-SEM and observed an incomplete film formation caused by the alkaline environment and the presence of complexing ions, as it is confirmed herein.

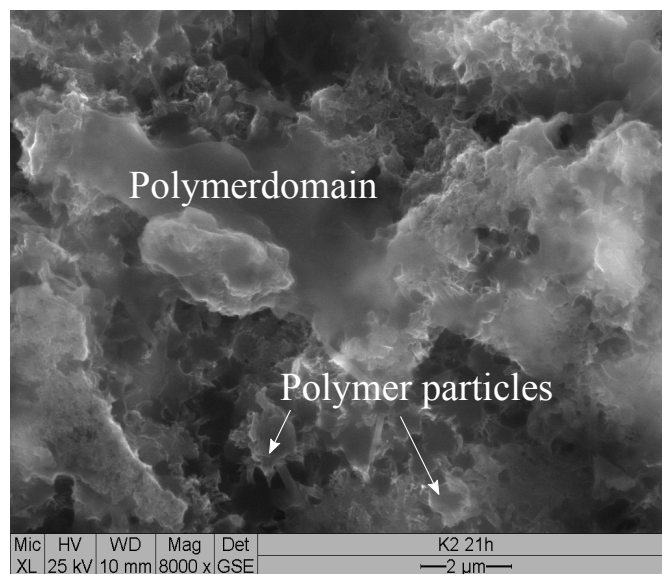


**Figure 4.6:** Microstructure of the polymer-modified cement paste P1 with  $w/c = 0.40$  and  $p/c = 0.20$  at a material age of 21 hours after production.

The polymer particles in cement paste P2 appear to be finer. This is most probably related to the smaller particle sizes of the polymer in the dispersion (see Table 4.4). In comparison with sample P1, smaller polymer domains are visible. The polymer particles are not filmed because the MFT ( $30^{\circ}\text{C}$ ) was not reached during the processing. The polymers are well distributed between the cementitious structure, which was also reported by Bode [65], who investigated the same polymer dispersion (P2) as it was used in this thesis.

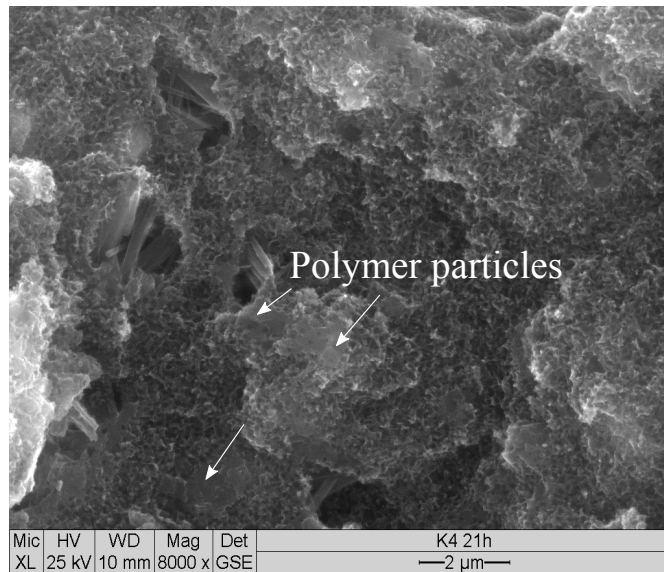


**Figure 4.7:** Microstructure of the polymer-modified cement paste P2 with  $w/c = 0.40$  and  $p/c = 0.20$  at a material age of 21 hours after production.

In cement paste P3, the polymers seem to be even finer distributed than in the other cement pastes. Polymer domains covering the cementitious hydration products are observed. The polymers are partially filmed but also single particles are visible. In all polymer-modified cement pastes, only a low amount of ettringite crystals is observed, which might refer to the reduced degree of hydration in comparison with the reference. Dimmig [15] and Silva et al. [41] also reported a delayed growth of ettringite in polymer-modified cement pastes.

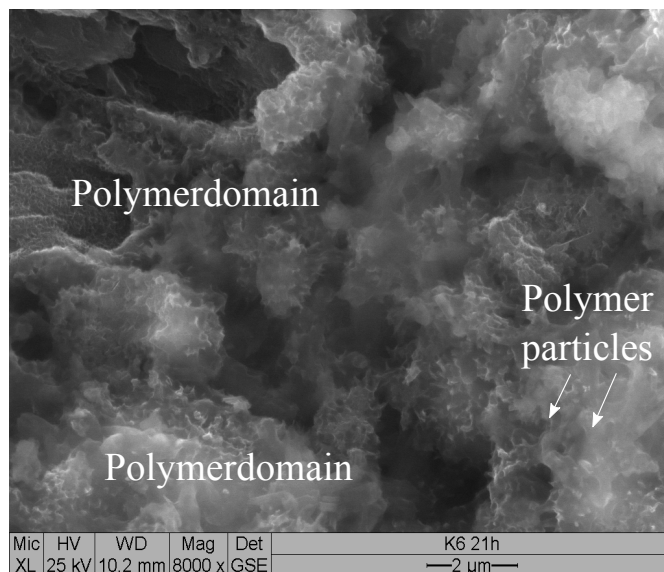


**Figure 4.8:** Microstructure of the polymer-modified cement paste P3 with  $w/c = 0.40$  and  $p/c = 0.20$  at a material age of 21 hours after production.

### 4.6.2.3 Fresh cement paste properties

For a constant water-to-cement ratio of 0.40, the polymer-modified cement pastes show an improved workability in comparison with the conventional cement paste, see Figure 4.9. With increasing  $p/c$ -ratio, the slump is increased. This mainly stems from the ball-bearing effect of the polymer particles, the entrained air, and surfactants in the polymer dispersions, which support the dispersing, e.g. [18]. The polymer dispersions P2 and P3 increase the slump more considerably than the polymer powder does, most probably due to the smaller particle sizes of the polymer and due to their surfactants.

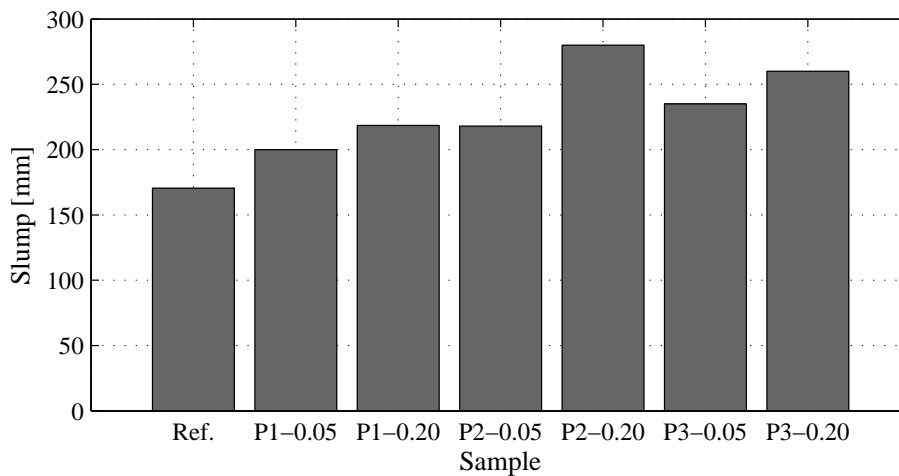


**Figure 4.9:** Consistencies of unmodified and polymer-modified cement pastes with  $w/c = 0.40$ .

### 4.6.2.4 Hardened cement paste properties

**Density and porosity** The particle density of the cement pastes decreases as a consequence of the polymer modification, see Table 4.8. The higher the polymer content, the lower the particle density is. The reason for that is the low density of the polymers (see Table 4.4) in comparison with that of cement, which amounts to  $3.15 \text{ g cm}^{-3}$  [308].

Bode [65] investigated the bulk density of polymer-modified mortars for varying storage conditions but no clear tendencies concerning the influences of the polymers were revealed. Herein, the bulk densities of the polymer-modified cement pastes are lower than those of the plain paste. This is, besides the addition of polymers, due to the increased air void content, as quantified from the total porosity. The polymers contain surfactants or other additives that can entrap air in the mixtures. Sample P3-0.20 shows a significantly higher porosity than the reference does. About 8% additional pores are formed in comparison with the unmodified cement paste. On the contrary, the porosity of sample P2-0.20 is

within the range of the reference, which is related to its pronounced slump flow. The low viscosity allows the cement paste to deaerate and to form a denser microstructure.

However, the exact composition of the polymer dispersions and powders is not given. They might contain further technical additives, such as anti-foaming agents, which can influence the amount of entrapped air. Thus, generalized conclusions about the influences of polymer additions on the porosity, and properties of fresh and hardened cement-based mixes in general, cannot be drawn. Polymer dispersions having the same chemical composition can have different effects of cement-based materials due to their varying additives.

**Table 4.8:** Density and porosity of the cement pastes ( $w/c=0.40$ ).

Specimen	Time [d]	Particle density [g cm <sup>-3</sup> ]	Bulk density [g cm <sup>-3</sup> ]	Total porosity [%]
Ref.	2	2.20	1.93	12.1
	7	2.21	1.95	11.6
	28	2.19	1.98	9.8
P1 - 0.05	2	2.18	1.77	18.8
	7	2.19	1.81	17.5
	28	2.17	1.85	14.5
P1 - 0.20	2	2.02	1.67	17.3
	7	2.03	1.68	17.3
	28	2.02	1.72	14.7
P2 - 0.05	2	2.19	1.88	14.3
	7	2.17	1.87	14.0
	28	2.17	1.92	10.7
P2 - 0.20	2	2.02	1.77	12.1
	7	1.99	1.76	11.4
	28	1.99	1.77	10.9
P3 - 0.05	2	2.17	1.81	16.5
	7	2.17	1.84	15.3
	28	2.15	1.87	13.2
P3 - 0.20	2	2.01	1.60	20.3
	7	2.01	1.61	19.8
	28	1.99	1.64	17.5

**Compressive strength and dynamic modulus** The entrapped air and the polymer inclusions cause discontinuities in the microstructural network [66], which reduce the compressive strength of the cement pastes, see Figure 4.10. The specimens modified with a polymer-to-cement ratio of 0.20 exhibit lower compressive strengths compared with specimens with a polymer-to-cement ratio of 0.05. Sample P3-0.20 exhibits lower



strength values than the cement pastes P1-0.20 and P2-0.20 do, which refers to the increased porosity, see Table 4.8. The modification with polymer P2 entails slightly larger compressive strengths than it does with polymer P1. This stems from the low porosity in the specimens modified with polymer P2.

The experimental results partly coincide with the compressive strengths of PCC reported by Flohr [76], who used the same polymer modifications. He claimed that the polymers lead to reduced compressive strengths, but a clear influence of the polymer quantity added was not observed. One reason for the diverging results might be that besides the polymer modification, the compressive strength of polymer-modified cement-based materials is determined based on several factors, such as the curing conditions, the mix proportion, the nature of the raw materials, and the testing procedures [18]. Furthermore, Flohr investigated concretes instead of cement pastes and varied the  $w/c$ -ratio for different mixtures, which does not allow for a generic comparison.

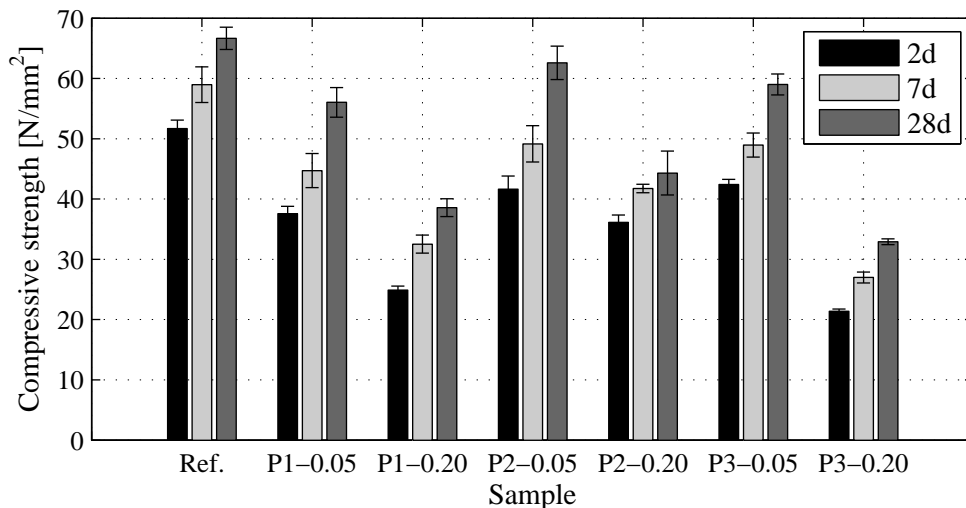


**Figure 4.10:** Compressive strengths of the unmodified and polymer-modified cement pastes with  $w/c = 0.40$ , determined 2 days, 7 days, and 28 days after the production.

The same trends as for the compressive strength can be observed for the dynamic modulus. Polymer-modified cement pastes provide a lower elasticity than conventional cement pastes do (Figure 4.11). This stems from the low elastic modulus of the polymers, which is considerably smaller than that of the cementitious components is, see Section 4.6.1. Further reasons are the retarded hydration reaction and the large porosity in the polymer-modified samples. For a given time, the unmodified cement paste exhibits the largest dynamic modulus. With increasing polymer content, the dynamic moduli are reduced. On average, an increase of the  $p/c$ -ratio from 0.05 up to 0.20 leads to a reduction of the dynamic modulus of 30%. The specimen P3-0.20 exhibits the lowest dynamic modulus, which is

related to the increased porosity, on the one hand, and the soft butadiene, on the other hand. According to Flohr [76], the polymers additionally act as sliding planes inside the material, which entails a more ductile behavior and increased plastic and viscous deformations. The polymer particles are embedded between the C-S-H phases and other hydration products and therefore hinder the interdigitation of the crystalline structures, see also Section 4.6.2.2.

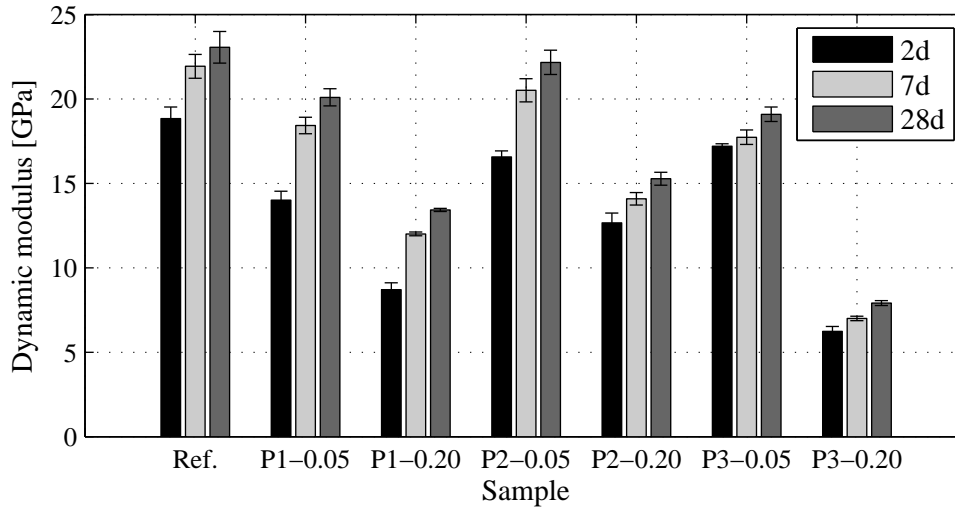


**Figure 4.11:** Dynamic moduli of unmodified and polymer-modified cement pastes with  $w/c = 0.40$ , determined 2 days, 7 days, and 28 days after the production.

**Length changes** In the literature, no consensus exists as to whether or not the polymer modification provokes extended shrinkage strains (see Section 2.1.5). Herein, the experimental results of Bode [65] and Dimmig [15], who reported an increased shrinkage behavior, are confirmed. The authors partially used the same polymer dispersions, as in the present study. The polymer-modified cement pastes exhibit larger length changes than the plain reference paste. The total length changes are depicted in Figure 4.12. Individual shrinkage parts, such as drying or autogeneous shrinkage, are not differentiated. Apparently, the lengths of the polymer-modified cement paste specimens change more considerably than those of the unmodified paste. The length change of the unmodified cement paste amounts to only  $0.2 \text{ mm m}^{-1}$  after 28 days, whereas it amounts to  $0.6 \text{ mm m}^{-1}$  for specimen P1-0.20 and to  $1.1 \text{ mm m}^{-1}$  for P2-0.20, respectively. Sample P3-0.20 exhibits a length change of  $1.6 \text{ mm m}^{-1}$ , which goes along with its low stiffness. Similar trends are observed for the cement pastes with a  $p/c$ -ratio of 0.05. The specimen P3-0.05 shows the most pronounced shrinkage activity, followed by the pastes P2-0.05 and P1-0.05. Notably, although the pastes modified with polymer P2 exhibit a larger stiffness than the samples modified with polymer P1, the latter exhibit smaller length changes.

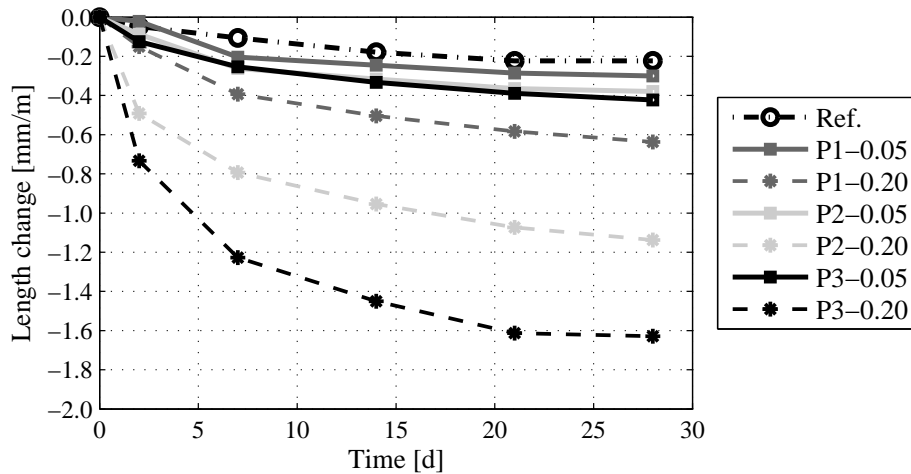


**Figure 4.12:** Length changes of plain and polymer-modified cement pastes with  $w/c = 0.40$  during the first 28 days after production.

**Micromechanical (elastic) properties** The results of the nanoindentation tests obtained using the Express Test option on cement pastes at 28 days after the production are presented in Figure 4.13. The indentation moduli of the cement pastes are shown, including the standard deviations of the measurements. Three different phases are distinguished. However, all samples exhibited a high surface roughness, see Section 4.3.4.5, rendering the test evaluation difficult. The high surface roughness is likely due to the difficulty to polish heterogeneous surfaces with hard inclusions, as it might be the case for hardened cement pastes. Usually, a high surface roughness entails an increased scatter and a reduction of the measured indentation moduli [160, 161]. Therefore, the presented results should be interpreted against the background of a high surface roughness; only trends are discussed in the following.

The indentation moduli of the phases identified in the unmodified reference paste agree remarkably well with experimental results published in the literature [149, 165]. Accordingly, the three phases identified using the deconvolution technique most likely refer to low-density C-S-H ( $\approx 22$  GPa), high-density C-S-H ( $\approx 35$  GPa), and a mix of C-S-H with portlandite ( $\approx 48$  GPa), as Vandamme and Ulm [165] reported previously. In this thesis, only substoichiometric cement pastes with  $w/c$ -ratios lower than 0.42, containing a small amount of unhydrated clinker, were investigated. However, unhydrated clinker grains could not be differentiated using the statistical nanoindentation technique, which was also observed by Sebastiani et al. [298]. This may also be related to the limitations of the method, as discussed in Section 2.2.4.

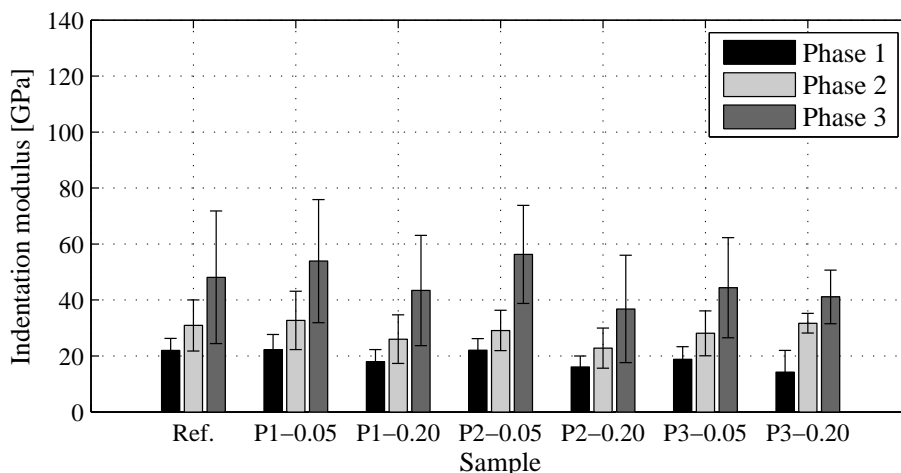


**Figure 4.13:** Indentation moduli derived from nanoindentation tests using the Express Test (ET) option for unmodified and polymer-modified cement pastes with  $w/c = 0.40$ , measured 28 days after the production.

For the polymer-modified cement pastes, also three different phases were identified. The absence of a further phase, which could be assigned to a new hydration product type, indicates that the polymer modification rather influences the microstructural morphology than the intrinsic nature of the hydration products. Furthermore, pure polymer compounds might be too small to be identified separately through nanoindentation testing with the ET method. However, Wilson et al. [162] investigated cement pastes with natural pozzolan and found that morphological changes of the hydration products and the chemical modifications compensated each other. A similar coupled SEM study could not be performed in the present study, such that the existence of polymer-cement compounds or modified hydration products could neither be confirmed nor excluded.

The mix proportion, particularly the  $p/c$ -ratio, mainly influences the indentation moduli of the material phases present in the hardened cement pastes. This agrees well with the experimental observations of Wang et al. [173]. The higher the  $p/c$ -ratio, the smaller are the indentation moduli. The lower indentation moduli are related to three different effects: (i) the more porous microstructure of the polymer-modified cement pastes compared with the reference, (ii) the retarded hydration reaction due to the adsorption of polymer particles on cementitious constituents and the complexation of calcium ions, as described in Section 2.1.2.2, and (iii) the low stiffness of the polymers.

The size of the indenter is larger than the characteristic scale of the cementitious microstructure is, such that the nanoindentation tests cannot provide information about individual phases of the cement pastes, see Figure 4.14. Thus, the micromechanical phases identified

herein represent compounds consisting of both cementitious and polymer components. The indentation moduli of all three phases are reduced in the presence of polymers, indicating that the polymer particles are evenly adsorbed on all of the cementitious constituents. For detailed information about the adsorption behavior of the polymers on the cementitious phases, adsorption measurements as described by Schirmer [21] should be performed.

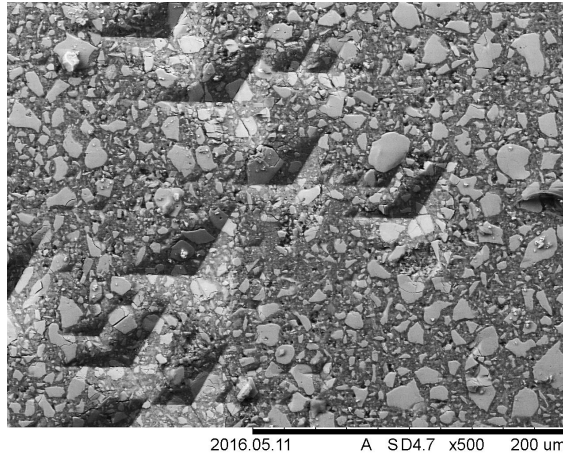


**Figure 4.14:** Indents in the reference cement paste, observed using a scanning electron microscope (TM3000, HITACHI, Bruker, USA).

The corresponding phase volume fractions determined at material ages of 28 days and 56 days are presented in Figure 4.15. The evolutions of the volume fractions reveal that the amounts of Phase 2, identified as high-density C-S-H, and Phase 3, identified as a composite of Portlandite and C-S-H phases, increase with the time whereas the amount of Phase 1, identified as low-density C-S-H, decreases. This refers to the formation of denser hydration products as a consequence of the ongoing hydration process. The higher the hydration degree, the larger the amount of high-density C-S-H [111, 155]. The phase volume fractions of Phase 1 at 28 days are larger for the polymer-modified cement pastes than for the reference specimen. This is related to the high porosity and the lower hydration degrees in polymer-modified cement pastes.

At the hydration age of 28 days, nanoindentation tests with the continuous stiffness measurement (CSM) method were also performed. Two indentation depths were evaluated: 200 nm and 900 nm. In Figure 4.16, the results of the lower indentation depth are presented. With only 17 to 20 indents on each sample, no statistically sufficient number of data points was achieved. Furthermore, the high roughness of the specimens influences the results from the CSM method at very low indentation depths; still, three different mechanical phases could be identified.

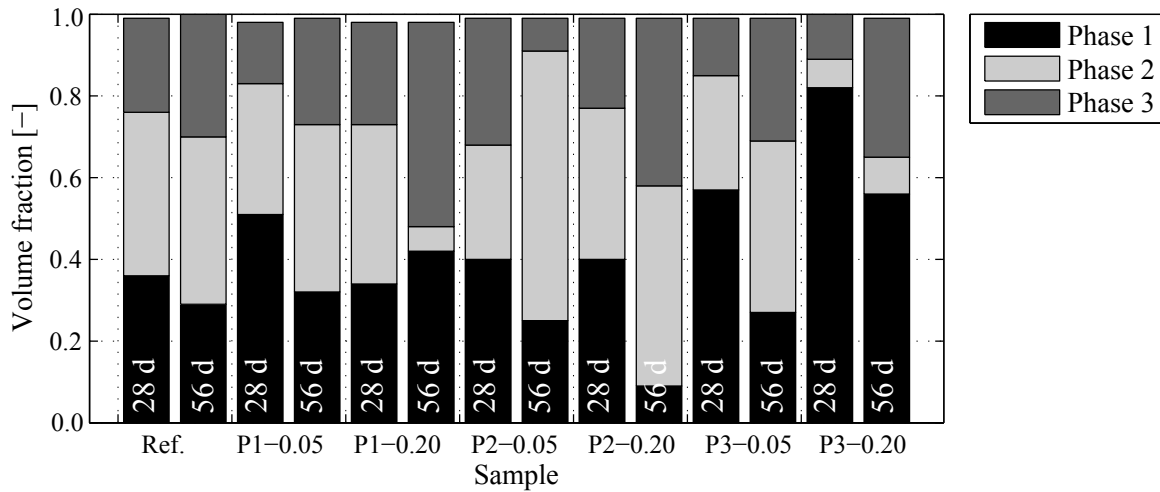


**Figure 4.15:** Phase volume fractions derived from nanoindentation tests using the Express Test (ET) option for unmodified and polymer-modified cement pastes with  $w/c = 0.40$ , measured 28 and 56 days after the production.

In contrast to the ET method, the CSM tests revealed a phase with an indentation modulus of up to 120 GPa in the reference paste and in the samples P1-0.05 and P3-0.05 at an indentation depth of 200 nm. This phase most likely refers to unhydrated clinker in the substoichiometric cement pastes. For cement pastes with a  $p/c$ -ratio of 0.20, the unhydrated clinker grains are probably covered by polymer layers that reduce the indentation moduli significantly. The differences between the results obtained with the ET and the CSM method are discussed in the following.

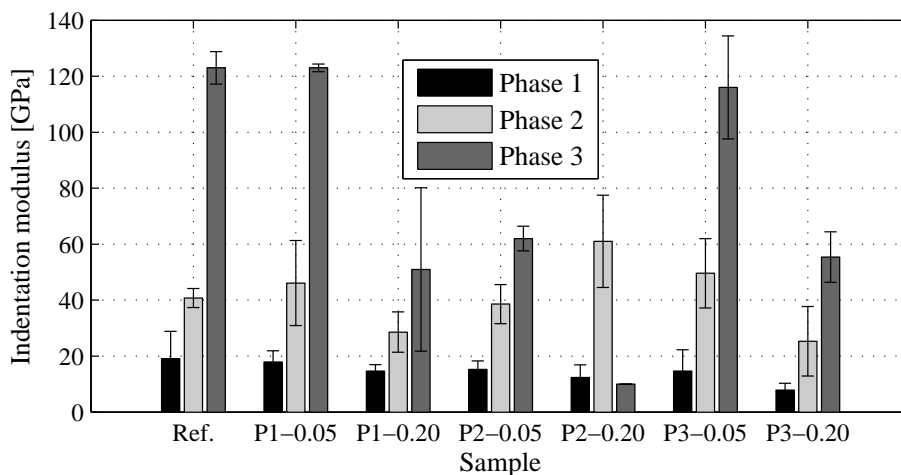


**Figure 4.16:** Indentation moduli derived from nanoindentation tests using the CSM option for unmodified and polymer-modified cement pastes with  $w/c = 0.40$ , measured at an indentation depth of 200 nm on 28-days-old-samples.

The mean indentation moduli enable a direct quantitative comparison between the results of the ET and the CSM method. For this purpose, the mean values of the empirical distributions obtained from the nanoindentation tests are computed. The results of the CSM investigations are presented for indentation depths of 200 nm and 900 nm; the latter is close to the indentation depth chosen for the ET method.

The nanoindentation measurements indicate reduced mean indentation moduli as a consequence of the polymer modification, see Figure 4.17. The higher the polymer content, the lower are the mean indentation moduli. These trends coincide with the elastic moduli determined with macroscopic cement paste specimens, compare Figures 4.13 and 4.11. On both microscopic and macroscopic length scales it is shown that the elastic moduli of the mixes modified with the polymers P1 and P2 are similar. The elastic moduli of the pastes modified with polymer P3 are lower, whereas the plain reference exhibits the largest moduli. The indentation moduli obtained with the CSM measurement at an indentation depth of 200 nm are larger than for the other measurements. This probably stems from the detection of the unhydrated clinker phase as described above and likely from carbonation processes, which densify the surfaces of the specimens. The results obtained with the CSM method at an indentation depth of 900 nm and the ET method are close to each other for low polymer contents because the indentation depths are comparable. For polymer-modified cement pastes with a  $p/c$ -ratio of 0.20, the indentation moduli identified from the CSM method are lower than those from the ET method. As polymers tend to be stiffer at higher strain rates [309], the large strain rate difference between the ET and CSM testing methods may influence the nanoindentation results.

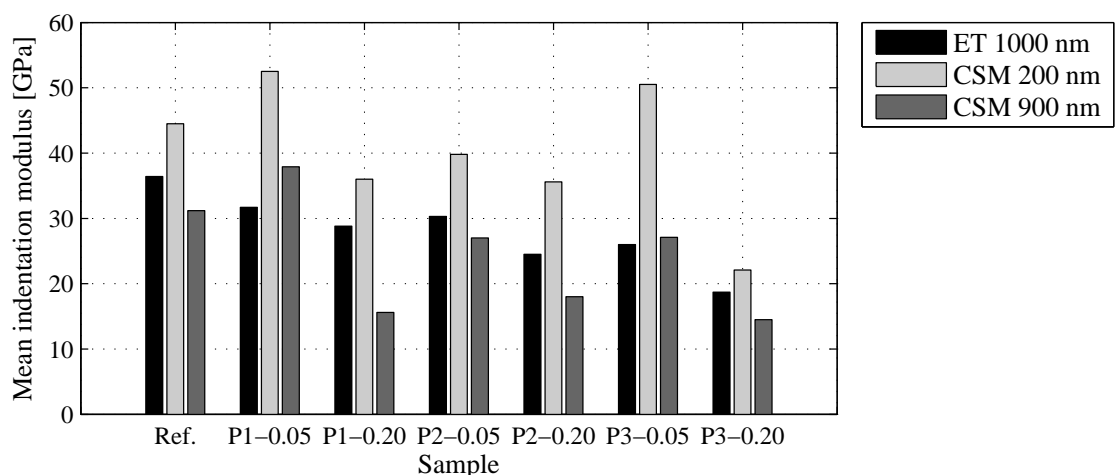


**Figure 4.17:** Mean indentation moduli of the cement pastes with  $w/c = 0.40$  obtained from nanoindentation investigations using the ET method (indentation depth: 1000 nm) and the CSM method at two indentation depths (200 nm and 900 nm).

**Micromechanical (creep) properties** The displacements that the cement pastes exhibited during the nanoindentation creep tests increase nonlinearly over time, see Figure 4.18. The reference paste without polymers shows the smallest displacements. For the cement pastes with a  $p/c$ -ratio of 0.20, larger displacements are observed than for the cement pastes with a  $p/c$ -ratio of 0.05. This is related to possible sliding effects of the polymers within the cementitious matrix and their low stiffness. Cement pastes modified with polymer P3 exhibit larger displacements than cement pastes with P1 and P2 do.

The trends observed for the micromechanical creep tests agree well with the previously described measurements of the load-independent length changes, compare Figures 4.18 and 4.12. The results of both experiments clearly reveal a more pronounced deformation behavior of the polymer-modified cement pastes compared with the reference paste. Both the microscopic and the macroscopic tests illustrate that the cement pastes modified with polymer P3 exhibit larger strains than the polymer-modified pastes P1 and P2 for a given  $p/c$ -ratio. Though the elastic moduli of the latter two pastes are close to each other, paste P2 exhibits a more pronounced deformation behavior than paste P1 does.

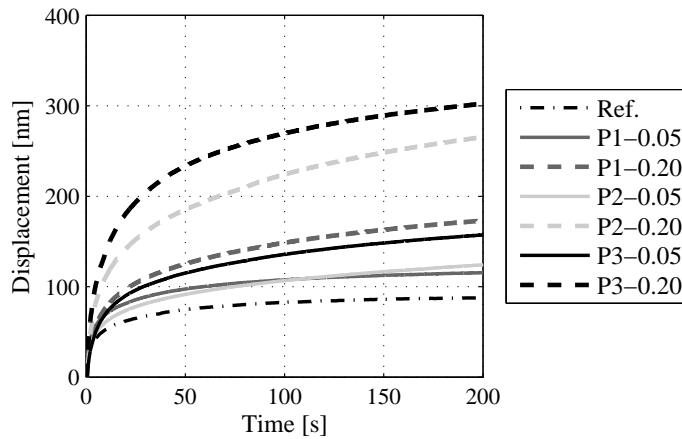


**Figure 4.18:** Displacements of the cement pastes during the nanoindentation creep tests.

Averaged curves are shown; on each sample, 7 to 9 single tests were performed.

The contact creep functions computed with Eq. (4.9) illustrate the more pronounced creep activity of polymer-modified cement pastes even more clearly, see Figure 4.19 (a). Particularly, cement pastes having a  $p/c$ -ratio of 0.20 exhibit a faster gain of the contact creep function compared with cement pastes having a  $p/c$ -ratio of 0.05. For a given  $p/c$ -ratio, the cement pastes modified with polymer P3 show the largest creep activity. The more pronounced viscoelastic behavior of the cement pastes with P3 agrees well with the micromechanical viscoelastic properties of the polymer specimens (see Subsection 4.6.1), which revealed that polymer P3 exhibits the largest loss modulus of the three polymers.



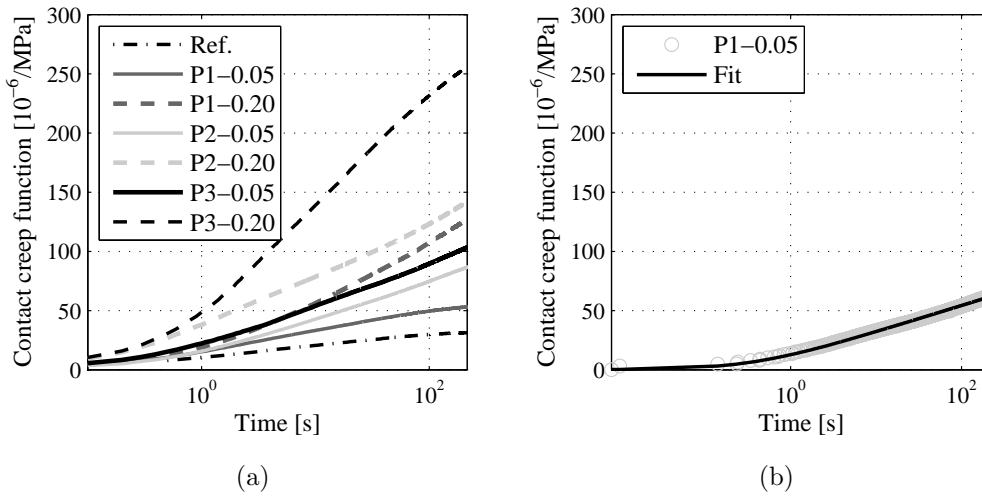


**Figure 4.19:** Contact creep functions  $L(t) - 1/M$  of cement pastes obtained by nanoindentation creep tests (a). The creep parameters are identified by fitting the contact creep function with a logarithmic function, shown exemplary for sample P1-0.05 (b).

The creep parameters obtained by fitting the contact creep function with the logarithmic function according to Eq. (4.10) are shown in Table 4.9. The plain reference paste exhibits the largest creep modulus, which reveals that the rate of logarithmic creep is lower than that of the polymer-modified cement pastes is. Again, the cement pastes with a  $p/c$ -ratio of 0.20 exhibit the lowest contact creep moduli indicating a more pronounced creep activity. The characteristic time provides information about the creep kinetics. It characterizes the time at which creep starts exhibiting logarithmic kinetics. For the reference, the creep starts to exhibit logarithmic kinetics after a transient period of about four seconds, which is in accordance with results reported in the literature [166]. The characteristic times of the polymer-modified cement pastes are much larger, showing that logarithmic creep starts at later time instants. However, the identified quantities exhibit large scatter, which was also observed by Wei et al. [310]. The authors conducted nanoindentation creep tests on cement pastes and reported large stochastic deviations of up to 115% for the creep modulus and 84% for the characteristic time for different experimental repetitions. Albeit, the obtained values for  $C_i$  and  $\tau_i$  are indicators for the creep behavior of cement pastes, and first trends about the creep activity can be deduced from the nanoindentation creep tests.

Notably, Vandamme et al. [165] and Zhang et al. [166] showed that the results derived from the nanoindentation creep tests are proportional to creep properties determined with years-long macroscopic creep tests on concrete samples. Therefore, the nanoindentation creep tests provide valuable quantitative statements about the long-term creep kinetics

of concrete, without the need to perform long-lasting macroscopic creep tests. Different cement paste mixes can be categorized with respect to their creep behavior within a few minutes.

**Table 4.9:** Contact creep modulus  $C_i$  and characteristic time  $\tau_i$  obtained from nanoindentation tests on unmodified and polymer-modified cement pastes with  $w/c = 0.40$ .

Sample	Contact creep modulus [GPa]	Characteristic time [s]
Ref.	$218 \pm 66$	$3.8 \pm 0.8$
P1-0.05	$199 \pm 56$	$4.1 \pm 0.9$
P1-0.20	$60 \pm 20$	$12.6 \pm 2.1$
P2-0.05	$94 \pm 45$	$19.6 \pm 3.4$
P2-0.20	$41 \pm 23$	$23.4 \pm 5.7$
P3-0.05	$82 \pm 34$	$16.6 \pm 3.6$
P3-0.20	$32 \pm 12$	$22.5 \pm 6.2$

### 4.6.3 Mortars

#### 4.6.3.1 Fresh mortar properties

The measurement results characterizing the fresh mortars are summarized in Table 4.10. With increasing polymer-to-cement ratio, the slump of the mortars is higher, as it has also been observed for the cement pastes (see Section 4.6.2.3). Reasons are the entrapped air porosity and the polymer particles supporting the ball-bearing effect as well as the surfactants in the polymer dispersions.

The air void content of the fresh mixtures is increased due to the polymer modification, particularly for the mortars modified with polymer P3. The sample P2-0.20 shows the lowest air void content, which refers to its high slump. The low viscosity allows the fresh mortar to deaerate.

With the polymer modification, the fresh mortar density is lowered, depending on the  $p/c$ -ratio. This is a consequence of the low density of the polymers and the increased air void contents in the specimens.

**Table 4.10:** Properties of fresh plain and polymer-modified mortars with  $w/c = 0.40$ .

Sample	Slump [mm]	Air void content [Vol.-%]	Fresh mortar density [g cm <sup>-3</sup> ]
Ref.	115	3.6	2.27
P1-0.05	115	4.9	2.25
P1-0.20	140	6.0	2.18
P2-0.05	130	4.4	2.27
P2-0.20	210	1.8	2.19
P3-0.05	150	18.0	1.92
P3-0.20	180	25.0	1.73

#### 4.6.3.2 Hardened mortar properties

The compressive strength of the mortars decreases with an increasing dosage of polymer. The same trends can be observed for the static modulus and the dynamic modulus. The unmodified reference exhibits the largest moduli of all mortars after 2, 7, and 28 days. The lowest moduli exhibits sample P3-0.20, which is mainly the result of the high porosity, see Table 4.8, and the addition of soft butadiene. Reasons for the lower mechanical quantities are (i) the retarded cement hydration in comparison to conventional cementitious materials, (ii) the increased porosity, as inferred from the bulk density, and (iii) the low stiffness of the polymers. Flohr [76] also observed that the polymers form sliding planes in the microstructure that act as lubricants when the material is subjected to compressive loads.

**Table 4.11:** Properties of hardened plain and polymer-modified mortars with  $w/c = 0.40$ .

Sample	Time [d]	Bulk density [g cm <sup>-3</sup> ]	Compressive strength [N mm <sup>-2</sup> ]	Static modulus [N mm <sup>-2</sup> ]	Dynamic modulus [N mm <sup>-2</sup> ]
Ref.	2	2.24	53.8 ± 2.3	36,100 ± 400	43,100 ± 600
	7	2.24	65.7 ± 4.9	37,700 ± 700	45,700 ± 600
	28	2.24	72.1 ± 2.0	42,000 ± 900	47,800 ± 700
P1-0.05	2	2.18	51.3 ± 1.4	30,800 ± 800	39,200 ± 700
	7	2.19	65.4 ± 1.0	34,600 ± 400	41,800 ± 500
	28	2.18	67.8 ± 4.1	34,200 ± 800	43,900 ± 400
P1-0.20	2	2.11	37.6 ± 1.3	19,500 ± 1,000	28,500 ± 500
	7	2.10	50.3 ± 0.9	23,600 ± 500	31,600 ± 600
	28	2.09	59.7 ± 2.9	26,900 ± 400	33,300 ± 600
P2-0.05	2	2.17	54.2 ± 2.4	29,900 ± 300	38,200 ± 300
	7	2.17	60.1 ± 2.8	33,400 ± 200	40,900 ± 400
	28	2.15	73.1 ± 4.1	35,200 ± 400	42,900 ± 400
P2-0.20	2	2.20	44.8 ± 0.8	23,300 ± 600	31,700 ± 100
	7	2.18	57.7 ± 1.4	24,600 ± 300	34,300 ± 200
	28	2.11	63.9 ± 2.1	27,600 ± 400	36,100 ± 200
P3-0.05	2	1.86	18.0 ± 0.8	19,600 ± 800	27,800 ± 300
	7	1.87	31.0 ± 1.8	21,200 ± 800	29,400 ± 200
	28	1.84	37.4 ± 2.7	23,000 ± 200	30,800 ± 200
P3-0.20	2	1.72	11.0 ± 0.1	10,000 ± 500	13,800 ± 100
	7	1.76	19.8 ± 0.3	11,800 ± 200	15,100 ± 100
	28	1.67	29.2 ± 0.5	12,500 ± 300	16,100 ± 100

## 4.6.4 Concretes

### 4.6.4.1 Fresh concrete properties

The polymers also affect the properties of fresh concrete. The slump of the unmodified reference is very low and below the intended measurement range. The slumps of the concrete mixtures with polymers added are significantly higher. The increase of the slump due to the polymer modification is even more pronounced at the concrete scale than for the mortars. This is the result of the larger maximum particle size of the aggregates in concrete. The surface at which polymer particles can adsorb is reduced in comparison with the mortars and more polymer particles remain in the mixing water and boost the ball-bearing effect. The fresh concrete density of the PCC with high polymer contents is also reduced due to the low density of the polymers and the high air void contents. The air void content is particularly increased for the samples P1-0.20 and P3-0.20. The polymer modification does not affect the fresh concrete temperature.

**Table 4.12:** Properties of fresh unmodified and polymer-modified concretes with  $w/c = 0.40$ .

Sample	Slump [mm]	Air void content [Vol.-%]	Fresh concrete density [g cm <sup>-3</sup> ]	Fresh concrete temperature [°C]
Ref.	<340	2.3	2.37	22
P1-0.05	350	3.3	2.37	21
P1-0.20	410	6.0	2.26	20
P2-0.05	390	2.7	2.37	20
P2-0.20	500	2.8	2.30	21
P3-0.05	360	2.9	2.36	20
P3-0.20	480	13.0	2.07	20

### 4.6.4.2 Hardened concrete properties

On the scale of concrete, the same trends as for the cement pastes and the mortars are observed (see Table 4.13). With the polymer addition, the compressive strength, the static moduli, and the dynamic moduli are reduced in comparison with the reference. For the concretes, the influence of the polymers is lower than on the scales of mortar and cement paste because the type and amount of the aggregates, rather than the polymer admixtures, affect the elastic modulus of concrete [311]. Still, sample P3-0.20 exhibits the

#### 4.6. Results

lowest mechanical quantities of all mixtures, which coincides with the previously obtained results.

**Table 4.13:** Properties of hardened plain and polymer-modified concretes with  $w/c = 0.40$ .

Sample	Time [d]	Bulk density [g cm <sup>-3</sup> ]	Compressive strength [N mm <sup>-2</sup> ]	Static modulus [N mm <sup>-2</sup> ]	Dynamic modulus [N mm <sup>-2</sup> ]
Ref.	2	2.37	48.4 ± 1.6	34,800	41,100
	7	2.40	57.6 ± 4.2	37,600	43,500
	28	2.38	75.3 ± 2.1	38,400	45,400
P1-0.05	2	2.37	42.5 ± 0.4	31,900	39,300
	7	2.36	50.2 ± 2.1	33,400	41,700
	28	2.36	62.4 ± 2.7	33,900	43,800
P1-0.20	2	2.29	27.9 ± 0.3	23,300	34,100
	7	2.28	37.4 ± 0.3	24,700	35,800
	28	2.28	53.2 ± 1.3	27,800	37,800
P2-0.05	2	2.37	44.1 ± 1.2	31,900	39,500
	7	2.37	53.5 ± 2.1	36,700	41,400
	28	2.36	66.9 ± 0.5	38,000	42,500
P2-0.20	2	2.34	36.9 ± 1.5	23,600	36,700
	7	2.34	47.5 ± 0.4	26,600	38,600
	28	2.32	56.2 ± 1.3	30,300	40,600
P3-0.05	2	2.39	42.6 ± 0.1	35,600	41,600
	7	2.40	49.0 ± 0.7	35,600	42,100
	28	2.38	59.3 ± 1.3	39,000	44,500
P3-0.20	2	2.09	16.4 ± 0.8	12,000	24,800
	7	2.08	22.6 ± 0.4	15,200	25,800
	28	2.08	32.7 ± 0.9	16,700	28,600

## 4.7 Summary

An experimental multiscale study with polymer-modified cement pastes, mortars, and concretes was conducted. The water-to-cement ratio was kept constant for all mixes to ensure comparability. Three different polymers were used for the modification: one redispersible powder (P1) and two dispersions (P2 and P3) with varying chemical compositions. Two polymer-to-cement ratios were considered. On each scale, a plain reference mix was investigated as well.

The polymer modification improves the workability of cement-based materials. With increasing polymer content, the slump of the fresh mixtures is increased. The lower viscosity is caused by the interaction between the polymers, their additives, and the cementitious constituents, which could introduce entrapped air during the mixing process. The ball-bearing effect of the air voids and the polymer particles eventually improves the workability of the mixes. Particularly, the polymers P2 and P3 influence the consistency considerably, which might be related to the smaller particle sizes of the polymers in the dispersions compared with the powder.

The determination of the compressive strengths and the elastic moduli across the scales reveals the following observations. At a given time, the unmodified mixes exhibit the largest strength and stiffness. The polymer modification leads to reduced compressive strengths and elastic moduli. The more polymers are added, the lower are those mechanical quantities. On the one hand, this is related to the retarded hydration process in polymer-modified cement-based materials. With increasing polymer content, the hydration reaction between clinker and water is slowed down, and lower degrees of hydration are measured in comparison with the plain reference. On the other hand, polymer-modified cement-based materials exhibit a higher porosity, which also decreases the strength and stiffness. One further reason is the low stiffness of the polymers, as it was quantified by means of nanoindentation tests.

The results obtained by means of macroscopic mechanical (standard) tests are confirmed by nanoindentation investigations. Both, the micromechanical elastic and creep properties of the cement pastes were determined experimentally. The comparison between the results obtained on the microscopic and the macroscopic scales reveals that the influences of the polymers on the elastic moduli and on the deformation behavior can be estimated by means of nanoindentation tests. By way of example, the reference mix exhibits the highest elastic modulus, independent of the experimental length scale at which it is determined. The specimens modified with a  $p/c$ -ratio of 0.05 show lower indentation moduli and macroscopic elastic moduli. The elastic moduli of the cement pastes, mortars,

and concretes modified with the polymers P1 and P2 are similar, whereas the moduli of the mixtures modified with polymer P3 are slightly lower. This is related to the chemical composition of P3, which contains soft butadiene. Furthermore, the mixes with P3 exhibit high amounts of entrapped air, caused by interaction processes between the polymer, its additives, and cementitious constituents during mixing. Similar relations hold between the nanoindentation creep tests and shrinkage measurements on macroscopic cement paste specimens. Both experiments reveal that the polymer-modified cement pastes exhibit a more pronounced deformation behavior than the plain paste. With increasing  $p/c$ -ratio, larger deformations are measured.

Cement-based materials containing the polymer P2 exhibit slightly larger compressive strengths and elastic moduli compared with cement pastes, mortars, and concretes modified with polymer P1. Notably, both polymers P1 and P2 consist of styrene acrylate copolymers. On the contrary, the pastes with polymer P2 exhibit larger deformations than the pastes with P1 do. Specimens modified with polymer P3 exhibit lower strengths and moduli, which refers to the increased air void content compared with the other mixtures and the low stiffness of polymer P3 consisting of styrene butadiene.



# 5 | Experimental characterization and semi-analytical modeling of polymer-modified cement pastes and concretes at early ages

The increasing use of polymer-modified cement-based materials in construction requires not only information about the long-term behavior of the material, but also about the early-age properties. Remarkably, building materials only exhibit a satisfactory long-term durability, if they are not damaged at early ages. Effects of early loading on young concrete as well as the resulting creep strains are significant for the design of structures [200, 201]. Thus, research regarding the early-age behavior of cement-based materials is of fundamental importance.

In the following, the elastic and viscoelastic properties of polymer-modified cement pastes and concretes are investigated. Both experimental and computational approaches have been applied, as they have proven to be successful in the context of conventional cement-based materials. The experimental campaign, which was carried out at the Institute for Mechanics of Materials and Structures at the Technical University of Vienna, and the corresponding results are presented (Sections 5.1 and 5.2). In Section 5.3, the experimental database is exploited in form of multiscale modeling based on continuum micromechanics. The focus is on the prediction of the elastic stiffness as well as of the creep strains.

## 5.1 Experimental campaign

As regards the experimental characterization of the early-age evolutions of the elastic stiffness and the creep properties of conventional cement-based materials, novel short-term creep tests were developed recently, see Section 2.3.3. They include regularly-

repeated sequences of loading and unloading steps with a duration of a few minutes only. During such short periods, the hydration reaction between the cement clinker and water does not progress significantly. Irfan-ul-Hassan et al. [207] developed a creep testing protocol, which is applied to polymer-modified cement pastes and concretes in the following. Karte et al. [312] reported on a preliminary test setup for characterizing the early-age stiffness evolution of cement pastes.

### 5.1.1 Mixture design

Three different mixtures of cement pastes and concretes were investigated, among them one reference mix without polymers and two different polymer-modified mixes. For all of them, the initial  $w/c$ -ratio was set constant at 0.40. The specimens were produced with Portland cement (CEM I 42.5 N, Austria, see Section 4.1.1), distilled water, and where required polymers. The concretes additionally contained oven-dried aggregates (“Pannonia Kies”, Austria) consisting of quartz gravel with a maximum diameter of 8 mm. The initial aggregate-to-cement mass ratio was 3.0. The polymer-modified cement pastes and concretes were prepared with the polymers P2 and P3 because they induce larger strains than polymer P1. For the early-age testing, the  $p/c$ -ratio was restricted to 0.10 (and not to 0.20, as in Section 4) to ensure a sufficiently large stiffness and to avoid damage in the specimens, which were subjected to loads since very early ages. For the sake of convenience, the cement pastes and concretes are solely denominated as ‘P2’ and ‘P3’ in the following.

The investigations allow for an improved estimation of the influences of the polymers on the behavior of cement-based materials. The comprehensive mechanical characterization of the polymers at early ages is fundamental for the development of a multiscale model for polymer-modified cement-based materials, which is described in Section 5.3.

### 5.1.2 Quasi-isothermal differential calorimetry

Quasi-isothermal differential calorimetry is used for quantifying the temporal evolution of the hydration degree. This way, a specific value of the hydration degree can be assigned to each microstructure tested during the sequential short-term creep tests. The hydration kinetics of the cement pastes were investigated using a quasi-isothermal calorimeter (ToniCAL Trio 7339, Toni Technik GmbH, Germany), which was employed to monitor the heat evolution during the first eight days after production at a temperature of 20 °C. For each measurement, a test tube was filled with 10 g of cement. The liquids (water and, if required, polymer dispersion) were injected via a syringe and thoroughly mixed with the solid binder after sealing the calorimeter and waiting for stationary conditions.

From the measurements, the evolution of the degree of hydration  $\xi$  is derived as the ratio of the accumulated specific heat release  $Q(t)$  at a certain time  $t$  and the latent heat of Portland cement, which amounts to 500 J/g:

$$\xi = \frac{Q(t)}{500\text{J/g}}. \quad (5.1)$$

The results confirm the observations reported in Section 4.6.2.1. The polymers slow down the hydration reaction between clinker particles and water, see Figure 5.1 (a). This is particularly clearly visible during the acceleration period in which the heat rates of the polymer-modified cement pastes are slightly reduced compared with the reference. Furthermore, the heat quantities of the polymer-modified cement pastes are lowered in comparison with the unmodified cement paste. This entails a reduced hydration degree at given time instants, see Figure 5.1 (b). After a time period of 190 hours, the accumulated heat release of the reference paste amounts to 310 J g<sup>-1</sup>, while 270 J g<sup>-1</sup> were measured for the polymer-modified pastes. The hydration degrees of the cement pastes P2 and P3 are by 15 % lower than that of the reference. Differences concerning the hydration degrees of the two different polymer-modified cement pastes are insignificant.

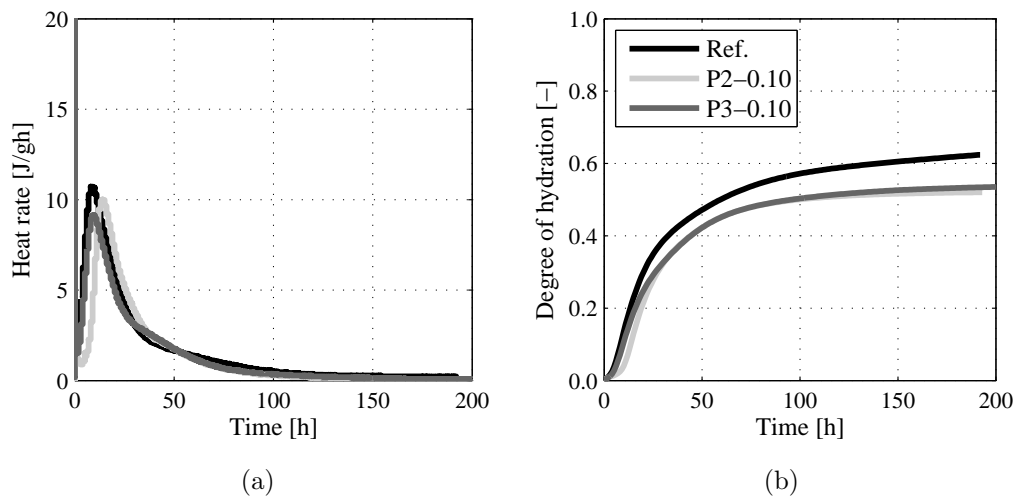


**Figure 5.1:** Time-dependent evolution of the heat rate (a) and the degree of hydration (b) for an unmodified cement paste with  $w/c = 0.40$  and for polymer-modified cement pastes with  $w/c = 0.40$  and  $p/c = 0.10$ , derived from quasi-isothermal calorimetry measurements.

### 5.1.3 Experimental setup of the short-term creep tests

The production, storage, and preparation of the specimens followed the protocol reported in [207]. For the creep tests, cylindrical specimens with a diameter of 70 mm and a height of 300 mm were used. After production, the sealed specimens were stored in a temperature controlled chamber at 20 °C. At an age of 20 h, the specimens were demolded and the end faces were flattened [313]. To avoid water evaporation, the specimens were wrapped with several layers of food preservation foil after demolding.

The whole test setup comprising the specimen and the measurement equipment was placed inside a temperature controlled chamber at constant temperature of 20 °C throughout the entire testing period, see Figure 5.2 (a). For the creep tests, a universal testing machine of type Zwick Roell Z050 (Ulm, Germany) was used. A central and homogeneous load introduction through uniform uniaxial tractions was achieved via two metal cylinders including bottlenecks attached at the two end faces of the specimen, see Figure 5.2 (b). With the chosen test arrangement, shear-free stress states in the central measurement zone were achieved [312]. Undesired shear stresses might result from friction in the interfaces between specimen and metal cylinders.

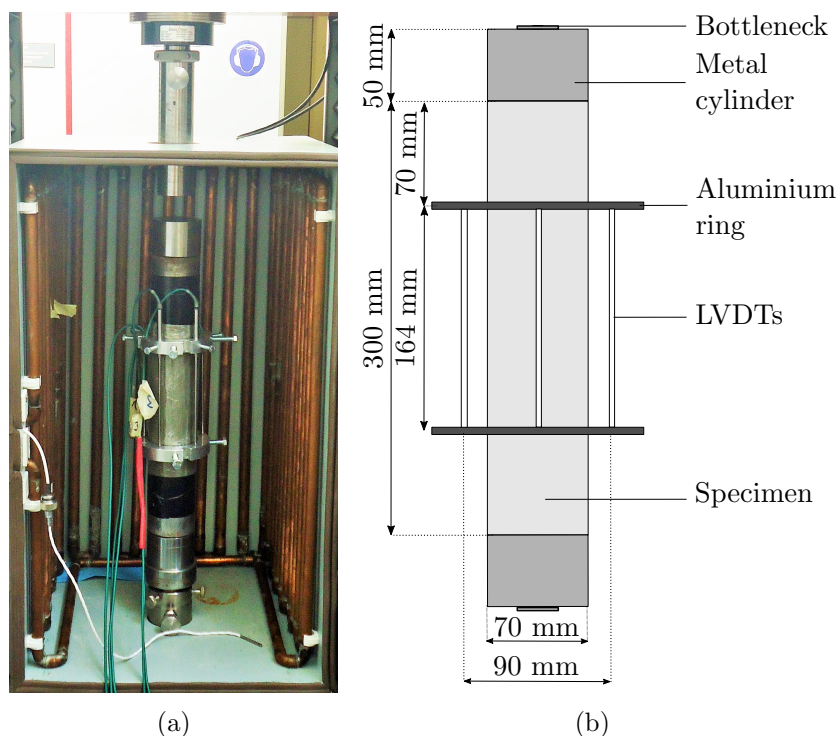


**Figure 5.2:** The experimental setup of the short-term creep tests: the whole test setup inside a climate chamber (a) and schematic representation, including the specimen, metal cylinders with bottlenecks, and the LVDTs (b).

Five linear variable differential transducers (LVDTs) of type Solartron were used for quantifying the deformations in the central regions of the specimens. The evenly distributed LVDTs were fixed between two aluminium rings, which were screwed on the specimen in a distance of 164 mm. Before the first load application, the correct position of the specimen was checked and eccentricity was eliminated. As for the further analyses, the average of the five LVDT readings was taken.

#### 5.1.4 Test regime

The creep testing protocol comprised quasi-instantaneous compressive loading and unloading steps. Once per hour, a compressive load was applied to the specimen for a duration of three minutes. Between two subsequent creep tests, the specimen was subjected to a permanent compressive force of 0.2 kN to avoid a shift of the whole test setup. Creep strains resulting from this small loading are negligible [207]. The test was performed under force control. The specimens were loaded with a force rate amounting to  $7.697 \text{ kN s}^{-1}$  and unloaded with a force rate of  $3.849 \text{ kN s}^{-1}$ , which refer to specimen-related stress rates of  $2 \text{ MPa s}^{-1}$  and  $1 \text{ MPa s}^{-1}$  respectively.

The load levels had to be selected carefully to avoid possible damage of the samples. In order to stay within the elastic limit of the materials, e.g. [314, 315], load levels being smaller or equal to 15 % of the expected compressive strength at the time of testing were employed [207]. The strength evolution of the reference mixes was obtained by combining (i) the temporal evolution of the hydration degree derived from quasi-isothermal calorimetry, see Figure 5.1 (b), with (ii) a validated multiscale model for the compressive strength of hydrating cement pastes, see [107, 316] for modeling details. Afterward, computed strength values were multiplied by 15 % and by the cross-sectional area of the specimens, see Figure 5.3 (a) for the age-dependent loading plateaus. During the weekend and over night, the load levels remained constant and were not updated due to safety reasons.

The polymer-modified specimens are expected to exhibit lower compressive strengths than unmodified cement pastes and concretes [2, 90], see Section 2.1.4. In particular, their compressive strength was estimated to amount to only 50 % of the strength of their unmodified analogue at the same hydration degree. Based on the hydration degrees of the polymer-modified cement pastes obtained from calorimetry testing, the compressive strengths were computed using the multiscale model [107, 316]. These values were multiplied by 7.5 % and by the cross-sectional area to obtain the loads, see Figures 5.3 (b) and (c). However, the results obtained for both plain and polymer-modified cement pastes are comparable because the load levels stay within the elastic limit of the material.

In total, 168 hourly repeated three-minutes-long uniaxial compressive creep tests were carried out on each specimen, spanning material ages from 21 hours to approximately eight days. With that, the time-dependent deformations under load are separated from the microstructural evolution due to the hydration process. The duration of each individual creep test is so short that the microstructure remains in very good approximation unaltered during every single creep test. In contrast, subsequent creep tests refer to different microstructures, implying that the tested materials are less than eight days old. [207]

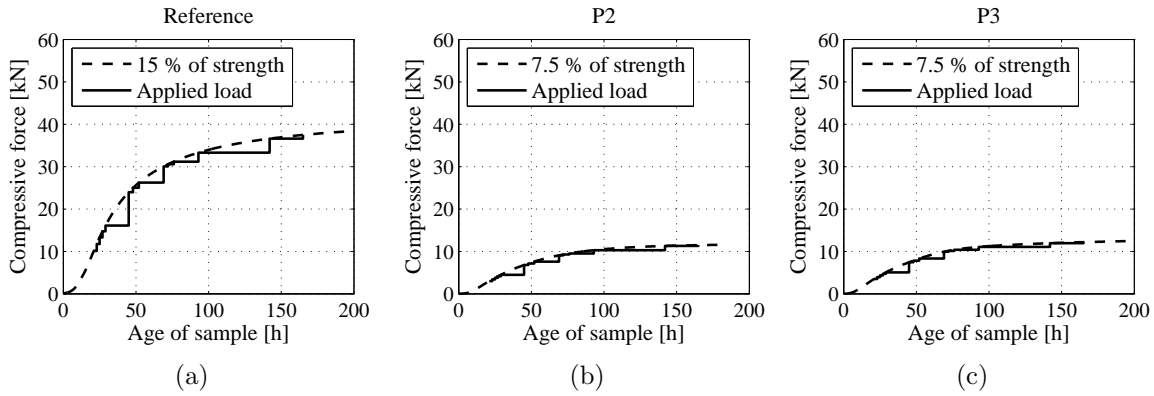


**Figure 5.3:** Loading regimes defined for the creep tests on unmodified (a) and polymer-modified cement pastes and concretes containing polymer P2 (b) and polymer P3 (c).

### 5.1.5 Test evaluation

From each individual creep test, the elastic and creep properties can be identified quasi-continuously, following the test evaluation that Irfan-ul-Hassan et al. [207] proposed. The strain evolution is quantified based on the LVDT readings as follows

$$\varepsilon_{\text{total}}(t) = \frac{1}{5\ell_0} \sum_{i=1}^5 \Delta\ell_i(t) \quad (5.2)$$

with  $\ell_0$  measurement length amounting to 164 mm  
 $\ell_i$  readings of the  $i$ -th LVDT.

The stress evolution is obtained as

$$\sigma(t) = \frac{F(t)}{A} \quad (5.3)$$

with  $F$  applied compressive force  
 $A$  cross-sectional area of the specimens,  $A = 3848.5 \text{ mm}^2$ .

Point-wisely defined stress-strain diagrams provide access to the unloading modulus  $E_u$ , which is derived from the unloading path [312]. The unloading modulus serves as a first estimate for the Young's modulus  $E$ . The creep strains,  $\varepsilon_{\text{creep}}$ , are derived as the difference between the total strains,  $\varepsilon_{\text{total}}$ , measured by the LVDT, and the instantaneous elastic strains,  $\varepsilon_{\text{elastic}}$ , as follows:

$$\varepsilon_{\text{creep}}^{\text{exp}}(t) = \varepsilon_{\text{total}}^{\text{exp}}(t) - \varepsilon_{\text{elastic}}^{\text{exp}}(t) = \varepsilon_{\text{total}}^{\text{exp}}(t) - \frac{\sigma(t)}{E}. \quad (5.4)$$

Based on the assumption that the Young's modulus would be equal to the unloading modulus as  $E = E_u$ , Eq. (5.4) yields a creep strain evolution that exhibits a so-called tensile undershooting [207], see Fig. 5.4 (a). At the beginning of the loading process, "nonphysical" tensile creep strains are observed, indicating that the unloading modulus is not a satisfactory estimate for the Young's modulus and that the latter is still underestimated. This also illustrates that significant creep strains develop already during the loading phase of each early-age creep test. An improved estimate of  $E$  is sought, which is obtained by progressively increasing its values in Eq. (5.4) until the tensile undershooting disappears. Then, the creep strains are compressive throughout the whole test, see Figure 5.4 (b). With this procedure, the Young's modulus reaches values that are approximately 3 % to 4 % higher than the unloading modulus. The Young's modulus derived from the ultra-short non-aging creep test agrees remarkably well with dynamic elastic moduli of the same cement pastes (having identical composition in terms of the mixture design and the raw materials) as measured by means of ultrasonic experiments [207].

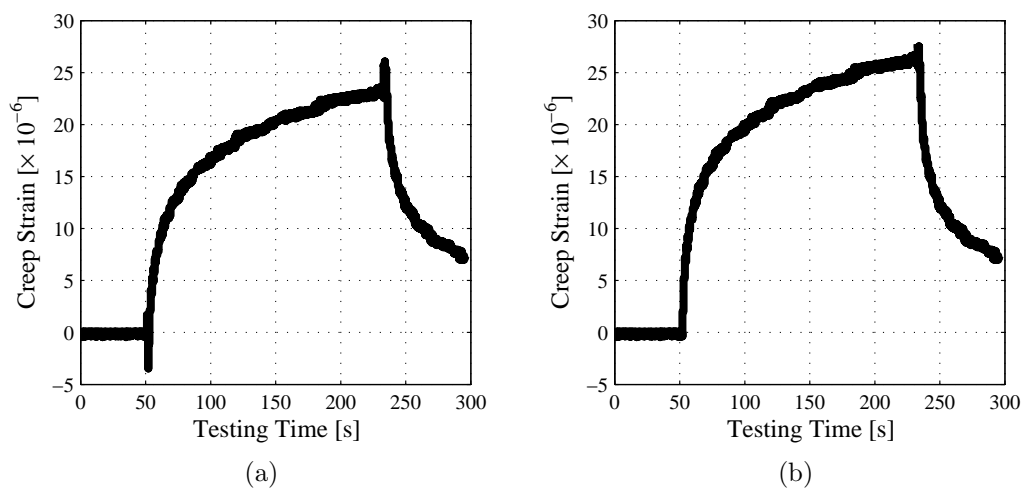


**Figure 5.4:** Creep strain evolution according to Eq. (5.4) for polymer-modified cement paste (P2) with  $w/c=0.40$  and  $p/c=0.10$  at an age of 100 hours under a load of 10.66 kN before (a) and after (b) adapting the Young's modulus.

The short-term creep tests also allow for a quasi-continuous quantification of the creep modulus  $E_c$  and the power-law exponent  $\beta$ . The quantities are derived using a power-law type creep function which was proposed by Tamtsia and Beaudoin [317]. Accordingly, the creep compliance rate is defined as

$$\frac{dJ(t)}{dt} = C \left( \frac{t - \tau}{t_{\text{ref}}} \right)^\gamma \quad (5.5)$$

with  $t_{\text{ref}}$  reference time amount to 1 d = 86,400 s  
 $\tau$  time instant of sudden loading  
 $C$  creep compliance rate at time  $t = \tau + t_{\text{ref}}$   
 $\gamma$  dimensionless power-law exponent.

The solution of Eq. (5.5) for sudden loading at time instant  $\tau$  up to stress level  $\sigma_0$  reads as [207]

$$\varepsilon_{\text{total}}^{\text{model}}(t) = \frac{\sigma_0}{E} + \frac{\sigma_0}{E_c} \left( \frac{t - \tau}{t_{\text{ref}}} \right)^\beta \quad t \geq \tau \quad (5.6)$$

with  $\sigma_0/E$  elastic answer of material at time  $\tau$   
 $E_c$  creep modulus at time  $t = \tau + t_{\text{ref}}$ ;  $E_c = (\gamma + 1)/(Ct_{\text{ref}})$   
 $\beta$  dimensionless power-law exponent;  $\beta = \gamma + 1$ .

Determining the strains with Eq. (5.6) requires the knowledge of two quantities, namely the creep modulus and the power-law exponent. For their identification, it is considered that creep strains develop already during the loading phase. To this end, the creep strain evolution is computed by means of the superposition principle according to Boltzmann [213], at which the stress history is subdivided into  $n$  consecutive small loading steps as

$$\varepsilon_{\text{creep}}^{\text{model}}(t) = \sum_{i=1}^n \left[ \sigma(t_i) - \sigma(t_{i-1}) \right] \frac{1}{E_c} \left( \frac{t - t_i}{t_{\text{ref}}} \right)^\beta. \quad (5.7)$$

$E_c$  and  $\beta$  are identified simultaneously for every single creep test by minimizing the root of the sum of squared errors between the experimental and the modeled creep strain evolutions as follows

$$\mathcal{E}_{\text{error}}(E_c, \beta) = \sqrt{\frac{1}{N} \sum_{i=1}^N \left[ \varepsilon_{\text{creep}}^{\text{exp}}(t_i) - \varepsilon_{\text{creep}}^{\text{model}}(t_i) \right]^2} \rightarrow \min. \quad (5.8)$$

$N$  is the number of measurement readings that are used for the test evaluation, including the loading and the holding phase. Due to the computational costs, only every fifth measurement reading is considered. Eq. (5.8) yields an optimization problem that is solved iteratively according to the procedure described in [207].



## 5.2 Experimental results

### 5.2.1 Evolution of the elastic properties

The Young's modulus of cement-based materials increases monotonously with the material age due to the ongoing hydration process, see Figure 5.5 (a). In comparison with the reference, the polymer-modified cement pastes exhibit a lower Young's modulus. At 150 hours after production of the specimens, it is about 30 to 40 % lower than the Young's modulus of the plain paste. The stiffness of the cement paste modified with P2 is larger than that of the specimen made with P3, as it is also reported in Section 4.

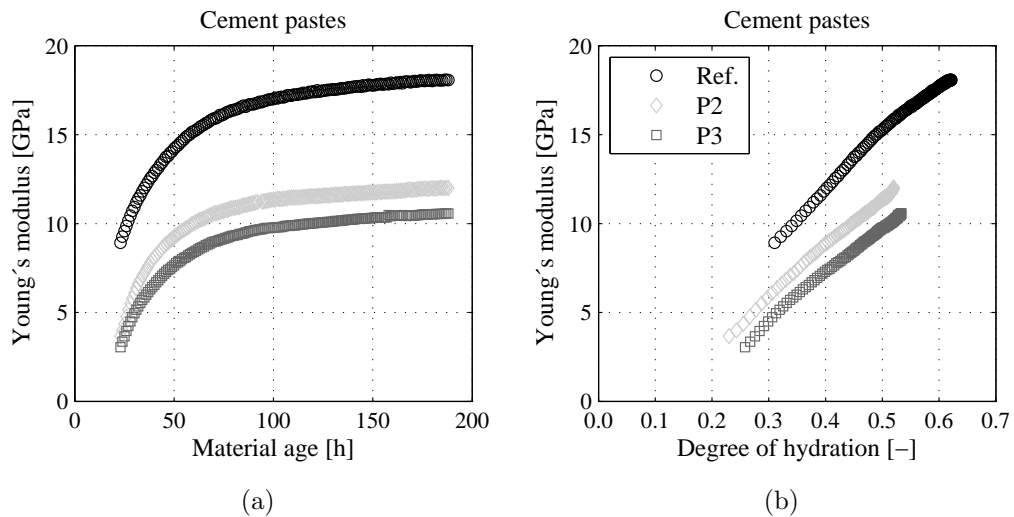


**Figure 5.5:** Evolutions of the Young's moduli of the plain cement paste with  $w/c = 0.40$  and of the two polymer-modified cement pastes P2 and P3 with  $w/c = 0.40$  and  $p/c = 0.10$  as functions of the material age (a) and the degree of hydration (b).

The evolution the Young's modulus of cement pastes is in very good approximation linear with respect to the degree of hydration, see Figure 5.5 (b). For a specific degree of hydration, the Young's modulus of the polymer-modified cement pastes is smaller than that of the reference is. This implies that the delayed hydration reaction is not the only reason for the lower stiffness of the polymer-modified cement pastes. Rather, the polymers themselves result in reduced elastic moduli of the pastes due to their low stiffness, see Section 4.6.1. The chemical basis of the polymers also plays an important role. The Young's modulus of cement pastes modified with polymer P2 is larger than that of cement pastes with P3 is, although both cement pastes contain the same polymer quantity. First, this is related to the lower stiffness of polymer P3, which contains soft butadiene, compared to P2 consisting of a styrene-acrylate copolymer, see Section 4.6.1. Second, the differences

between the stiffness evolutions might be explained by entrapped air, which could have been introduced during the mixing process, e.g. [69]. In order to estimate the volume fraction of entrapped air, the macroscopic bulk densities of the specimens were determined experimentally, directly after demolding. Also, the particle density was measured using the helium pycnometer AccuPyc 1330. Both the bulk density and the particle density provide access to the total porosity of the cement paste specimens, see Table 5.1. The difference between the bulk density of the reference paste and that of paste P2 can be explained by the addition of the polymer, which has a smaller density compared to the cementitious components. The difference between the bulk densities of pastes P2 and P3 indicates that air voids were entrapped into the latter. Paste P2 is assumed to contain no entrapped air. The volume fraction of the additional air voids in paste P3 is derived as the difference between the porosities of paste P2 and of paste P3 as 3.9 %, compare also Section 4.6.2.4.

**Table 5.1:** Bulk and particle density and porosity of the cement pastes.

<b>Specimen</b>	<b>Bulk density</b> [g cm <sup>-3</sup> ]	<b>Particle density</b> [g cm <sup>-3</sup> ]	<b>Porosity</b> [%]
Reference	1.99	2.21	9.9
P2	1.88	2.12	11.3
P3	1.79	2.11	15.2

For the concretes, the same trends can be observed, see Figure 5.6. The concrete without polymers exhibits the largest Young’s modulus, followed by the sample modified with P2. The concrete modified with polymer P3 shows a significantly lower Young’s modulus than the concrete P2 does. This indicates that the interactions between polymer P3 and the cementitious components or aggregates lead to higher air void contents than for polymer P2. The observation is confirmed by comparing the total porosities of the concrete specimens, see Table 5.2. The porosity of the concrete modified with P3 is considerably larger compared with the concretes P2 and P3. The volume fraction of the entrapped air of the latter paste is estimated as 9.8 %.

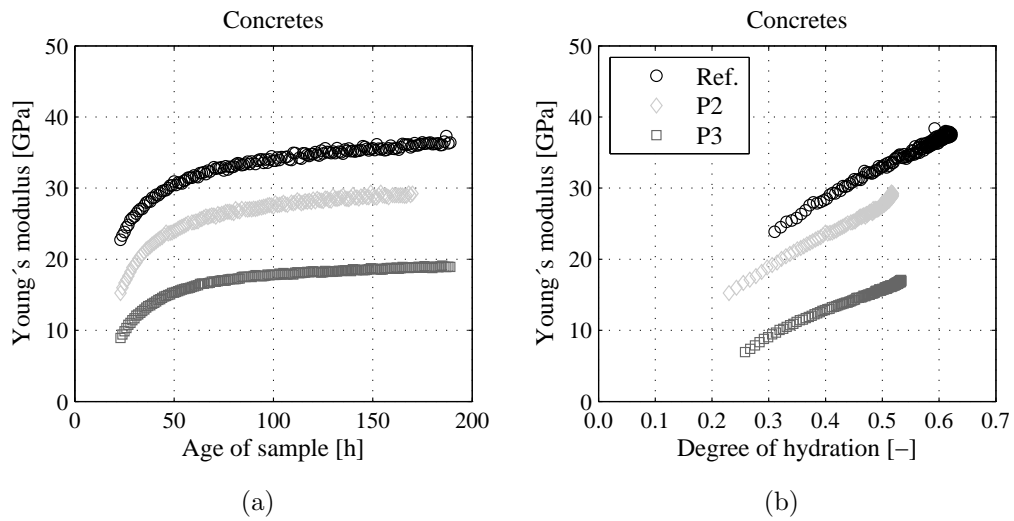


**Figure 5.6:** Evolutions of the Young's moduli of unmodified concrete with  $w/c = 0.40$  and of the two polymer-modified concretes with  $w/c = 0.40$  and  $p/c = 0.10$  as functions of the material age (a) and the degree of hydration (b).

**Table 5.2:** Bulk density, particle density, and total porosity of the concretes.

Concrete	Bulk density [g cm <sup>-3</sup> ]	Particle density [g cm <sup>-3</sup> ]	Porosity [%]
Reference	2.30	2.57	10.5
P2	2.21	2.52	12.3
P3	1.97	2.53	22.1

## 5.2.2 Evolution of the creep properties

The creep modulus is a measure for the creep activity of the material. A large creep modulus indicates a low creep rate. The creep compliance, which is the inverse of the creep modulus,  $1/E_c$ , decreases monotonously with increasing material age in cement pastes, see Figure 5.7. The decay of the creep compliance over the material age refers a progressively decreasing creep activity of the specimens, which is in accordance with the literature. There, it also has been reported that the creep rate of concrete subjected to a constant load decreases with the time in the range below the creep strength [318, 319].

The creep compliances of the polymer-modified cement pastes are larger than those of the reference paste, particularly at sample ages up to 75 hours. At later ages, the creep compliances of the pastes P2 and P3 decrease more rapidly than those of the reference

paste. Also, the creep compliance of paste P3 is larger than that of paste P2. This agrees with the already discussed differences concerning the elastic stiffness. These results illustrate the more pronounced creep activity of the polymer-modified cement pastes, which might be explained by (i) possible sliding effects of the polymers in the microstructure disconnecting the cementitious network, and (ii) by the increased stress concentration into cement hydrates resulting from the entrapped air.

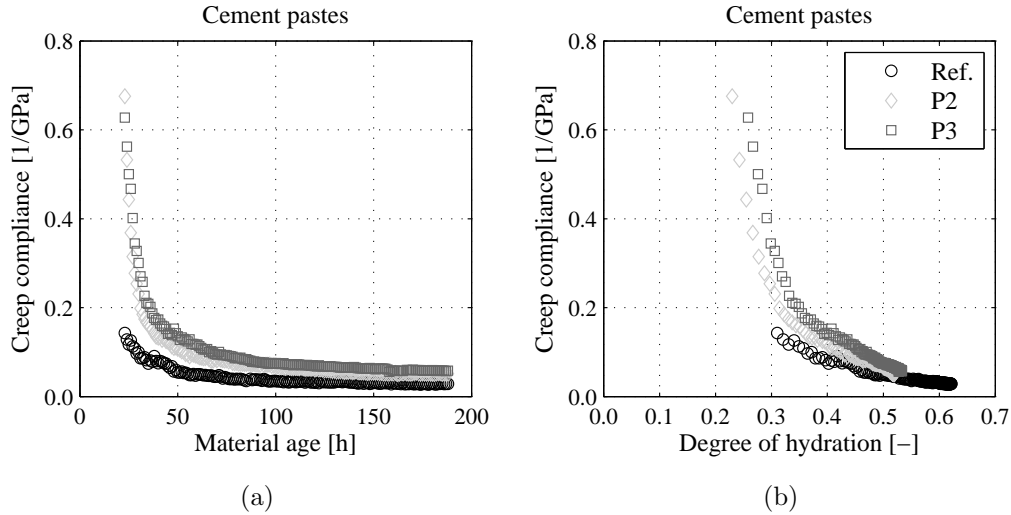


**Figure 5.7:** Evolutions of the creep compliances of unmodified cement paste with  $w/c = 0.40$  and of the two polymer-modified cement pastes with  $w/c = 0.40$  and  $p/c = 0.10$  as functions of the material age (a) and the degree of hydration (b).

The creep compliance that the concrete specimens exhibit is smaller than for the cement pastes due to the addition of non-creeping aggregates, see Figure 5.8. However, an increased creep activity due to the polymer modification is also illustrated. The concrete modified with polymer P3 exhibits the largest creep compliance.

The power-law exponent  $\beta$  decreases slightly and monotonously with increasing material age, see Figure 5.9 (a). No remarkable differences between the three cement pastes are visible, indicating that the power-law exponent is less sensitive to the mixture composition than the creep compliance and the Young's modulus are. Irfan-ul-Hassan et al. [207] also observed that  $\beta$  is virtually the same for cement pastes varying according to their  $w/c$ -ratio. For a material age of about 70 h, the power-law exponent is almost constant and reaches values around 0.25. The relation between the power-law exponent and the degree of hydration is almost linear, see Figure 5.9 (b).

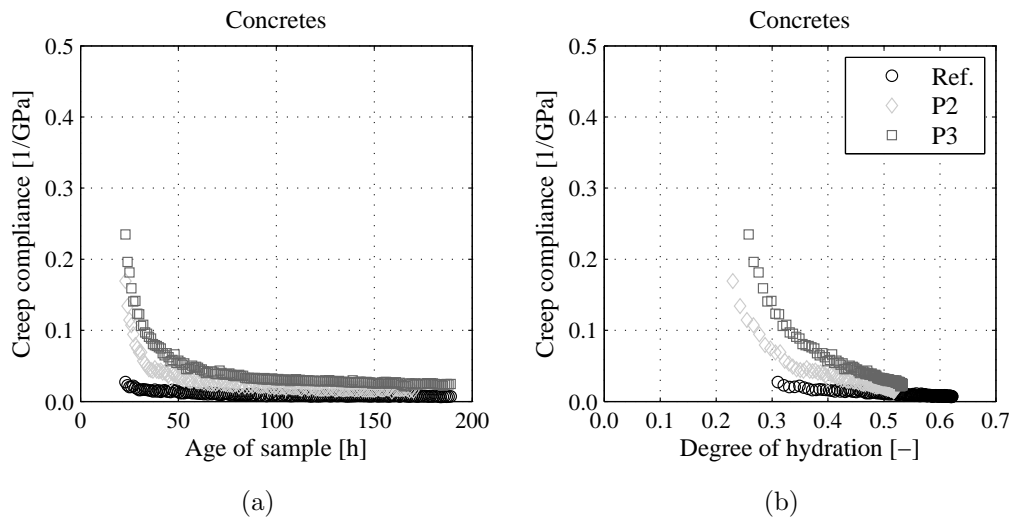


**Figure 5.8:** Evolutions of the creep compliances of unmodified concrete with  $w/c = 0.40$  and of the two polymer-modified concretes with  $w/c = 0.40$  and  $p/c = 0.10$  as functions of the material age (a) and the degree of hydration (b).

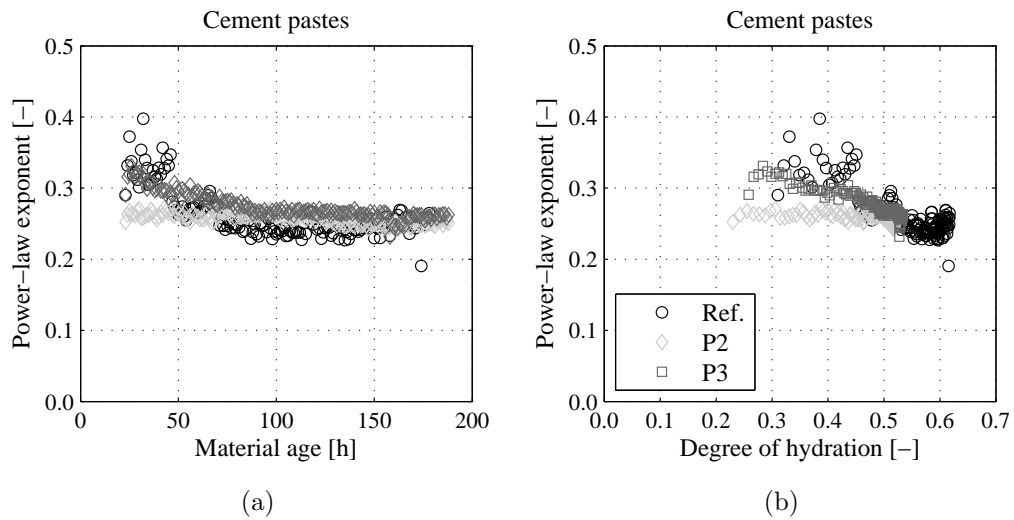


**Figure 5.9:** Evolutions of the power-law exponents of unmodified cement paste with  $w/c = 0.40$  and of the two polymer-modified cement pastes with  $w/c = 0.40$  and  $p/c = 0.10$  as functions of the material age (a) and the degree of hydration (b).

The power-law exponent obtained from creep tests on concrete specimens is within the same range as the power-law exponent obtained with cement pastes, see Figure 5.10. Again, no significant differences among the three concrete mixtures are observed.

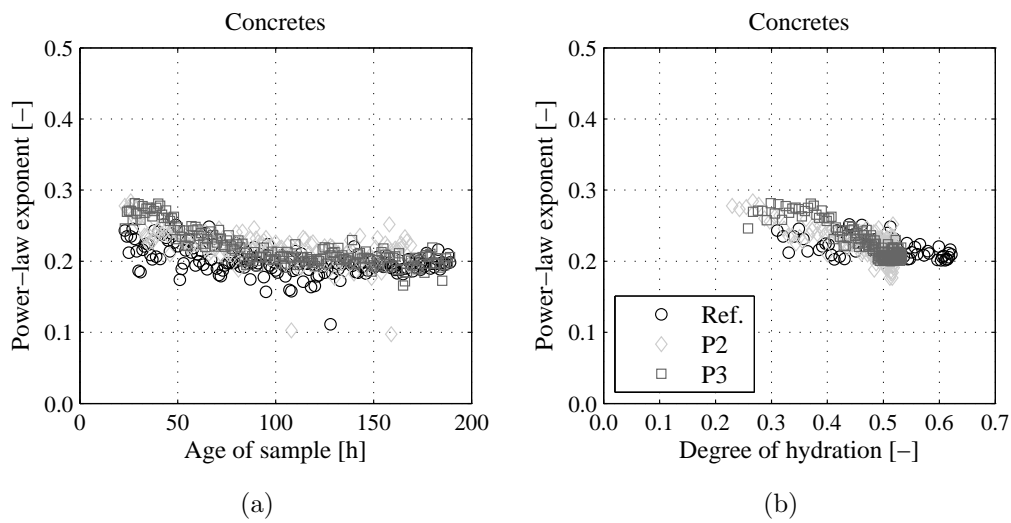


**Figure 5.10:** Evolutions of the power-law exponents of unmodified concrete with  $w/c = 0.40$  and of the two polymer-modified concretes with  $w/c = 0.40$  and  $p/c = 0.10$  as functions of the material age (a) and the degree of hydration (b).

### 5.2.3 Evolution of the creep strains

To evaluate the creep behavior of the cement pastes and concretes in more detail, the creep strains that the specimens exhibited during the creep tests are compared for specific time instants and for different hydration degrees. To this end, the experimentally determined creep strains evolutions are divided by the plateau stress, i.e. the stress subjected to the tested specimen during the holding phase. The experimental creep strain evolution is also compared with the modeled creep strains according to the power-law creep function prescribed in Eq. (5.7), underlining that the modeled creep strains allow for an almost perfect fit of the measurements.

The normalized creep strains of the three cement pastes at given material ages are shown in Figure 5.11 at material ages amounting to 30, 50, and 150 hours. Apparently, the polymer-modified cement pastes exhibit larger creep strains than the reference paste does. At a material age of 30 hours, the viscous creep strains of the polymer-modified cement pastes are approximately four times larger than the corresponding creep strains of the reference are. The differences between the creep strains in unmodified and polymer-modified cement pastes decline with increasing material age. Still, after 150 hours of hydration, the creep strains of the polymer-modified cement pastes are twice as large as the strains of the reference. For a given degree of hydration, the creep strains exhibited by the two polymer-modified cement pastes are almost similar to each other, see Figure 5.12.

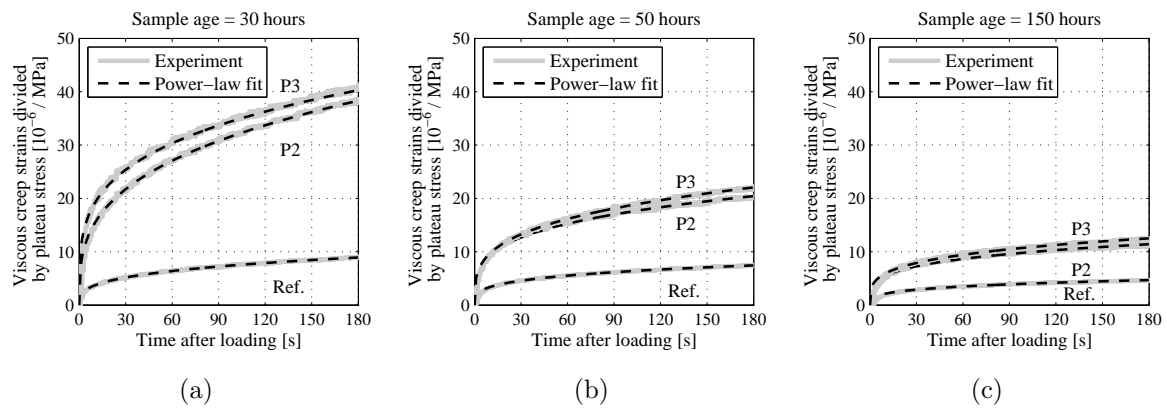


**Figure 5.11:** Experimentally determined creep strain evolutions and corresponding power-law fits at material ages of 30 hours (a), 50 hours (b), and 150 hours (c) for unmodified cement paste with  $w/c=0.40$  and two polymer-modified cement pastes with  $w/c=0.40$  and  $p/c=0.10$ .

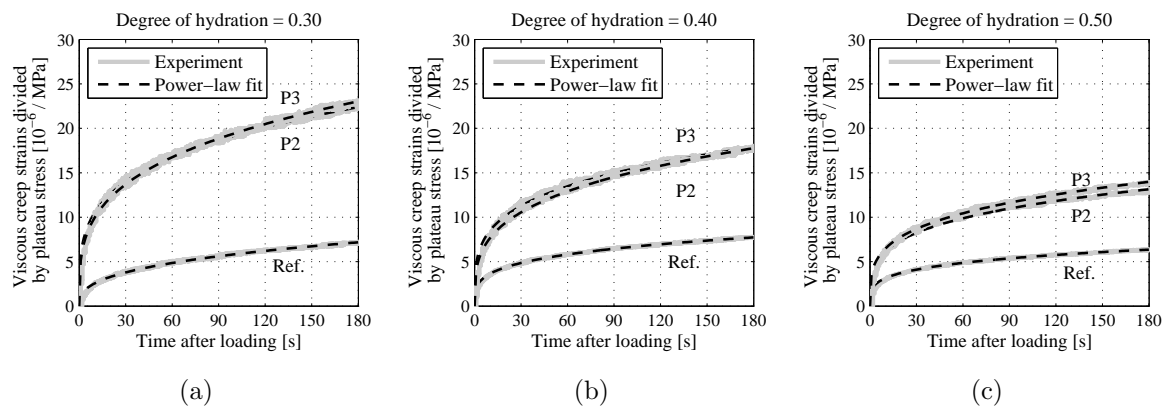


**Figure 5.12:** Experimentally determined creep strain evolutions and corresponding power-law fits at given hydration degrees amounting to 0.30 (a), 0.40 (b), and 0.50 (c) for unmodified cement paste with  $w/c=0.40$  and two polymer-modified cement pastes with  $p/c=0.10$ .

At the concrete scale, the differences between the two polymer-modified specimens are more pronounced, see Figures 5.13 and 5.14. For a given material age as well as for a specific hydration degree, the creep strains of concrete P3 are larger than those of concrete P2 are. This is related to the larger porosity in concrete P3 and the significantly lower stiffness of concrete P3 than of concrete P2. Furthermore, polymer P3 is more elasticising than polymer P2 is, and thus supports the formation of sliding planes within the hardened matrix more considerably. The differences between the strains of polymer-modified concretes and the reference mix are smaller compared with the results obtained at the cement paste scale. This is a consequence of the dominant role of the non-creeping aggregates [311].

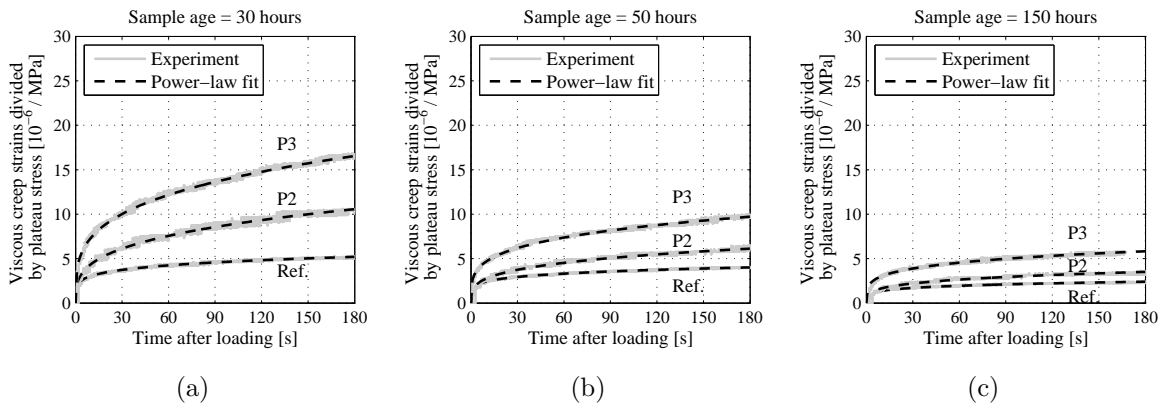


**Figure 5.13:** Experimentally determined temporal creep strain evolutions and corresponding power-law fits after 30 hours (a), 50 hours (b), and 150 hours (c) for unmodified concrete with  $w/c=0.40$  and two polymer-modified concretes with  $w/c=0.40$  and  $p/c=0.10$ .

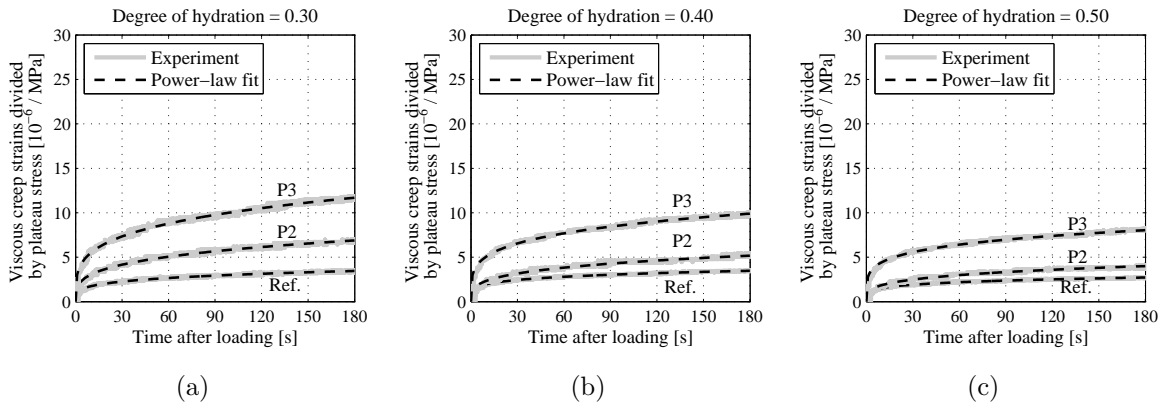


**Figure 5.14:** Experimentally determined creep strain evolutions and corresponding power-law fits at given hydration degrees amounting to 0.30 (a), 0.40 (b), and 0.50 (c) for plain concrete with  $w/c=0.40$  and two polymer-modified concretes with  $p/c=0.10$ .

### 5.2.4 Assumption of a constant power-law exponent

From a material age of about 70 hours on, the evolution of  $\beta$  becomes almost constant and reaches values around 0.25, see Figure 5.9. The introduction of a constant power-law exponent is further motivated by research results of Königsberger et al. [120]. The authors identified the power-law creep exponent of the hydrate needles by means of a top-down identification approach. It amounts to 0.25. Remarkably, when predicting the macroscopic creep properties of hydrating cement pastes, the micromechanics-based multiscale model suggests that the power-law exponent of cement paste is practically constant and equal to 0.25 [120].



Thus, it is tested whether or not the assumption of a constant power-law exponent amounting to 0.25 yields a similar evolution of the creep compliance as obtained by means of a varying power-law exponent, as described previously. To this end, the creep compliance is identified considering a constant  $\beta$  of 0.25 for the two polymer-modified cement pastes. The optimization problem according to Eq. (5.8) is re-written to include one variable only as follows

$$\mathcal{E}_{\text{error}}(E_c) = \sqrt{\frac{1}{N} \sum_{i=1}^N \left[ \varepsilon_{\text{creep}}^{\text{exp}}(t_i) - \varepsilon_{\text{creep}}^{\text{model}}(t_i) \right]^2} \rightarrow \min . \quad (5.9)$$

The evolutions of the creep compliances, obtained for the cement pastes P2 and P3 with the modified data evaluation strategy considering a constant power-law exponent of 0.25, are shown in Figure 5.15. They are only slightly smaller than the corresponding results referring to varying values of  $\beta$ . In addition, the residual values of the error functions in Eqs. (5.8) and (5.9) are very similar, underlining that the individual creep tests can be well approximated by means of a constant  $\beta$ . For the two polymer-modified cement pastes and both cases of the power-law exponent, the relative error amounts to approximately 1%, which is more or less equal to the measurement noise [207]. The introduction of a pre-defined constant value of the power-law exponent saves computational time for the evaluation of the creep properties.

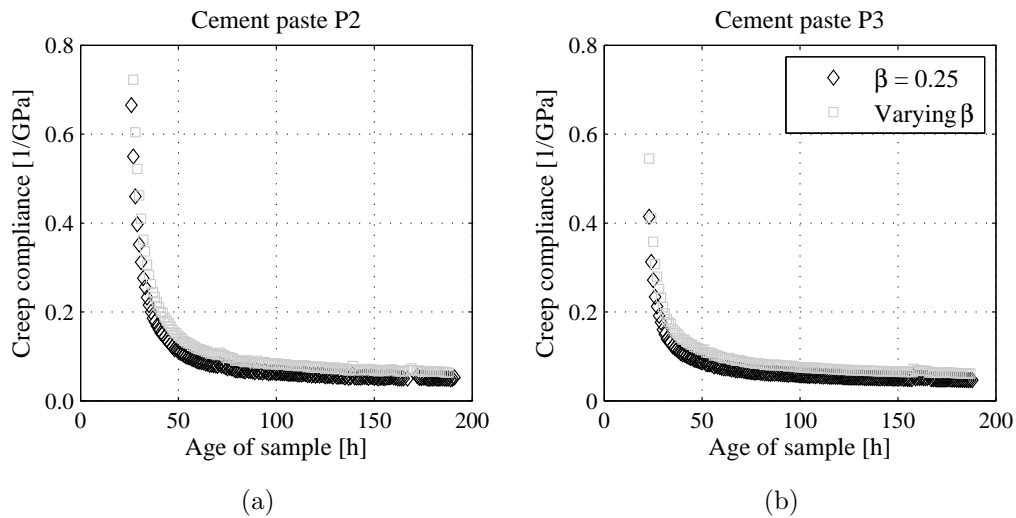


**Figure 5.15:** Creep compliances of the polymer-modified cement pastes P2 (a) and P3 (b) derived assuming both a constant and a varying power-law exponent over the material age.

## **5.3 Semi-analytical multiscale modeling of polymer-modified cement-based materials**

The elaborated experimental database motivates the exploitation in form of multiscale modeling. Multiscale models based on continuum micromechanics are promising approaches to predict the mechanical behavior of polymer-modified cement-based materials because these models incorporate microstructural specifics.

In the sequel, the micromechanical representation of polymer-modified cement-based materials is discussed. Furthermore, an existing multiscale model for the homogenization of the elastic stiffness and creep properties, which has been proven to be successful for the application to conventional cement-based materials, is extended towards the use for polymer-modified cement pastes, mortars, and concretes.

### **5.3.1 Micromechanical representation of polymer-modified cement-based materials**

As regards the multiscale modeling within the framework of continuum micromechanics, appropriate micromechanical representations of the materials are required. Herein, the state-of-the-art representation of conventional cement pastes [107], see Section 2.2.3.2, is extended towards polymer-modified cement-based materials, see Figure 5.16. A polymer phase is introduced at the same scale as the hydration products and the water- and air-filled capillary pores, i.e. at the hydrate foam scale, one scale below the RVE of cement paste. The polymers are modeled as spherical inclusions, which is motivated by ESEM investigations of the microstructure, see Sections 2.1.2.2 and 4.6.2.2, as well as by the spherical shape of the polymer particles in the dispersions and powders, see Figure 2.1. The introduction of the polymers at the hydrate foam scale is further corroborated by their small particle sizes, see Table 4.4.

At the scale of cement paste, entrapped air voids are additionally considered in order to account for the increased porosity resulting from interaction processes between the polymers, their technical additives, and the cementitious constituents, as discussed in Section 5.2.

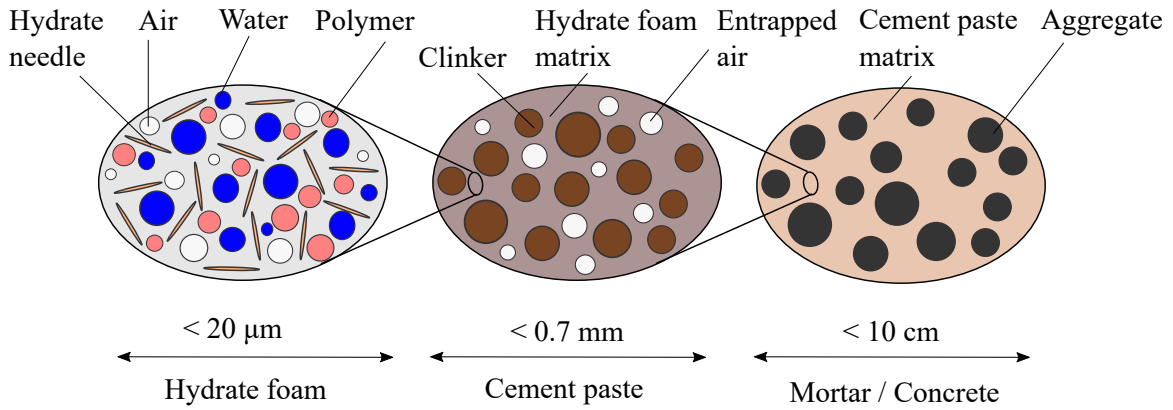


**Figure 5.16:** Micromechanical representation of polymer-modified cement-based materials, separating the scales of hydrate foam, cement paste, and mortar / concrete. The two-dimensional sketches refer to three-dimensional representative volume elements.

### 5.3.2 Model input parameters

Besides the micromechanical representation, two further categories of model input parameters need to be adapted for the multiscale modeling of polymer-modified cement-based materials: the phase volume fractions and the elastic parameters.

The evolving volume fractions of the material phases in cement pastes can be described by means of the Powers-Acker hydration model [283, 284], see Section 3.3.1. This hydration model needs to be extended to incorporate the polymer phase and the entrapped air porosity additionally. The phase volume fractions are functions of the mix design, expressed by means of the  $w/c$ -ratio and the  $p/c$ -ratio, as well as of the maturity state of the material, expressed by means of the hydration degree  $\xi$ . The hydration process in the presence of polymers has already been studied intensively, see Sections 2.1.2.1 and 4.6.2.1. The experimental results revealed that the polymers do not alter the nature of the hydration process, they rather change its kinetics, due to adsorption and complexation mechanisms. Therefore, hydration products consisting of both organic and inorganic components, as claimed by Beeldens et al. [56], are not considered in the following.

The volume fraction of the polymers is assumed to remain constant throughout the hydration reaction. The “cement paste”-related volume fraction of the polymer may be quantified based on the mix design as

$$f_{\text{pol}}^{\text{cp}} = \frac{V_{\text{pol}}}{V_{\text{clin}} + V_{\text{water}} + V_{\text{pol}}} = \frac{\frac{p}{\rho_p}}{\frac{c}{\rho_c} + \frac{w}{\rho_w} + \frac{p}{\rho_p}} = \frac{(p/c) \frac{\rho_w}{\rho_p}}{\frac{\rho_w}{\rho_c} + (w/c) + (p/c) \frac{\rho_w}{\rho_p}} \quad (5.10)$$

with  $c, w, p$  initial masses of cement, water, and the polymer  
 $\rho_c, \rho_w, \rho_p$  mass densities of cement, water, and the polymer.

The ‘‘cement paste’’-related volume fractions of the other four phases (clinker, water, hydrates, and air) may be adapted from Powers’ hydration model, reading as

$$\begin{aligned} f_{\text{clin}}^{\text{cp}} &= \frac{20(1 - \xi)}{20 + 63(w/c)} (1 - f_{\text{pol}}^{\text{cp}}) \geq 0, \\ f_{\text{water}}^{\text{cp}} &= \frac{63 [(w/c) - 0.42\xi]}{20 + 63(w/c)} (1 - f_{\text{pol}}^{\text{cp}}) \geq 0, \\ f_{\text{hyd}}^{\text{cp}} &= \frac{43.15\xi}{20 + 63(w/c)} (1 - f_{\text{pol}}^{\text{cp}}), \\ f_{\text{air}}^{\text{cp}} &= \frac{3.31\xi}{20 + 63(w/c)} (1 - f_{\text{pol}}^{\text{cp}}). \end{aligned} \tag{5.11}$$

The phase volume fractions at the hydrate foam scale follow as [107]

$$f_j^{\text{hf}} = \frac{f_j^{\text{cp}}}{1 - f_{\text{clin}}^{\text{cp}}}, \quad j \in \{\text{hyd, water, air, pol}\}. \tag{5.12}$$

Further extension of the Powers’ model accounts for the entrapped air voids, which have to be particularly considered for the cement pastes, mortars, and concretes modified with polymer P3. The entrapped air  $\Phi$  is introduced at the scale of cement paste, see Figure 5.16. Then, the ‘‘cement paste’’-related volume fractions of unhydrated clinker and of the hydrate foam are re-formulated, such that

$$f_{\text{clin}}^{\text{cp}} + f_{\text{hf}}^{\text{cp}} + \Phi = 1. \tag{5.13}$$

The adapted expressions for the unhydrated clinker  $f_{\text{clin}}^{\text{cp}}$  and the hydrate foam  $f_{\text{hf}}^{\text{cp}}$  read as

$$f_{\text{clin}}^{\text{cp}} = \frac{20(1 - \xi)}{20 + 63(w/c)} (1 - f_{\text{pol}}^{\text{cp}}) (1 - \Phi) \geq 0, \tag{5.14}$$

$$f_{\text{hf}}^{\text{cp}} = 1 - \Phi - f_{\text{clin}}^{\text{cp}}. \tag{5.15}$$

The evolutions of the ‘‘cement paste’’-related volume fractions as functions of the degree of hydration are shown in Figure 5.17, for both unmodified (a) and polymer-modified cement pastes, without (b) and with consideration of entrapped air (c).

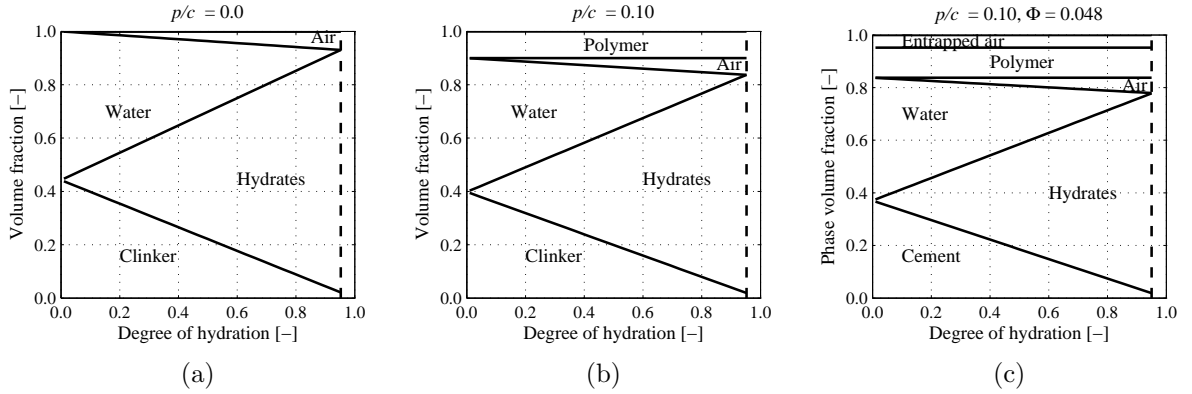


**Figure 5.17:** Evolution of the “cement paste”-related volume fractions for unmodified cement paste with  $w/c = 0.40$  (a) and for polymer-modified cement paste with  $w/c = 0.40$  and  $p/c = 0.10$  (b) and  $w/c = 0.40$ ,  $p/c = 0.10$ , and  $\Phi = 0.048$  (c), as functions of the degree of hydration.

The random microstructure of cement pastes allows for assigning a linear elastic, isotropic behavior to the material phases within the RVE depicted in Figure 5.16. The stiffness tensor  $\mathbb{C}_j$  of a material phase  $j$  can be expressed as:

$$\mathbb{C}_j = 3k_j\mathbb{I}^{\text{vol}} + 2\mu_j\mathbb{I}^{\text{dev}}. \quad (5.16)$$

The bulk moduli  $k_j$  and the shear moduli  $\mu_j$  characterize the intrinsic elastic properties of the material phases, see Table 5.3.  $\mathbb{I}^{\text{vol}}$  and  $\mathbb{I}^{\text{dev}}$  denote the volumetric and deviatoric parts of the fourth-order identity tensor  $\mathbb{I}$  with the components  $I_{rstu} = \frac{1}{2}(\delta_{rt}\delta_{su} + \delta_{ru}\delta_{st})$  and  $\mathbb{I}^{\text{dev}} = \mathbb{I} - \mathbb{I}^{\text{vol}}$  with  $\mathbb{I}^{\text{vol}} = \frac{1}{3}(\mathbf{1} \otimes \mathbf{1})$ .  $\mathbf{1}$  denotes the symmetric second-order identity tensor. The Kronecker delta  $\delta_{rs}$  has the components  $\delta_{rs} = 1$  for  $r = s$  and 0, otherwise.

The elastic constants of the cementitious constituents are intrinsic, and they are reported in the literature. For the polymers, the micromechanical elastic properties were determined by means of nanoindentation tests, see Section 4.6.1. Water is a fluid; therefore, its solid stiffness is equal to zero. The elastic properties of the aggregates might vary, according to the specific type. The bulk and shear moduli reported in Table 5.3 refer to aggregates consisting of quartz, following the recommendation of Irfan-ul-Hassan et al. [227]. For the early-age creep tests presented herein, the same type of aggregates as in the study by Irfan-ul-Hassan et al. was used.

**Table 5.3:** Elastic properties of the material phases in polymer-modified cement-based materials.

Phase	Bulk modulus $k$ [GPa]	Shear modulus $\mu$ [GPa]	Source
Air	$k_{\text{air}} = 0$	$\mu_{\text{air}} = 0$	
Water	$k_{\text{water}} = 0$	$\mu_{\text{water}} = 0$	
Hydrates	$k_{\text{hyd}} = 18.69$	$\mu_{\text{hyd}} = 11.76$	[107, 111, 120]
Clinker	$k_{\text{clin}} = 116.70$	$\mu_{\text{clin}} = 53.80$	[120, 149]
Aggregates	$k_{\text{agg}} = 37.80$	$\mu_{\text{agg}} = 44.30$	[320]
Polymer P1	$k_{\text{P1}} = 1.72$	$\mu_{\text{P1}} = 0.37$	see Section 4.2.1
Polymer P2	$k_{\text{P2}} = 1.02$	$\mu_{\text{P2}} = 0.22$	see Section 4.2.1
Polymer P3	$k_{\text{P3}} = 0.92$	$\mu_{\text{P3}} = 0.20$	see Section 4.2.1

### 5.3.3 Homogenization of isotropic elastic stiffness properties of polymer-modified cement pastes

The homogenization and upscaling of the elastic stiffness properties from the hydrate foam scale up to the cement paste scale is performed adapting Eqs. (2.18) and (2.19). Then, the homogenized stiffness of the hydrate foam reads as [107]

$$\begin{aligned}
 \mathbb{C}_{hf}^{\text{hom}} = & \left\{ \sum_j f_j^{hf} \mathbb{C}_j : \left[ \mathbb{I} + \mathbb{P}_{\text{sph}}^{hf} : (\mathbb{C}_j - \mathbb{C}_{hf}^{\text{hom}}) \right]^{-1} + f_{\text{hyd}}^{hf} \mathbb{C}_{\text{hyd}} \right. \\
 & : \int_0^{2\pi} \int_0^\pi \left[ \mathbb{I} + \mathbb{P}_{\text{cyl}}^{hf}(\varphi, \vartheta) : (\mathbb{C}_{\text{hyd}} - \mathbb{C}_{hf}^{\text{hom}}) \right]^{-1} \frac{\sin\vartheta d\vartheta d\varphi}{4\pi} \left. \right\} \\
 & : \left\{ \sum_j f_j^{hf} : \left[ \mathbb{I} + \mathbb{P}_{\text{sph}}^{hf} : (\mathbb{C}_j - \mathbb{C}_{hf}^{\text{hom}}) \right]^{-1} + f_{\text{hyd}}^{hf} \right. \\
 & : \int_0^{2\pi} \int_0^\pi \left[ \mathbb{I} + \mathbb{P}_{\text{cyl}}^{hf}(\varphi, \vartheta) : (\mathbb{C}_{\text{hyd}} - \mathbb{C}_{hf}^{\text{hom}}) \right]^{-1} \frac{\sin\vartheta d\vartheta d\varphi}{4\pi} \left. \right\}^{-1}.
 \end{aligned} \tag{5.17}$$

In Eq. (5.17),  $j$  comprises the phases air, water, and polymer.

The matrix-inclusion composite cement paste consists of the hydrate foam matrix, spherical clinker inclusions, and potentially entrapped air pores. Therefore, the homogenized stiffness

of cement paste reads as

$$\mathbb{C}_{cp} = \left\{ f_{hf}^{cp} \mathbb{C}_{hf} + f_{clin}^{cp} \mathbb{C}_{clin} : [\mathbb{I} + \mathbb{P}_{sph} : (\mathbb{C}_{clin} - \mathbb{C}_{hf})]^{-1} \right\} \\ : \left\{ f_{hf}^{cp} \mathbb{I} + f_{clin}^{cp} : [\mathbb{I} + \mathbb{P}_{sph} : (\mathbb{C}_{clin} - \mathbb{C}_{hf})]^{-1} + \Phi : [\mathbb{I} - \mathbb{P}_{sph} : \mathbb{C}_{hf}]^{-1} \right\}^{-1} . \quad (5.18)$$

For upscaling the elastic stiffness properties up to the scales of mortar and concrete, Eqs. (2.20) and (2.21) can be applied.

### 5.3.3.1 Validation

The multiscale modeling of polymer-modified cement-based materials requires a lot of flexibility, given that numerous types of polymers and technical additives are available and that different polymer quantities can be added to the mixes. As shown experimentally, the polymer modification considerably influences the early-age elastic and creep behavior of cementitious materials. This is the result of the delayed hydration kinetics as well as of the small elastic stiffness and the pronounced viscoelastic behavior of the polymers. Cement-polymer-interactions may further influence the mechanical properties of polymer-modified cement-based materials.

In the sequel, the predictive capability of the proposed homogenization approach for polymer-modified cement-based materials is evaluated. To test the universality of the multiscale model, the model responses are compared with two different types of experiments: the early-age creep tests, presented in Section 5.2, and the dynamic elastic moduli determined for polymer-modified cement pastes, mortars, and concretes, see Section 4. Table 5.4 delivers an overview of the mixture characteristics that the experiments provide. They are required as input parameters for the multiscale homogenization.

It is also desirable to compare the model predictions with independent experimental data reported in the literature. However, only one literature source was found that provides the necessary information regarding the mixture composition, elastic stiffness, and maturity of the material. In most publications, the hydration degrees corresponding to the measured elastic moduli are not given. However, in the PhD thesis of Flohr [76] all required data are summarized for different polymer-modified concretes, modified with four different polymer types and two  $p/c$ -ratios. Notably, three of the four polymers investigated by Flohr were also used for the experiments presented in this thesis. These experimental data are also compared with the response of the extended multiscale model.

**Table 5.4:** Validation experiments and corresponding mixture characteristics.

Experiment	Scale of interest	Polymer type	$p/c$ -ratio	$w/c$ -ratio
Early-age creep test	Cement paste, Concrete	P2, P3	0.10	0.40
Dynamic (elastic) modulus	Cement paste, Mortar, Concrete	P1, P2, P3	0.05, 0.20	0.40
Dynamic (elastic) modulus Flohr [76]	Concrete	P1, P2, P3, one further styrene acrylate	0.07, 0.10	0.33 ... 0.59

### Comparison with experimental data from ultra-short creep tests

The predictive capability of the presented homogenization approach is assessed by comparing the model-predicted stiffness evolutions with the experimental results derived from the ultra-short creep tests. For conventional cement-based materials, the multiscale model was already validated elsewhere [107]. Therefore, the model reliably estimates the experimentally determined stiffness of the plain cement paste and of the plain concrete, see Figure 5.18.

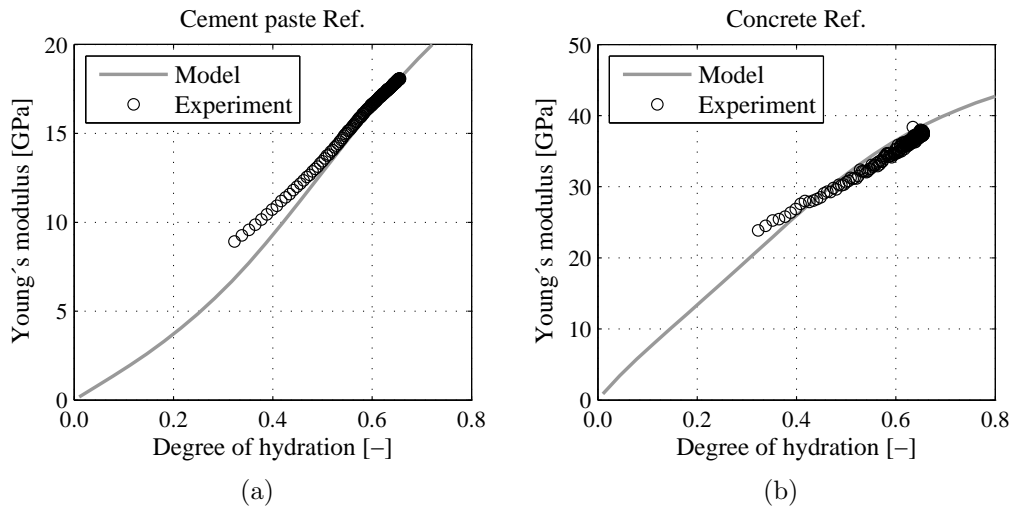


**Figure 5.18:** Comparison of the model-predicted and the experimentally determined Young's moduli derived from the ultra-short creep tests for the plain cement paste (a) and the plain concrete (b) with  $w/c = 0.40$ .

The model responses also agree satisfactory well with the experimental stiffness evolutions of both polymer-modified cement pastes, see Figure 5.19. With a few modifications regarding the morphological representation of the material and the hydration model, the



multiscale model was successfully extended to polymer-modified cement-based materials. Notably, the model is therewith applicable to cement pastes that are modified by polymers having a varying chemical composition.

For very early hydration stages below a degree of hydration of 0.3, the model overestimates the stiffness of cement paste P3 with a difference of less than 1 GPa. This might be related to the retarded growth of hydrate needles, as reported in the literature [40], see also Section 2.1.2.2. This observation could be incorporated into the model by varying the shape of the hydrates for very early hydration states. As described in Section 2.2.3, the onset of the stiffness increase is delayed in the case when spherical hydration products instead of needle-shaped hydrates are modeled. Thus, a maturity-dependent variation of the aspect ratio of the hydration products might improve the model capability for very young cement pastes modified with polymer P3. A variety of shapes of the hydration products with progressing hydration reaction has also been considered by Königsberger et al. [141], who derived the solid C-S-H aspect ratio as a function of the specific precipitation space. However, comparing the difference between model and experiment with the probabilistic model responses shown in Figure 3.7 reveals that the deviation is within the range of the stochastic scatter of the model output resulting from the uncertainties inherent in the input parameters. Therefore, the difference is not considered as being significantly large.

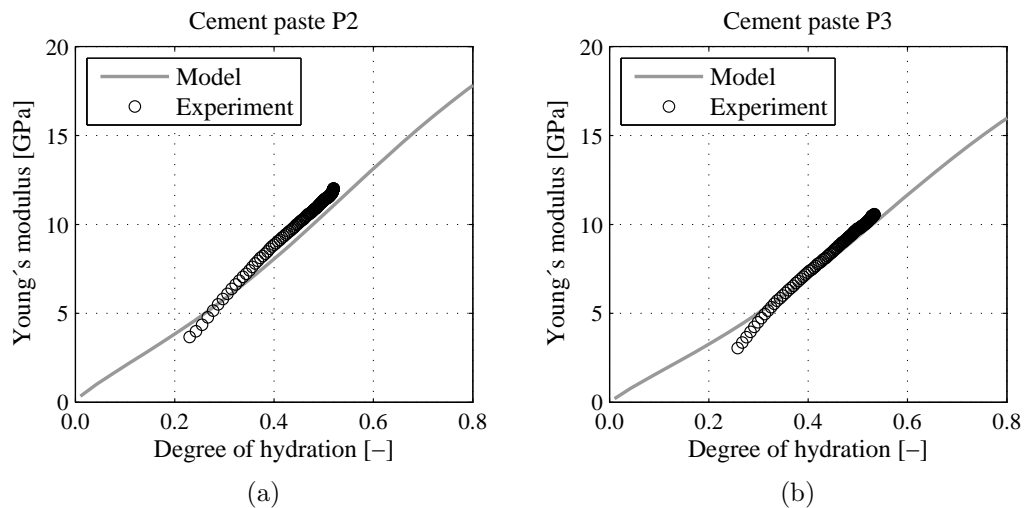


**Figure 5.19:** Comparison of the model-predicted and the experimentally determined Young's moduli derived from the ultra-short non-aging creep tests for the polymer-modified cement pastes P2 (a) and P3 (b) with  $w/c = 0.40$  and  $p/c = 0.10$ .

The comparison between model responses and experiments is also carried out on the scale of concrete. A good agreement is derived, see Figure 5.20. Notably, for concrete P3 entrapped air with a volume fraction of 9.8% is considered.

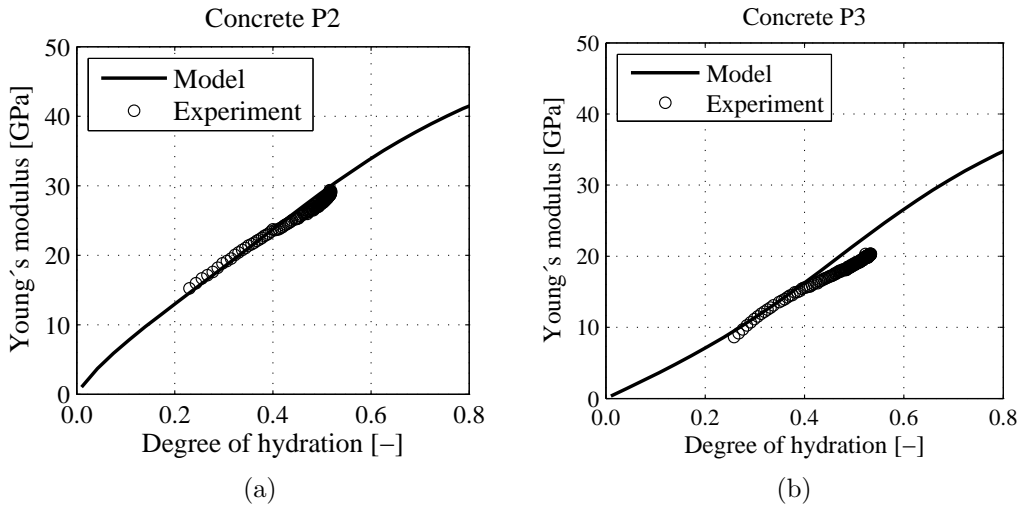


**Figure 5.20:** Comparison of the model-predicted and the experimentally determined Young's moduli derived from the ultra-short non-aging creep tests for the polymer-modified concretes P2 (a) and P3 (b) with  $w/c = 0.40$  and  $p/c = 0.10$ .

#### Comparison with experimental data from multiscale study of Section 4

The model responses are also compared with the experimental dynamic elastic moduli of polymer-modified cement pastes, mortars, and concretes, determined at 2, 7, and 28 days after production, see Section 4. It is worth mentioning that only experimental mean values are shown, and that the experimental data actually exhibit a stochastic scatter. As regards the modeling, entrapped air according to the Tables 4.8, 4.11, and 4.13 is considered. At the scales of mortar and concrete, the volume fractions of entrapped air were derived by comparing the macroscopic bulk densities of the specimens, using fractional arithmetics.

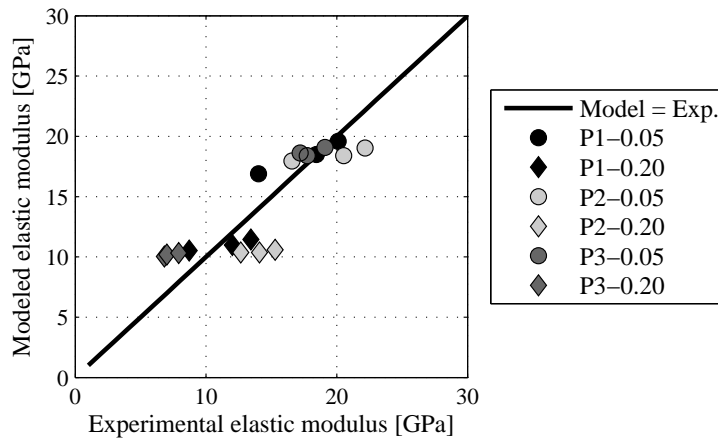
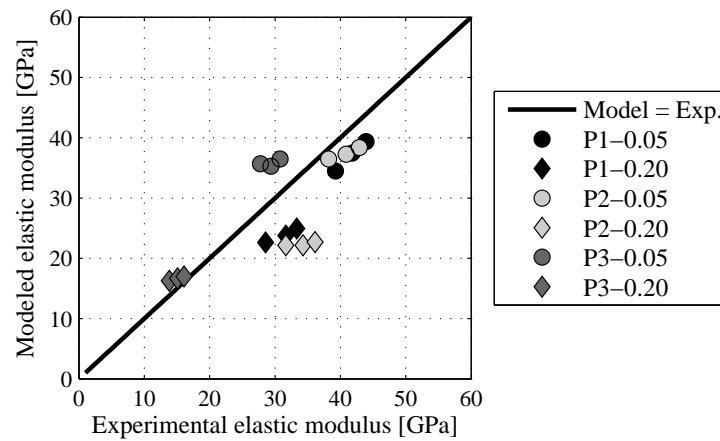
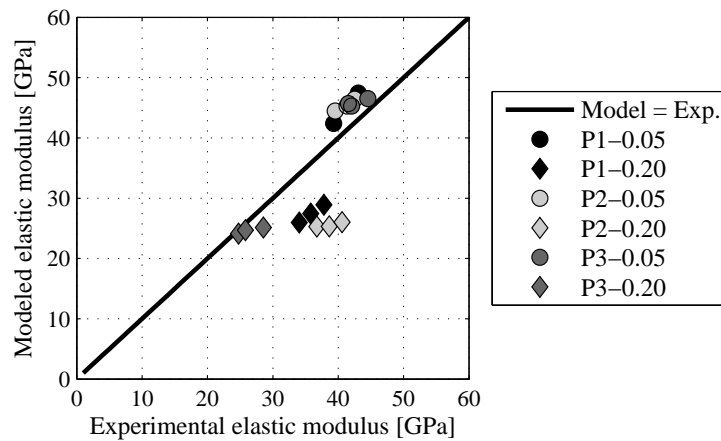


**Figure 5.21:** Experimentally determined versus model-predicted Young's moduli of polymer-modified cement pastes. The straight line represents the perfect agreement between model and experiment (Exp.).

The comparison between the model-predicted Young's moduli and the experimental results of the macroscopic cement paste, mortar, and concrete specimens are shown in Figures 5.21, 5.22, and ??, respectively. Across the scales, a good agreement between the modeled and experimentally determined Young's moduli is obtained. However, the elastic moduli of the mixes P2-0.20 and P3-0.20 are considerably underestimated by the model. For these two mixes, the difference between model output and experiment is even larger than the expected scatter of the model output due to the uncertain input parameters is, compare Figure 5.22 with Figure 3.7. The predictive capability of the model may be improved by investigating the microstructural specifics of the mixes in the future. The other mixes are well represented by the model.



(a)



(b)

**Figure 5.22:** Experimentally determined versus model-predicted Young's moduli of polymer-modified mortars (a) and concretes (b). The straight line represents the perfect agreement between model and experiment (Exp.).

### Comparison with experimental data of Flohr

Furthermore, the model predictions are compared with the experimentally determined dynamic elastic moduli of different PCC that Flohr [76] reported, see Figure 5.23. The predictive capability of the model is sufficiently good, given that different mixture compositions with several water-to-cement ratios and four types of polymers were investigated. Notably, three of the four polymers correspond to the polymers used in the present study. Therefore, the micromechanical properties were given. For the fourth polymer, a dispersion consisting of a styrene acrylate copolymer, the elastic properties of polymer P1 were considered because their MFT are similar.

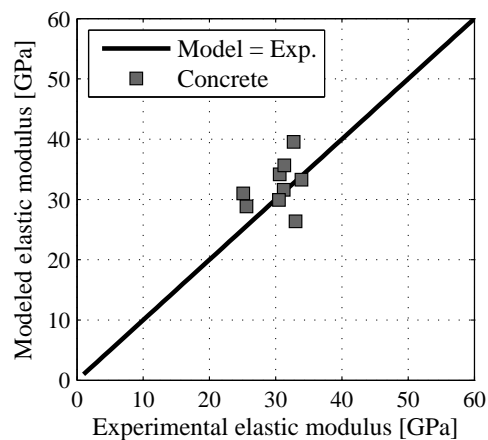


**Figure 5.23:** Comparison of model-predicted Young’s moduli with experimental data of Flohr [76].

The coefficient of determination  $R^2$  amounts to 0.79. Thus, the multiscale model is able to also provide reliable estimates for the Young’s moduli of polymer-modified cement-based materials, where only the mixture design and the type of polymer are known. Detailed information concerning the exact composition of the cement or the polymers are not required. However, one major limitation of the multiscale approach presented herein is that it is limited to mixes produced with Portland cements. Current modeling activities aim at extending the homogenization methods to blended cements, e.g. [141, 321, 322].

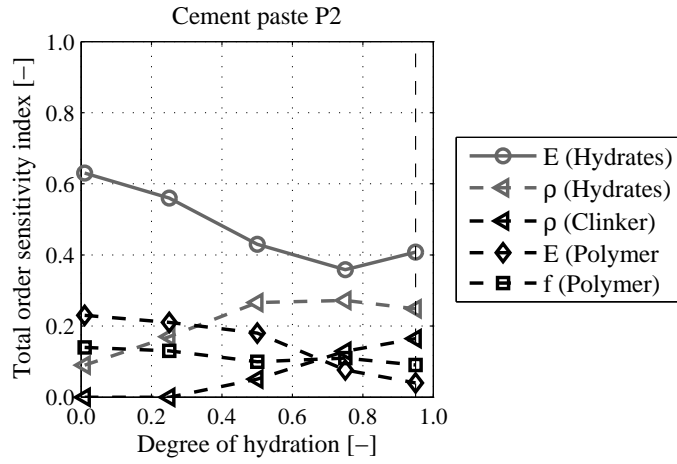
#### 5.3.3.2 Sensitivity of the model responses w.r.t. the elastic properties of the polymers

The elastic properties of the polymers were determined experimentally by means of nanoindentation tests and, therefore, they exhibit uncertainties due to experimental dispersion. Furthermore, the varying water content in the solid polymer specimens might influence the measured elastic properties. Another source of uncertainty is the volume

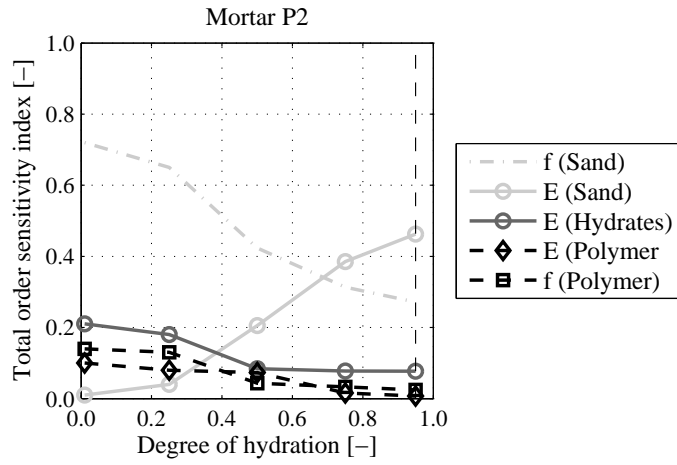
fraction of the polymers in the mixture that might vary due to imprecise weighing. This was the motivation to quantify the sensitivity of the model responses with respect to the uncertainties concerning the elastic properties and the volume fraction of the polymers. The influences of these uncertainties on the model-predicted Young's moduli of polymer-modified cement pastes, mortars, and concretes are investigated by means of the sensitivity analysis presented in Section 3.1.

Based on Figure 4.2 and in analogy to Section 3.3.2, a log-normal distribution is assigned to the elastic modulus of the polymer, with a mean value of 0.6 GPa and a standard deviation amounting to 0.5. The standard deviation is chosen to be larger than the experimentally determined scatter in order to cover a wide range of possible values. The mean value of the log-normally distributed Poisson's ratio is set equal to 0.40, which is confirmed by ultrasonic measurements on solid specimens made of the same polymers used in the present thesis [128]. The corresponding standard deviation amounts to 10%. The polymer volume fractions are considered to be uniformly distributed, spanning a range between 0.08 and 0.12. The results of the sensitivity analysis – more precisely the total order sensitivity indices on the scales of cement paste, mortar, and concrete – are shown in Figure 5.24, exemplary for the mixes modified with the polymer P2 for an initial  $p/c$ -ratio of 0.10. Only the parameters that influence the model responses are shown.

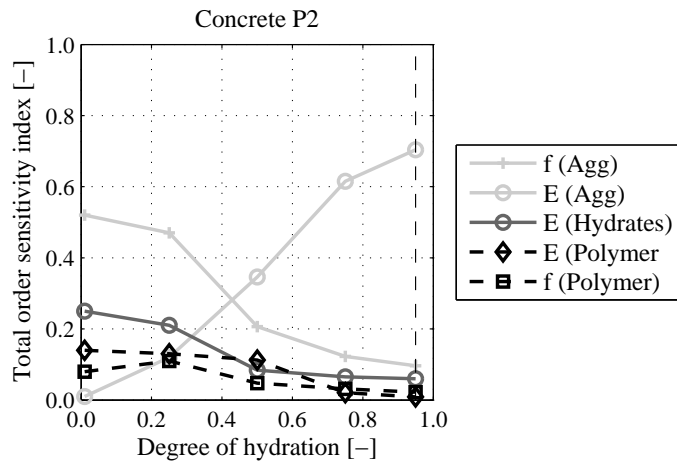
Apparently, the elastic stiffness of the polymers plays a minor role for the model-predicted stiffness evolutions of polymer-modified mortars and concretes. The influence is slightly larger at the scale of cement paste. The low stiffness of the polymers in comparison with the cementitious components can explain their low sensitivity indices. The polymers rather act as pores than as stiffening elements in the matrix. Therefore, their exact stiffness value is of minor importance because it is low in any case. In comparison with the results of the sensitivity analysis for conventional cement-based materials (see Figure 3.8), the influence of the Young's modulus of the hydrates is lowered. This is reasonable because in PCC cementitious and polymer constituents together form the matrix, and not only the hydrates. The total order sensitivity index of the polymer volume fraction reaches values up to 0.15. Therefore, this parameter is less important for the model response than the parameters referring to the main constituents, such as the hydrates and aggregates.



(a)



(b)



(c)

**Figure 5.24:** Evolution of total order sensitivity indices for the input parameters in the multiscale model for polymer-modified cement-based materials as functions of the degree of hydration, compared on three length scales: cement paste (a), mortar (b), and concrete (c).  $f$  – Volume fraction,  $E$  – Young’s modulus,  $\rho$  – mass density.

### 5.3.4 Homogenization of creep properties of polymer-modified cement pastes

For some applications, such as the use of sprayable polymer cement concretes (SPCC) for tunnel linings [323, 324], the pronounced creep activity of PCC can be beneficial, because creep decreases compressive stresses in the tunnel lining, which result from inward moving ground mass [186, 325]. However, in most other cases the large creep strains of PCC are not desirable. Therefore, the quantitative estimation regarding the viscoelastic early-age behavior of polymer-modified cement-based materials is of significant importance. The following section aims at understanding and quantifying the micromechanical origin of the pronounced creep activity of polymer-modified cement-based materials.

#### 5.3.4.1 Elastic and viscoelastic phase properties

For conventional cement pastes, the macroscopic creep behavior has been attributed to the hydrates only [118, 194, 196]. The other material phases, namely the capillary pores, the unhydrated clinker, and the entrapped air, are considered to exhibit purely elastic behavior, expressed as

$$\boldsymbol{\sigma}_j(t) = \mathbb{C}_j : \boldsymbol{\varepsilon}_j(t), \quad j \in \{\text{pore, clin, entrapped air}\}. \quad (5.19)$$

However, in polymer-modified cement pastes, not only the hydration products, but also the polymers are considered to exhibit viscoelastic behavior, reading as [284]

$$\begin{aligned} \boldsymbol{\sigma}_j(t) &= \int_{-\infty}^t \mathbb{R}_j(t - \tau) : \frac{\partial \boldsymbol{\varepsilon}_j(\tau)}{\partial \tau} d\tau, \\ \boldsymbol{\varepsilon}_j(t) &= \int_{-\infty}^t \mathbb{J}_j(t - \tau) : \frac{\partial \boldsymbol{\sigma}_j(\tau)}{\partial \tau} d\tau, \end{aligned} \quad j \in \{\text{hyd, pol}\} \quad (5.20)$$

with

$\boldsymbol{\sigma}$	stresses of phase $j$
$\boldsymbol{\varepsilon}$	strains of phase $j$
$\mathbb{R}_j$	relaxation tensor function of phase $j$
$\mathbb{J}_j$	creep tensor function of phase $j$ .

The creep and relaxation tensor functions of any phase  $j$  are linked by means of the following convolution condition [326]

$$\int_{-\infty}^t \mathbb{J}_j(t - \tau) : \mathbb{R}_j(\tau) d\tau = \int_{-\infty}^t \mathbb{R}_j(t - \tau) : \mathbb{J}_j(\tau) d\tau = t\mathbb{I}. \quad (5.21)$$

The relaxation tensor functions of the elastic phases are time-invariant according to Eq. (5.19) and read as

$$\mathbb{R}_j = \mathbb{C}_j = 3k_j\mathbb{I}^{\text{vol}} + 2\mu_j\mathbb{I}^{\text{dev}}, \quad j \in \{\text{pore, clin, entrapped air}\}. \quad (5.22)$$

$k_j$  and  $\mu_j$  are the bulk and shear moduli of the phases, as summarized in Table 5.3.

As described in Section 2.3.5, Königsberger et al. [120] performed a top-down analysis of more than 500 short-term early-age creep tests of conventional cement pastes, differing regarding the water-to-cement ratio. The authors found out that one universal isochoric creep tensor function for the microscopic hydrates is capable of explaining the experimental results. It has the following form

$$\mathbb{J}_{\text{hyd}}(t - \tau) = \frac{1}{3k_{\text{hyd}}}\mathbb{I}^{\text{vol}} + \frac{1}{2} \left[ \frac{1}{\mu_{\text{hyd}}} + \frac{1}{\mu_{c,\text{hyd}}} \left( \frac{t - \tau}{t_{\text{ref}}} \right)^{\beta_{\text{hyd}}} \right] \mathbb{I}^{\text{dev}}. \quad (5.23)$$

In Eq. (5.23),  $\mu_{c,\text{hyd}}$  and  $\beta_{\text{hyd}}$  denote the universal shear creep modulus and the power-law creep exponent of the hydrates. They were identified by Königsberger et al. [120] and amount to

$$\mu_{c,\text{hyd}} = 20.93 \text{ GPa}, \quad \beta_{\text{hyd}} = 0.251. \quad (5.24)$$

As for the polymers, an isochoric creep behavior is also considered. Motivated by the literature, according to which the creep behavior of solid polymer specimens during macroscopic creep tests can be modeled by means of a power-law [327, 328, 329], a creep tensor function in analogy to the hydrates is introduced as

$$\mathbb{J}_{\text{pol}}(t - \tau) = \frac{1}{3k_{\text{pol}}}\mathbb{I}^{\text{vol}} + \frac{1}{2} \left[ \frac{1}{\mu_{\text{pol}}} + \frac{1}{\mu_{c,\text{pol}}} \left( \frac{t - \tau}{t_{\text{ref}}} \right)^{\beta_{\text{pol}}} \right] \mathbb{I}^{\text{dev}}. \quad (5.25)$$

$\mu_{c,\text{pol}}$  and  $\beta_{\text{pol}}$  denote the shear creep modulus and the power-law creep exponent of the polymers. Their direct experimental characterization is not feasible. Therefore, they are identified by means of a top-down analysis within the framework of continuum micromechanics.

#### 5.3.4.2 Homogenization of the viscoelastic properties of polymer-modified cement pastes

The homogenization of the viscoelastic properties is performed in the theoretical framework of non-aging viscoelasticity applying the correspondence principle [218]. Accordingly, the viscoelastic phase behavior is transformed from the time domain to the Laplace-Carson



(LC) domain. The LC transform  $f^*(p)$  of a time-dependent function  $f(t)$  is given as

$$f^*(p) = p \int_0^{\infty} f(t) e^{-pt} dt \quad (5.26)$$

$p$  is the complex variable in the Laplace Carson domain. LC transforms of a time-dependent quantity  $(..)$  are indicated by the symbol  $(..)^*$ .

Applying the LC transform (5.26) to the viscoelastic phase behavior according to Eqs. (5.20) and considering Eq. (5.19) results in the following algebraic relations between LC transformed phase stresses  $\sigma_j^*$  and strains  $\epsilon_j^*$ , reading as

$$\sigma_j^*(p) = \mathbb{R}_j^*(p) : \epsilon_j^*(p), \quad \epsilon_j^*(p) = \mathbb{J}_j^*(p) : \sigma_j^*(p), \quad (5.27)$$

where interestingly

$$\mathbb{J}_j^*(p) = [\mathbb{R}_j^*(p)]^{-1}. \quad (5.28)$$

Thereby, Eq. (5.27) becomes formally identical to a linear elastic law. Thus, homogenization schemes can be applied, in analogy to elasticity, to the homogenization of the viscoelastic properties in the LC domain.

As for the purely elastic phases according to Eq. (5.22), the LC transformed relaxation tensor functions are equal to the stiffness tensors:

$$\mathbb{R}_j^* = \mathbb{C}_j = 3k_j \mathbb{I}^{\text{vol}} + 2\mu_j \mathbb{I}^{\text{dev}} \quad j \in \{\text{pore, clin, entrapped air}\}. \quad (5.29)$$

The transformation of the creep tensor functions of the hydrates, given in Eq. (5.23), and of the polymers, given in Eq. (5.25), considering the transformation rule (5.26) and Eq. (5.28), yields relaxation tensor functions in the LC domain as [120]:

$$\begin{aligned} \mathbb{R}_j^*(p) &= 3k_j \mathbb{I}^{\text{vol}} + 2\mu_j^*(p) \mathbb{I}^{\text{dev}} \\ &= 3k_j \mathbb{I}^{\text{vol}} + 2 \left[ \frac{1}{\mu_j} + \frac{1}{\mu_{c,j}} \left( \frac{1}{t_{\text{ref}}} \right)^{\beta_j} \Gamma(\beta_j + 1) p^{-\beta_j} \right]^{-1} \mathbb{I}^{\text{dev}}, \quad j \in \{\text{hyd, pol}\}. \end{aligned} \quad (5.30)$$

$\Gamma$  denotes the gamma function.

The homogenization of the viscoelastic properties is performed in analogy to Eqs. (2.18) and (2.19), such that the homogenized relaxation tensor functions of the hydrate foam,

$\mathbb{R}_{hf}^*$ , and of the cement paste,  $\mathbb{R}_{cp}^*$ , read as [120]

$$\begin{aligned}
 \mathbb{R}_{hf}^*(p) = & \left\{ \sum_j f_j^{hf} \mathbb{R}_j^*(p) : \left[ \mathbb{I} + \mathbb{P}_{\text{sph}}^{hf,*}(p) : \left( \mathbb{R}_j^*(p) - \mathbb{R}_{hf}^*(p) \right) \right]^{-1} + f_{\text{hyd}}^{hf} \mathbb{R}_{\text{hyd}}^*(p) \right. \\
 & : \left. \int_0^{2\pi} \int_0^\pi \left[ \mathbb{I} + \mathbb{P}_{\text{cyl}}^{hf,*}(p, \varphi, \vartheta) : \left( \mathbb{R}_{\text{hyd}}^*(p) - \mathbb{R}_{hf}^*(p) \right) \right]^{-1} \frac{\sin \vartheta d\vartheta d\varphi}{4\pi} \right\} \\
 & : \left\{ \sum_j f_j^{hf} : \left[ \mathbb{I} + \mathbb{P}_{\text{sph}}^{hf,*}(p) : \left( \mathbb{R}_j^*(p) - \mathbb{R}_{hf}^*(p) \right) \right]^{-1} + f_{\text{hyd}}^{hf} \right. \\
 & : \left. \int_0^{2\pi} \int_0^\pi \left[ \mathbb{I} + \mathbb{P}_{\text{cyl}}^{hf,*}(p, \varphi, \vartheta) : \left( \mathbb{R}_{\text{hyd}}^*(p) - \mathbb{R}_{hf}^*(p) \right) \right]^{-1} \frac{\sin \vartheta d\vartheta d\varphi}{4\pi} \right\}^{-1}, \tag{5.31} \\
 & j \in \{\text{pol}, \text{pore}\}.
 \end{aligned}$$

$$\begin{aligned}
 \mathbb{R}_{cp}^*(p) = & \left\{ f_{\text{hf}}^{cp} \mathbb{R}_{hf}^*(p) + \sum_k f_k^{cp} \mathbb{R}_k^*(p) : \left[ \mathbb{I} + \mathbb{P}_{\text{sph}}^{hf,*}(p) : \left( \mathbb{R}_k^*(p) - \mathbb{R}_{hf}^*(p) \right) \right]^{-1} \right\} \\
 & : \left\{ f_{\text{hf}}^{cp} \mathbb{I} + \sum_k f_k^{cp} : \left[ \mathbb{I} + \mathbb{P}_{\text{sph}}^{hf,*}(p) : \left( \mathbb{R}_k^*(p) - \mathbb{R}_{hf}^*(p) \right) \right]^{-1} \right\}^{-1}, \tag{5.32} \\
 & k \in \{\text{clin}, \text{entrapped air}\}.
 \end{aligned}$$

The “hydrate foam”-related and the “cement paste”-related volume fractions are computed with Eqs. (5.10) – (5.15). The creep tensor functions in the LC domain,  $\mathbb{J}_{\text{hf}}^*$  and  $\mathbb{J}_{\text{cp}}^*$ , follow from inversion of the relaxation tensor functions according to Eq. (5.28).

The “cement paste”-related creep tensor function is finally back-transformed numerically from the LC-domain to the time domain in order to obtain the modeled creep tensor function as  $\mathbb{J}_{cp}^{\text{mod}}(t - \tau)$ . Scheiner and Hellmich [118] applied the Gaver-Wynn-Rho algorithm [330, 331] and performed the computations in a multi-precision number format. This procedure is also applied herein, see Appendix A.4.

In the following, the viscous part of the modeled creep function in the time domain as

$$\mathbb{J}_{v,cp}^{\text{model}}(t - \tau) = \mathbb{J}_{cp}^{\text{model}}(t - \tau) - \mathbb{J}_{cp}^{\text{model}}(t=0) \tag{5.33}$$

is of interest and provides the basis for the comparison between modeling results and experimental data. This will allow for the sought quantification of the polymer creep function. The characteristic creep properties of the polymers are identified based on the modeled creep function according to Eq. (5.33) and the experimental counterpart obtained from the ultra-short creep tests on polymer-modified cement pastes, see Section 5.2.3.

### 5.3.4.3 Identification of the polymer creep properties

The creep properties of the polymer particles,  $\mu_{c,\text{pol}}$  and  $\beta_{\text{pol}}$ , are identified based on the experimentally determined creep functions, see Section 5.2.3. To this end, three different approaches are followed. In particular, it is first assumed that the polymers exhibit universal creep parameters. Then, it is investigated if the creep properties of the polymer phases are indeed age-dependent. In this context, two cases are distinguished: (i) only the shear creep modulus is considered to be age-dependent, and (ii) both the shear creep modulus and the power-law creep exponent are considered to be age-dependent.

#### Universal polymer creep properties

First, it is considered that the polymer particles exhibit universal, i.e. age-independent, creep parameters. The two constants,  $\mu_{c,\text{pol}}$  and  $\beta_{\text{pol}}$ , are identified by minimizing the error between experimental and model-predicted uniaxial viscous creep function, defined as

$$\mathcal{E} = \frac{1}{n_\xi n_t} \sum_{i=1}^{n_\xi} \sum_{j=1}^{n_t} |J_{v,cp}^{\text{model}}(t_j) - J_{v,cp}^{\text{exp}}(t_j)|. \quad (5.34)$$

The sum over  $n_\xi$  refers to varying hydration degrees of the material and amounts to 168 per specimen. The sum over  $n_t$  accounts for 180 time steps, with  $t_k \in [1, 180]$ . The model-predicted viscous creep function  $J_{v,cp}^{\text{model}}$  is obtained as the 1111-component of the creep tensor function defined in Eq. (5.33). The experimental viscous creep function  $J_{v,cp}^{\text{exp}}$  refers to the viscous part of Eq. (5.6) and reads as

$$J_{v,cp}^{\text{exp}}(t - \tau) = \frac{1}{E_{c,cp}^{\text{exp}}} \left( \frac{t - \tau}{t_{\text{ref}}} \right)^{\beta_{cp}^{\text{exp}}}. \quad (5.35)$$

The optimization problem formulated in Eq. (5.35) is solved using the Nelder-Mead algorithm, independently for the two polymer-modified cement pastes P2 and P3. The obtained optimal universal creep parameters read as

$$\begin{aligned} \mu_{c,\text{P2}} &= 0.609 \text{ GPa}, & \beta_{\text{P2}} &= 0.143, \\ \mu_{c,\text{P3}} &= 0.616 \text{ GPa}, & \beta_{\text{P3}} &= 0.216. \end{aligned} \quad (5.36)$$

The mean errors amount to  $1.7 \times 10^{-6}$  /MPa and  $1.9 \times 10^{-6}$  /MP for the pastes P2 and P3, respectively. The identified shear creep moduli of the polymers are by two orders of magnitude lower than those of the hydration products, compare Eqs. (5.36) and (5.24). The

universal polymer creep properties allow for a reliable representation of the experimentally determined creep strains, see Figure 5.25. This underlines the microscopic origin of the larger creep activity of polymer-modified cement pastes, stemming from the viscoelastic behavior of the polymer particles. However, the agreement between model and experiment is clearly not perfect, motivating the quest for an improved identification strategy.

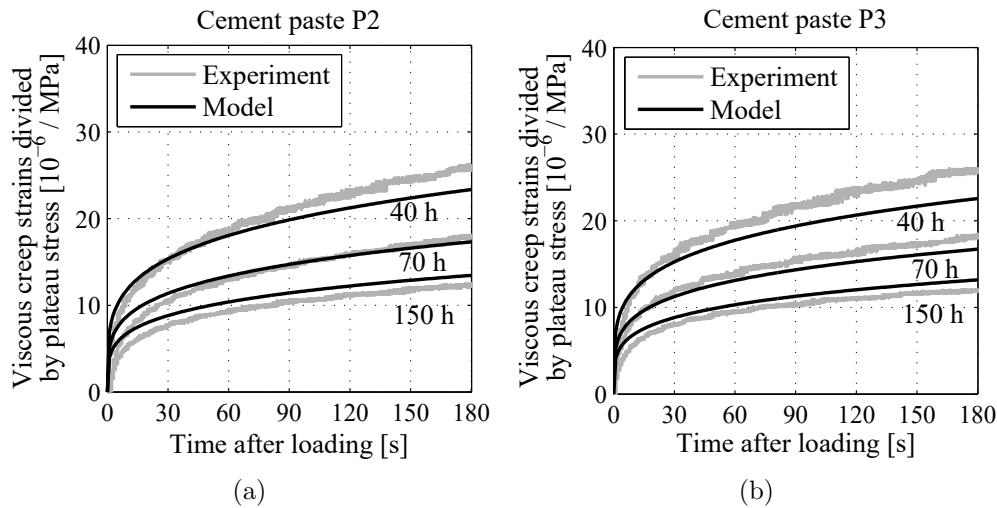


**Figure 5.25:** Comparison of experimentally determined and model-predicted viscous strains of polymer-modified cement pastes P2 (a) and P3 (b) at material ages of 40 h, 70 h, and 150 h, considering constant (universal) polymer creep properties.

### Age-dependent polymer creep properties

Creep tests on macroscopic solid polymer specimens revealed that the creep activity of polymers decreases with decreasing relative humidity to which the polymers are exposed [332, 333, 334]. The polymer phase within the cement pastes is also subjected to considerable decreases of the internal relative humidity, resulting from self-desiccation, i.e. from the water-consuming hydration process. Lura et al. [335] showed that the internal relative humidity in a cement paste sample with  $w/c = 0.37$  decreased from 98% to 92%, within the first few days after mixing. Notably, the resulting capillary pressure increased virtually linearly with the hydration degree  $\xi$ , in the regime  $\xi > 30\%$ , see [227]. As for mortars and concretes, the self-desiccation-induced capillary underpressure was shown to result in water migration from the open porosity of the aggregates into the cement paste matrix [227]. A similar mechanism is assumed to reduce the water content of the polymers. This was the motivation to consider age-dependent creep properties of the polymer phase. In this context, two different identification strategies are investigated: (i) only the shear creep modulus is considered to be age-dependent, and (ii) both the shear creep modulus and the power-law creep exponent are assumed to be age-dependent.

As for the first approach, different values for the power-law creep exponent are selected, such that  $\beta_{\text{pol}} \in \{0.1, 0.3, 0.4, 0.5, 0.6, 0.7, 0.8, 0.9, 1.1, 1.3\}$ . For each one of these  $\beta_{\text{pol}}$ , the creep tests are individually analyzed in order to identify the optimal shear creep moduli. Remarkably, the mean errors obtained according to Eq. (5.34) are virtually constant for power-law creep exponents having values within the interval  $\beta_{\text{pol}} \in [0.4, 0.8]$ , see Figure 5.26. Thus, for the further steps, the central value is chosen:  $\beta_{\text{P2}} = \beta_{\text{P3}} = 0.6$ . The corresponding modeled creep strains agree very well with the experimental data, see Figure 5.27. The respective mean errors amount to  $2.7 \times 10^{-7}$  /MPa for paste P2 and to  $2.9 \times 10^{-7}$  /MPa for paste P3, and they are by one order of magnitude smaller than the mean errors obtained for consideration of universal (constant) polymer creep properties, see Table 5.5. This illustrates that the creep properties of the polymer particles in hydrating cement pastes undergo changes.

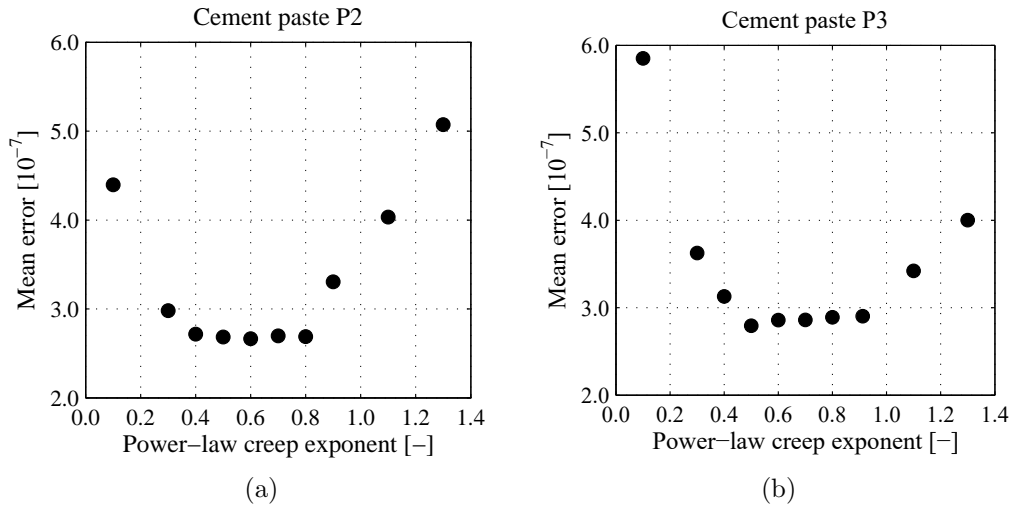


**Figure 5.26:** Mean errors according to Eq. (5.34) for age-independent power-law creep exponents and for age-dependent shear creep moduli for paste P2 (a) and paste P3 (b).

**Table 5.5:** Mean errors  $\mathcal{E}$  according to Eq. (5.34) for universal and age-dependent polymer creep properties.

Shear creep modulus	Power-law creep exponent	Polymer	Mean error $\mathcal{E}$
universal	universal	P2	$1.709 \times 10^{-6}$
universal	universal	P3	$1.927 \times 10^{-6}$
age-dependent	universal	P2	$2.665 \times 10^{-7}$
age-dependent	universal	P3	$2.857 \times 10^{-7}$
age-dependent	age-dependent	P2	$1.975 \times 10^{-7}$
age-dependent	age-dependent	P3	$2.227 \times 10^{-7}$

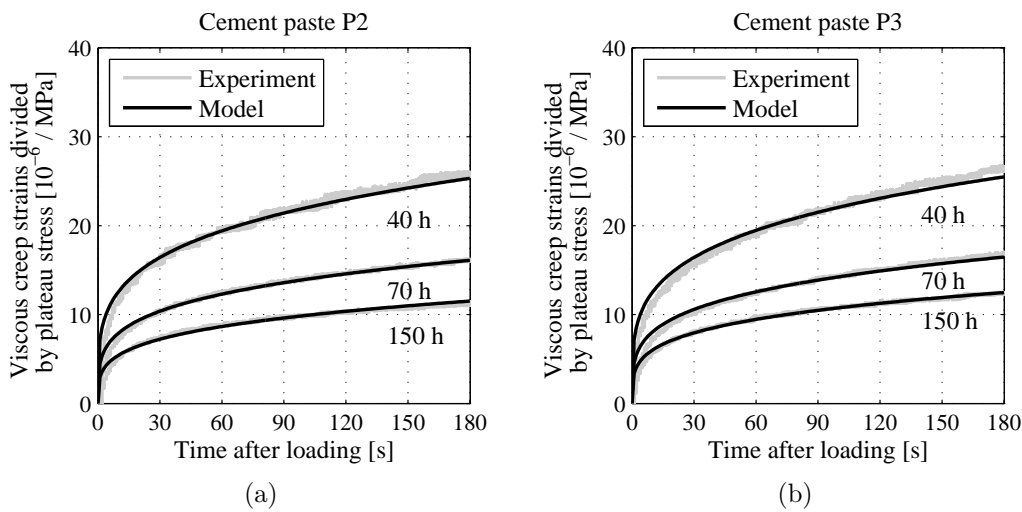


**Figure 5.27:** Comparison of experimental and computed creep strains of polymer-modified cement pastes P2 (a) and P3 (b) at ages of 40 h, 70 h, and 150 h, considering age-dependent shear creep moduli and constant power-law creep exponents.

The optimal shear creep moduli, obtained considering a constant power-law creep exponent, increase bilinearly with increasing material age. For material ages up to 40 h, the shear creep moduli first increase up to  $\mu_{c,P2} \approx 0.10$  GPa and  $\mu_{c,P3} \approx 0.14$  GPa, respectively. Thereafter, the hourly increase is significantly smaller. After one week of hydration, the identified values amount to  $\mu_{c,P2} \approx 0.23$  GPa and  $\mu_{c,P3} \approx 0.26$  GPa, respectively. On the one hand, the increasing shear creep modulus, and the concomitant decrease of the creep activity of the polymers can be explained by the progressive decrease of the internal relative humidity. On the other hand, it does not satisfactorily account for the bilinear evolution of the shear creep moduli. Therefore, a second microstructural effect appears to be involved. Tian et al. [59] claimed that the polymer particles are not uniformly distributed within the hydrating cementitious microstructure. Instead, the polymer particles flocculate, referred to as localization. Probably, these agglomerates exhibit a larger creep activity than the individual polymer particles. Tian et al. [59] further observed by means of ESEM investigations, among others, such as Bijen and Su [51], Dimmig-Osburg [58], and Schirmer [21], that the cementitious hydrates grow through the adsorbed polymer layers. The first branch of the bilinear evolution of the shear creep modulus with the material age might refer to the progressive destruction of the polymer agglomerates. However, there is a need of more experimental evidence in order to support this explanation. It would be beneficial to measure the evolution of the internal relative humidity of the hydrating polymer-modified cement pastes, as the measurement data would provide the necessary physical background to evaluate the self-desiccation-induced changes of the creep behavior of the polymers.

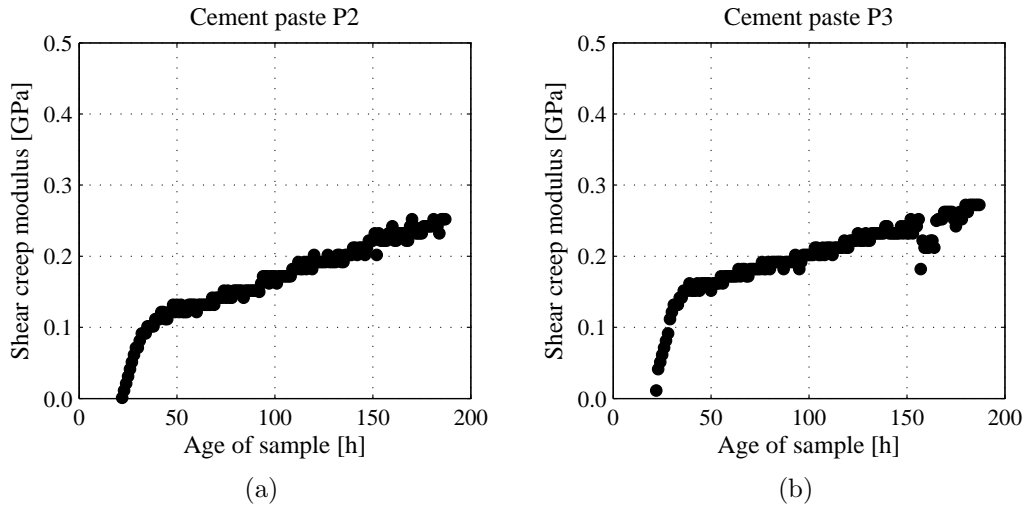


**Figure 5.28:** Evolutions of the shear creep modulus as functions of the material age, considering time-independent power-law creep exponents  $\beta_{P2} = \beta_{P3} = 0.6$ , for paste P2 (a) and paste P3 (b).

Within the second identification approach, all 168 tests per specimen are reanalyzed. The optimal values of both the creep shear modulus and the power-law creep exponent are identified simultaneously, such as to minimize the mean error according to Eq. (5.34). Therefore, both the creep shear modulus and the power-law creep exponent are considered to be age-dependent, evolving with the maturity of the material. The identified shear creep moduli and the identified power-law creep exponents increase nonlinearly with increasing material age, see Fig. 5.29. In comparison with Fig. 5.28, the evolutions of the shear creep modulus as well as of the power-law creep exponent exhibit a larger scatter. Most likely, this is related to the more complex optimization problem of the second identification strategy, which involves the determination of two variables. Therewith, the two variables may span an area with several minimal values close to each other, rendering the identification of the optima more challenging.

The shear creep modulus increases rapidly up to material ages of about 40 hours. Between ages of 40 and 110 hours, it is almost constant at values of  $\mu_{c,P2} \approx 0.08$  GPa and  $\mu_{c,P3} \approx 0.11$  GPa, respectively. Then, the shear creep modulus increases again more rapidly and reaches, one week after production, values of  $\mu_{c,P2} \approx 0.60$  MPa and  $\mu_{c,P3} \approx 0.40$  MPa, respectively. The power-law creep exponents, in turn, are virtually constant,  $\beta_{P2} \approx \beta_{P3} \approx 0.95$ , at material ages of less than 100 h. Afterwards, they decrease and finally stabilize around  $\beta_{P2} \approx 0.3$  or  $\beta_{P3} \approx 0.4$ , respectively. The corresponding mean errors, according to (5.34), amount to  $2.0 \times 10^{-7}$  for paste P2 and to  $2.2 \times 10^{-7}$  for paste P3. These values are by approximately 25% smaller compared to those obtained with a

constant power-law exponent, see Table 5.5. The experimentally measured creep strains are reproduced even more accurately, see Fig. 5.30. This goes along with larger computational costs, compared to the first approach.

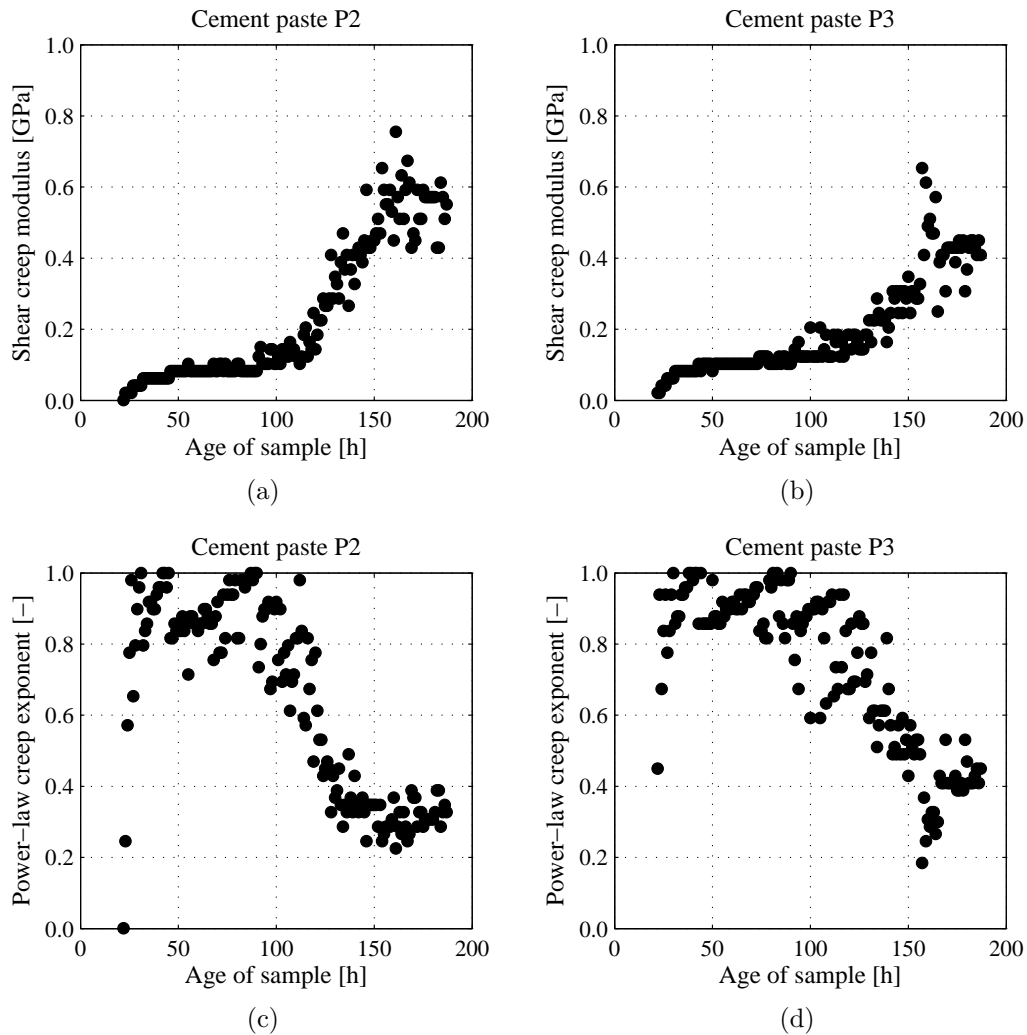


**Figure 5.29:** Evolutions of the shear creep modulus and the power-law creep exponent as functions of the material age, for paste P2 (a), (c) and paste P3 (b), (d), respectively.



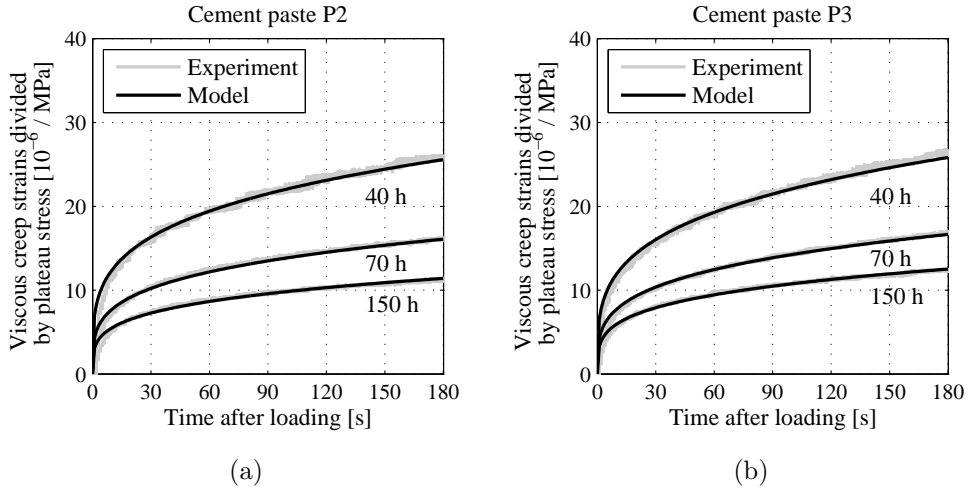


**Figure 5.30:** Comparison of experimental and computed creep strains of polymer-modified cement pastes P2 (a) and P3 (b) at ages of 40 h, 70 h, and 150 h, considering both age-dependent shear creep moduli and age-dependent power-law creep exponents.

### 5.3.5 Creep homogenization of polymer-modified concretes

In the following, it is investigated if the experimental results of the short-term creep tests on polymer-modified concretes, see Figure 5.13, can also be predicted by the micromechanics-based multiscale model. To this end, the upscaling procedure is extended to the scale of concrete, considering the morphological representation depicted in Figure 5.16.

The homogenized relaxation tensor at the concrete scale,  $\mathbb{R}_{concrete}^*$ , reads as

$$\mathbb{R}_{concrete}^*(p) = \left\{ f_{cp}^{concrete} \mathbb{R}_{cp}^*(p) + f_{agg}^{concrete} \mathbb{R}_{agg}^* : \left[ \mathbb{I} + \mathbb{P}_{sph}^{cp,*}(p) : \left( \mathbb{R}_{agg}^* - \mathbb{R}_{cp}^*(p) \right) \right]^{-1} \right\} : \left\{ f_{cp}^{concrete} \mathbb{I} + f_{agg}^{concrete} : \left[ \mathbb{I} + \mathbb{P}_{sph}^{cp,*}(p) : \left( \mathbb{R}_{agg}^* - \mathbb{R}_{cp}^*(p) \right) \right]^{-1} \right\}^{-1}. \quad (5.37)$$

In Eq. (5.37), it is considered that the aggregates exhibit elastic properties according to Eq. (5.19). The “concrete”-related volume fractions of the aggregates and the cement paste matrix can be computed using Eq. (3.15). For the upscaling, the polymer creep properties according to the three identification strategies presented in Section 5.3.4.3 are applied. The comparison of experimental and computed creep strains of the polymer-modified concretes is shown in Figure 5.31, separately for the three approaches. The corresponding mean errors are summarized in Table 5.6.

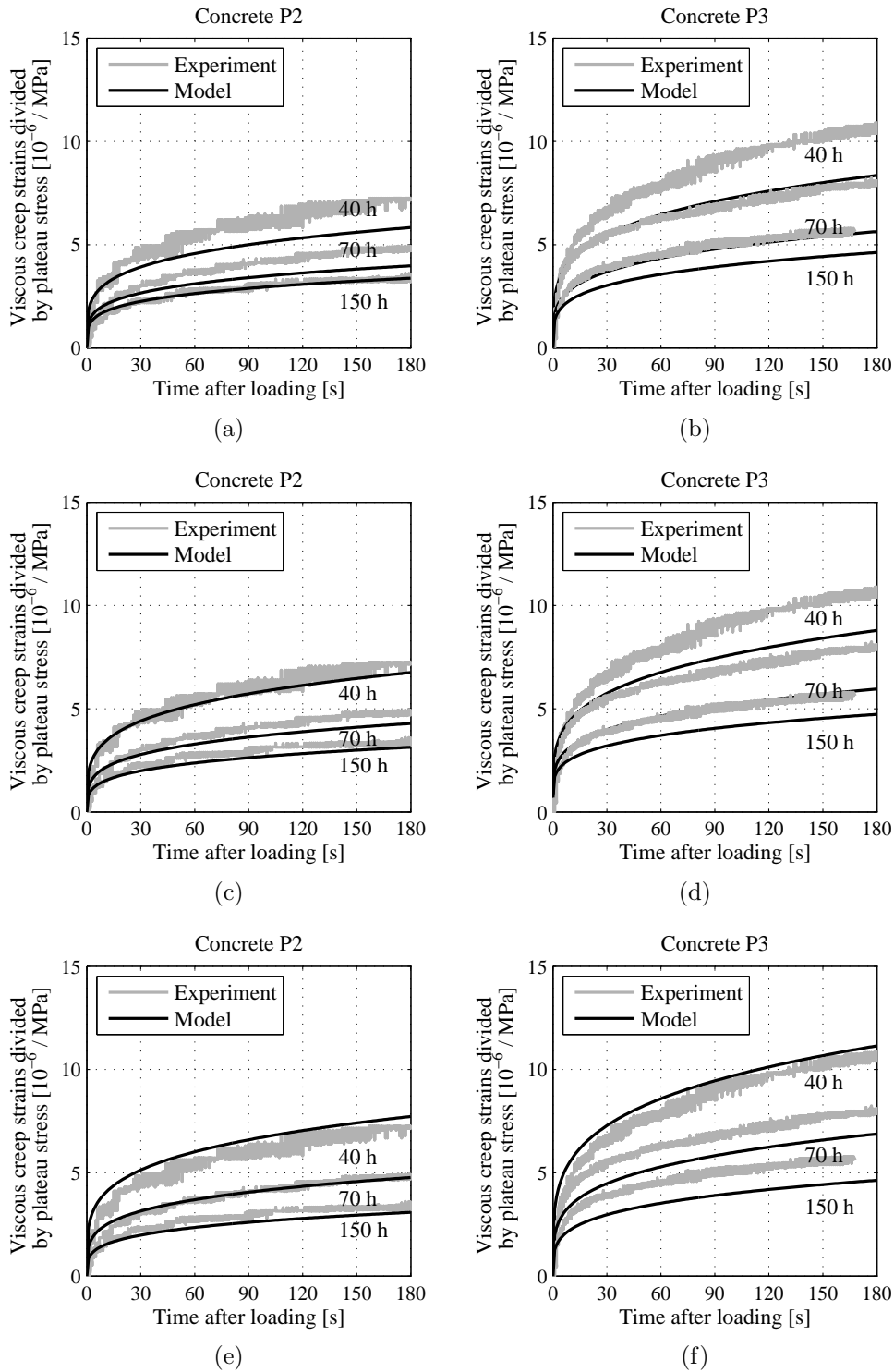


**Figure 5.31:** Comparison of experimental and computed creep strains of polymer-modified concretes P2 and P3 at material ages of 40 h, 70 h, and 150 h, considering constant (universal) polymer creep properties (a) and (b), age-dependent shear creep moduli and constant power-law creep exponents (c) and (d), and age-dependent shear creep moduli and power-law creep exponents (e) and (f).

The multiscale model allows for quite reliable estimations of the creep strains that the polymer-modified concretes exhibit during the short-term creep tests. Considering universal, i.e. age-independent, polymer creep properties entails underestimated model predictions. Similarly to the cement paste scale, the predictive quality improves when age-dependent polymer creep properties are applied. The means errors for concrete P2 are slightly lower than for concrete P3.

Further studies could investigate if the model predictions are improved when the water migration model of Irfan-ul-Hassan et al. [227], see Section 2.3.5, is applied. To this end, it has to be tested if the water uptake capacity and the paste void-filling extend identified by the authors are still valid for the polymer-modified concretes. Notably, in this thesis the same type of aggregates (quartz gravel) as in [227] was used. Irfan-ul-Hassan et al. [227] showed that the mean predictions errors could be reduced by one order of magnitude when the water-migration model is considered.

**Table 5.6:** Creep homogenization of polymer-modified concretes: Mean errors  $\mathcal{E}$  according to Eq. (5.34) for universal and age-dependent polymer creep properties.

Shear creep modulus	Power-law creep exponent	Polymer	Mean error $\mathcal{E}$
universal	universal	P2	$2.373 \times 10^{-6}$
universal	universal	P3	$2.547 \times 10^{-6}$
age-dependent	universal	P2	$5.461 \times 10^{-7}$
age-dependent	universal	P3	$6.857 \times 10^{-7}$
age-dependent	age-dependent	P2	$3.068 \times 10^{-7}$
age-dependent	age-dependent	P3	$4.953 \times 10^{-7}$

## 5.4 Summary

The early-age elastic and creep behavior of polymer-modified cement pastes and concretes was investigated by means of both experimental and semi-analytical approaches. Hourly-repeated short-term creep tests provide insight into the early-age evolutions of the elastic stiffness and the creep properties of the materials. The elastic modulus, the creep modulus, and the power-law exponent of the macroscopic specimens were quantified quasi-continuously from the first day after production up to material ages of eight days. The experimental results revealed that the stiffness of cement-based materials is reduced as a consequence of the polymer modification, comparing specimens with the same water-to-cement mass ratio, geometrically identical shapes, and identical curing conditions. Polymer P3 entails a lower Young's modulus of the cement pastes and concretes than polymer P2 does. This is related to the higher entrapped air void porosity in the samples modified with polymer P3, as it was also observed in Section 4. The smaller stiffness of the polymer-modified cement-based materials goes along with a more pronounced creep activity than the unmodified reference specimens exhibit. The cement pastes and concretes modified with the polymers P2 and P3 exhibit larger creep compliances and creep strains than the unmodified materials at given time instants. The power-law exponent is less sensitive to the mixture design than the other quantities are.

Multiscale models based on the principles of continuum micromechanics are able to reliably predict the elastic and creep properties of polymer-modified cement-based materials. An existing micromechanics-based model for the quantification of the stiffness, creep, and strength of conventional hydrating cement pastes [107] is extended towards consideration of polymer particles and of entrapped air porosity. The polymers are introduced at the scale of hydrate foam, while the entrapped air pores are considered at the significantly larger scale of cement paste. Furthermore, a constant volume fraction of the polymers during the hydration process is assumed. The elastic properties of the polymers were obtained by means of nanoindentation tests on polymer films. The extended multiscale model is able to satisfactorily estimate the Young's moduli derived from the ultra-short creep tests and from the mechanical tests reported in Section 4. The considered mixture designs comprise three different types of polymers as well as polymer-to-cement mass ratios ranging from 0.05 to 0.20. The sensitivity of the model responses with respect to uncertainties regarding the elastic stiffness properties of the polymers is low. Thus, the multiscale model can be applied to cement-based materials modified with different polymers. It may furthermore help to reduce the number of time-consuming experiments because it reliably describes the elastic properties of polymer-modified cement-based materials with different mixture compositions.

The model was further extended for the creep homogenization of polymer-modified cement-based materials. By means of a top-down analysis, the experimental data of the early-age creep tests were exploited in order to investigate the micromechanical origin of the pronounced creep activity of the materials. It was found out that an isochoric power-law-type creep behavior of the polymers might describe the large creep strains of the cement pastes. In contrast to the hydrates, the polymers do not exhibit a universal creep behavior. The creep activity of the polymer particles decreases with ongoing hydration process. This very likely refers to the self-desiccation resulting from the hydration reaction and the associated decrease of the internal relative humidity in hydrating cement pastes. Further microscopic aspects, such as the increased film formation of the polymers and the penetration of growing hydrates through polymer agglomerates, appear to be involved. The macroscopic creep behavior of polymer-modified cement pastes can be satisfactorily represented when the power-law creep exponent is considered to be age-independent (constant). In that case, the shear creep modulus of the polymer particles was found to follow a bilinear trend during the first week after production. The agreement between model-predicted and experimentally-determined results can be further improved when considering that both the shear creep modulus and the creep exponent of the polymers are age-dependent and, thus, evolving functions. This entails considerable additional computational efforts.



## 6 | Comparison of empirical and multiscale modeling approaches

It is a vital issue to evaluate if the assumptions and hypotheses used to design structures made of conventional concretes are also valid for PCC. Present models in codes and standards may not take into account the complexity of polymer-modified cement-based materials and, therefore, may lead to inaccurate estimations of fundamental mechanical properties. Thus, it needs to be investigated if models that are commonly used in design can be applied to PCC.

Standard models are mostly empirical. That means, they rely on quantitative relations between variables without considering intrinsic mechanisms and theories behind the phenomena for which the models are developed. Empirical models are often based on experimental data from which fitted parameters without a physical meaning are derived. On the contrary, multiscale models within the framework of continuum micromechanics are based on material constants; no fitted parameters are used preferably.

In Section 6.1, it is investigated if analytical models prescribed in codes and norms are able to reliably predict the elastic modulus of polymer-modified concrete. Experimental data reported in Section 4.6.4.2 are used for the comparison with the model responses. Section 6.2 focuses on the creep of concrete. Empirical creep models and the multiscale approach are compared with experimental long-term creep tests reported in the literature.

### 6.1 Prediction of elasticity

#### 6.1.1 Empirical models for the prediction of the elastic modulus

During the past few decades, several analytical models for the estimation of the elastic Young's modulus of conventional concrete have been developed and incorporated into standards and guidelines. Most formulas relate the initial or secant modulus at a given time

to the compressive strength of concrete, as the sole indicator of the mechanical concrete performance. In some models, the density of concrete is also taken into account. Due to the dominant role of the aggregates, selected models consider the type of the aggregates via correction factors. Notably, the empirical formulas require *a priori* knowledge of these composition-dependent quantities. However, many different factors influence the elastic modulus of concrete so that the computed quantity always differs from the actual value [336, 337].

An overview about the analytical models considered within this thesis is given in Table 6.1. Therein, formulations proposed by national institutions such as the American Concrete Institute (ACI), the Spanish ministry of development, who reported the Spanish Code on Structural Concrete (EHE), the Brazilian Association of technical standards (NBR), the International Federation for Structural Concrete (CEB-FIP), and the American Association of Highway and Transportation Officials (AASHTO) are summarized. Based on experimental data collected in comprehensive databases or based on their own experimental studies, several further authors, such as Hueste et al. [338], Gutierrez and Canova [339], and Lim et al. [340] proposed formulations for the assessment of the concrete Young's modulus.

The responses of the models for a normal-weight concrete ( $\rho = 2400 \text{ kg m}^{-3}$ ) containing aggregates of type quartzite are shown in Figure 6.1. Expectedly, the predicted elastic modulus increases with the compressive strength. For a given compressive strength, the responses of the different formulas vary in their predictions between 8 GPa and 15 GPa. The scatter results from the different formulations of the models.

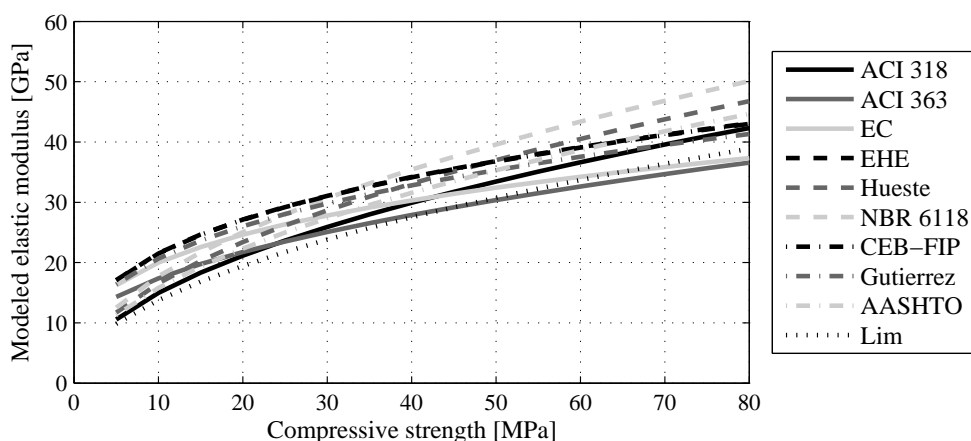


**Figure 6.1:** Estimations of the Young's modulus of concrete as functions of the compressive strength using the formulations summarized in Table 6.1.



**Table 6.1:** Empirical models for the determination of the elastic modulus.  $f_c$  – concrete compressive strength [MPa],  $\rho$  – concrete density [ $\text{kg m}^{-3}$ ],  $\alpha$  – correction factor [-].

Model [MPa]	Remark	Source
$E = 4730(f_c)^{0.5}$		ACI 318 [341]
$E = 3320(f_c)^{0.5} + 6890$		ACI 363 R [342]
$E = 22,000(f_c)^{0.3}$		EC 2 [211]
$E = 10,000(f_c)^{1/3}$		EHE [343]
$E = 5230(f_c)^{0.5}$		Hueste et al. [338]
$E = 5600(f_c)^{0.5}$		NBR 6118 [344]
$E = 21,500\alpha(f_c/10)^{1/3}$	$\alpha = 1.2$ for basalt, dense limestone; $\alpha = 1.0$ for quartzite; $\alpha = 0.9$ for limestone; $\alpha = 0.7$ sandstone	CEB-FIP [345]
$E = 8340\alpha(f_c)^{1/3}$	$\alpha = 1.2$ for basalt, dense limestone; $\alpha = 1.15$ for quartzite; $\alpha = 0.9$ for limestone; $\alpha = 0.6$ sandstone	Gutierrez and Canova [339]
$E = 0.043\alpha\rho^{1.5}(f_c)^{0.5}$	$\alpha$ : correction factor for type of aggregate; no specific value recommended; should be taken as 1.00;	AASHTO [346]
$E = 4400\sqrt{f_c} \left( \frac{\rho}{2400} \right)^{1.4}$		Lim et al. [340]

### 6.1.2 Predictive capabilities of the empirical models applied to PCC

In the following, it is tested if the empirical models are able to reliably estimate the Young's modulus of polymer-modified concrete. To this end, the formulations are fed with the experimentally determined compressive strengths of PCC, see Section 4.6.4.2. The empirical models require the cylinder compressive strength of concrete. Thus, the experimental compressive strengths obtained for cubic specimens with an edge length of 100 mm (Table 4.13) are converted into the cylinder compressive strength of concrete [347]. Also, the storage conditions following DIN EN 12390-2 [348] are taken into account as

$$\begin{aligned}
 f_{c,\text{dry}, 150 \text{ mm}} &= 0.97 \cdot f_{c,\text{dry}, 100 \text{ mm}}, \\
 f_{c,\text{cube}} &= 0.92 \cdot f_{c,\text{dry}, 150 \text{ mm}}, \\
 f_{c,\text{cyl}} &= 0.80 \cdot f_{c,\text{cube}}.
 \end{aligned} \tag{6.1}$$

The densities of the PCC, which some models require, are summarized in Table 4.13.

The responses of the models given in Table 6.1 are compared with the experimentally determined static elastic moduli of polymer-modified concretes at a material age of 28 days, as the models aim at the assessment of the secant moduli. The comparison between the experimental data, i.e. the static elastic moduli of the six different PCC investigated in Section 4.6.4.2 at 28 days, and the predictions of the ten analytical models are shown in Figure 6.2. Notably, There is no clear tendency about the predictive capabilities of the models. Some models, such as the EHE, NBR 6116 and the CEB-FIP, overestimate the Young's modulus of PCC. Others, such as the ACI 363 and the model by Lim et al., underestimate the stiffness. Therefore, the prognosis qualities of the models have to be individually evaluated.

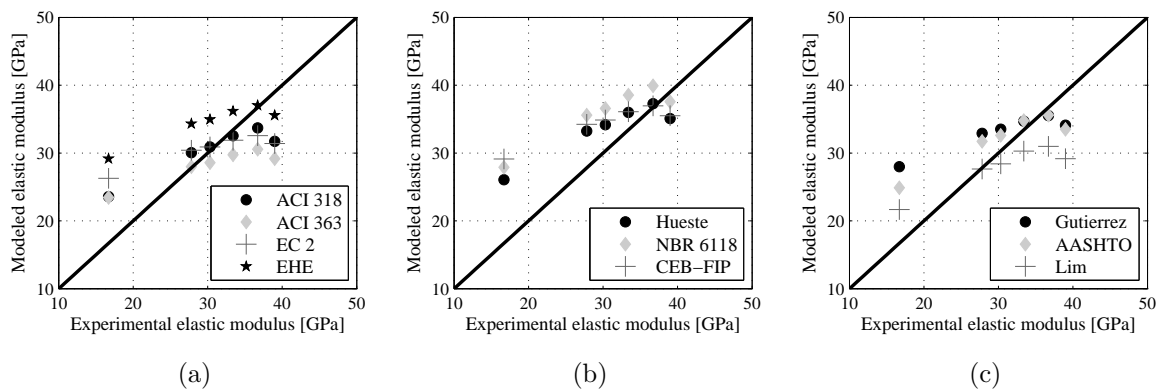


**Figure 6.2:** Comparison between experimentally determined and model-predicted elastic moduli of polymer-modified concretes.

The goodness-of-fit between experiment and prediction for the different models warrants further evaluation. A quantitative measure of the differences between model response  $Y$  and experiment  $\hat{Y}$  is the mean absolute percentage error  $\mathcal{E}_{\text{MAPE}}$ , which is given as

$$\mathcal{E}_{\text{MAPE}} = \frac{100}{n} \sum_{i=1}^n \left| \frac{\hat{Y} - Y}{\hat{Y}} \right|. \quad (6.2)$$

For each model, the mean absolute percentage error is computed, separately for the concrete mixtures having a  $p/c$ -ratio of 0.05 and of 0.20, see Table 6.2. The experimental elastic moduli of the PCC obtained at material ages of 28 days and the corresponding model responses are compared.

For the lower  $p/c$ -ratio, most of the empirical models estimate the Young's modulus of PCC satisfactorily well, i.e. the mean error amounts to less than 10%. Particularly, the

models CEB-FIP, EHE, and Hueste show a good agreement with the experiments. The predictions of the models ACI 363 and Lim are worse compared with the other models. For a  $p/c$ -ratio of 0.20, the differences between experiments and model responses are larger for most of the models. The model responses of EHE, NBR 6118, and CEB-FIP differ from the actual elastic moduli by more than 30%. The models ACI 318, ACI 363, EC 2, and Lim reveal the best predictions. The predictive capability of the multiscale model is better than that of the phenomenological models for a  $p/c$ -ratio of 0.05. For a  $p/c$ -ratio of 0.20, the prediction error for the multiscale model is only slightly worse than the best empirical models. One drawback of applying the empirical models is that there is no model that reliably predicts the elastic moduli of both PCC with  $p/c = 0.05$  and with  $p/c = 0.20$ . Some of the models are appropriate for the concretes with a low polymer content. However, their predictive capability is worse for the concretes with a high polymer content. Thus, they are not generally applicable for estimating the elastic moduli of PCC.

**Table 6.2:** Goodness-of-fit, represented by the mean absolute percentage error  $\mathcal{E}_{\text{MAPE}}$  [%]. The values are averaged for all investigated PCC.

Model	$p/c = 0.05$	$p/c = 0.20$
ACI 318	10.2	13.0
ACI 363	18.0	11.6
EC 2	12.1	14.1
EHE	6.0	31.6
Hueste	6.5	25.0
NBR 6118	9.0	33.4
CEB-FIP	5.9	31.3
Gutierrez	6.8	26.2
AASHTO	7.0	19.3
Lim	17.4	9.4
Multiscale	3.5	15.2

## 6.2 Prediction of creep

### 6.2.1 Empirical creep compliance functions

The creep behavior of concrete is also incorporated in standards and guidelines. Several different approaches were proposed to determine the creep coefficient and the creep compliance of concrete. Among these proposals, the five most widely used creep prediction models are considered within this thesis:

- ACI209 by the American Concrete Institute [179]
- Model Code 2010 [180] by the International Federation for Structural Concrete, originally published in the Model Code 90-99 [349]
- B3 by Bažant and Bajewa [261, 350, 262]
- B4 by Bažant, Wendner and Hubler [351]
- GL2000 by Gardner and Lockman [181]

#### 6.2.1.1 Model according to ACI209

The creep model according to the American Concrete Institute is based on a product ansatz, which combines an aging function and a hyperbolic time function. Basic and drying creep are not distinguished. The compliance function reads as

$$J(t, \tau) = \frac{1}{E_\tau} + \frac{(t - \tau)^\psi}{d + (t - \tau)^\psi} \varphi_{c, \infty} \quad (6.3)$$

with

$E_\tau$	elastic modulus at beginning of loading
$\psi, d$	constants depending on the shape and size of the specimen; for conventional concrete : $\psi = 0.60$ and $d = 10$ d
$\varphi_{c, \infty}$	ultimate creep coefficient.

The ultimate creep coefficient  $\varphi_{c, \infty}$  can be estimated as follows

$$\varphi_{c, \infty} = 2.35 \gamma_{la} \gamma_{RH} \gamma_a \gamma_{v/s} \gamma_{sl} \gamma_{f-a} \quad (6.4)$$

with

$\gamma_{la}$	concrete age at beginning of loading
$\gamma_{RH}$	relative humidity
$\gamma_a$	air void volume
$\gamma_{v/s}$	volume/surface ratio

$\gamma_{sl}$  slump  
 $\gamma_{f-a}$  fine-aggregate ratio.

### 6.2.1.2 Model MC90

Analogously to the model ACI209, the model MC90 uses a product formulation. An ultimate creep coefficient is combined with a hyperbolic time function. The creep coefficient is defined as

$$\varphi_c(t, \tau) = \varphi_{c,\infty} \beta_c(t, \tau) = \varphi_{c,\infty} \left[ \frac{t - \tau}{\beta_H + (t - \tau)} \right]^{0.3}. \quad (6.5)$$

The factor  $\beta_H$  considers the influence of the drying creep on the creep rate and reads as

$$\beta_H = 1.5h \left[ 1 + (1.2RH)^{18} \right] + 250\alpha_3 \leq 1500\alpha_3 \quad (6.6)$$

with  $h$  effective width  
 $RH$  relative humidity  
 $\alpha_3$  correction factor, refers to the concrete strength.

The ultimate creep coefficient  $\varphi_{c,\infty}$  is computed considering the concrete strength  $f_c$ , the humidity, and the hydration speed as follows

$$\varphi_{c,\infty} = \varphi_{RH} \beta(f_c) \beta(\tau) \quad (6.7)$$

with

$$\varphi_{RH} = \left[ 1 + \frac{1 - RH}{0.1h^{1/3}} \alpha_1 \right] \alpha_2, \quad (6.8)$$

$$\beta(f_c) = \frac{16.8}{\sqrt{f_c}}, \quad (6.9)$$

$$\beta(\tau) = \frac{1}{0.1 + (\tau_{eff})^{0.2}}. \quad (6.10)$$

$\tau_{eff}$  is the effective age of the concrete at time instant  $\tau$ . It depends on the type of the cement and the temperature and, thus, takes into account the cement hydration progress.  $\alpha_1$  and  $\alpha_2$  are further correction factors, depending on the concrete strength. The compliance function is calculated as follows

$$J(t, \tau) = \frac{1}{E_\tau} + \frac{\varphi_c(t, \tau)}{E_{28}}. \quad (6.11)$$

In Eq. (6.11), the Young's moduli of the concrete at 28 days,  $E_{28}$ , and at the time instant of loading,  $\tau$ , are considered.

### 6.2.1.3 Model B3

The model B3 is based on the summation ansatz. Accordingly, the creep compliance is the sum of the instantaneous compliance  $q_1$ , the basic creep compliance  $C_0(t, \tau)$ , and the drying creep compliance  $C_d(t, \tau, t_d)$ . The latter takes into account the age of concrete at the beginning of drying  $t_d$ .

$$J(t, \tau) = q_1 + C_0(t, \tau) + C_d(t, \tau, t_d). \quad (6.12)$$

The basic creep compliance explicitly considers a visco-elastic part via the parameters  $q_2, q_3$  as well as a visco-plastic part via the parameter  $q_4$ . To each of them, a specific time function is assigned as

$$C_0(t, \tau) = q_2 Q(t, \tau) + q_3 \ln [1 + (t - \tau)^n] + q_4 \ln \left( \frac{t}{\tau} \right). \quad (6.13)$$

$Q(t, \tau)$  is an approximate binomial integral; for the computation of  $Q(t, \tau)$ , the reader is referred to [194, 352]. The drying creep compliance is defined as

$$C_d(t, \tau, t_0) = q_5 \sqrt{e^{-8H(t, t_0)} - e^{-8H(\tau, t_0)}}, \quad (6.14)$$

in which  $H(t)$  and  $H(\tau)$  denote the mean pore moisture content of the concrete at the time instants  $t$  and  $\tau$ . The parameters  $q_1 \dots q_5$  depend on the water-to-cement ratio  $w/c$ , the aggregate-to-cement ratio  $a/c$ , the compressive strength at 28 days  $f_{c,28}$ , the cement content  $c$ , and the ultimate shrinkage strain  $\varepsilon_{sh,\infty}$  as

$$\begin{aligned} q_1 &= \frac{0.6}{E_{c,28}}, \\ q_2 &= 2.33 \cdot 10^{-5} c^{0.5} f_{c,28}^{-0.9}, \\ q_3 &= 0.29 (w/c)^4 \cdot q_2, \\ q_4 &= 2.03 \cdot 10^{-5} (a/c)^{-0.7}, \\ q_5 &= \frac{1.90 \cdot 10^{-4}}{f_{c,28} \varepsilon_{sh,\infty}^{0.6}}. \end{aligned} \quad (6.15)$$

### 6.2.1.4 Model B4

The model B4 is the successor of the model B3. With several improvements, the range of applicability is extended to modern concretes including admixtures.

The compliance function has the same form as presented in Eq. (6.12). The compliance functions for the basic creep and the creep due to simultaneous drying are defined similarly

to Eqs. (6.13) and (6.14). The parameters  $q_1 \dots q_5$  are defined as follows:

$$\begin{aligned}
 q_1 &= \frac{p_1}{E_{28}}, \\
 q_2 &= \frac{p_2}{1\text{GPa}} \left( \frac{w/c}{0.38} \right)^{p_{2w}}, \\
 q_3 &= p_3 q_2 \left( \frac{a/c}{6} \right)^{p_{3a}} \left( \frac{w/c}{0.38} \right)^{p_{3w}}, \\
 q_4 &= \frac{p_4}{1\text{GPa}} \left( \frac{a/c}{6} \right)^{p_{4a}} \left( \frac{w/c}{0.38} \right)^{p_{4w}}, \\
 q_5 &= \frac{p_5}{1\text{GPa}} \left( \frac{a/c}{6} \right)^{p_{5a}} \left( \frac{w/c}{0.38} \right)^{p_{5w}} |k_h \varepsilon_{sh\infty}(\tilde{T}_\tau)|^{p_{5\varepsilon}}.
 \end{aligned} \tag{6.16}$$

The factors  $p_{2\dots5a}$  and  $p_{2\dots5w}$  as well as  $p_{5\varepsilon}$  depend on the type of the cement.  $k_h$  is a factor that takes into account the humidity.  $\varepsilon_{sh\infty}(\tilde{T}_\tau)$  is the shrinkage correction for the effect of aging on the elastic stiffness.

### 6.2.1.5 Model GL2000

This model is purely based on empirical data. In particular, it was developed using the experimental creep data of the RILEM database [199]. The model only requires a few input parameters, namely the relative humidity, the cement type, the geometry, and the elastic modulus of the concrete. According to the model G2000, the creep compliance increases steadily, even for a large loading duration. The creep coefficient refers to the 28-day value of the elastic modulus and reads as follows:

$$\begin{aligned}
 \varphi_{c,28}(t, \tau) &= \Phi(t, t_d) \left[ 2 \left( \frac{(t - \tau)^{0.3}}{(t - \tau)^{0.3} + 14} \right) + \left( \frac{7}{\tau} \right)^{0.5} \left( \frac{t - \tau}{t - \tau + 7} \right)^{0.5} \right] \\
 &+ \Phi(t, t_d) \left[ 2.5(1 - 1.086RH^2) \left( \frac{t - \tau}{t - \tau + 0.15 \left( \frac{V}{S} \right)^2} \right)^{0.5} \right].
 \end{aligned} \tag{6.17}$$

The parameter  $\Phi(t, t_d)$  takes into account the drying of concrete before loading and is given by

$$\Phi(t, t_d) = \left[ 1 - \left( \frac{\tau - t_d}{\tau - t_d + 0.15 \left( \frac{V}{S} \right)^2} \right)^{0.5} \right]^{0.5}. \tag{6.18}$$

The creep compliance function is calculated similarly to Eq. (6.11).

A detailed overview about the input parameters for each creep model is given in Appendix A.5.

### 6.2.2 Application of the empirical creep models to PCC

Flohr [76, 353] conducted two long-term uniaxial compressive creep tests with polymer-modified concrete. Concrete cylinders with a diameter of 10 cm and a height of 30 cm were investigated. For the polymer modification, a redispersible powder (corresponds to polymer P1 used in the present thesis, see Table 4.4 for more details about the characteristics) was used. The  $p/c$ -ratio was 0.15. The experimental parameters, including the boundary conditions of the tests, are given in Table 6.3. The main differences between the two tests refer to the concrete age at which the tests started, the duration of the loading, the applied stress, and the  $w/c$ -ratio of the concretes.

In the following, it is investigated if the macroscopic creep models given in codes and guidelines are able to estimate the creep behavior of the PCC during the long-term creep tests reliably. Furthermore, both the experimentally determined and the computed strains, obtained with the empirical creep models, are compared with the response from the multiscale approach. It is evaluated if the multiscale model, which incorporates microstructural characteristics (see Section 5.3), is better able to predict the creep behavior of PCC than the models solely defined at the macroscopic material scale can.

The input parameters as given in Table 6.3 are employed; no further parameters are adapted. In contrast, Keitel et al. [6, 91] optimized the model input parameters using a quasi-Newton algorithm [7] as well as a Particle swarm optimizer [6] to minimize the coefficient of variation between experiment and model predictions. They showed that the parameter identification significantly improves the predictive capabilities of the creep models for PCC, particularly of the models B3 and ACI209. Still, such parameter calibration requires experimental data and the parameters need to be re-identified for the predictions of further experiments and of PCC with varying mixture designs. In this thesis, the formulations proposed for standard concrete were applied to the PCC, avoiding the inverse identification of model input parameters.



**Table 6.3:** Experimental parameters and boundary conditions of the long-term creep tests with PCC by Flohr [76, 353].

Parameter		Test 1	Test 2
<b>Testing conditions</b>			
Concrete age at loading $\tau$	[d]	75	265
Concrete age when drying starts $t_d$	[d]	7	7
Duration $d$	[d]	28	154
Applied stress $\sigma$	[N mm <sup>-2</sup> ]	16.4	24.8
<b>Ambient conditions</b>			
Relative humidity $RH$	[-]	0.65	0.65
Temperature $T$	[°C]	20	20
<b>Specimen</b>			
Volume-surface ratio $V/S$	[-]	2.14	2.14
<b>Concrete mixture</b>			
Cement type		CEM I 32.5 R	CEM I 32.5 R
Maximum aggregate size	[mm]	16	16
Cement content $c$	[kg m <sup>-3</sup> ]	350	350
Water content $c$	[kg m <sup>-3</sup> ]	175	143.5
Water-to-cement ratio $w/c$		0.50	0.41
Aggregate-to-cement ratio $a/c$		4.85	4.85
Fine aggregate percentage $f - a$	[%]	32	32
<b>Concrete properties</b>			
Air content $\alpha_a$	[%]	5.90	4.90
Slump $s$	[cm]	60	42
Unit weight of concrete $\gamma_c$	[kg m <sup>-3</sup> ]	2250	2350
Compressive strength at 28 days $f_{c,28,cyl}$	[N mm <sup>-2</sup> ]	28.9	36.2
Hydration degree at time $\tau$		0.78	0.80
Porosity at 90 d	[%]	14.4	10.7

The creep predictions from the multiscale model presented in this thesis follow a power-law-type creep function, as it was observed during the minutes-long creep tests. On the contrary, for loading durations of several months to several years, the creep strains evolve logarithmically [166, 354]. Logarithmic creep is expressed by a linear relation between the deformations and the logarithm of the time. The power-law-type creep, in turn, is expressed by an overlinear relation between the creep deformations and the logarithm of time [207]. According to Irfan-ul-Hassan et al. [207], the creep of cement pastes first exhibits power-law creep rates and, after an intermediate transition phase, it exhibits logarithmic creep rates. Therewith, the first part of the creep functions can be represented by means of the power law introduced in Section 5.1.5. The final part of the creep functions can be represented by means of the logarithmic function shown in Eq. (4.10) with the fitting parameters  $C$  and  $\tau$ . However, the micromechanical creep tests presented in Section 4.6.2.4 revealed that the polymer-modified cement pastes start exhibiting power-law type creep behavior at significantly later time instants than the plain reference paste. Furthermore, it is of interest to evaluate the predictive capability of the multiscale model without introducing fitted parameters. Thus, the multiscale model is employed to estimate the creep strains that the PCC exhibit during the long-term creep tests, being aware that the actual creep behavior transforms into logarithmic creep after a few weeks. As regards the polymer creep properties, the age-independent shear creep modulus and the age-independent power-law exponent according to Eq. (5.36)<sub>1</sub> are applied for the sake of convenience. The creep properties of polymer P2 are considered because it consists of the same copolymers like polymer P1.

The comparison between the experimentally determined strains and the model predictions is shown in Figure 6.3 for Test 1 and in Figure 6.4 for Test 2. As Keitel et al. [6, 91] already observed, the macroscopic creep models mostly underestimate the experimental creep strains of both Test 1 and Test 2 considerably. For Test 1, the models ACI209 and MC90 perform better than the models B3, B4, and GL2000, which predict almost no increase of the creep strains after an initial period. The models ACI209 and MC90 also provide better predictions for Test 2 than the models GL2000 and B3 do. The main reason for the unsatisfactory predictions of the macroscopic models is that the creep-magnifying effect of the polymers is not considered. Furthermore, the low stiffness of the polymer phase is not taken into account.

The multiscale approach provides predictions that are within the range of the best empirical models. For Test 1, the multiscale model response is slightly lower than for the models ACI209 and MC90. For Test 2, the multiscale prediction is very similar to those of the models ACI209 and MC90. Still, the experimental strains are also underestimated by the

multiscale model. This is related to the previously described effect that the multiscale model only covers a power-law type creep behavior. Thus, the creep estimations might be improved by introducing a logarithmic formulation. One further aspect is that the multiscale approach was originally developed for explaining non-aging short-term tests where the microstructure of the material remains constant and drying is minimized. Within the long-term creep tests, the PCC are subjected to loads for several days weeks such that the hydration process is not constant; hydration-induced microstructure changes are possible and so-called aging creep might occur. Thus, the model needs to be further extended for such cases. Recently, the Eshelby problem was extended for aging viscoelasticity [355]. Furthermore, the applied load levels were equal to 56 % of the compressive strength for Test 1 and 68 % for Test 2. Therefore, they might cause creep strains which are beyond the range of linear creep, for which the multiscale model is intended to use.

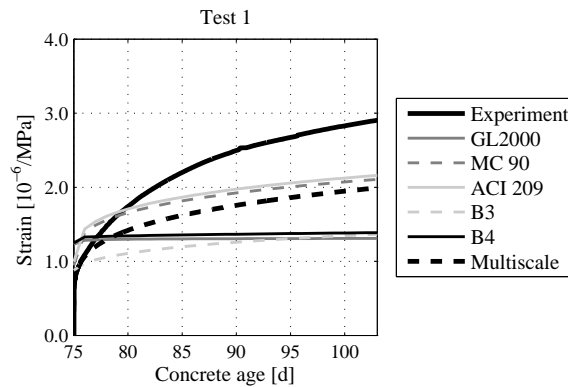


**Figure 6.3:** Experimentally determined creep strains by Flohr (Test 1) compared with the responses of empirical models and of a multiscale approach.

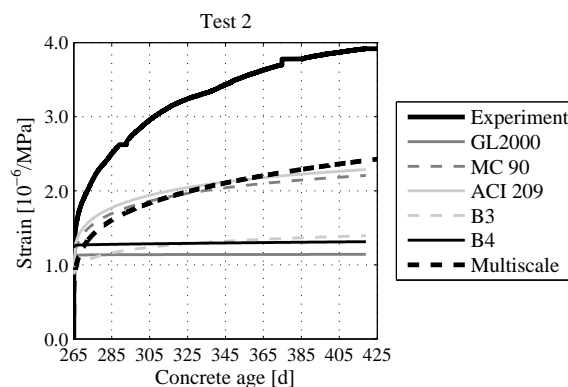


**Figure 6.4:** Experimentally determined creep strains by Flohr (Test 2) compared with the responses of empirical models and of a multiscale approach.



## 7 | Summary and conclusions

In construction, the decision for the building material concrete is increasingly dependent on its durability, sustainability, and economy. In order to fulfill the specific demands, it is required to improve the resistance capability of concrete. In this context, the modification of the binder matrix with polymers is already well established. However, the procedures to optimize the concrete performance partially entail considerable changes of the mechanical properties. Furthermore, the increasing use of new generations of concrete calls for improved prognosis models that satisfactorily estimate the mechanical behavior. Common prediction models according to guidelines and standards often only take into account the compressive strength as a decisive parameter; further material parameters, such as the elastic stiffness and the tensile strength, are not considered.

Multiscale models based on the principles of continuum micromechanics rely on the philosophy that the modeling of the macroscopic material behavior requires taking into account the underlying physical mechanisms at the microscopic scale. The aim of this thesis was to extend existing semi-analytical multiscale models to the application for polymer-modified cement-based materials. Thereupon, it was of further interest to answer whether or not the adapted multiscale model is better able to predict the mechanical behavior of such materials than macroscopic empirical models can.

As a first step, the characteristics of a semi-analytical multiscale model, which was originally developed for conventional concrete, were investigated. A probabilistic evaluation methodology comprising sensitivity and uncertainty analyses was described. On the one hand, the influences of the uncertain input parameters on the uncertainty of the model output were quantified. On the other hand, the effect of the choice concerning the hydration model was evaluated. Two hydration models were considered for the analysis: the Powers-Acker hydration model [283, 284] and the hydration model that Bernard et al. [111] proposed and Pichler et al. [116] refined. The following conclusions can be drawn:

- The uncertainty of the model response is magnified across the scales. The Young's modulus at the cement paste scale exhibits a lower uncertainty than the Young's

---

modulus at the concrete scale. This is related to the smaller number of input parameters at the lower scale. The uncertainty of the model output also increases with the maturity of the material due to ongoing hydration processes.

- The elastic parameters as well as the volume fractions of the main constituents of mortar and concrete, namely sand and aggregates, are mostly responsible for the model output uncertainty, which is underlined by their large total sensitivity indices. Besides, the chosen probabilistic parameters of the aggregates at the concrete scale affect the total order sensitivity indices considerably. In the case of applying the Bernard model, the kinetic parameters also play an important role for the Young's moduli across the scales, particularly so during early hydration stages.
- The choice of the hydration model is of rather minor importance for the uncertainty of the model output, though both hydration models require a different amount of model input parameters. The total uncertainty with respect to the Bernard model is slightly higher than that w.r.t. the Powers model, particularly for hydration degrees larger than 0.6. Thus, the Powers model, which requires a significantly smaller number of input parameters than the Bernard model, was considered for the subsequent investigations.

An experimental multiscale study was carried out to investigate the influences of the polymer modification on the mechanical behavior of cement-based materials. Besides, the experiments provided data for both model calibration and validation. Three polymers were used, differing according to the delivery form and the chemical composition. The cement pastes, mortars, and concretes were prepared with two different polymer-to-cement ratios. The study combined microstructural characterization with macroscopic (standard) testing and revealed the following results:

- First, the properties of the fresh mixtures were measured, illustrating that the polymer modification improves the workability of cement-based materials. The polymer dispersions increase the consistency more considerably than the redispersible powder. The lower viscosity of the fresh mixes is caused by the ball-bearing effect of polymer particles and of air voids, most likely entrapped during mixing due to the interaction processes between the polymers, their technical additives, and cementitious constituents. The particle sizes of the polymers are slightly lower in the dispersions than in the powder, which increases the viscosity more considerably. Surfactants further support the dispersing of the polymers in the mixtures.
- The polymer modification entails a delayed hydration process. For a given time, the degree of hydration of polymer-modified cement pastes is lowered compared with the

unmodified cement paste. Furthermore, an extended dormant period and lowered heat rates during the acceleration period are observed. The higher the  $p/c$ -ratio, the more pronounced the retardation of the hydration process is. In the literature, chemical and physical retardation mechanisms are discussed frequently.

- The microstructure of polymer-modified cement pastes is determined by both polymer and cementitious components. For a sufficiently large polymer-to-cement ratio, polymer domains embedded in between the cementitious matrix are visible. In dependence on the minimum film forming temperature, the polymers are coalesced and might form films. It was also found that the same dosage of different polymers may cause different amounts of entrapped air in the hardened cement-based materials. This is caused by polymer-cement interactions, particularly by the technical additives that the polymers contain. Usually, they are not known explicitly, rendering general statements on the influences of polymers on cement-based materials difficult.
- The polymer-modified materials exhibit lower compressive strengths and elastic moduli than the plain mixtures for a given water-to-cement ratio do. The higher the polymer content, the lower are those mechanical quantities. This is the result of (i) the delayed hydration process, (ii) the small stiffness of the polymers and, for some polymer types, (iii) the increased porosity resulting from interactions between the polymers, their additives, and the cement or the aggregates. The increased creep activity might result from (i) possible sliding effects of the polymers within the binder matrix and (ii) the increased stress concentration into cement hydrates due to entrapped air.
- The experimental results obtained with macroscopic mechanical tests are confirmed via nanoindentation investigations. The mean indentation moduli of the polymer-modified cement pastes decrease with increasing  $p/c$ -ratio. Nanoindentation creep tests also underline that the polymer modification leads to a more pronounced creep behavior. The more polymers added, the larger are the displacements that the specimens subjected to a sustained load exhibited. These trends were also observed in mechanical tests with macroscopic specimens. Therefore, the nanoindentation tests provide reliable estimations of the mechanical behavior of macroscopic specimens of cement-based materials for different polymer modifications and  $p/c$ -ratios. One further advantageous aspect is that the nanoindentation tests are less time-consuming than standard mechanical tests and require only millimeter- or centimeter-sized samples, such that a smaller amount of raw materials is needed.

---

Particular attention was paid to the early-age elastic and creep behavior of PCC. A recently developed experimental campaign [207] was carried out and extended to PCC. The focus was set on the linear creep of undamaged specimens so that load levels being equal or smaller than 7.5% of the estimated compressive strength at time instant of testing were applied. The elastic and creep properties were quantified quasi-continuously from material ages of 21 hours up to eight days, revealing the following results:

- The polymer-modified cement pastes and concretes exhibit smaller Young's moduli than the unmodified reference mixtures do.
- The creep behavior of the polymer-modified cement pastes and concretes is more pronounced relative to the plain mixtures, which is shown by the smaller creep moduli and the larger creep compliance compared with the reference. At very early sample ages (up to 30 hours), the creep strains of the polymer-modified cement pastes are up to four times higher than those of the reference. At 150 hours, they are still two times higher.
- The power-law exponent is less sensitive to the mixture design than the elastic modulus and the creep modulus; it is virtually the same for all three investigated mixes.

The experimental data were exploited for the extension of an existing semi-analytical multiscale model to polymer-modified cement-based materials. Different aspects of the multiscale modeling of PCC are discussed in this thesis:

- A standard multiscale model for the representation of the elastic stiffness, strength, and creep properties of hydrating cement pastes was extended towards consideration of polymer particles and entrapped air. The polymers are introduced as spheres at the scale of hydrate foam. The spherical air voids enter the larger scale of cement paste.
- The evolutions of the volume fractions in polymer-modified cement pastes can be estimated based on the Powers model, which is extended towards the consideration of a constant polymer volume fraction and of entrapped air porosity.
- The elastic stiffness of the polymers, which was determined by means of nanoindentation tests on polymer films, is by one magnitude lower than of the cementitious constituents. Thus, the polymers - micromechanically - more or less act as a pore phase within the cementitious network.



- Homogenization methods of continuum micromechanics were shown to be useful when it comes to the estimation of the early-age evolution of the elastic stiffness of PCC. Special attention deserves the interaction of the polymers and their additives with the other raw materials, which may result in entrapping a significant amount of air during the production. This porosity needs to be appropriately considered in the multiscale model.
- The semi-analytical multiscale approach also allows to explain the micromechanical origin of the pronounced creep activity of polymer-modified cement-based materials. An isochoric power-law-type creep function for the polymers was applied to identify the polymer creep properties. Based on the experimentally obtained creep functions, a top-down identification was performed. It was observed that the shear creep modulus of the polymers is by two orders of magnitude smaller than that of the hydration products is. In contrast to the hydrates that exhibit universal creep properties, the polymer creep properties are age-dependent and evolve with the hydration process. The creep activity of the polymers decreases with the time which is most likely related to the self-desiccation of the cement paste due to the water-consuming hydration reaction and the continuous decrease of the internal relative humidity in hydrating cement pastes. Further microstructural affects, such as the polymer film formation and the growth of the hydrates into polymer agglomerates, appear to be involved.
- Notably, the experimentally determined macroscopic creep behavior of hydrating polymer-modified cement-based materials can be satisfactorily reproduced when considering that the power-law creep exponent of the polymer particles is age-independent and, thus, constant. In that case, the shear creep modulus of the polymer particles was found to follow a bilinear trend during the first week after production. Considering that both the shear creep modulus and the creep exponent of the polymers are age-dependent and, thus, evolving functions, improves the agreement between modeling results and experiments, but at the cost of considerable additional computational efforts.

The predictive capability of the proposed semi-analytical multiscale model for polymer-modified cement-based materials was compared with empirical macroscopic models aimed at the prediction of the elastic stiffness and of concrete creep strains. The following observations were made:

- The empirical models satisfactorily predict the Young's modulus of PCC with a  $p/c$ -ratio of 0.05. The predictive capability of the models is worse for PCC with a

---

$p/c$ -ratio of 0.20. The multiscale model performs slightly better than the empirical models and exhibits a smaller mean absolute percentage error for PCC with a  $p/c$ -ratio of 0.05. Its predictive capability is almost as good as the empirical models with the smallest prediction errors for PCC with a  $p/c$ -ratio of 0.20.

- Regarding creep, the empirical models according to guidelines and standards clearly underestimate the creep strains of polymer-modified concrete during long-term creep tests.
- The multiscale approach provides predictions that are within the range of the best empirical models. The multiscale model might be improved by considering the water-migration model of Irfan-ul-Hassan et al. [227], by extending its applicability to nonlinear creep, and by taking into account aging viscoelasticity.

In summary, a significant amount of knowledge has been gained. The multiscale model based on continuum micromechanics turned out to be a valuable method in predicting elastic and creep properties of polymer-modified cement-based materials across the scales. Very remarkably, the multiscale model can be applied to PCC with differing polymer modifications and polymer contents. Thus, the model may help to reduce the number of tests characterizing the elastic and viscoelastic behavior of polymer-modified cement-based materials in the future. Estimations for the influences of different polymers on the elastic moduli and the creep behavior of cement pastes, mortars, and concretes can be obtained based on the model. The development of reliable prognosis models for PCC represents an important step towards the use in construction and accelerates their implementation in guidelines.

## 8 | Outlook

There is still a lot of motivation for future research on polymer-modified cement-based materials and their modeling and simulation.

Besides the elasticity and creep, the uniaxial compressive strength is the main mechanical property for the design of structures, and it is commonly used in codes and guidelines. Thus, the multiscale model for polymer-modified cement-based materials should be extended for the prediction of the compressive strength. Several approaches that relate the microscopic failure mode to the macroscopic strength of conventional cement-based materials have already been proposed [108, 109, 134, 110].

The knowledge about the microstructural formation of polymer-modified cement-based materials is prerequisite for the development of multiscale prediction models. By means of advanced microscopic or tomography methods, the microstructure of PCC could be investigated in more detail. It could be answered if and which types of organic-inorganic compounds, as mentioned in the literature, e.g. [56], are formed. Their existence could be also studied by means of nanoindentation testing coupled with SEM-EDS analyses. Such experimental setups already proved the existence of C-S-H / Portlandite composites. Furthermore, the shape of the hydration products during the hydration process in the presence of polymers could be investigated using ESEM, cryo-SEM, or soft X-ray transmission microscopy. Therewith, the nucleation and the growth of the cementitious crystals could be observed. The information could be used to improve the morphological representation of polymer-modified cement pastes in the context of multiscale modeling. Instead of solely modeling the hydrates as needles, an maturity-dependent shape of the hydrates could be introduced to account for the inhibited formation of the hydrates in the presence of polymers, as claimed by Silva et al. [40]. Similar approaches have already been proposed by Königsberger et al. [141] for conventional cement pastes, referred to as C-S-H densification model.

The data obtained from high resolution X-ray micro-computed tomography measurements with polymer-modified cement pastes could be used to generate a three-dimensional

---

(3D) digital microstructure of the material, consisting of unhydrated clinker particles, hydration products, pore space, and a polymer phase. With that, a representative volume element could be defined and mechanical properties, such as the elastic modulus, could be predicted using 3D finite element analysis. This microstructure-based modeling of the effective mechanical properties turned out to be successful for conventional cement pastes [356, 357, 358]. The applicability of this approach to polymer-modified cement-based materials needs to be proven. FEM simulations also open the door for predictions of construction components made of PCC.

The focus of the experimental creep campaign presented herein was the linear creep. Still, the nonlinear creep is of great importance for PCC and thus, deserves a deeper investigation. The creep tests could be repeated at load levels higher than 30% of the concrete compressive strength. Furthermore, the multiscale prediction model could be extended for the range of nonlinear creep, including material failure at microscopic scales.

The mechanical properties of polymer-modified cement-based materials are dependent on the temperature because of the strong temperature dependency of the polymers. To encourage the application of PCC in construction, the mechanical behavior at different environmental conditions should be known. Thus, the mechanical properties of PCC could be determined at elevated temperatures. In particular, the microstructural formation at different temperatures could be studied. Within this context, the behavior of PCC exposed to fire is of further interest. The semi-analytical multiscale model could be extended for the consideration of temperature effects.

# Bibliography

- [1] H. Klee. *The cement sustainability initiative: recycling concrete: Report of the World Business Council for Sustainable Development*. World Business Council for Sustainable Development, Conches-Geneva, 2009.
- [2] Y. Ohama and V. S. Ramachandran. Polymer-modified mortars and concretes: Properties and process technology. In V. S. Ramachandran, editor, *Concrete Admixtures Handbook*. 1996.
- [3] P. S. Mangat, R. Baggott, and D. A. Evans. Creep characteristics of polymer modified concrete under uniaxial compression. *3rd International Congress of Polymers in Concrete, Koriyama, Japan*, pages 193–208, 1982.
- [4] A. Çolak. Properties of plain and latex modified Portland cement pastes and concretes with and without superplasticizer. *Cement and Concrete Research*, 35(8):1510–1521, 2005.
- [5] T. Heidolf. *Zeit- und beanspruchungsabhängiges Tragverhalten von polymermodifiziertem Beton unter mehrfach wiederholter Beanspruchung*. Dissertation, Bauhaus-Universität, Weimar, Germany, 2007.
- [6] H. Keitel and A. Dimmig-Osburg. Prediction of creep deformation of PCC using models of standard cement concrete. In J. Barroso de Aguiar, S. Jalali, A. Camoes, and R. M. Ferreira, editors, *13th International Congress on Polymers in Concrete, Madeira, Portugal*, 2010.
- [7] H. Keitel, A. Dimmig-Osburg, and V. Zabel. Characterization of Time-dependent Deformations of Polymer Modified Cement Concrete (PCC). In K. Gürlebeck and C. Könke, editors, *18th International Conference on the Application of Computer Science and Mathematics in Architecture and Civil Engineering, Weimar, Germany*, 2009.

- [8] S. Akihama, H. Morita, S. Watanabe, and H. Chita. Improvement of Mechanical Properties of Concrete Through the Additions of Polymer Latex. *Special Publication*, 40:319–338, 1973.
- [9] S. Chandra and Y. Ohama. *Polymers in Concrete*. CRC Press, Boca Raton, Florida, 1994.
- [10] A. Dimmig-Osburg, U. Freundt, A. Flohr, D. Michael, and K. A. Bode. Use of Polymer-modified Concrete in Bridge Construction, Part I. *Concrete Plant and Precast Technology*, 76(6):42–55, 2010.
- [11] A. Dimmig-Osburg, U. Freundt, A. Flohr, K. A. Bode, and D. Michael. Use of Polymer-modified Concrete in Bridge Construction - Part II. *Concrete Plant and Precast Technology*, 77(6):30–39, 2011.
- [12] A. Dimmig-Osburg. Innovations Based on PCC. *Advanced Materials Research*, 687:369–377, 2013.
- [13] D. W. Fowler. Polymers in concrete: A vision for the 21st century. *Cement and Concrete Composites*, 21:449–452, 1999.
- [14] Y. Ohama, D. van Gemert, and M. Ota. Introducing process technology and applications of polymer-modified mortar and concrete in construction. *International Journal for Restoration of Buildings and Monuments*, 19(6):369–392, 2013.
- [15] A. Dimmig. *Einflüsse von Polymeren auf die Mikrostruktur und die Dauerhaftigkeit kunststoffmodifizierter Mörtel (PCC)*. Dissertation, Bauhaus-Universität, Weimar, Germany, 2002.
- [16] D. Urban and K. Takamura. *Polymer dispersions and their industrial applications*. Wiley VCH-Verlag, Weinheim, 2002.
- [17] W.-P. Ettl. *Kunstharze und Kunststoffdispersionen für Mörtel und Betone: Struktur der Polymere, Planung, Bemessung, Prüfung*. Beton-Verlag, Düsseldorf, 1998.
- [18] Y. Ohama. Polymer-based Admixtures. *Cement and Concrete Composites*, 20:189–212, 1998.
- [19] E. W. Nägele. *Dispersions-Baustoffe*. Müller, 1989.
- [20] U. Schirmer and A. Osburg. Interactions between non-ionic additives and cement phases. *Advanced Materials Research*, 1129:492–499, 2015.

- 
- [21] U. Schirmer. *Die Adsorption von Dispersionspartikeln und Schutzkolloiden an Oberflächen von Zementphasen und Phasen der Zusatzstoffe*. Dissertation, Bauhaus-Universität, Weimar, Germany, 2018.
- [22] A. Dimmig, B. Rothenhäusser, and S. Sachsse. The influence of redispersibility and of the polymer powders composition on the freeze-thaw resistance of polymer modified mortar. In H.-B. Fischer and J. Stark, editors, *14th Internationale Baustofftagung, Weimar, Germany*, pages 2.1095–2.1103, 2000.
- [23] P.A. Steward, J. Hearn, and M.C. Wilkinson. An overview of polymer latex film formation and properties. *Advances in Colloid and Interface Science*, 86(3):195–267, 2000.
- [24] M. Gretz and J. Plank. An ESEM investigation of latex film formation in cement pore solution. *Cement and Concrete Research*, 41(2):184–190, 2011.
- [25] S. Erkselius, L. Wadsö, and O. J. Karlsson. Drying rate variations of latex dispersions due to salt induced skin formation. *Journal of colloid and interface science*, 317(1):83–95, 2008.
- [26] S. Ugur and M. S. Sunay. Investigation of particle size effect on film formation of polystyrene latexes using fluorescence technique. *Colloids and Surfaces A: Physicochemical and Engineering Aspects*, 510:283–292, 2016.
- [27] A. Dimmig-Osburg. Neues Modell der Ausbildung der Mikrostruktur kunststoffmodifizierter Mörtel. *Betonwerk + Fertigteil-Technik BFT*, 71(10):26–36, 2005.
- [28] F. Merlin, H. Guitouni, H. Mouhoubi, S. Mariot, F. Vallée, and F. van Damme. Adsorption and heterocoagulation of nonionic surfactants and latex particles on cement hydrates. *Journal of colloid and interface science*, 281(1):1–10, 2005.
- [29] J. Plank and M. Gretz. Study on the interaction between anionic and cationic latex particles and portland cement. *Colloids and Surfaces A: Physicochemical and Engineering Aspects*, 330(2–3):227–233, 2008.
- [30] S. Chandra and P. Flodin. Interactions of polymers and organic admixtures on Portland cement hydration. *Cement and Concrete Research*, 17(6):875–890, 1987.
- [31] H. Ma, Y. Tian, and Z. Li. Interactions between Organic and Inorganic Phases in PA- und PU/PA-Modified-Cement-Based Materials. *Journal of Materials in Civil Engineering*, 23(10):1412–1421, 2011.

- [32] S. Baueregger, M. Perello, and J. Plank. Role of PVOH and kaolin on colloidal stability of liquid and powder EVA and SB latexes in cement pore solution. *Colloids and Surfaces A: Physicochemical and Engineering Aspects*, 434:145–153, 2013.
- [33] Y. Jin. *Interaction between vinyl acetate-ethylene latex stabilized with polyvinyl alcohol and Portland cement*. Dissertation, Technische Universität, Berlin, Germany, 2016.
- [34] J. A. Larbi and J.M.J.M. Bijen. Interaction of polymers with Portland cement during hydration: A study of the chemistry of the pore solution of polymer-modified cement systems. *Cement and Concrete Research*, 20(1):139–147, 1990.
- [35] Z. Su, J.M.J.M. Bijen, and J. A. Larbi. Influence of polymer modification on the hydration of portland cement. *Cement and Concrete Research*, 21(4):535–544, 1991.
- [36] Z. Su. *Microstructure of Polymer Cement Concrete*. Dissertation, University of Technology, Delft, The Netherlands, 1995.
- [37] J. Cheung, A. Jeknavorian, R. Roberts, and D. A. Silva. Impact of admixtures on the hydration kinetics of portland cement. *Cement and Concrete Research*, 41(12):1289–1309, 2011.
- [38] K. M. Atkins, R. N. Edmonds, and A. J. Majumdar. The hydration of Portland and aluminous cements with added polymer dispersions. *Journal of Materials Science*, 26:2372–2378, 1991.
- [39] S. Zeng, N. R. Short, and C. L. Page. Early-age hydration kinetics of polymer-modified cement. *Advances in Cement Research*, 8(29):1–9, 1996.
- [40] D. A. Silva and P.J.M. Monteiro. Hydration evolution of C<sub>3</sub>S–EVA composites analyzed by soft X-ray microscopy. *Cement and Concrete Research*, 35(2):351–357, 2005.
- [41] D. A. Silva and P.J.M. Monteiro. The influence of polymers on the hydration of Portland cement phases analyzed by soft X-ray transmission microscopy. *Cement and Concrete Research*, 36(8):1501–1507, 2006.
- [42] D. Jansen, F. Götz-Neunhoeffler, J. Neubauer, and W.-D. Hergeth. XRD in-situ Untersuchungen zum Einfluss von Polymeren auf die Ettringit-Bildung in zementären Systemen. *Voneinander lernen - Innovationen in Bauchemie und Lackchemie*, pages 353–354, 2008.



- 
- [43] R. Wang, X.-G. Li, and P.-M. Wang. Influence of polymer on cement hydration in SBR-modified cement pastes. *Cement and Concrete Research*, 36(9):1744–1751, 2006.
- [44] R. Wang, L. Yao, and P.-M. Wang. Mechanism analysis and effect of styrene-acrylate copolymer powder on cement hydrates. *Construction and Building Materials*, 41:538–544, 2013.
- [45] M. Wang, R. Wang, H. Yao, S. Farhan, S. Zheng, Z. Wang, C. Du, and H. Jiang. Research on the mechanism of polymer latex modified cement. *Construction and Building Materials*, 111:710–718, 2016.
- [46] X. Kong, S. Emmerling, J. Pakusch, M. Rueckel, and J. Nieberle. Retardation effect of styrene-acrylate copolymer latexes on cement hydration. *Cement and Concrete Research*, 75:23–41, 2015.
- [47] X. Kong, J. Pakusch, D. Jansen, S. Emmerling, J. Neubauer, and F. Goetz-Neuhoeffer. Effect of polymer latexes with cleaned serum on the phase development of hydrating cement pastes. *Cement and Concrete Research*, 84:30–40, 2016.
- [48] S. Baueregger, M. Perello, and J. Plank. Impact of carboxylated styrene–butadiene copolymer on the hydration kinetics of OPC and OPC/CAC/AH: The effect of  $\text{Ca}^{2+}$  sequestration from pore solution. *Cement and Concrete Research*, 73:184–189, 2015.
- [49] D. van Gemert and A. Beeldens. Evolution in modeling microstructure formation in polymer-cement concrete. *Restoration of Buildings and Monuments*, 19(2-3):97–108, 2013.
- [50] Y. Ohama. Principle of latex modification and some typical properties of latex-modified mortars and concretes adhesion; binders (materials); bond (paste to aggregate); carbonation; chlorides; curing; diffusion;. *Materials Journal*, 84(6), 1987.
- [51] J. Bijen and Z. Su. Polymer cement concrete: a contribution to modeling of the microstructure. *Proceedings of TC 113, Symposium on properties and test methods for concrete-polymer composites, Oostende (Belgium)*, pages 19–27, 1995.
- [52] E. Sakai and J. Sugita. Composite mechanism of polymer modified cement. *Cement and Concrete Research*, 25(1):127–135, 1995.
- [53] M. Puterman and W. Malorny. Some doubts and ideas on the microstructure formation of PCC. In F. Saudrolini, editor, *Proceedings of IX International Congress on Polymers in Concrete*, pages 167–178, 1998.

- [54] H. Schorn and M. Schiekkel. Shape and distribution of polymer particles in PCC, investigated by ESEM. In D. Fowler, editor, *Proceedings of 10th ICPIIC*, 2001.
- [55] M. U. K. Afridi, Y. Ohama, K. Demura, and M. Z. Iqbal. Development of polymer films by the coalescence of polymer particles in powdered and aqueous polymer-modified mortars. *Cement and Concrete Research*, 33(11):1715–1721, 2003.
- [56] A. Beeldens, D. van Gemert, H. Schorn, Y. Ohama, and L. Czarnecki. From microstructure to macrostructure: an integrated model of structure formation in polymer-modified concrete. *Materials and Structures*, 38:601–607, 2005.
- [57] A. Dimmig-Osburg, I. Pietsch, and J. Pietsch. Polymer additives and their influence on the cement microstructure in the early stage of hardening. *ZKG International*, 59(5):72–83, 2006.
- [58] A. Dimmig-Osburg. Microstructure of PCC - Effects of polymer components and additives. In K.-S. Yeon, editor, *Proceedings of the 12th International Congress on Polymers in Concrete*, volume Vol. 1, September 27-28, 2009.
- [59] Y. Tian, X.-y. Jin, N.-g. Jin, R. Zhao, Z.-j. Li, and H.-y. Ma. Research on the microstructure formation of polyacrylate latex modified mortars. *Construction and Building Materials*, 47(Supplement C):1381–1394, 2013.
- [60] H. Ma and Z. Li. Microstructures and mechanical properties of polymer modified mortars under distinct mechanisms. *Construction and Building Materials*, 47:579–587, 2013.
- [61] K. L. Scrivener, A. K. Crumbie, and P. Laugesen. The Interfacial Transition Zone (ITZ) Between Cement Paste and Aggregate in Concrete. *Interface Science*, 12(4):411–421, 2004.
- [62] S. Wei, J. A. Mandel, and S. Said. Study of the interface strength in steel fiber-reinforced cement-based composites. *Journal Proceedings*, 83(4), 1986.
- [63] J.M.J.M. Bijen. Polymeren in Beton: Polymers in Concrete. *Cement*, 5:60–69, 1991.
- [64] F. Xu, M. Zhou, J. Chen, and S. Ruan. Mechanical performance evaluation of polyester fiber and SBR latex compound-modified cement concrete road overlay material. *Construction and Building Materials*, 63:142–149, 2014.
- [65] K. A. Bode. *Aspekte der kohäsiven und adhäsiven Eigenschaften von PCC*. Dissertation, Bauhaus-Universität, Weimar, 2009.

- 
- [66] Y. Ohama, K. Demura, K. Kobayashi, Y. Satoh, and M. Morikawa. Pore size distribution and oxygen diffusion resistance of polymer-modified mortars. *Cement and Concrete Research*, 21(2):309–315, 1991.
- [67] Y. Ohama, K. Demura, M. Hamatsu, and M. Kakegawa. Properties of Polymer-Modified Mortars Using Styrene-Butyl Acrylate Latexes With Various Monomer Ratios. *Materials Journal*, 88(1), 1991.
- [68] I. Ray, A. P. Gupta, and M. Biswas. Physicochemical studies on single and combined effects of latex and superplasticiser on portland cement mortar. *Cement and Concrete Composites*, 18:343–355, 1996.
- [69] M. Ramli and A. A. Tabassi. Effects of polymer modification on the permeability of cement mortars under different curing conditions: A correlational study that includes pore distributions, water absorption and compressive strength. *Construction and Building Materials*, 28(1):561–570, 2012.
- [70] G. Barluenga and F. Hernández-Olivares. SBR latex modified mortar rheology and mechanical behaviour. *Cement and Concrete Research*, 34(3):527–535, 2004.
- [71] F. Eren, E. Gödek, M. Keskinates, K. Tosun-Felekoğlu, and B. Felekoğlu. Effects of latex modification on fresh state consistency, short term strength and long term transport properties of cement mortars. *Construction and Building Materials*, 133:226–233, 2017.
- [72] S. Kubens and O. H. Wallevik. The effect of polymer emulsion on rheological properties of pcc mixtures. In J. Barroso de Aguiar, S. Jalali, A. Camoes, and R. M. Ferreira, editors, *13th International Conference on Polymers in Concrete*, pages 313–320, February 10-12, 2010.
- [73] M. Gierloff. *Beeinflussung von Betoneigenschaften durch Zusatz von Kunststoffdispersionen*. Dissertation, Technische Universität, Berlin, Germany, 1983.
- [74] H. Schorn. *Betone mit Kunststoffen und anderen Instandsetzungsbaustoffen: ein baustoffliches Lehrbuch mit Kommentaren zum Technischen Regelwerk*. Ernst & Sohn-Verlag für Architektur und technische Wissenschaften, Berlin, 1990.
- [75] R. Wang and P. Wang. Function of styrene-acrylic ester copolymer latex in cement mortar. *Materials and Structures*, 43(4):443–451, 2010.

- [76] A. Flohr. *Der Einfluss von Polymermodifikationen, unterschiedlichen Gesteinskörnungen und Gesteinskörnungssubstitutionsmaterial auf das Verformungs- und Bruchverhalten von Beton*. Dissertation, Bauhaus-Universität, Weimar, Germany, 2013.
- [77] M. M. Al-Zahrani, M. Maslehuddin, S. U. Al-Dulaijan, and M. Ibrahim. Mechanical properties and durability characteristics of polymer- and cement-based repair materials. *Cement and Concrete Composites*, 25(4–5):527–537, 2003.
- [78] B. Chen and J. Liu. Mechanical properties of polymer-modified concretes containing expanded polystyrene beads. *Construction and Building Materials*, 21(1):7–11, 2007.
- [79] A. Konietzko. *Polymerspezifische Auswirkungen auf das Tragverhalten modifizierter zementgebundener Betone (PCC)*. Dissertation, Technische Universität, Braunschweig, Germany, 1988.
- [80] L. Lohaus and S. Anders. Effects of polymer modification on the mechanical and fracture properties of high and ultra-high strength concrete. *International Congress on Polymers in Concrete*, 2(4):183–190, 2004.
- [81] M. Doğan and A. Bideci. Effect of Styrene Butadiene Copolymer (SBR) admixture on high strength concrete. *Construction and Building Materials*, 112:378–385, 2016.
- [82] L. Bureau, A. Alliche, P. Pilvin, and S. Pascal. Mechanical characterization of a styrene-butadiene modified mortar. *Materials Science and Engineering: A*, 308:233–240, 2001.
- [83] A. A. E. Aliabdo and A. E. M. Abd-Elmoaty. Experimental investigation on the properties of polymer modified SCC. *Construction and Building Materials*, 34:584–592, 2012.
- [84] K. P. Grosskurth. Morphology and Long Term Behavior of Polymer Cement Concrete. *MRS Proceedings*, 179:273–281, 1989.
- [85] B. Muhammad, M. Ismail, A. A. Yussuf, and A.R.B. Muhammad. Elastomeric influence of natural rubber latex on cement mortar at high temperatures using thermal degradation analysis. *Construction and Building Materials*, 25(5):2223–2227, 2011.
- [86] A. Muthadhi and S. Kothandaraman. Experimental investigations on polymer-modified concrete subjected to elevated temperatures. *Materials and Structures*, 47(6):977–986, 2014.

- 
- [87] A. G. Bishara, J. D. Rose, and Y.M.A Read. Shrinkage and creep characteristics of latex-modified concrete. *Journal of American Concrete Institute*, 75(5):204–208, 1978.
- [88] V. Bokan-Bosiljkov and F. Saje. Creep of polymer-cement concrete at normal and elevated temperatures. *Journal of Mechanical Behavior of Materials*, 9(2):147–161, 1998.
- [89] T. Heidolf. Zeitvariantes Trag- und Schädigungsverhalten von mehrfach wiederholt beanspruchtem polymermodifizierten Beton (PCC). *Beton- und Stahlbetonbau*, 104(11):706–716, 2009.
- [90] A. Flohr and A. Dimmig-Osburg. Study on the load-deformation behavior of modified cement concrete. *Advanced Materials Research*, 687:198–203, 2013.
- [91] H. Keitel. *Bewertungsmethoden für die Prognosequalität von Kriechmodellen des Betons*. Dissertation, Bauhaus-Universität, Weimar, Germany, 2011.
- [92] N. B. Eden and J. E. Bailey. The mechanical properties and tensile failure mechanism of a high strength polymer modified portland cement. *Journal of Materials Science*, 19(8):2677–2690, 1984.
- [93] L. Göbel, A. Osburg, and T. Lahmer. Study of analytical models of the mechanical behavior of polymer-modified concrete. In K. Gürlebeck and T. Lahmer, editors, *20th International Conference on the Application of Computer Science and Mathematics in Architecture and Civil Engineering*, Weimar, Germany, 2015.
- [94] J. F. Unger and S. Eckardt. Multiscale modeling of concrete. *Archives of Computational Methods in Engineering*, 18:341–393, 2011.
- [95] M. Shahidi, B. Pichler, and C. Hellmich. Viscous interfaces as source for material creep: A continuum micromechanics approach. *European Journal of Mechanics - A/Solids*, 45:41–58, 2014.
- [96] C. Pichler. *Multiscale characterization and modeling of creep and autogeneous shrinkage of early-age cement-based materials*. Dissertation, Technische Universität, Wien, Austria, 2007.
- [97] M. F. Horstemeyer. Multiscale modeling: A review. In J. Leszczynski and M. K. Shukla, editors, *Practical Aspects of Computational Chemistry: Methods, Concepts and Applications*, pages 87–135. Springer Netherlands, Dordrecht, 2010.

- [98] G. A. Pavliotis and A. Stuart. *Multiscale methods: Averaging and homogenization*. Springer Science & Business Media, New York, USA, 2008.
- [99] C. K. Lee, C.-C. Sun, and C. C. Mei. Computation of permeability and dispersivities of solute or heat in periodic porous media. *International Journal of Heat and Mass Transfer*, 39(4):661–676, 1996.
- [100] N. Bakhvalov and G. Panasenko. *Homogenisation: Averaging Processes in Periodic Media: Mathematical Problems in the Mechanics of Composite Materials*. Springer Science & Business Media, 2012.
- [101] P. Kanouté, D. P. Boso, J. L. Chaboche, and B. A. Schrefler. Multiscale methods for composites: A review. *Archives of Computational Methods in Engineering*, 16(1):31–75, 2009.
- [102] J. Füssl, R. Lackner, J. Eberhardsteiner, and H. A. Mang. Failure modes and effective strength of two-phase materials determined by means of numerical limit analysis. *Acta Mechanica*, 195:185–202, 2008.
- [103] M. Hlobil, V. Šmilauer, and G. Chanvillard. Micromechanical multiscale fracture model for compressive strength of blended cement pastes. *Cement and Concrete Research*, 83:188–202, 2016.
- [104] L. Contrafatto, M. Cuomo, and S. Gazzo. A concrete homogenisation technique at meso-scale level accounting for damaging behaviour of cement paste and aggregates. *Computers & Structures*, 173:1–18, 2016.
- [105] J. D. Eshelby. The determination of the elastic field of an ellipsoidal inclusion, and related problems. *Proceedings of the Royal Society of London A: Mathematical, Physical and Engineering Sciences*, 241(1226):376–396, 1957.
- [106] B. Pichler, S. Scheiner, and C. Hellmich. From micron-sized needle-shaped hydrates to meter-sized shotcrete tunnel shells: micromechanical upscaling of stiffness and strength of hydrating shotcrete. *Acta Geotechnica*, 3(4):273–294, 2008.
- [107] B. Pichler and C. Hellmich. Upscaling quasi-brittle strength of cement paste and mortar: A multi-scale engineering mechanics model. *Cement and Concrete Research*, 41(5):467–476, 2011.
- [108] M. Königsberger, B. Pichler, C. Hellmich, and J. Olek. Micromechanics of ITZ-Aggregate Interaction in Concrete Part I: Stress Concentration. *Journal of the American Ceramic Society*, 97(2):535–542, 2014.

- [109] M. Königsberger, B. Pichler, C. Hellmich, and J. Olek. Micromechanics of ITZ-Aggregate Interaction in Concrete Part II: Strength Upscaling. *Journal of the American Ceramic Society*, 97(2):543–551, 2014.
- [110] M. Königsberger, M. Hlobil, B. Delsaute, S. Staquet, C. Hellmich, and B. Pichler. Hydrate failure in ITZ governs concrete strength: A micro-to-macro validated engineering mechanics model. *Cement and Concrete Research*, 103:77–94, 2018.
- [111] O. Bernard, F.-J. Ulm, and E. Lemarchand. A multiscale micromechanics-hydration model for the early-age elastic properties of cement-based materials. *Cement and Concrete Research*, 33(9):1293–1309, 2003.
- [112] G. Constantinides and F.-J. Ulm. The effect of two types of C-S-H on the elasticity of cement-based materials: Results from nanoindentation and micromechanical modeling. *Cement and Concrete Research*, 34(1):67–80, 2004.
- [113] J. Sanahuja, L. Dormieux, and G. Chanvillard. Modelling elasticity of a hydrating cement paste. *Cement and Concrete Research*, 37(10):1427–1439, 2007.
- [114] J. Lee, Y. Xi, K. Willam, and Y. Jung. A multiscale model for modulus of elasticity of concrete at high temperatures. *Cement and Concrete Research*, 39(9):754–762, 2009.
- [115] M. Shahidi, B. Pichler, and C. Hellmich. How interface size, density, and viscosity affect creep and relaxation functions of matrix-interface composites: a micromechanical study. *Acta Mechanica*, 227:229–252, 2016.
- [116] C. Pichler, R. Lackner, and H. A. Mang. A multiscale micromechanics model for the autogenous-shrinkage deformation of early-age cement-based materials. *Engineering Fracture Mechanics*, 74(1-2):34–58, 2007.
- [117] C. Pichler and R. Lackner. A multiscale creep model as basis for simulation of early-age concrete behavior. *Computers and Concrete*, 5(4):295–328, 2008.
- [118] S. Scheiner and C. Hellmich. Continuum microviscoelasticity model for aging basic creep of early-age concrete. *Journal of Engineering Mechanics*, 135(4):307–323, 2009.
- [119] J. Sanahuja. Effective behaviour of ageing linear viscoelastic composites: Homogenization approach. *International Journal of Solids and Structures*, 50(19):2846–2856, 2013.

- [120] M. Königsberger, M. Irfan-ul Hassan, B. Pichler, and C. Hellmich. Downscaling based identification of nonaging power-law creep of cement hydrates. *Journal of Engineering Mechanics*, 142(12):4016106, 2016.
- [121] F. Lavergne, K. Sab, J. Sanahuja, M. Bornert, and C. Toulemonde. An approximate multiscale model for aging viscoelastic materials exhibiting time-dependent poisson's ratio. *Cement and Concrete Research*, 86:42–54, 2016.
- [122] A. Zaoui. Continuum mechanics: A survey. *Journal of Engineering Mechanics*, 128(8):808–816, 2002.
- [123] A. V. Hershey. The elasticity of an isotropic aggregate of anisotropic cubic crystals. *Journal of Applied Mechanics*, 21:236, 1954.
- [124] R. Hill. Elastic properties of reinforced solids: Some theoretical principles. *Journal of the Mechanics and Physics of Solids*, 11(5):357–372, 1963.
- [125] E. Kröner. Bounds for effective elastic moduli of disordered materials. *Journal of the Mechanics and Physics of Solids*, 25(2):137–155, 1977.
- [126] L. Dormieux, D. Kondo, and F.-J. Ulm. *Microporomechanics*. John Wiley & Sons, 2006.
- [127] W. R. Drugan and J. R. Willis. A micromechanics-based nonlocal constitutive equation and estimates of representative volume element size for elastic composites. *Journal of the Mechanics and Physics of Solids*, 44(4):497–524, 1996.
- [128] L. Göbel, A. Osburg, and B. Pichler. The mechanical performance of polymer-modified cement pastes at early ages: ultra-short non-aging creep tests and multiscale homogenization. *Construction and Building Materials*, 173:495–507, 2018.
- [129] B. Pichler, C. Hellmich, and J. Eberhardsteiner. Spherical and acicular representation of hydrates in a micromechanical model for cement paste: prediction of early-age elasticity and strength. *Acta Mechanica*, 203(3-4):137–162, 2009.
- [130] F.-J. Ulm and H. M. Jennings. Does C–S–H particle shape matter? A discussion of the paper ‘Modelling elasticity of a hydrating cement paste’, by Julien Sanahuja, Luc Dormieux and Gilles Chanvillard. CCR 37 (2007) 1427–1439. *Cement and Concrete Research*, 38(8–9):1126–1129, 2008.



- 
- [131] J. Sanahuja, L. Dormieux, and G. Chanvillard. A reply to the discussion “does C–S–H particle shape matter?” F.-J. Ulm and H. Jennings of the paper “modelling elasticity of a hydrating cement paste”. *Cement and Concrete Research*, 38(8–9):1130–1134, 2008.
- [132] E. Stora, Q.-C. He, and B. Bary. Influence of inclusion shapes on the effective linear elastic properties of hardened cement pastes. *Cement and Concrete Research*, 36(7):1330–1344, 2006.
- [133] J. Stark and B. Möser. Nano- and microstructure of Portland cement paste. In *International RILEM Workshop on Frost Resistance of Concrete*, pages 15–28. RILEM Publications SARL, 2002.
- [134] P. Termkhajornkit, Q. Huy Vu, R. Barbarulo, S. Daronnat, and G. Chanvillard. Dependence of compressive strength on phase assemblage in cement pastes: Beyond gel–space ratio — experimental evidence and micromechanical modeling. *Cement and Concrete Research*, 56:1–11, 2014.
- [135] J. Chen, Z. Li, and X. Jin. Morphological effect of C–S–H gel on the elastic behaviour of early-age cement-based materials. *Magazine of Concrete Research*, 69(12):629–640, 2017.
- [136] F.-J. Ulm, G. Constantinides, and F. H. Heukamp. Is concrete a poromechanics material? A multiscale investigation of poroelastic properties. *Materials and Structures*, 37:43–58, 2004.
- [137] N. Bilaniuk and G.S.K. Wong. Speed of sound in pure water as a function of temperature. *The Journal of the Acoustical Society of America*, 93(3):1609–1612, 1993.
- [138] Z. Hashin. Analysis of composite materials - a survey. *Journal of Applied Mechanics*, 50(3):481–505, 1983.
- [139] R. Hill. A self-consistent mechanics of composite materials. *Journal of the Mechanics and Physics of Solids*, 13(4):213–222, 1965.
- [140] B. Pichler and C. Hellmich. Estimation of influence tensors for eigenstressed multi-phase elastic media with nonaligned inclusion phases of arbitrary ellipsoidal shape. *Journal of Engineering Mechanics*, 136(8):1043–1053, 2010.

- [141] M. Königsberger. *Multiscale microstructural modeling in cement and concrete: from hydration to poroelasticity, creep, and strength*. Dissertation, Technische Universität, Wien, Austria, 2016.
- [142] N. Laws. The determination of stress and strain concentrations at an ellipsoidal inclusion in an anisotropic material. *Proceedings of the Royal Society of London, Series A* 241:376–396, 1957.
- [143] T. Mori and K. Tanaka. Average stress in matrix and average elastic energy of materials with misfitting inclusions. *Acta Metallurgica*, 21(5):571–574, 1973.
- [144] Y. Benveniste. A new approach to the application of Mori-Tanaka’s theory in composite materials. *Mechanics of Materials*, 6(2):147–157, 1987.
- [145] C. Pichler, R. Lackner, and H. A. Mang. Multiscale Model for Creep of Shotcrete - From Logarithmic-Type Viscous Behavior of CSH at the mm-Scale to Macroscopic Tunnel Analysis. *Journal of Advanced Concrete Technology*, 6(1):91–110, 2008.
- [146] D. Tabor. *The hardness of metals*. Clarendon, 1951.
- [147] X. Li and B. Bhushan. A review of nanoindentation continuous stiffness measurement technique and its applications. *Materials Characterization*, 48(1):11–36, 2002.
- [148] J. Nemecek. *Nanoindentation of Heterogeneous Structural Materials*. Habilitation, Czech Technical University, Prague, 2009.
- [149] K. Velez, S. Maximilien, D. Damidot, G. Fantozzi, and F. Sorrentino. Determination by nanoindentation of elastic modulus and hardness of pure constituents of portland cement clinker. *Cement and Concrete Research*, 31(4):555–561, 2001.
- [150] G. Constantinides, F.-J. Ulm, and K. van Vliet. On the use of nanoindentation for cementitious materials. *Materials and Structures*, 36(3):191–196, 2003.
- [151] G. Constantinides, K. S. Ravi C., F.-J. Ulm, and K. van Vliet. Grid indentation analysis of composite microstructure and mechanics: Principles and validation. *Materials Science and Engineering: A*, 430(1-2):189–202, 2006.
- [152] F.-J. Ulm, M. Vandamme, C. Bobko, J. Alberto Ortega, K. Tai, and C. Ortiz. Statistical Indentation Techniques for Hydrated Nanocomposites: Concrete, Bone, and Shale. *Journal of the American Ceramic Society*, 90(9):2677–2692, 2007.
- [153] M. Vandamme, F.-J. Ulm, and P. Fonollosa. Nanogranular packing of C–S–H at substochiometric conditions. *Cement and Concrete Research*, 40(1):14–26, 2010.

- 
- [154] J. Němeček, J. Králík, and J. Vondřejc. Micromechanical analysis of heterogeneous structural materials. *Cement and Concrete Composites*, 36:85–92, 2013.
- [155] H. M. Jennings. A model for the microstructure of calcium silicate hydrate in cement paste. *Cement and Concrete Research*, 30(1):101–116, 2000.
- [156] M. Vandamme and F.-J. Ulm. Nanogranular origin of creep. *PNAS*, 106(26):10395–10397, 2009.
- [157] J. J. Chen, L. Sorelli, M. Vandamme, F.-J. Ulm, and G. Chanvillard. A Coupled Nanoindentation/SEM-EDS Study on Low Water/Cement Ratio Portland Cement Paste: Evidence for C–S–H/Ca(OH)<sub>2</sub> Nanocomposites. *Journal of the American Ceramic Society*, 93(5):1484–1493, 2010.
- [158] P. Trtik, B. Münch, and P. Lura. A critical examination of statistical nanoindentation on model materials and hardened cement pastes based on virtual experiments. *Cement and Concrete Composites*, 31(10):705–714, 2009.
- [159] M. Miller, C. Bobko, M. Vandamme, and F.-J. Ulm. Surface roughness criteria for cement paste nanoindentation. *Cement and Concrete Research*, 38(4):467–476, 2008.
- [160] E. Donnelly, S. P. Baker, A. L. Boskey, and M.C.H. van der Meulen. Effects of surface roughness and maximum load on the mechanical properties of cancellous bone measured by nanoindentation. *Journal of Biomedical Materials Research Part A*, 77A(2):426–435, 2006.
- [161] J.-Y. Kim, J.-J. Lee, Y.-H. Lee, J.-il Jang, and D. Kwon. Surface roughness effect in instrumented indentation: A simple contact depth model and its verification. *Journal of Materials Research*, 21(12):2975–2978, 2006.
- [162] W. Wilson, J. M. Rivera-Torres, L. Sorelli, A. Durán-Herrera, and A. Tagnit-Hamou. The micromechanical signature of high-volume natural pozzolan concrete by combined statistical nanoindentation and SEM-EDS analyses. *Cement and Concrete Research*, 91(Supplement C):1–12, 2017.
- [163] W. Wilson, L. Sorelli, and A. Tagnit-Hamou. Automated coupling of Nanoindentation and Quantitative Energy-Dispersive Spectroscopy (NI-QEDS): A comprehensive method to disclose the micro-chemo-mechanical properties of cement pastes. *Cement and Concrete Research*, 2017.

- [164] M. Vandamme, C. A. Tweedie, G. Constantinides, F.-J. Ulm, and K. van Vliet. Quantifying plasticity-independent creep compliance and relaxation of viscoelastic materials under contact loading. *Journal of Materials Research*, 27:302–312, 2011.
- [165] M. Vandamme and F.-J. Ulm. Nanoindentation investigation of creep properties of calcium silicate hydrates. *Cement and Concrete Research*, 52:38–52, 2013.
- [166] Q. Zhang, R. Le Roy, M. Vandamme, and B. Zuber. Long-term creep properties of cementitious materials: Comparing microindentation testing with macroscopic uniaxial compressive testing. *Cement and Concrete Research*, 58:89–98, 2014.
- [167] H. Lee, V. Vimonsatit, and P. Chindapasirt. Mechanical and micromechanical properties of alkali activated fly-ash cement based on nano-indentation. *Construction and Building Materials*, 107:95–102, 2016.
- [168] J. Nemecek, V. Smilauer, and L. Kopecky. Nanoindentation characteristics of alkali-activated aluminosilicate materials. *Cement and Concrete Composites*, 33:163–170, 2011.
- [169] V. Z. Zadeh and C. P. Bobko. Nanoscale mechanical properties of concrete containing blast furnace slag and fly ash before and after thermal damage. *Cement and Concrete Composites*, 37:215–221, 2013.
- [170] C. Hu and Z. Li. Property investigation of individual phases in cementitious composites containing silica fume and fly ash. *Cement and Concrete Composites*, 57:17–26, 2015.
- [171] Z. He, C. Qian, Y. Zhang, F. Zhao, and Y. Hu. Nanoindentation characteristics of cement with different mineral admixtures. *Science China Technological Sciences*, 56(5):1119–1123, 2013.
- [172] Z. D. Rong, W. Sun, H. J. Xiao, and W. Wang. Effect of silica fume and fly ash on hydration and microstructure evolution of cement based composites at low water–binder ratios. *Construction and Building Materials*, 51:446–450, 2014.
- [173] R. Wang, R. Lackner, and P.-M. Wang. Effect of Styrene-Butadiene Rubber Latex on Mechanical Properties of Cementitious Materials Highlighted by Means of Nanoindentation. *Strain*, 47(2):117–126, 2011.
- [174] A. M. Díez-Pascual, M. A. Gómez-Fatou, F. Ania, and A. Flores. Nanoindentation in polymer nanocomposites. *Progress in Materials Science*, 67:1–94, 2015.

- 
- [175] E. G. Herbert, W. C. Oliver, and G. M. Pharr. Nanoindentation and the dynamic characterization of viscoelastic solids. *Journal of Physics D: Applied Physics*, 41(7):74021, 2008.
- [176] G. M. Odegard, T. S. Gates, and H. M. Herring. Characterization of viscoelastic properties of polymeric materials through nanoindentation. *Experimental Mechanics*, 45(2):130–136, 2005.
- [177] C. C. White, P. L. Drzal, and M. R. VanLandingham. Viscoelastic characterization of polymers using dynamic instrumented indentation. *MRS Proceedings*, 841, 2004.
- [178] Z. Chen. *Nanoindentation testing of soft polymers: Computation, experiments and parameters identification*. Dissertation, Universität des Saarlandes, Saarbrücken, 2013.
- [179] ACI209. Prediction of Creep, Shrinkage and Temperature Effects in Concrete Structures: Reported by aci committee 209.
- [180] Comite Euro-International du Beton. CEB-FIP model code 1990. *Tech. rep. Comite Euro-International du Beton*, 1-3, 1993.
- [181] N. J. Gardner and M. J. Lockman. Design provisions for drying shrinkage and creep of normal-strength concrete. *ACI Materials Journal*, 98:159–167, 2001.
- [182] Z. P. Bažant and S. Bajewa. Creep and shrinkage prediction model for analysis and design of concrete structures – model B3. *Materials and Structures*, 28(6):357–365, 1995.
- [183] Z. P. Bažant, M. H. Hubler, and R. Wendner. Model B4 for creep, drying shrinkage and autogeneous shrinkage of normal and high-strength concretes with multi-decade applicability: TC-242-MDC multi-decade creep and shrinkage of concrete: material model and structural analysis. *RILEM Materials and Structures*, 2014.
- [184] Z. P. Bažant and G.-H. Li. Unbiased statistical comparison of creep and shrinkage prediction models. *ACI Materials Journal*, 105(6):610–621, 2008.
- [185] Z. P. Bažant, M. H. Hubler, and Q. Yu. Pervasiveness of excessive segmental bridge deflections: Wake-up call for creep. *ACI Structural Journal*, 108(6):766–774, 2011.
- [186] J. Sercombe, C. Hellmich, F.-J. Ulm, and H. A. Mang. Modeling of early-age creep of shotcrete. I: Model and Model Parameters. *Journal of Engineering Mechanics*, pages 284–291, 2000.

- [187] S. Ullah, B. Pichler, S. Scheiner, and C. Hellmich. Influence of shotcrete composition on load-level estimation in natm-tunnel shells: Micromechanics-based sensitivity analyses. *International Journal for Numerical and Analytical Methods in Geomechanics*, 36(9):1151–1180, 2011.
- [188] M. H. Tadros, N. Al-Omaishi, S. J. Sequirant, and J. G. Gallt. Prestress losses in pretensioned high-strength concrete bridge girders. *Transportation Research Board*, 496, 2003.
- [189] A. A. Al-Manaseer, Z. P. Bažant, J. J. Brooks, R. G. Burg, and Carreira, D.J., Chiorino, M.A.,... & Hansen, W. Report on factors affecting shrinkage and creep of hardened concrete. *Concrete International*, 21, 2005.
- [190] Z. P. Bažant, A. B. Hauggaard, Se. Bajewa, and F.-J. Ulm. Microprestress-Solidification Theory for Concrete Creep. I: Aging and Drying Effects. *Journal of Engineering Mechanics*, 123(11):1188–1194, 1997.
- [191] Z. P. Bažant. Viscoelasticity of solidifying porous material – concrete. *Journal of Engineering Mechanics*, 103(6), 1977.
- [192] F. Vogt. On the flow and extensibility of concrete. *Brun i Komm.*, page 24, 1935.
- [193] C. G. Lynam. Growth and movement in portland cement concrete. *London*, 1934.
- [194] Z. P. Bažant and S. Prasannan. Solidification Theory for concrete creep. I: Formulation. *Journal of Engineering Mechanics*, 115(8):1691–1703, 1989.
- [195] Z. P. Bažant. Prediction of concrete creep and shrinkage: past, present and future. *Nuclear Engineering and Design*, 203(1):27–38, 2001.
- [196] A. M. Neville. Creep of concrete as a function of its cement paste content. *Magazine of Concrete Research*, 16(46):21–30, 1964.
- [197] I. H. Woolson. Some remarkable tests indicating flow of concrete under pressure. *Engineering News*, 54(18):459–460, 1905.
- [198] W. K. Hatt. Notes on the effect of time element in loading reinforced concrete beams. *Proc. ASTM*, 7:421–433, 1907.
- [199] Z. P. Bažant and G.-H. Li. Comprehensive database on concrete creep and shrinkage. *ACI Materials Journal*, 105(6):635–637, 2008.
- [200] F. Benboudjema and J.-M. Torrenti. Early-age behaviour of concrete nuclear containments. *Nuclear Engineering and Design*, 238(10):2495–2506, 2008.

- 
- [201] B. Craeye, G. de Schutter, H. van Hughes, and A. van Cotthem. Early age behaviour of concrete supercontainers for radioactive waste disposal. *Nuclear Engineering and Design*, 239(1):23–35, 2009.
- [202] W. Jiang, G. de Schutter, and Y. Yuan. Degree of hydration based prediction of early age basic creep and creep recovery of blended concrete. *Cement and Concrete Composites*, 48:83–90, 2014.
- [203] C. Boulay, S. Staquet, B. Delsaute, J. Carette, M. Crespini, O. Yazoghli-Marzouk, É. Merliot, and S. Ramanich. How to monitor the modulus of elasticity of concrete, automatically since the earliest age? *Materials and Structures*, 47(1):141–155, 2014.
- [204] B. Delsaute, C. Boulay, J. Granja, J. Carette, M. Azenha, C. Dumoulin, G. Karaiskos, A. Deraemaeker, and S. Staquet. Testing Concrete E-modulus at Very Early Ages Through Several Techniques: An Inter-laboratory Comparison. *Strain*, 52(2):91–109, 2016.
- [205] C. H. Lee and K. C. Hover. Early-age stiffening of paste, mortar, and concrete in lab and field. *ACI Materials Journal*, 113(1):83–94, 2016.
- [206] B. Delsaute, C. Boulay, and S. Staquet. Creep testing of concrete since setting time by means of permanent and repeated minute-long loadings. *Cement and Concrete Composites*, 73:75–88, 2016.
- [207] M. Irfan-ul Hassan, B. Pichler, R. Reihnsner, and C. Hellmich. Elastic and creep properties of young cement paste, as determined from hourly repeated minute-long quasi-static tests. *Cement and Concrete Research*, 82:36–49, 2016.
- [208] L. Su, Y.-F. Wang, S.-Q. Mei, and P.-F. Li. Experimental investigation on the fundamental behavior of concrete creep. *Construction and Building Materials*, 152(Supplement C):250–258, 2017.
- [209] A. M. Neville. *Properties of concrete*. Longman, London, 4 edition, 1995.
- [210] ACI209. Prediction of creep, shrinkage and temperature effects in concrete structures: Reported by aci committee 209.
- [211] Eurocode 2: Bemessung und Konstruktion von Stahlbeton- und Spannbetontragwerken - Teil 1-1: Allgemeine Bemessungsregeln und Regeln für den Hochbau; Deutsche Fassung EN 1992-1-1:2004 + AC:2010, 2004.

- [212] J. Diener. *Beitrag zur physikalisch und geometrisch nichtlinearen Berechnung langzeitbelasteter Bauteile aus Stahlbeton und Spannbeton unter besonderer Berücksichtigung des nichtlinearen Kriechens und der Rißbildung*. Dissertation, Bauhaus-Universität, Weimar, Germany, 1998.
- [213] L. Boltzmann. Zur Theorie der elastischen Nachwirkung. *Annalen der Physik*, 241(11):430–432, 1878.
- [214] C. Hua, P. Acker, and A. Ehlacher. Analyses and models of the autogenous shrinkage of hardening cement paste. *Cement and Concrete Research*, 25(7):1457–1468, 1995.
- [215] C. Hua, A. Ehlacher, and P. Acker. Analyses and models of the autogenous shrinkage of hardening cement paste II. Modelling at scale of hydrating grains. *Cement and Concrete Research*, 27(2):245–258, 1997.
- [216] P. Havlasek and M. Jirasek. Multiscale modeling of drying shrinkage and creep of concrete. *Cement and Concrete Research*, 85:55–74, 2016.
- [217] T. Honorio, B. Bary, and F. Benboudjema. Multiscale estimation of ageing viscoelastic properties of cement-based materials: A combined analytical and numerical approach to estimate the behaviour at early age. *Cement and Concrete Research*, 85:137–155, 2016.
- [218] N. Laws and R. McLaughlin. Self-consistent estimates for the viscoelastic creep compliances of composite materials. *Proceedings of the Royal Society of London A: Mathematical, Physical and Engineering Sciences*, 359(1697):251–273, 1978.
- [219] Q. V. Le, F. Meftah, Q.-C. He, and Y. Le Pape. Creep and relaxation functions of a heterogeneous viscoelastic porous medium using the mori-tanaka homogenization scheme and a discrete microscopic retardation spectrum. *Mechanics of Time-Dependent Materials*, 11(3):309–331, 2007.
- [220] V. Šmilauer and Z. P. Bažant. Identification of viscoelastic c-s-h behavior in mature cement paste by fft-based homogenization method. *Cement and Concrete Research*, 40(2):197–207, 2010.
- [221] N. Lahellec and P. Suquet. Effective behavior of linear viscoelastic composites: A time-integration approach. *International Journal of Solids and Structures*, 44(2):507–529, 2007.



- 
- [222] Q. H. Vu, R. Brenner, O. Castelnau, and H. Moulinec. Effective behaviour of viscoelastic polycrystals and associated local fields inferred from homogenization: Incremental collocation approach. *Procedia Engineering*, 10:177–182, 2011.
- [223] J.-M. Ricaud and R. Masson. Effective properties of linear viscoelastic heterogeneous media: Internal variables formulation and extension to ageing behaviours. *International Journal of Solids and Structures*, 46(7–8):1599–1606, 2009.
- [224] J. Sanahuja and S. Huang. Mean-field homogenization of time-evolving microstructures with viscoelastic phases: Application to a simplified micromechanical model of hydrating cement paste. *Journal of Nanomechanics and Micromechanics*, 7(1), 2017.
- [225] M. Shahidi, B. Pichler, R. Wendner, S. Scheiner, and C. Hellmich. Interfacial micromechanics assessment of rheological chain models and their application to early-age creep of concrete. In Ch. Hellmich, B. Pichler, and J. Kollegger, editors, *CONCREEP 10 - CD-Proceedings of the International Conference on Mechanics and Physics of Creep, Shrinkage, and Durability of Concrete and Concrete Structures*, 2015.
- [226] B. T. Tamtsia and J. J. Beaudoin. Basic creep of hardened cement paste a re-examination of the role of water. *Cement and Concrete Research*, 30(9):1465–1475, 2000.
- [227] M. Irfan-ul Hassan, M. Königsberger, R. Reihnsner, C. Hellmich, and B. Pichler. How water-aggregate interactions affect concrete creep: A multiscale analysis. *Journal of Nanomechanics and Micromechanics*, 7(4):4017019, 2017.
- [228] T. Most. Assessment of structural simulation models by estimating uncertainties due to model selection and model simplification. *Computer and Structures*, 89(17–18):1664–1672, 2011.
- [229] H. Keitel, G. Karaki, T. Lahmer, S. Nikulla, and V. Zabel. Evaluation of coupled partial models in structural engineering using graph theory and sensitivity analysis. *Engineering Structures*, 33(12):3726–3736, 2011.
- [230] H. Keitel, B. Jung, H. B. Motra, and H. Stutz. Quality assessment of coupled partial models considering soil–structure coupling. *Engineering Structures*, 59:565–573, 2014.
- [231] K. Gürlebeck, D. Hofmann, and D. Legatiuk. Categorical approach to modelling and to coupling of models. *Mathematical Methods in the Applied Sciences*, 40(3):523–534, 2017.

- [232] S. Marzban and T. Lahmer. Conceptual implementation of the variance-based sensitivity analysis for the calculation of the first-order effects. *Journal of Statistical Theory and Practice*, 10(4):589–611, 2016.
- [233] E. Bombasaro. *Investigation of different vortex shedding models, based on sensibility and probability methods to evolve probabilistic models*. Dissertation, Technische Universität, Wien, 2011.
- [234] T. Abbas and G. Morgenthal. Framework for the sensitivity and uncertainty quantification in the flutter assessment of bridges. *Probabilistic Engineering Mechanics*, 43:91–105, 2016.
- [235] T. Knabe, M. Datcheva, T. Lahmer, F. Cotecchia, and T. Schanz. Identification of constitutive parameters of soil using an optimization strategy and statistical analysis. *Computers and Geotechnics*, 49:143–157, 2013.
- [236] H. B. Motra. *Quality Assessment Methods for Experimental Models in Structural Engineering*. Dissertation, Bauhaus-Universität, Weimar, Germany, 2015.
- [237] B. Jung. *Evaluation of Coupled Partial Models for the Assessment of Restraint Effects in Concrete Structures*. Dissertation, Bauhaus-Universität, Weimar, Germany, 2015.
- [238] L. Göbel, T. Lahmer, and A. Osburg. Uncertainty analysis in multiscale modeling of concrete based on continuum micromechanics. *European Journal of Mechanics - A/Solids*, 65:14–29, 2017.
- [239] N. Gaber, G. Foley, P. Pascual, N. Stiber, E. Sunderland, B. Cope, and Z. Zaleem. Guidance on the development, evaluation, and application of environmental models. *Council for Regulatory Environmental Modeling*, 2009.
- [240] E. Hampe. Von der unsicheren Sicherheit zur sicheren Unsicherheit. *Bautechnik*, 66(10):329–335, 1989.
- [241] M. D. McKay, R. J. Beckham, and W. J. Conover. A comparison of three methods for selecting values of input variables in the analysis from a computer code. *Technometrics*, 21:239–245, 1979.
- [242] A. Saltelli, M. Ratto, T. Andres, F. Campolongo, J. Cariboni, D. Gatelli, M. Saisana, and S. Tarantola. *Global Sensitivity Analysis: The Primer*. John Wiley & Sons, West Sussex, England, 2008.

- 
- [243] D. M. Hamby. A review of techniques for parameter sensitivity analysis of environmental models. *Environmental Monitoring and Assessment*, 32:135–154, 1994.
- [244] B. Sudret. Global sensitivity analysis using polynomial chaos expansions. *Reliability Engineering & System Safety*, 93(7):964–979, 2008.
- [245] I. M. Sobol. Sensitivity estimates for nonlinear mathematical models. *Mathematical Modelling and Computational Experiment*, 1(4):407–414, 1993.
- [246] G. Karaki. *Assessment of coupled models of bridges considering time-dependent vehiculr loading*. Dissertation, Bauhaus-Universität, Weimar, 2011.
- [247] A. Saltelli, P. Annoni, I. Azzini, F. Campologno, M. Ratto, and S. Tarantola. Variance based sensitivity analysis of model output. Design and estimator for the total sensitivity index. *Computer Physics Communications*, 181(2):259–270, 2010.
- [248] T. Homma and A. Saltelli. Importance measures in global sensitivity analysis of nonlinear models. *Reliability Engineering and System Safety*, 52(1):1–17, 1996.
- [249] A. Saltelli. Making best use of model evaluations to compute sensitivity indices. *Computer Physics Communications*, 145(2):280–297, 2002.
- [250] B. Jung, G. Morgenthal, D. Xu, and H. Schröter. Quality assessment of material models for reinforced concrete flexural members. *Structural Concrete*, 16(1):125–136, 2015.
- [251] E. Zio and G. E. Apostolakis. Two methods for the structural assessment of model uncertainty by experts in performance assessments of radioactive waste repositories. *Reliability Engineering and System Safety*, 54(2-3):225–241, 1996.
- [252] M. E. Riley and R. V. Grandhi. A method for the quantification of model-form and parametric uncertainties in physics-based simulations. In *52nd AIAA/ASME/ASCE/AHS/ASC Structures, Structural Dynamics and Materials Conference*, 4.-7. April 2011.
- [253] H. O. Madsen and Z. P. Bažant. Uncertainty analysis of creep and shrinkage effects in concrete structures. *ACI Journal*, 80:116–127, 1983.
- [254] Z. P. Bažant and J.-K. Kim. Improved prediction model for time-dependent deformations of concrete: Part 3-Creep at drying. *Materials and Structures*, 25(1):21–28, 1992.

- [255] R. W. Howells, R. J. Lark, and B. I. G. Barr. A sensitivity study of parameters used in shrinkage and creep prediction models. *Magazine of Concrete Research*, 57(10):589–602, 2005.
- [256] C. Q. Li and R. E. Melchers. Reliability analysis of creep and shrinkage effects. *Journal of Structural Engineering*, 118(9):2223–2237, 1992.
- [257] E. H. Khor, D. V. Rosowsky, and M. G. Stewart. Probabilistic analysis of time-dependent deflections of rc flexural members. *Computers and Structures*, 79(16):1461–1472, 2001.
- [258] B.-S. Choi, A. Scanlon, and P. A. Johnson. Monte Carlo simulation of immediate and time-dependent deflections of reinforced concrete beams and slabs. *ACI Structural Journal*, 101(5):633–641, 2004.
- [259] B. Teplý, Z. Keršner, and D. Novák. Sensitivity study of BP-KX and B3 creep and shrinkage models. *Materials and Structures*, 29(8):500–505, 1996.
- [260] Z. P. Bažant, L. Panula, J.-K. Kim, and Y. Xi. Improved prediction model for time-dependent deformations of concrete: Part 6—simplified code-type formulation. *Materials and Structures*, 25(4):219–223, 1992.
- [261] Z. P. Bažant and S. Bajewa. Creep and shrinkage prediction model for analysis and design of concrete structure - model B3. *ACI Special Publications*, 194:1–84, 1995.
- [262] Z. P. Bazant and S. Baweja. Justification and refinements of model B3 for concrete creep and shrinkage 2. Updating and theoretical basis. *Materials and Structures*, 28(8):488, 1995.
- [263] I. H. Yang. Uncertainty and sensitivity analysis of time-dependent effects in concrete structures. *Engineering Structures*, 29(7):1366–1374, 2007.
- [264] I. H. Yang. Uncertainty and updating of long-term prediction of prestress forces in PSC box girder bridges. *Computers & Structures*, 83(25-26):2137–2149, 2005.
- [265] H. Keitel and A. Dimmig-Osburg. Uncertainty and sensitivity analysis of creep models for uncorrelated and correlated input parameters. *Engineering Structures*, 32(11):3758–3767, 2010.
- [266] H. Keitel. Quantifying sources of uncertainty for creep models under varying stresses. *Journal of Structural Engineering*, 139:949–957, 2013.

- 
- [267] H. Keitel, A. Dimmig-Osburg, L. Vandewalle, and L. Schueremans. Selecting creep models using bayesian methods. *Materials and Structures*, 45:1513–1533, 2012.
- [268] A. Clement, C. Soize, and J. Yvonnet. Uncertainty quantification in computational stochastic multiscale analysis of nonlinear elastic materials. *Computational Methods in Applied Mechanics and Engineering*, 254:61–82, 2013.
- [269] B. Kouchmeshky and N. Zabaras. Microstructure model reduction and uncertainty quantification in multiscale deformation processes. *Computational Materials Science*, 48(2):213–227, 2010.
- [270] M. Koslowski and A. Strachan. Uncertainty propagation in a multiscale model of nanocrystalline plasticity. *Reliability Engineering and System Safety*, 96(9):1161–1170, 2011.
- [271] N. Vu-Bac, T. Lahmer, H. Keitel, J. Zhao, X. Zhuang, and T. Rabczuk. Stochastic predictions of bulk properties of amorphous polyethylene based in molecular dynamics simulations. *Mechanics of Materials*, 68:70–84, 2014.
- [272] N. Vu-Bac, R. Rafiee, X. Zhuang, T. Lahmer, and T. Rabczuk. Uncertainty quantification for multiscale modeling of polymer nanocomposites with correlated parameters. *Composites: Part B*, 68:446–464, 2015.
- [273] A. G. Reisinger, D. H. Pahr, and P. K. Zysset. Sensitivity analysis and parametric study of elastic properties of an unidirectional mineralized bone fibril-array using mean field methods. *Biomechanics and Modeling in Mechanobiology*, 9(5):499–510, 2010.
- [274] V. Smilauer, M. Leps, and Z. Vittingerova. On influence of microstructure parameters on cement paste performance: results from micromechanical modelling and optimization. In E. Schlangen and G. de Schutter, editors, *International RILEM Symposium on Concrete Modelling - ConMod'2008*, pages 657–663, 2008.
- [275] J. F. Unger. *Neural networks in a multiscale approach for concrete*. Dissertation, Bauhaus-Universität, Weimar, 2009.
- [276] N. Venkovic, L. Sorelli, B. Sudret, T. Yalamas, and R. Gagné. Uncertainty propagation of a multiscale poromechanics-hydration model for poroelastic properties of cement paste at early-age. *Probabilistic Engineering Mechanics*, 32:5–20, 2013.

- [277] M. Berveiller, Y. Le Pape, Julien Sanahuja, and A. Giorla. Sensitivity analysis and uncertainty propagation in multiscale modeling of concrete. In H. I. Ling, A. Smyth, and R. Betti, editors, *Proceedings of the Fourth Biot Conference on Poromechanics, Including the Second Frank L. DiMaggio Symposium*, June 8-10, 2009.
- [278] L. Göbel, A. Osburg, and T. Lahmer. Assessment of a continuum micromechanics-based multiscale model for concrete by means of sensitivity analysis and uncertainty propagation. In M. Papadrakakis, V. Papadopoulos, G. Stefanou, and V. Plevris, editors, *VII European Congress on Computational Methods in Applied Sciences and Engineering*, volume 4, pages 7905–7921, 5-10 June 2016.
- [279] R. Krstulović and P. Dabić. A conceptual model of the cement hydration process. *Cement and Concrete Research*, 30(5):693–698, 2000.
- [280] T. Knudsen. The dispersion model for hydration of portland cement I. General concepts. *Cement and Concrete Research*, 14(5):622–630, 1984.
- [281] D. P. Bentz. Influence of water-to-cement ratio on hydration kinetics: Simple models based on spatial considerations. *Cement and Concrete Research*, 36(2):238–244, 2006.
- [282] M. Königsberger, C. Hellmich, and B. Pichler. Densification of C-S-H is mainly driven by available precipitation space, as quantified through an analytical cement hydration model based on NMR data. *Cement and Concrete Research*, 88:170–183, 2016.
- [283] T. C. Powers and T. L. Brownyard. Studies of the Physical Properties of Hardened Portland Cement Paste. *Research Laboratories of the Portland Cement Association Bulletin*, 43(9):101–132, 1948.
- [284] P. Acker. Micromechanical analysis of creep and shrinkage mechanisms. In F.-J. Ulm, Z. P. Bažant, and F. H. Wittmann, editors, *Creep, Shrinkage and Durability Mechanics of Concrete and Other Quasi-brittle Materials: Proceedings of the Sixth International Conference CONCREEP-6@MIT*, pages 15–26. Elsevier, 2001.
- [285] P. D. Tennis and H. M. Jennings. A model for two types of calcium silicate hydrate in the microstructure of portland cement pastes. *Cement and Concrete Research*, 30(6):855–863, 2000.
- [286] M. Avrami. Kinetics of phase change. A general theory. *Journal of Chemical Physics*, 7:1103–1112, 1939.

- 
- [287] K. Fuji and W. Kondo. Kinetics of the hydration of tricalcium silicate. *Journal of the American Ceramic Society*, 57:492–502, 1974.
- [288] DIN EN. 196-1. Methods of testing cement–Part 1: Determination of strength, European Committee for standardization (26), 2005.
- [289] L. Göbel, M. Königsberger, A. Osburg, and B. Pichler. Viscoelastic Behavior of Polymer-modified Cement Pastes: Insight From Downscaling Short-term Macroscopic Creep Tests by Means of Multiscale Modeling. *Applied Sciences*, 8(4):487, 2018.
- [290] J. Hay and E. Herbert. Measuring the complex modulus of polymers by instrumented indentation testing. *Experimental Techniques*, 37(3):55–61, 2013.
- [291] L. E. Copeland and J. C. Hayes. The determination of non-evaporable water in hardened portland cement paste. *ASTM Bull.*, 194:70–74, 1953.
- [292] DIN EN. 1015-3:2007-05: Prüfverfahren für Mörtel für Mauerwerk - Teil 3: Bestimmung der Konsistenz für Frischmörtel (mit Ausbreittisch), Deutsche Fassung EN 1015-3:1999+A1:2004+A2:2006.
- [293] W. Brameshuber. *Selbstverdichtender Beton*. Verlag Bau + Technik, Düsseldorf, 2004.
- [294] DIN EN. Prüfverfahren für Mörtel für Mauerwerk - Teil 11: Bestimmung der Biegezug- und Druckfestigkeit von Festmörtel; Deutsche Fassung EN 1015-11:1999+A1:2006.
- [295] J. Stark and H. Krug. *Baustoffpraktikum. Schriftenreihe des F.A. Finger-Institutes für Baustoffkunde. Bd. 1 bis 3*. Universitätsverlag Weimar, 2000.
- [296] DIN EN. Produkte und Systeme für den Schutz und die Instandsetzung von Betontragwerken - Prüfverfahren - Teil 4: Bestimmung des Schwindens und Quellens; Deutsche Fassung EN 12617-4:2002.
- [297] J. Hay, P. Agee, and E. Herbert. Continuous stiffness measurement during instrumented indentation testing. *Experimental Techniques*, 34(3):86–94, 2010.
- [298] M. Sebastiani, R. Moscatelli, F. Ridi, P. Baglioni, and F. Carassiti. High-resolution high-speed nanoindentation mapping of cement pastes: Unravelling the effect of microstructure on the mechanical properties of hydrated phases. *Materials & Design*, 97:372–380, 2016.

- [299] W. C. Oliver and G. M. Pharr. Measurement of hardness and elastic modulus by instrumented indentation: Advances in understanding and refinements to methodology. *Journal of Materials Research*, 19(01):3–20, 2004.
- [300] W. C. Oliver and G. M. Pharr. An improved technique for determining hardness and elastic modulus using load and displacement sensing indentation experiments. *Journal of Materials Research*, 7(6):1564–1583, 1992.
- [301] DIN EN. Prüfverfahren für Mörtel für Mauerwerk - Teil 7: Bestimmung des Luftgehaltes von Frischmörtel; Deutsche Fassung EN 1015-7:1998.
- [302] DIN EN. Prüfverfahren für Mörtel für Mauerwerk - Teil 6: Bestimmung der Rohdichte von Frischmörtel; Deutsche Fassung EN 1015-6:1998+A1:2006.
- [303] DIN EN. Prüfung von Festbeton - Teil 13: Bestimmung des Elastizitätsmoduls unter Druckbelastung (Sekantenmodul); Deutsche Fassung EN 12390-13:2013.
- [304] DIN EN. Prüfung von Beton in Bauwerken - Teil 4: Bestimmung der Ultraschallgeschwindigkeit; Deutsche Fassung EN 12504-4:2004.
- [305] DIN EN. Prüfung von Frischbeton - Teil 5: Ausbreitmaß; Deutsche Fassung EN 12350-5:2009.
- [306] DIN EN. Prüfung von Frischbeton - Teil 6: Frischbetonrohddichte; Deutsche Fassung EN 12350-6:2009.
- [307] DIN EN. Prüfung von Festbeton - Teil 3: Druckfestigkeit von Probekörpern; Deutsche Fassung EN 12390-3:2009.
- [308] K. Weschke. *Baustoffe für tragende Bauteile*. Bauverlag GmbH, Wiesbaden und Berlin, 2 edition, 1988.
- [309] J. Richeton, S. Ahzi, K. S. Vecchio, F. C. Jiang, and R. R. Adharapurapu. Influence of temperature and strain rate on the mechanical behavior of three amorphous polymers: Characterization and modeling of the compressive yield stress. *International Journal of Solids and Structures*, 43(7–8):2318–2335, 2006.
- [310] Y. Wei, S. Liang, and X. Gao. Indentation creep of cementitious materials: Experimental investigation from nano to micro length scales. *Construction and Building Materials*, 143:222–233, 2017.



- 
- [311] M. G. Alexander and T. I. Milne. Influence of Cement Blend and Aggregate Type on the Stress-Strain Behavior and Elastic Modulus of Concrete. *Materials Journal*, 92(3):227–235, 1995.
- [312] P. Karte. *Experimental determination of the stiffness evolution of young cement pastes with and without fly-ash as cement replacement material*. Diplomarbeit, Technische Universität, Wien, Austria, 2014.
- [313] I. Fischer, B. Pichler, E. Lach, C. Terner, E. Barraud, and F. Britz. Compressive strength of cement paste as a function of loading rate: Experiments and engineering mechanics analysis. *Cement and Concrete Research*, 58:186–200, 2014.
- [314] M. F. Ruiz, A. Muttoni, and P. G. Gambarova. Relationship between nonlinear creep and cracking of concrete under uniaxial compression. *Journal of Advanced Concrete Technology*, 5(3):383–393, 2007.
- [315] H. Rüsch. Researches toward a general flexural theory for structural concrete. *ACI Journal*, 57(1):1–28, 1960.
- [316] B. Pichler, C. Hellmich, J. Eberhardsteiner, J. Wasserbauer, P. Termkhajornkit, R. Barbarulo, and G. Chanvillard. Effect of gel–space ratio and microstructure on strength of hydrating cementitious materials: An engineering micromechanics approach. *Cement and Concrete Research*, 45:55–68, 2013.
- [317] B. T. Tamtsia, J. J. Beaudoin, and J. Marchand. The early age short-term creep of hardening cement paste: Load-induced hydration effects. *Cement and Concrete Composites*, 26(5):481–489, 2004.
- [318] V. Kristek and Z. Smerda. Creep and shrinkage of concrete elements and structures. *SNTL-Publishers of Technical Literature, Prague*, 1988.
- [319] Z. P. Bažant, editor. *Mathematical Modeling of Creep and Shrinkage of Concrete*. John Wiley & Sons, 1988.
- [320] J. D. Bass. *Elasticity of Minerals, Glasses, and Melts, Mineral Physics and Crystallography: A Handbook of Physical Constants*. 1995.
- [321] F. Lavergne, A. Ben Fraj, I. Bayane, and J. F. Barthélémy. Estimating the mechanical properties of hydrating blended cementitious materials: An investigation based on micromechanics. *Cement and Concrete Research*, 104:37–60, 2017.

- [322] M. Hlobil. Microstructure-based evolution of compressive strength of blended mortars: A continuum micromechanics approach. *Advanced Materials Research*, 1144:121–127, 2017.
- [323] M. Ito, S. Aoki, T. Hirata, K. Hayakawa, H. Abe, and S. Tottri. Development of high quality patching method by applying wet spraying, using polymer cement mortar and set accelerating agent. *JSCE Journal of Construction Engineering and Management*, 62(3):459–472, 2006.
- [324] J.-H. Lee, H.-H. Kim, S.-K. Park, R.-O. Oh, H.-D. Kim, and C.-G. Park. Mechanical properties and durability of latex-modified fiber-reinforced concrete: A tunnel liner application. *Advances in Materials Science and Engineering*, 2018:1–14, 2018.
- [325] C. Hellmich, J. Sercombe, F.-J. Ulm, and H. Mang. Modeling of early-age creep of shotcrete. II: Application to tunneling. *Journal of Engineering Mechanics*, 126:292–299, 2000.
- [326] F. R. Schwarzl and L.C.E. Struik. Analysis of relaxation measurements. *Advances in molecular relaxation processes*, 1(3):201–255, 1968.
- [327] S. P. Zaoutsos, G. C. Papanicolaou, and A. H. Cardon. On the non-linear viscoelastic behaviour of polymer-matrix composites. *Composites Science and Technology*, 58(6):883–889, 1998.
- [328] M. Kapnistos, M. Lang, D. Vlassopoulos, W. Pyckhout-Hintzen, D. Richter, D. Cho, T. Chang, and M. Rubinstein. Unexpected power-law stress relaxation of entangled ring polymers. *Nature Materials*, 7:997–1002, 2008.
- [329] V. S. Chevali, D. R. Dean, and G. M. Janowski. Flexural creep behavior of discontinuous thermoplastic composites: Non-linear viscoelastic modeling and time–temperature–stress superposition. *Composites Part A: Applied Science and Manufacturing*, 40(6–7):870–877, 2009.
- [330] J. Abate and P. P. Valkó. Multi-precision laplace transform inversion. *International Journal for Numerical Methods in Engineering*, 60(5):979–993, 2004.
- [331] P. P. Valkó and J. Abate. Comparison of sequence accelerators for the gaver method of numerical laplace transform inversion. *Computers & Mathematics with Applications*, 48(3):629–636, 2004.

- 
- [332] R. D. Maksimov, E. A. Sokolov, and V. P. Mochalov. Effect of temperature and humidity on the creep of polymer materials. *Polymer Mechanics*, 11(6):834–839, 1975.
- [333] R. Scaffaro, R. Tzankova Dintcheva, and F. P. La Mantia. A new equipment to measure the combined effects of humidity, temperature, mechanical stress and uv exposure on the creep behaviour of polymers. *Polymer Testing*, 27(1):49–54, 2008.
- [334] X. Liu, R. D. Wildman, and I. A. Ashcroft. Experimental investigation and numerical modelling of the effect of the environment on the mechanical properties of polyurethane lacquer films. *Journal of Materials Science*, 47(13):5222–5231, 2012.
- [335] P. Lura, O. M. Jensen, and K. van Breugel. Autogenous shrinkage in high-performance cement paste: An evaluation of basic mechanisms. *Cement and Concrete Research*, 33(2):223–232, 2003.
- [336] A. A. Tasnimi. Mathematical model for complete stress-strain curve prediction of normal, light-weight and high-strength concretes. *Magazine of Concrete Research*, 56(1):23–34, 2004.
- [337] İ. B. Topçu, T. Bilir, and A. R. Boğa. Estimation of the modulus of elasticity of slag concrete by using composite material models. *Construction and Building Materials*, 24(5):741–748, 2010.
- [338] M. B. D. Hueste, P. Chompreda, D. Trejo, and D. B. H. Cline. Mechanical properties of high strength concrete for prestressed concrete bridge girders. *Texas Department of Transportation*, 2003.
- [339] P. A. Gutierrez and M. F. Canovas. The modulus of elasticity of high performance concrete. *Materials and Structures*, 28(10):559–568, 1995.
- [340] J. C. Lim and T. Ozbakkaloglu. Stress–strain model for normal- and light-weight concretes under uniaxial and triaxial compression. *Construction and Building Materials*, 71:492–509, 2014.
- [341] American Concrete Institute. Building Code Requirements for Structural Concrete (ACI 318-11) and Commentary, August 2008.
- [342] American Concrete Institute. State-of-the-Art Report on High-Strength Concrete. ACI363-R. 1992.
- [343] Ministerio de Fomento, Spain. Code on Structural Concrete (EHE-08), 2010.

- [344] Brazilian Association of technical standards NBR 6118. Design of concrete structures., 2003.
- [345] CEB-FIP. High-strength concrete: State of the art report. 197:61, 1990.
- [346] AASHTO. Intern bridge design specifications and commentary. 2006.
- [347] DIN EN. 1045-2:2008: Tragwerke aus Beton, Stahlbeton und SPannbeton - Teil 2: Beton - Festlegung, Eigenschaften, Herstellung und Konformität - Anwendungsregeln zu DIN EN 206-1.
- [348] DIN EN. Prüfung von Festbeton - Teil 2: Herstellung und Lagerung von Probekörpern für Festigkeitsprüfungen; Deutsche Fassung EN 12390-2:2009.
- [349] CEB - Comite Euro-International du Beton. Structural Concrete: Textbook on Behaviour, Design and Performance - Updated Knowledge of the CEB/FIP Model Code 90: Volume 1-3. 1999.
- [350] Z. P. Bažant and S. Baweja. Justification and refinements of model B3 for concrete creep and shrinkage 1. statistics and sensitivity. *Materials and Structures*, 28(7):415–430, 1995.
- [351] R. Wendner, M. H. Hubler, and Z. P. Bažant. The B4 model for multi-decade creep and shrinkage prediction. In Franz-Josef Ulm, H. M. Jennings, and R. Pellenq, editors, *Mechanics and physics of creep, shrinkage, and durability of concrete*, pages 429–436, 2013.
- [352] Z. P. Bažant and S. Prasannan. Solidification Theory for Concrete Creep. II: Verification and Application. *Journal of Engineering Mechanics*, 115(8):1704–1725, 1989.
- [353] A. Flohr. *Stoffliche Aspekte des Einflusses einer Polymermodifikation auf die statischen und dynamischen Eigenschaften von Konstruktionsbeton*. Diplomarbeit, Bauhaus-Universität, Weimar, Germany, 2005.
- [354] Z. P. Bažant, M. H. Hubler, and Q. Yu. Pervasiveness of excessive segmental bridge deflections: Wake-up call for creep. *ACI Structural Journal*, 108(6):766–774, 2011.
- [355] F. Lavergne, K. Sab, J. Sanahuja, M. Bornert, and C. Toulemonde. Homogenization schemes for aging linear viscoelastic matrix-inclusion composite materials with elongated inclusions. *International Journal of Solids and Structures*, 80:545–560, 2016.

- [356] E. Schlangen and J.G.M. van Mier. Experimental and numerical analysis of micromechanisms of fracture of cement-based composites. *Cement and Concrete Composites*, 14(2):105–118, 1992.
- [357] C.-J. Haecker, E. J. Garboczi, J. W. Bullard, R. B. Bohn, Z. Sun, S. P. Shah, and T. Voigt. Modeling the linear elastic properties of portland cement paste. *Cement and Concrete Research*, 35(10):1948–1960, 2005.
- [358] V. Šmilauer and Z. Bittnar. Microstructure-based micromechanical prediction of elastic properties in hydrating cement paste. *Cement and Concrete Research*, 36(9):1708–1718, 2006.
- [359] S. Torquato. *Random Heterogeneous Materials: Microstructure and Macroscopic Properties*. Springer Science & Business Media, New York, 16 edition, 2013.
- [360] P. Acker. Swelling, shrinkage and creep: a mechanical approach to cement hydration. *Materials and Structures / Concrete Science and Engineering*, 37(4):237–243, 2004.
- [361] D. P. Gaver. Observing stochastic processes, and approximate transform inversion. *Operations Research*, 14(3):444–459, 1966.

# A | Appendix

## A.1 Computation of Hill tensors

The Hill tensors account for the shape of material phases within the RVE. For a spherical phase  $p$ , the Hill tensor reads as

$$\mathbb{P}_{\text{sph}} = \mathbb{S}_{\text{sph}} : \mathbb{C}_{\infty}^{-1}, \quad (\text{A.1})$$

where  $\mathbb{S}_{\text{sph}}$  represents the Eshelby tensor of a spherical phase. Decomposing  $\mathbb{S}_{\text{sph}}$  into its volumetric and deviatoric parts yields

$$\mathbb{S}_{\text{sph}} = \alpha \mathbb{I}^{\text{vol}} + \beta \mathbb{I}^{\text{dev}} \quad (\text{A.2})$$

with

$$\alpha = \frac{3k_{\infty}}{3k_{\infty} + 4\mu_{\infty}} \quad \text{and} \quad \beta = \frac{6(k_{\infty} + 2\mu_{\infty})}{5(3k_{\infty} + 4\mu_{\infty})}. \quad (\text{A.3})$$

For a cylindrical inclusion, with axis pointing in  $e_3$ -direction, the Hill tensors read as

$$\mathbb{P}_{\text{cyl}} = \mathbb{S}_{\text{cyl}} : \mathbb{C}_{\infty}^{-1}. \quad (\text{A.4})$$

The non-zero components of the corresponding Eshelby tensors  $\mathbb{S}_{\text{cyl}}$  are obtained as

$$\begin{aligned}
 \mathbb{S}_{\text{cyl},1111} &= \mathbb{S}_{\text{cyl},2222} = \frac{9}{4} \frac{k_\infty + \mu_\infty}{3k_\infty + 4\mu_\infty}, \\
 \mathbb{S}_{\text{cyl},1122} &= \mathbb{S}_{\text{cyl},2211} = \frac{1}{4} \frac{3k_\infty - 5\mu_\infty}{3k_\infty + 4\mu_\infty}, \\
 \mathbb{S}_{\text{cyl},1133} &= \mathbb{S}_{\text{cyl},2233} = \frac{1}{2} \frac{3k_\infty - 2\mu_\infty}{3k_\infty + 4\mu_\infty}, \\
 \mathbb{S}_{\text{cyl},1212} &= \frac{1}{4} \frac{3k_\infty + 7\mu_\infty}{3k_\infty + 4\mu_\infty}, \\
 \mathbb{S}_{\text{cyl},1313} &= \mathbb{S}_{\text{cyl},2323} = \frac{1}{4}.
 \end{aligned} \tag{A.5}$$

The tensor  $\mathbb{S}_{\text{cyl}}$  exhibits the following symmetries  $\mathbb{S}_{\text{cyl},ijkl} = \mathbb{S}_{\text{cyl},jikl} = \mathbb{S}_{\text{cyl},ijlk} = \mathbb{S}_{\text{cyl},jilk}$ .

In addition, the isotropic average of a transversally isotropic tensor  $\mathbb{T}$  can be written as [359]

$$\int_0^{2\pi} \int_0^\pi \mathbb{T}(\varphi, \vartheta) \frac{\sin\vartheta}{4\pi} d\vartheta d\varphi = \sum_{i=1}^3 \sum_{j=1}^3 \left[ \frac{1}{3} T_{iijj} \mathbb{I}^{\text{vol}} + \frac{1}{5} \left( T_{ijij} - \frac{1}{3} T_{iijj} \right) \mathbb{I}^{\text{dev}} \right]. \tag{A.6}$$

## A.2 Hydration kinetic laws of the Bernard model

This appendix summarizes the kinetic laws reported in [111]. Three stages are distinguished.

1. Dissolution of the clinker phases during the first few hours. This stage is expressed by a constant reaction rate (i.e.  $\tilde{A} = 1$ ). When a threshold degree of hydration  $\xi_{x0}$  is reached, the dissolution process is finished.

$$\tau_x(T, \phi) = \frac{t_{x0} \phi_0}{\xi_{x0} \phi} \exp \left[ \frac{E_{ax}}{R} \left( \frac{1}{T} - \frac{1}{T_0} \right) \right]. \quad (\text{A.7})$$

2. Nucleation and growth kinetic according to the Avrami phase evolution model [286]:

$$-\ln [1 - (\xi_x - \xi_{x0})] = \left\{ k \frac{\phi_0}{\phi} \exp \left[ -\frac{E_{ax}}{R} \left( \frac{1}{T} - \frac{1}{T_0} \right) \right] (t - t_{x0}) \right\}^\kappa, \quad (\text{A.8})$$

where  $k$  is the rate constant,  $\kappa$  the reaction order and

$$\tilde{A} = \frac{1 - (\xi_x - \xi_{x0})}{\{-\ln[1 - (\xi_x - \xi_{x0})]\}^{1/\kappa-1}}, \quad \tau_x(T, \phi) = \frac{1}{\kappa k} \frac{\phi_0}{\phi} \exp \left[ \frac{E_{ax}}{R} \left( \frac{1}{T} - \frac{1}{T_0} \right) \right]. \quad (\text{A.9})$$

3. Restriction of the hydration kinetics by diffusion of dissolved ions through a thickening layer of hydration products that are formed around the unhydrated clinker grains [287].

$$(1 - \xi_x)^{1/3} = -\frac{(2D)^{1/2}}{R} (t - \bar{t}_x)^{1/2} + (1 - \bar{\xi}_x)^{1/3}, \quad (\text{A.10})$$

where  $D$  is the diffusion coefficient,  $R$  is the average initial radius of the clinker particles of the cement and

$$\tilde{A} = \frac{(1 - \xi_x)^{2/3}}{(1 - \bar{\xi}_x)^{1/3} - (1 - \xi_x)^{1/3}}, \quad \tau_x(T, \phi) = \frac{R^2 \phi_0}{3D \phi} \exp \left[ \frac{E_{ax}}{R} \left( \frac{1}{T} - \frac{1}{T_0} \right) \right]. \quad (\text{A.11})$$



## A.3 Model input parameters and their stochastic properties

### A.3.1 Input parameters for the Powers model

**Table A.1:** Input parameters and their stochastic properties (mean, standard deviation - SD, probability density function - PDF) for the Powers model (\*\* - assumptions). logn - lognormal distribution, unif - uniform distribution.

Parameter	Mean	SD	PDF	Reference
Densities - $\rho$ [kg dm <sup>-3</sup> ]				
Clinker	3.15	0.15	logn	Weschke [308], **
Hydrates	2.073	0.10	logn	Constantinides [112], **
Sand	2.648	0.15	logn	Bass [320], **
Aggregates	2.648	0.15	logn	Bass [320], **
Elastic parameters - $k$ [GPa]				
Clinker	116.7	15.0	logn	Königsberger [120], **
Hydrates	18.7	2.5	logn	Königsberger [120], **
Sand	37.8	10.0	logn	Königsberger [120], **
Aggregate	37.8	10.0	logn	Königsberger [120], **
Elastic parameters - $\mu$ [GPa]				
Clinker	53.8	7.0	logn	Königsberger [120], **
Hydrates	11.8	2.0	logn	Irfan-ul-Hassan [227], **
Aggregate	44.3	10.0	logn	Irfan-ul-Hassan [227], **
Mixture parameters - $f$				
Sand content	3	–	unif (2, 4)	**
Aggregate content	5	–	unif (4, 6)	**

### A.3.2 Input parameters for the Bernard model

**Table A.2:** Input parameters and their stochastic properties (mean, standard deviation - SD, probability density function - PDF) for the Bernard model (\*\* - assumptions). logn - lognormal distribution, unif - uniform distribution.

Parameter	Mean	SD	PDF	Reference
Elastic parameters - $E$ [GPa]				
C <sub>3</sub> S	135	7.0	logn	Acker [360], Velez [149]
C <sub>2</sub> S	140	20.0	logn	Acker [360], Velez [149]
C <sub>3</sub> A	145	10.0	logn	Acker [360], Velez [149]
C <sub>3</sub> S	125	25.0	logn	Acker [360], Velez [149]
Portlandite	38	5.0	logn	Constantinides and Ulm [112]
C-S-H LD	21.7	2.2	logn	Constantinides and Ulm [112]
C-S-H HD	29.4	2.4	logn	Constantinides and Ulm [112]
Elastic parameters - $k$ [GPa]				
Sand	37.8	10.0	logn	Königsberger [120], **
Aggregate	37.8	10.0	logn	Königsberger [120], **
Elastic parameters - $\mu$ [GPa]				
Sand	44.3	10.0	logn	Königsberger [120], **
Aggregate	44.3	10.0	logn	Königsberger [120], **
Mixture parameters - $f$				
Sand content	3	–	unif (2, 4)	**
Aggregate content	5	–	unif (4, 6)	**

**Table A.3:** Input parameters and their stochastic properties (mean, standard deviation - SD, probability density function - PDF) for the Bernard model (\*\* - assumptions).  
logn - lognormal distribution, unif - uniform distribution.

Parameter	Mean	SD	PDF	Reference
Activation energies - $E_{aX}/\mathcal{R}$ [K]				
C <sub>3</sub> S	4500	-	unif (4110, 4890)	Bernard [111], Venkovic [276]
C <sub>2</sub> S	2500	-	unif (2285, 2715)	Bernard [111], Venkovic [276]
C <sub>3</sub> A	5500	-	unif (5025, 5975)	Bernard [111], Venkovic [276]
C <sub>4</sub> AF	4200	-	unif (3835, 4565)	Bernard [111], Venkovic [276]
Quantitative phase composition $m_x$				
C <sub>3</sub> S	0.622	-	unif (0.568, 0.676)	Venkovic [276]
C <sub>2</sub> S	0.152	-	unif (0.126, 0.178)	Venkovic [276]
C <sub>3</sub> A	0.106	-	unif (0.097, 0.115)	Venkovic [276]
C <sub>4</sub> AF	0.009	-	unif (0.008, 0.010)	Venkovic [276]
Densities - $\rho$ [kg dm <sup>-3</sup> ]				
Clinker	3.15	0.15	logn	Weschke [308], **
Sand	2.648	0.15	logn	Bass [320], **
Aggregates	2.648	0.15	logn	Bass [320], **

**Table A.4:** Input parameters and their stochastic properties (mean, standard deviation - SD, probability density function - PDF) for the Bernard model (\*\* - assumptions).  
logn - lognormal distribution, unif - uniform distribution.

Parameter	w/c-ratio	$\tau_{x,0}$	Mean	SD	PDF	Reference
Kinetic parameters: Reaction order – $\kappa_X$ [-]						
C <sub>3</sub> S	0.4	12.7	1.79	0.18	logn	Bernard [111]
	0.5	11.9	1.72	0.17	logn	Bernard [111]
	0.6	11.2	1.69	0.17	logn	Bernard [111]
C <sub>2</sub> S	0.4	66.1	1.03	0.10	logn	Bernard [111]
	0.5	60.9	0.96	0.10	logn	Bernard [111]
	0.6	59.8	0.90	0.10	logn	Bernard [111]
C <sub>3</sub> A	0.4	53.5	1.07	0.11	logn	Bernard [111]
	0.5	49.2	1.00	0.10	logn	Bernard [111]
	0.6	42.6	0.93	0.09	logn	Bernard [111]
C <sub>4</sub> AF	0.4	24.2	2.37	0.24	logn	Bernard [111]
	0.5	21.4	2.30	0.23	logn	Bernard [111]
	0.6	17.9	2.23	0.22	logn	Bernard [111]
Kinetic parameters: Diffusion coefficient – $D_X$ [-]						
C <sub>3</sub> S	0.4		$1.05 \cdot 10^{-10}$	$0.13 \cdot 10^{-10}$	logn	Bernard [111]
	0.5		$1.64 \cdot 10^{-10}$	$0.32 \cdot 10^{-10}$	logn	Bernard [111]
	0.6		$6.42 \cdot 10^{-10}$	$0.77 \cdot 10^{-10}$	logn	Bernard [111]
C <sub>2</sub> S	0.4		$6.64 \cdot 10^{-10}$	$0.80 \cdot 10^{-10}$	logn	Bernard [111]
	0.5		$6.64 \cdot 10^{-10}$	$0.80 \cdot 10^{-10}$	logn	Bernard [111]
	0.6		$6.64 \cdot 10^{-10}$	$0.80 \cdot 10^{-10}$	logn	Bernard [111]
C <sub>3</sub> A	0.4		$2.64 \cdot 10^{-10}$	$0.32 \cdot 10^{-10}$	logn	Bernard [111]
	0.5		$2.64 \cdot 10^{-10}$	$0.32 \cdot 10^{-10}$	logn	Bernard [111]
	0.6		$2.64 \cdot 10^{-10}$	$0.32 \cdot 10^{-10}$	logn	Bernard [111]
C <sub>4</sub> AF	0.4		$1.05 \cdot 10^{-10}$	$0.13 \cdot 10^{-10}$	logn	Bernard [111]
	0.5		$2.64 \cdot 10^{-10}$	$0.32 \cdot 10^{-10}$	logn	Bernard [111]
	0.6		$6.42 \cdot 10^{-10}$	$0.77 \cdot 10^{-10}$	logn	Bernard [111]

## A.4 The Gaver-Wynn-Rho Algorithm

The GWR algorithm is given in [330]. An analytic solution for the inverse LC transform is given with the Post-Widder formula as

$$f_k(t) = \frac{(-1)^k}{k!} p^{k+1} \frac{d^k}{dp^k} \hat{f}(p) \rightarrow f(t) \text{ for } k \rightarrow \infty. \quad (\text{A.12})$$

The numerical computation of the high-order derivatives might be difficult. Gaver [361] proposed a discrete form, which reads as

$$f_k(t) = \frac{(-1)^k \alpha (2k)!}{tk!(k-1)!} \Delta^k [\hat{f}(k\alpha/t)] \quad (\text{A.13})$$

with  $\alpha = \log(2)$   
 $\Delta$  difference operator,  $\Delta \hat{f}(nx) = \hat{f}((n+1)x) - \hat{f}(nx)$ .

The difference operator was expanded which yields

$$f_k(t) = \frac{\alpha(2k)!}{tk!(k-1)!} \sum_{j=0}^k (-1)^j \frac{k! f[(k+j)\alpha/t]}{j!(k-j)!}. \quad (\text{A.14})$$

An acceleration algorithm helps to improve the convergence of the Gaver functionals [331]. Accordingly,  $f(t)$  is approximated as

$$f(t) \approx f(t, M) = \rho_m^{(0)}. \quad (\text{A.15})$$

$M$  is an even integer and  $\rho_m^{(0)}$  is determined as follows:

$$\begin{aligned} \rho_{-1}^{(n)} &= 0, \quad \rho_0^{(n)}, \quad n \geq 0, \\ \rho_k^{(n)} &= \rho_{k-2}^{(n+1)} + \frac{k}{\rho_{k-1}^{(n+1)} - \rho_{k-1}^{(n)}}, \quad k \geq 1. \end{aligned} \quad (\text{A.16})$$

The computational precision requirement is defined as

$$\text{number of precision decimal digits} = (2.1)M. \quad (\text{A.17})$$

## A.5 List of input parameters for the empirical creep models

**Table A.5:** List of input parameters for the creep models.

Input parameter	ACI209	MC90	B3	B4	GL2000
Concrete age at loading	x	x	x	x	x
Concrete age when drying starts	x	x	x	x	x
Relative humidity	x	x	x	x	x
Volume-surface ratio	x	x	x	x	x
Cement type	x	x	x	x	x
Aggregate type				x	
Cement type	x	x	x	x	x
Cement content	x		x	x	
Water content			x		
Water-to-cement ratio			x	x	
Aggregate-to-cement ratio			x	x	
Fine aggregate percentage	x				
Air content	x				
Slump	x				
Unit weight of concrete	x			x	
Compressive strength at 28 days	x	x	x	x	x
Specimen geometry			x	x	
Curing method			x	x	



# Publications of the author

## International reviewed journals

Göbel, L.; Lahmer, T.; Osburg, A.: Uncertainty analysis in multiscale modeling of concrete based on continuum micromechanics. In: *European Journal of Mechanics - A/Solids*, 65:14-29, 2017

Göbel, L.; Bos, C.; Schwaiger, R.; Flohr, A.; Osburg, A.: Micromechanics-based investigation of the elastic properties of polymer-modified cementitious materials using nanoindentation and semi-analytical modeling. In: *Cement and Concrete Composites*, 88:100-114, 2018

Göbel, L.; Osburg, A.; Pichler, B.: The mechanical performance of polymer-modified cement pastes at early ages: ultra-short non-aging compression tests and multiscale homogenization. In: *Construction and Building Materials*, 173:495-507, 2018

Göbel, L.; Königsberger, M.; Osburg, A.; Pichler, B.: Viscoelastic behavior of polymer-modified cement pastes: Insight from downscaling short-term macroscopic creep tests by means of multiscale modeling. In: *Applied Sciences*, 8(4):487, 2018

## National reviewed journals

Göbel, L.; Mucha, F.; Kavrakov, I.; Abrahamczyk, L.; Kraus, M.: Einfluss realer Materialeigenschaften auf numerische Modellvorhersagen: Fallstudie Betonmast. In: *Bautechnik*, 95(2), 2018



## International conference papers

Göbel, L.; Osburg, A.; Lahmer, T.: Study of analytical models of the mechanical behavior of polymer-modified concrete. *20th International Conference on the Application of Computer Science and Mathematics in Architecture and Civil Engineering*, Editors: K. Gürlebeck and T. Lahmer, Weimar, Germany, 20 – 22 July 2015

Göbel, L.; Osburg, A.; Lahmer, T.: Assessment of a continuum micromechanics-based multiscale model for concrete by means of sensitivity analysis and uncertainty propagation. *VII European Congress on Computational Methods in Applied Sciences and Engineering*, Editors: M. Papadrakakis, V. Papadopoulos, G. Stefanou, V. Plevris, Volume IV, Crete Island, Greece, 5 — 10 June 2016

Göbel, L.; Mucha, F.; Jaouadi, Z.; Kavrakov, I.; Legatiuk, D.; Abrahamczyk, L.; Kraus, M.: Monitoring the structural response of reinforced concrete poles along high-speed railway tracks. *Proceedings of the International RILEM Conference Materials, Systems and Structures in Civil Engineering*, Editor: S. Thöns, pages 1-10, Copenhagen, Denmark, 21 – 25 August 2016

Göbel, L.; Bos, C.; Schwaiger, R.; Osburg, A.: Micromechanics-based prediction of the elastic properties of polymer-modified cementitious materials. *High Tech Concrete: Where Technology and Engineering Meet*, Editors: D.A. Hordijk and Luković, Maastricht, The Netherlands, 12 – 14 June 2017

Göbel, L.; Pichler, B.; Osburg, A.: Early-age experimental characterization and semi-analytical modeling of elasticity and creep of polymer-modified cement pastes. *Second International RILEM Conference On Early-Age Cracking and Serviceability in Cement-based Materials and Structures*, Editors: S. Staquet and D. Aggelis, Brussels, Belgium, 12 – 14 September 2017

Göbel, L.; Pichler, B.; Osburg, A.: Experimental analysis and micromechanics-based prediction of the elastic and creep properties of polymer-modified concrete at early ages. *International Congress of Polymers in Concrete*, Washington D.C., USA, 29 April – 1 May 2018

Flohr, A.; Göbel, L.; Osburg, A.: Microstructured polymers and their influence on the mechanical properties of PCC. *16th International Congress of Polymers in Concrete*, Washington D.C., USA, 29 April – 1 May 2018

Göbel, L.; Bos, C.; Schwaiger, R.; Osburg, A.: Relationship between microscopic and macroscopic mechanical properties of polymer-modified concrete. *The 4th International Conference on Service Life Design for Infrastructures*, Delft, The Netherlands, 26 – 29 August 2018

Göbel, L.; Osburg, A.: Korrelationen zwischen mikroskopischen und makroskopischen mechanischen Eigenschaften von polymermodifizierten Betonen. *20. Internationale Baustofftagung Ibausil*, Weimar, Germany, 12 – 14 September 2018

Göbel, L.; Königsberger, M.; Osburg, A.; Pichler, B.: Creep properties of polymer particles in polymer-modified cement pastes, quantified by means of multiscale modeling. *SynerCrete - Interdisciplinary Approaches for Cement-Based Materials and Structural Concrete: Synergizing Expertise and Bridging Scales of Space and Time*, Madeira Island, Funchal, Portugal, 24 – 26 October 2018

## Conference contributions

Schirmer, U.; Göbel, L.; Osburg, A.: Beschreibung von Phasengrenzen eines als Sichtbeton konzipierten PSCC. Poster presentation at the *GDCH-Wissenschaftsforum Chemie*, Dresden, Germany, 30 September – 02 October 2015

Göbel, L.; Bos, C.; Schwaiger, R.; Osburg, A.: Microstructural analysis of hardened polymer-modified cement pastes. Poster presentation at the *Annual KNMF User Meeting*, Karlsruhe, Germany, 21 – 22 February 2017

Göbel, L.: Influence of Experimentally Determined Material Properties on a Numerical Model. Poster presentation at the *Young Engineers Colloquium*, Bochum, Germany, 31 March 2017

Göbel, L.; Pichler, B.; Osburg, A.: Early-age elastic and viscoelastic properties of polymer-modified cement pastes derived from experimental and semi-analytical multiscale approaches. Presentation at the *GRK International Workshop 2017, Coupled Numerical and Experimental Models in Structural Engineering*, Weimar, Germany, 26 – 28 April 2017

Abrahamczyk, L.; Alkam, F.; Al Hanoun, H.; Göbel, L.; Jaouadi, Z.; Kraus, M.; Kavrakov, I.; Legatiuk, D.; Mucha, F.; Rau, S.: GRK 1462 - reference object “Poles” - monitoring system, lab experiments and long-term measurements. Presentation at the *GRK International Workshop 2017, Coupled Numerical and Experimental Models in Structural Engineering*, Weimar, Germany, 26 – 28 April 2017

Göbel, L.; Bos, C.; Bruns, M.; Schwaiger, R.; Osburg, A.: Entwicklung eines semi-analytischen Multiskalenmodells für polymermodifizierten Beton. Poster presentation at the *Tagung Bauchemie, Gesellschaft Deutscher Chemiker e.V.*, Weimar, Germany, 18 – 20 September 2017

Göbel, L.; Königsberger, M.; Osburg, A.; Pichler, B.: Early-age characterization and multi-scale modeling of polymer-modified cement pastes. Poster presentation at the *35th Danubia-Adria Symposium on Advances in Experimental Mechanics*, Sinaia, Romania, 25 – 28 September 2018